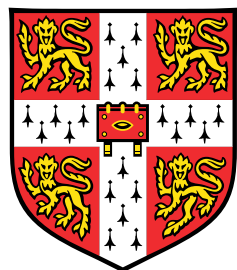


Towards Ultra-High Resolution Mode-localised MEMS Sensors



Milind Narasimha Pandit

Supervisor: Prof. Ashwin A Seshia

Advisor: Prof. Jim Woodhouse

Department of Engineering
University of Cambridge

This dissertation is submitted for the degree of

Doctor of Philosophy

Hughes Hall

October 2019

To Appa and Amma for encouraging me to take the leap of faith.

Declaration

I hereby declare that except where specific reference is made to the work of others, the contents of this dissertation are original and have not been submitted in whole or in part for consideration for any other degree or qualification in this, or any other university. This dissertation is my own work and contains nothing which is the outcome of work done in collaboration with others, except as specified in the text and Acknowledgements. This dissertation contains fewer than 65,000 words including appendices, bibliography, footnotes, tables and equations and has fewer than 150 figures.

Milind Narasimha Pandit
October 2019

Acknowledgements

My PhD experience has been enriched by the mentoring and support I have received from my supervisor – Prof. Ashwin Seshia, my advisor – Prof. Jim Woodhouse, my colleagues at the Nanoscience centre, and my family. They have all contributed towards my growth as a researcher and as a person.

Prof. Seshia has been instrumental to my progress in my PhD and my development as a researcher. His calm nature and his undoubted rigour in science resulted in a nurturing environment where I could reach my potential. Whether it be in meetings, conferences, or field trips, he has been a great role model to me and I have learnt so much under his mentorship. I really couldn't have asked for a better supervisor for my PhD.

I have never seen anyone enjoy and be fascinated by science more than Prof. Woodhouse. Sitting in his lectures and listening to him talk about mechanics, I developed a sense of inquisitiveness about my surroundings – similar to what I used to have as a child. Someday, I wish to be as mesmerised by science as he is.

This research was supported by the grants from Innovate UK and National Environmental Research Council. Members of the research team consisting of post-doctoral fellows – Dr. Chun Zhao and Dr. Guillermo Sobreviela, and engineers from Silicon Microgravity – Dr. Arif Mustafzade and Dr. Philipp Steinmann contributed in different capacities towards my PhD experience. Being mentored by so many experienced engineers helped me develop an understanding of theoretical methods, practical implementations, and problem solving skills that are crucial in any engineering project. I must convey my special thanks to Dr. Zhao and Dr. Sobreviela who acted as my mentors as well as my friends throughout this project. Dr. Zhao helped me understand and design the electronics that were key to the interface electronics. He was also instrumental in helping me build the theory surrounding the dynamics of the mode-localised sensors. Dr. Sobreviela played a key role in explaining nonlinear dynamics and noise processes in MEMS resonators to me. Dr. Mustafzade and Dr. Steinmann contributed towards ideas of building a low-noise experimental setup for the accelerometer. All of them were instrumental in contributing to my learning as a PhD student.

The nanoscience centre community was my family away from home. I count myself extremely fortunate for being part of this tight-knit community that is formed of my closest of friends and terrific mentors. I wish to convey my gratitude to everyone who made my four years here an enjoyable one; from mid-day lunches to late-night socials, the interactions I had with them formed the crux of maintaining my work-life balance throughout my PhD years. I want to thank Maria Kaimaki for always being full of energy and imparting that in every conversation we had; Géraldine Baekelandt, for being there throughout the course of my PhD with the right combination of advice and sassiness; Dr. Nicole Weckman, for being the perfect role model when I started my PhD and never short on advice when I most required it; Elisabeth Gill, for always giving me moral support whenever I was facing adversity; Théo Baissas, for mischievously bringing humour and lightness to any situation; and Kyata Chibalabala, for helping me integrate into my college and making my college life memorable. I want to include everyone else who contributed towards building a warm and open environment at the nanoscience centre – Dr. Iris Batalha, Lukas Vasadi, Sonja Kinna, Dr. Annabel Butcher, Dr. Eneko Axpe, Dr. Magali Ferro, Patrick Stipp, Dr. Atif Aziz, Dr. Simon Attwood, Dr Natasha Lewis, Malar Chellasivalingam, Dr. Adarsh Ganesan, Madan Parajuli, and Duo Zhang. Besides my colleagues at the nanoscience centre, I want to mention Margherita Gallieni and Xeno Kalogeropoulos who along with my friends from nano, made my Phd experience a very memorable one.

The journey of my PhD would have been less fulfilling if I was not able to share it with my partner Klaudia. She was the one who helped me come out of my shell in my first year and understand my potential. She was always there to listen to my frustrating days in the lab and to all the times I had a crisis about my life. She helped me persevere through those issues and was there to see me succeed in this endeavour. I am glad that you were there to witness my growth over the course of my PhD.

Finally, I want to thank my parents for always believing in my potential and backing my choice to pursue a PhD at the University of Cambridge. They gave me the hope to take the leap of faith and it has proved to be one of the greatest experiences of my life.

Abstract

Sensors employing mode localisation in weakly coupled resonators have been increasingly viewed as an alternative to resonant frequency shift based sensing. Much theory has been proposed highlighting the advantages of these sensors including the increased sensitivity and the promise of common mode rejection to first order environmental variations. This has led to the development of proof-of-concept sensors to sense physical quantities such as displacement, charge, mass, and acceleration. However, practical aspects of developing a sensor starting from design of a closed-loop implementation to understanding different operating regions with the aim of resolution analysis and noise optimisation have yet to be explored in depth. This work delves into these practical aspects of developing ultra-high resolution mode-localised MEMS sensors.

First, the mechanical sensor is integrated with a prototype closed-loop oscillator along with the interface electronics on a printed circuit board. Key aspects of sensors such as stability, noise floor, and bandwidth are analysed using this integrated sensor system. A critical observation is made on the improvement of stability of the amplitude ratio output metric over its frequency shift counterpart at large integration times therefore, highlighting the advantage of common mode rejection to environmental factors. The common mode rejection abilities of both mechanically and electrically coupled devices are next studied at different operating regions. These are then compared to the state-of-the-art differential frequency measurements. Amplitude ratio measurements in an electrically coupled device showed an order of magnitude better rejection to temperature variations over a mechanically coupled device. Furthermore, amplitude ratio measurements in the electrically coupled device were on par with the rejection offered by the differential frequency output in the same device. This result highlights the advantage of amplitude ratio measurements that are able to achieve the same common mode rejection with the help of a single oscillator instead of the two oscillators required in differential frequency output measurements.

The resolution of the mode-localised sensor is then explored with the purpose of optimising operating regions to achieve the best noise figure. A detailed theoretical analysis is first undertaken to optimise the amplitude ratio noise in different noise dominant regimes. It is

predicted that the resonator-based noise (such as thermo-mechanical noise) can be optimised by operating at an amplitude ratio of $\sqrt{2}$ and the electronic sourced noises can be optimised at an amplitude ratio of $\sqrt{1.5}$ in a single ended resonator drive configuration. Additionally, both sources of noise are predicted to decrease with the decrease of the coupling stiffness. This result is then validated using experimental data to verify the claim. A further noise reduction is sought by operating the coupled resonators in the nonlinear domain with interesting observations on the variations of the amplitude ratio output metric. The phase filtering offered by the bifurcation points in the nonlinear domain is utilised to further improve the noise by 4 times.

Finally, a mode-localised accelerometer design is proposed that employs a novel differential amplitude ratio output metric. Noise optimisation techniques are then used to optimise this novel output metric. A noise floor of $3 \mu\text{g}/\sqrt{\text{Hz}}$ with a stability of $3 \mu\text{g}$ is achieved thus, benchmarking the mode-localised accelerometer favourably with respect to other high-end commercial MEMS accelerometers. Additionally, their potential is demonstrated with a measurement of seismic activity. This measurement is then compared to reference data sourced from an accelerometer from the British Geological Survey. Lastly, suggestions are made to further optimise the resolution in the accelerometer to push the limits of amplitude ratio sensing thereby, putting mode-localised accelerometers at par with the best resonant accelerometers till date.

Table of contents

List of figures	xv
List of tables	xxi
Nomenclature	xxiii
1 Introduction	1
2 Mode-localised Sensing in Microsystems	5
2.1 Mode localisation: a historical context	5
2.1.1 Origins of mode localisation	5
2.1.2 Mode localisation in recent years	7
2.2 Theory	10
2.2.1 Eigenvalue solution	11
2.2.2 Transfer function solution	15
2.2.3 Butterworth Van-Dyke (BVD) model	17
2.3 Experiment	22
2.4 Results	25
2.4.1 Open-loop frequency response	25
2.4.2 Amplitude ratio and sensitivity	27
3 Designing a Mode-localised Sensor	31
3.1 Mechanical design summary	31
3.2 Electrical circuit design	33
3.2.1 Interface circuit	34
3.2.2 Closed-loop circuit	37
3.2.3 Closed-loop implementation using lock-in amplifiers	42
3.3 Experiment	42

3.3.1	Sensitivity analysis	43
3.3.2	Stability analysis	45
3.3.3	Bandwidth	47
4	Practical Limits to Common Mode Rejection in Weakly Coupled Resonators	51
4.1	Temperature fluctuations and MEMS resonators	51
4.2	Theory	53
4.2.1	Temperature dependence of output metrics	53
4.2.2	Variables with temperature dependence	56
4.3	Experiment	58
4.4	Results	61
4.4.1	Mechanically coupled device	61
4.4.2	Electrically coupled device	65
5	Noise Analysis	73
5.1	Sources of noise	73
5.1.1	Thermo-mechanical noise	74
5.1.2	Electronic noise	78
5.1.3	Amplitude ratio noise	85
5.2	Optimising amplitude ratio noise	86
5.2.1	Electrical noise dominant system	86
5.2.2	Resonator noise dominant system	89
5.3	Experiment	92
5.4	Results	94
5.4.1	Open-loop noise measurement	95
5.4.2	Closed-loop noise measurement	96
6	Nonlinear Characterisation of Mode-localised Sensor	101
6.1	Nonlinearity in MEMS resonators	101
6.2	Nonlinear model of a single resonator	103
6.3	Nonlinear model of coupled resonator system	106
6.4	Experiment	109
6.5	Results	110
6.5.1	Instability mapping	110
6.5.2	Sensitivity analysis	114
6.5.3	Noise floor	116

7 Mode-localised Accelerometer	121
7.1 Review of MEMS accelerometers	121
7.2 Theory	125
7.3 Experiment	128
7.4 Results	130
7.4.1 Scale factor	131
7.4.2 Noise floor	132
7.4.3 Bias stability	136
7.4.4 Bandwidth	137
7.4.5 Seismic measurement	140
8 Conclusion	143
8.1 Future work	145
8.2 Contribution of the author	147
8.2.1 Articles in international peer reviewed journals	147
8.2.2 Proceedings in international conferences	148
References	149
Appendix A Device Fabrication	165
Appendix B Resonator Model	167
Appendix C COMSOL® Simulations	171
C.1 Mechanically coupled device	171
C.2 Electrically coupled device	173
Appendix D Amplitude Ratio Noise	177
Appendix E Accelerometer Design	181
E.1 Resonator system	181
E.2 Electrical ports	184
E.3 Proof mass and force amplification levers	186

List of figures

2.1	Lumped unforced spring-mass model of 2-DoF coupled system	11
2.2	Analytical representation of the two output metrics in the two modes of 2-DoF coupled resonator system.	13
2.3	Lumped spring-mass-damper model of 2-DoF coupled system	15
2.4	Comparison between amplitude and amplitude ratio output metrics variations with stiffness perturbations in Single Ended Drive (SED) and Double Ended Drive (DED).	17
2.5	BVD model of a 1-DoF resonator system.	18
2.6	Simulated frequency response from the 1-DoF BVD model.	19
2.7	BVD model of a 2-DoF resonator system.	20
2.8	Frequency response of the coupled resonator system	20
2.9	Micrograph of an electrically coupled DETF resonator system	22
2.10	Experimental setup of the open-loop readout circuit	23
2.11	Open-loop frequency response curves of the two resonators at different states of symmetry due to applying perturbation voltage.	24
2.12	Eigenfrequencies of the in-phase and anti-phase modes and amplitudes of the anti-phase mode varying across different perturbation stiffness.	26
2.13	Amplitude ratio variation with input perturbation stiffness and the localised sensitivity to input perturbation.	27
3.1	Optical micrograph of the device.	33
3.2	Dual charge amplifier TIA using ADA4817-1 and OPA656	34
3.3	Simulated properties output noise, gain and, input-referred noise of the charge amplifier TIA configuration.	35
3.4	A second order band pass filter using ADA4898 OPAMP	36
3.5	Gain and bandwidth of the TIA	36
3.6	Experimental characterization of the gain and noise of the interface cirucit. .	37

3.7	Control loop including the resonator, amplifier and the feedback network.	38
3.8	Soft limiter circuit	39
3.9	Soft limiter operation	40
3.10	Phase shifter circuit	41
3.11	Mode-localised sensor integrated with the electronics on a PCB	41
3.12	Schematic of the experimental setup.	43
3.13	Sensitivity of various output metrics to stiffness perturbations in closed-loop (Black) and in open-loop (Red) configurations	44
3.14	Modified Allan variance of the measured a) amplitude ratio and b) frequency stability.	46
3.15	Experimental Input-referred stability.	47
3.16	Real-time monitoring of the amplitude ratio for different input perturbation frequencies (a) $f = 0.1$ Hz and (b) $f = 1$ Hz. The DC values of amplitude ratio for those particular perturbation voltages are shown in red.	47
3.17	Measured amplitude ratio, normalised to DC amplitude ratio, at different frequencies of perturbation.	48
4.1	A coupled resonator configuration used for amplitude ratio measurements .	53
4.2	Uncoupled resonators for differential frequency measurement	55
4.3	Micrographs and mode shapes of the two device structures under test. . . .	58
4.4	The measurement and temperature control setup.	60
4.5	Temperature and stiffness perturbation dependent variation in amplitude ratio and frequency in mechanical coupled resonators.	62
4.6	Sensitivity analysis of the mechanically coupled resonators.	63
4.7	Figure of merit for amplitude ratio and frequency output metrics.	64
4.8	Temperature and stiffness perturbation variation in electrically coupled res- onators.	66
4.9	Sensitivity and FOM analysis of the electrically coupled resonators.	67
4.10	Differential frequency sensitivity and cross sensitivity.	69
4.11	Figure of merit for amplitude ratio and frequency output metrics in electri- cally coupled device.	70
5.1	Simulated open-loop noise response	77
5.2	Peak open-loop noise when perturbations are added on Resonator 2	77
5.3	A transimpedance amplifier topology, with the main noise sources included schematically.	78

5.4	Schematic of forcing generated by the DC voltage sources	81
5.5	Schematic of two coupled resonators with the different DC sources and the noise associated with each source.	82
5.6	Noise comparisons in the two resonators with different noise forcings compared to the electronic pre-amplifier noise floor.	84
5.7	Input-referred noise when electrical pre-amplifier noise dominates in the sensing region.	89
5.8	Input-referred noise when resonator noise dominates in the sensing region. .	92
5.9	Optical micrograph of the electrostatically coupled resonators	93
5.10	Experimental setup to realise a closed-loop measurement.	94
5.11	Measured open-loop noise in each channel superimposed with the output voltage at the same perturbation voltage.	95
5.12	Noise spectral density of the output amplitudes of the two resonators with the different noise areas highlighted.	96
5.13	Noise spectral density of the amplitude ratio output metric at different operating amplitude ratios.	97
5.14	Localised sensitivity of amplitude ratio to input stiffness perturbations at different operating amplitude ratios.	98
5.15	Input-referred noise plotted against various amplitude ratios and coupling voltages.	99
6.1	Lumped spring-mass-damped model of a single nonlinear resonator.	103
6.2	Simulated frequency response (black dotted) and backbone curve (red dashed) for linear and nonlinear resonator.	106
6.3	Lumped spring-mass-damped system with nonlinear springs.	107
6.4	(Left) Simulated frequency response functions of the two resonators showing the <i>a-f</i> effect and (right) the frequency-phase and the amplitude ratio-phase plots showing the points where the two bifurcation points occur.	108
6.5	Optical micrograph of the device.	109
6.6	Circuit level schematic of the experimental setup.	110
6.7	Instability region mapping for the two resonators for each drive voltage. The linear response (at 10 mV drive level) is shown in black.	111
6.8	Experimental amplitude ratio-phase and frequency-phase plots showing the Bottom Bifurcation Point (BBP) and the Top Bifurcation Point (TBP).	112

6.9	Comparison of amplitude ratio at different drive voltages across a range of stiffness perturbations.	113
6.10	Sensitivity of the system to input stiffness perturbations at the top bifurcation point (TBP) and bottom bifurcation point (BBP) with dashed lines signifying the simulated results.	115
6.11	Output noise spectral density for the BBP and TBP for different drive power and different operating regions (i.e. different amplitude ratios).	117
6.12	Averaged noise around 30 Hz compared for the various different drive voltages at the TBP and BBP.	118
7.1	Lumped model of the differential 2-DoF coupled system	125
7.2	A schematic of the differential mode-localised accelerometer	126
7.3	Simulation showing the variation and the sensitivity of the two individual amplitude ratios and their difference across different perturbations at equilibrium point of AR=1	128
7.4	3-dimensional plot showing the variation of the amplitude ratio sensitivity at different individual amplitude ratios.	129
7.5	Optical micrograph of the accelerometer.	129
7.6	Circuit level schematic of the experimental setup.	131
7.7	Model of the differential mode-localised accelerometer.	132
7.8	Noise of the output metrics at AR=1 (left) and comparison of noise floor at different ARs	133
7.9	Input-referred noise floor compared at different ARs	133
7.10	Different amplitude noise sources dissected.	135
7.11	Differential amplitude ratio noise sources.	136
7.12	Bias stability characterisation of the MLRXL.	137
7.13	Open-loop characterisation of the proof mass.	138
7.14	Bandwidth analysis done at different amplitude ratios.	139
7.15	Data from the earthquake in Grimsby, UK on 9th June, 2018.	141
8.1	Prototype mass sensor design.	145
8.2	Parametric pump design for accelerometers.	146
A.1	Device fabrication process flow	166
B.1	3-d view (left) and top view (right) of the DETF resonator.	167
B.2	DETF element with geometrical variables and mode shapes assumed.	168

C.1	Mechanically coupled DETF device	171
C.2	Mode shapes of the mechanically coupled device across different perturbations showing the localisation of energy	172
C.3	Amplitude ratio variation and sensitivity to input perturbations of mechanically coupled device.	173
C.4	Electrically coupled DETF device	173
C.5	Mode shapes of the electrically coupled device across different perturbations showing the localisation of energy	174
C.6	Amplitude ratio variation and sensitivity to input perturbations of mechanically coupled device.	175
E.1	Optical micrograph of the coupled resonator system.	182
E.2	Open-loop sweep of one of the coupled resonator systems.	183
E.3	Optical micrograph of the suspensions of the proof mass.	186
E.4	A schematic of the lever for force amplification.	188

List of tables

2.1	Device parameters	22
3.1	Device parameters	33
4.1	Device parameters	59
5.1	Circuit parameters	80
5.2	Noise values for DC sources	82
6.1	Amplitude ratio at TBP and BBP at different drive voltages	114
7.1	Device parameters	130
7.2	Relationship between frequency difference between two modes and the bandwidth of the sensor.	140

Nomenclature

Greek Symbols

α	Thermal expansion coefficient
χ	Amplitude ratio equilibrium point
β	Cubic nonlinearity component
π	$\simeq 3.14\dots$
τ	Time constant

Subscripts

b	Bias
f	Feedback
p	Parasitic
Si	Silicon

Other Symbols

C	Capacitor
Δk	Perturbation stiffness
E	Elastic Young's modulus
e	Euler's number $\simeq 2.718\dots$
k_B	Boltzmann's constant ($1.38 \times 10^{-23} J/K$)
k	Resonator stiffness

k_c	Coupling stiffness
L	Inductor
m	Mass
R	Resistor
T	Ambient temperature in Kelvin
T_{CF}	Temperature coefficient

Acronyms / Abbreviations

AC	Alternating Current
AR	Amplitude Ratio
BBP	Bottom Bifurcation Point
BPF	Band Pass Filter
BVD	Butterworth Van-Dyke
C-C	Clamped-Clamped
CPM	Classical Perturbation Method
DC	Direct Current
DED	Double Ended Drive
DETF	Double Ended Tuning Fork
DoF	Degree of Freedom
FEM	Finite Element Modelling
FFT	Fast Fourier Transform
FOM	Figure of Merit
M-DoF	Multiple Degrees of Freedom
MEMS	Microelectromechanical System

MLRXL Mode-localised Resonant Accelerometer

MPM Modified Perturbation Method

NSD Noise Spectral Density

OCXO Oven Controlled Crystal Oscillator

PCB Printed Circuit Board

PLL Phase Locked Loop

PSD Power Spectral Density

RMS Root Mean Square

SED Single Ended Drive

SNR Signal to Noise Ratio

SOI Silicon On Insulator

SPICE Simulation Program with Integrated Circuit Emphasis

TBP Top Bifurcation Point

TIA Transimpedance Amplifier

Chapter 1

Introduction

Sensors are now ubiquitous. Mobile phones, automobiles, and any number of consumer electronics perform everything from finger-print recognition to airbag deployment with the help of sensors. In the span of a few decades, accelerated technological advancements have made sensors omnipresent in our lives. This was made possible with the scientific breakthrough of miniaturisation using microelectromechanical systems (MEMS) technology. MEMS describe electromechanical systems of microscopic scale lengths. Microfabrication technology used for manufacturing such devices was first shown by Nathanson [1] in 1967. Since then the technology has come leaps and bounds to being able to create devices that have capacitive gaps in the order of 13 nm [2]. Enabling technologies such as vacuum encapsulation [3] accelerated the development of MEMS resonators in the past decade. Due to their intrinsic advantage of high stability, MEMS resonators have been employed as accurate timing references [4, 5], filters [6, 7], and various sensors including but not limited to accelerometers [8–11], magnetometers, [12, 13], temperature [14], and pressure sensors [15].

Conventional MEMS resonant sensors use resonant frequency shifts as an output metric due to its quasi-digital nature. However, frequency shift output metric is limited by slow drift and random walk [16]. The resulting frequency instability of MEMS resonators can affect the long-term measurement accuracy. The long-term stability of the resonators is relevant in sensing applications that address low frequency variations in the measurand. Conventionally, long-term stability in frequency shift output is achieved by temperature compensation [17, 18] or differential cancellation specifically for sensing applications [19, 20]. These solutions have their own drawbacks. Temperature compensation electronics typically consume more power than oscillator electronics, which is less suitable for low power applications; whereas

differential cancellation becomes less effective in the presence of mismatch between the resonators [21].

This paves the way for mode-localised sensing [22, 23] that utilises an amplitude ratio output metric instead of the frequency shift output metric to provide enhanced common mode rejection capability [24, 25]. This type of sensor is based on the principle of vibration mode localisation [26], where the eigenstate or the ratio of amplitudes of two coupled resonators [27] changes when the system is subject to an external perturbation. This external perturbation can be an inertial force [28], electrostatic force [29, 30], or a mass change [31]. Furthermore, an elevated sensitivity to input measurand of up to four orders of magnitude [32] higher than conventional resonant sensors with frequency shift output paves the way for an improved input-referred stability.

Mode localisation has been studied in depth from a theoretical point of view [23, 33] with examples of experimental proof-of-concept [34, 29, 28, 22]. Yet, practical issues associated with implementing a mode-localised sensor such as oscillator design, studying operating regions, optimisation of noise, and resolution are topics that are still to be unravelled. It is important to understand the practical limitations with common mode rejection capabilities of the associated output metrics, the sources of noise that affect the coupled resonator system, and how to discern the operating point to achieve the goal of an ultra-high resolution mode-localised sensor. These aspects are analysed in depth and novel methods to improve the input-referred resolution are proposed in this thesis to advance the development of a mode-localised sensor of the same, if not better, performance than a commercial sensor employing frequency shift sensing.

Thesis overview

This thesis is split into five chapters discussing the dynamics of sensors utilising mode-localised weakly coupled resonators. The chapters discuss the theoretical study of these sensors that have been carried out till date and apply them to physical systems with the help of simulations and experimental data. Most experiments are performed on an electrically coupled device due to the added flexibility of tuning the coupling stiffness [23]. Furthermore, only a 2-DoF system is studied primarily due to the simplicity it offers with respect to tuning the device when fabrication tolerances affect the stiffness mismatch between the resonators. The higher the degrees of freedom, the more tuning ports are required making them less feasible for use as a practical sensor. A brief overview of the different chapters is provided below.

Chapter 2 introduces the concept of mode localisation in weakly coupled resonators and its development in the last five decades from its conception as ‘Anderson Localisation’ [35, 36]. It then discusses the various simulation techniques that can be used to predict the mechanical and electrical properties of the coupled resonator topology. Simulations are carried out in the form of eigenanalysis, transfer function analysis and Butterworth Van-Dyke (BVD) model analysis to cover all the different aspects of mode localisation. Finally, an experimental analysis is done to portray the application of the weakly coupled resonators as a sensor from inspecting the open-loop frequency response curves.

Chapter 3 discusses the design process taken to create an integrated, self-sustainable sensor in a closed-loop topology. The chapter delineates the design of a custom electrically coupled double ended tuning fork (DETF) resonator system, the interface circuit needed to readout the amplitude of vibrations, and the oscillator configuration implemented. Essentially, it introduces the basic building blocks of an integrated mode-localised device that can be used for applications as a physical sensor. Lastly, the stability, noise floor, and bandwidth (the three essential metrics of a sensor) of the amplitude ratio output metric are characterised while comparing it to traditional frequency shift output metric.

Chapter 4 inspects the validity of the superior common mode rejection capabilities of the mode-localised sensor from a practical standpoint. Experimental data is provided on a mechanically coupled and an electrically coupled device when operating at various temperatures to test the degree of the first order common mode rejection offered by those devices to temperature variations. The results are then compared to the state-of-the-art differential frequency measurements to gauge the advantage of using mode-localised sensors in rejecting temperature-based excursions of the output metric.

Chapter 5 includes a detailed description of all the major noise sources that affect the amplitude noise of the mode-localised sensor. Both thermo-mechanical and electronic noise sources are discussed and an expression is shown to derive the amplitude ratio noise from the noise in individual channels. Furthermore, ways to optimise the amplitude ratio noise in both thermo-mechanical and electronic noise dominant systems is presented depending on operating conditions of amplitude ratio and coupling stiffness. The theory is experimentally validated to bolster the conclusions drawn from the theoretical and analytical derivations.

Chapter 6 explores the nonlinear response of the coupled resonator system when experiencing large vibration amplitudes. It investigates the possibility of using the nonlinearity of the system to improve the signal to noise ratio of the weakly coupled resonators for sensing applications. Additionally, some of the unique ways in which operating in the nonlinear domain affects amplitude ratio are predicted using a simulation employing harmonic balance

method. Experimental data is shown for electrically coupled system to validate some of the features being predicted for the nonlinear weakly coupled resonators. Furthermore, the noise floor of the sensor is compared to its linear counterpart to test the improvement for sensing purposes.

Chapter 7 studies a custom hermetically sealed resonant mode-localised accelerometer designed to sense vibrations for applications as a seismometer. The design of the sensor is discussed along with introducing a novel differential amplitude ratio output metric that provides additional common mode rejection capabilities in a mechanically coupled sensor. Experimental studies of long-term stability, noise floor, and bandwidth are done. Lastly, a measurement of an earthquake is shown along with reference data to demonstrate the potential for mode-localised MEMS accelerometers to be utilised for seismic applications with comparable performance to existing seismometers.

Finally, Chapter 8 concludes with comments on possible future work and the route that mode-localised sensors can take hereafter.

Chapter 2

Mode-localised Sensing in Microsystems

This chapter introduces the basic principles underlying vibration mode localisation. The historical context is discussed commencing with work in the field of solid-state physics to solid mechanics and current applications in the field of MEMS. It outlines the theory of mode localisation in a coupled system using eigenanalysis, transfer function analysis, and BVD model analysis. Experimental results displaying the localisation of energy in a 2-DoF system using electrically coupled MEMS resonators are shown, bolstered with discussions around the practical issues regarding the experimental setup.

2.1 Mode localisation: a historical context

In mechanically identical coupled resonators, the vibration energy in a mode is shared equally between the resonators. Due to the effective dynamic symmetry in the system, the vibration mode extends spatially over the resonators. In a particular case of weak coupling between the two systems, a perturbation moving the system away from symmetry in the mechanical parameters such as stiffness or mass, leads to a spatial confinement of the modal vibration energy to one of the systems. This energy confinement can be quantified by an eigenstate or amplitude ratio measurement and is referred to as mode localisation.

2.1.1 Origins of mode localisation

Although discussions in this thesis will revolve around mode localisation in MEMS resonator systems, it is important to acknowledge the origins of mode localisation. Before its use in micro systems and resonator topology, mode localisation was first discovered by Anderson in the field of solid-state physics in 1958. Then, conductivity in an ideal crystal was described

by the Drude model that predicted electronic conductivity to be directly proportional to the mean free path that the free electron travels before colliding with positive ion site. The wave character of the electron paved the way to the explanation that electrons do not scatter upon colliding with the impurities but diffuse around them. This led to research on understanding how the conductivity of the lattice would change with an increase in these impurities. The popular theory at the time was that the transport of electrons reduces with the increase in the impurities in the crystal lattice. In his seminal paper [35], Anderson showed that beyond a critical amount of impurities in the semiconductor lattice, quantum-mechanical transport of electrons leads to the complete spatial confinement of the electron. This phenomenon gained the much deserved importance in the scientific community and is since then known as Anderson Localisation [36]. Since its conception, it has been applied beyond the field of semiconductor physics and is widely studied in the field of acoustics and structural dynamics.

In 1981, building on Anderson's work in solid-state physics, Hodges [37] showed that literature on periodic or symmetric acoustic systems can be misleading in a qualitative as well as a quantitative manner. He showed the effects of mode localisation in two simple mechanical models – a coupled pendulum system and vibrating string or beam constrained in its motion by a mass and spring. Using an external source to inject vibrational energy into the disordered systems, he showed that the vibrations could not propagate arbitrarily large distances but are confined close to the source. He further showed that the steady state response of the structure decays exponentially away from the source, even in the absence of any dissipation. In 1983, Hodges and Woodhouse [38] validated these theoretical predictions with experimental work that confirmed the effects of localisation in slightly disordered systems.

The work of Hodges and Woodhouse inspired many to conduct deeper analysis of the phenomenon through perturbation techniques. In 1987, Pierre and Dowell [39] used the Classical Perturbation Method (CPM) to obtain the localised modes of the perturbed system. Assuming that the eigenvalues and eigenvectors of the perturbed system were only slightly different from those of the unperturbed system, they were able to predict approximate solutions to the perturbed case using this method. They recognised that the coupling strength and the magnitude of the induced perturbations were closely related. Additionally, they showed that if the magnitude of perturbations were large in comparison to the coupling strength, the mode shapes would be highly localised. On the other hand, if the perturbations were smaller than the coupling strength, the mode shapes would be weakly localised. They recognised that CPM would be ideal to analyse a weakly localised system (where perturbations were smaller than the coupling stiffness) but would fail to predict the

solutions for a strongly localised system (where perturbations were greater than the coupling stiffness). The Modified Perturbation Method (MPM) was proposed in the same paper [39] as an alternative, efficient approach to arriving at the solution for strongly localised systems.

The Modified Perturbation Method was able to predict the occurrence of strong mode localisation by considering the coupling stiffness as an additional perturbation. Therefore, a disordered coupled system was the perturbed state and the disordered uncoupled system was the unperturbed state. Therefore, this method could be accurately used to describe strong localisation in weakly coupled systems. Two years later, Pierre and Cha [40] characterised strong localisation using MPM by stating that the degree of localisation increases as the ratio of modal coupling to perturbation decreases. They also showed that modal coupling decreases with increasing modes, and that localisation would occur more easily in higher groups of modes than in the lower ones. They concluded that if the coupling constraint is located at the node of a group of modes, the modes become very strongly localised; this result is carried into the design of weak coupling in MEMS resonators near their modal nodes.

Another phenomenon that has been closely associated with mode localisation is eigenvalue curve *veering*. Even before its proven connection to mode localisation, it was seen that when the symmetry is broken in weakly coupled identical mechanical structures, the modal eigenvalues ‘veer’ away from each other and swap trajectories [41, 42]. Pierre made the connection between strong mode localisation and eigenvalue curve *veering* in 1988 [43]. He analysed the system using MPM and showed that close eigenvalues were the common condition for both *veering* and strong mode localisation. Since his findings on pendulum and plate structures, many studies have been conducted with combined results of both eigenvalue curve *veering* and mode localisation on beams, rotors, disks, and many other structures [44–46].

2.1.2 Mode localisation in recent years

The study of mode localisation in solid mechanics paved the way for mode localisation in MEMS resonators. The promise of using electrical transduction, high stability, high quality factors, and the miniaturisation in MEMS devices opened up possibilities that were previously unachievable. MEMS devices had shown promising results as accurate timing references [47–50], filters [51, 52], and frequency shift-based resonant sensors in the form of mass sensors [53, 54], accelerometers [55–57], gyroscopes [58, 59], temperature [60], and pressure sensors [61]. However, the concepts of mode localisation in MEMS devices were unexplored until Spletzer *et al.* demonstrated the principle in the context of mass sensing

in 2006 [22]. They used a coupled cantilever configuration and reported to have achieved 20 times better sensitivity in eigenstate shifts than resonant frequency shifts when sensing a 154 pg of attached sphere of boro-silicate. Two years later, the same group showed that the sensitivity can be improved by increasing the number of coupled resonators [62]. They used a group of 15 coupled micro-cantilever arrays and achieved a 2 orders of magnitude sensitivity increase compared to their previous design of a 2-DoF system.

Soon after, a proof of concept for mass sensing, displacement sensing, and charge sensing using mode localisation in DETF, Free-Free beam, and ring resonators was shown by Thiruvenkatanathan *et al.* [63, 23, 29, 34]. Their work also included the use of a negative electrical coupling spring instead of a mechanical coupling spring that allowed the tuning of the *veering* gap and the sensitivity [23]. They were able to achieve 2-3 orders of magnitude improvement in sensitivity by measuring the shift in eigenstates compared to resonant frequency shift sensing. They also characterised many inherent features of mode localisation and concluded that the sensors were less likely to be affected by temperature and pressure drifts due to common mode rejection. Although in its early stages, this work paved the way for many others to investigate mode localisation in MEMS structures for various applications.

Mode localisation in MEMS resonators was extended to 3-DoF identical spring-mass systems to increase sensitivity (an order of magnitude more compared to 2-DoF) [64, 65]. It is generally not advantageous to have more than 2-DoF coupled system for mode-localised sensor applications since fabrication tolerances result in inherent asymmetries that deter the practicality of the sensor. This is due to the requirement of electrostatic tuning using the electrical spring softening effect to compensate for the asymmetries [23]. Thus, an increase in the number of resonators that need tuning, reduces the practicality of the sensor. Furthermore, sensing more than two amplitudes in such a system is impractical due to the noise and complexity added by the interface circuitry for each of the amplitudes. To address this issue, many groups have used M-DoF mode-localised systems but with only two output amplitudes for sensing. Zhao *et al.* proposed a novel approach at a 3-DoF system by making a middle resonator to have at least double the stiffness compared to the other two adjoining resonators [66, 67]. This increased the sensitivity by 2 orders of magnitude while utilising measurement schemes for only two resonators. His research also compared the output metrics of the eigenstate shift, frequency shift and amplitude ratio shift and concluded that amplitude ratio shift is the most sensitive [64].

Although there has been considerable work on characterising mode-localised devices in open-loop configurations, there has not been a concrete suggestion for the use of a self-oscillating loop compatible with the system so far. A self-oscillating loop maintains

the resonator at the necessary resonating frequency, making it one of the fundamental requirements of building a practical sensor [49]. Zhao *et al.* developed a transfer function method to theoretically recognise that the self-oscillating loop configuration for a 1-DoF sensor can be also used for a 3-DoF mode-localised sensor [68]. An advanced version of this configuration [69] is presented and implemented in this work.

The key application for mode localisation has been its application in developing accelerometers. The first implementation of such a sensor was by Zhang *et al.* who characterised the accelerometer in an open-loop circuit condition [28]. They used a differential perturbation configuration instead of a single perturbation configuration employed by their predecessors and showed that the sensitivity to amplitude ratio sensing can be increased twofold. Although they were able to achieve a sensitivity of $1.233/g$, they had a meagre resolution of 0.619 mg . They attributed this resolution to the noise of the electronic measuring system. Eventually, a closed-loop oscillation loop was also realised by Yang *et al.* using a Phase Locked Loop (PLL) configuration [70]. After their closed-loop implementation, the same group proposed multiple accelerometers designs with 3-DoF [71], and even 4-DoF [72] resonator systems that were designed to increase the sensitivity of the mode-localised resonators. The group has also consistently optimised its system and has shown improvement in stability achieved, with their latest work showing $157\mu g$. Although they show noise floors of a few μg , the methods they use to calculate the noise floor is contentious and not consistent with the stability values presented. Accurately calculating the amplitude ratio noise has been elaborated in Chapter 5.

Concurrently, modelling on the ultimate resolution offered by mode-localised resonators was being carried out. Juillard *et al.* [33, 73] showed through modelling that in a system dominated by thermo-mechanical noise, the resolution does not improve with a reduction in coupling stiffness; contradicting what was previously predicted by Thiruvenkatanathan *et al.* [74]. However, the analysis lacked any experimental evidence and the model hinged on a derived relation between the individual resonator amplitude noise and the amplitude ratio noise. Similarly, the method used by Juillard *et al.* has been discussed in Chapter 5 while introducing the transfer function method of deriving amplitude ratio noise.

Currently, methods used to model the noise of the amplitude ratio output metric rely on assuming its relations with the noise of the individual resonator amplitude and can only be regarded as an estimate of the amplitude ratio noise. The most accurate way of describing the amplitude ratio noise is by analysing the ratio of the two resonator amplitudes in real time and performing power spectral density (PSD) analysis to retrieve the true noise performance of the output metric. This method is pursued in detail in this work.

Other than their use for sensing, coupled resonators have been used as filters. Both active and passive electrical coupling have been realised to implement bandpass filters at various frequencies [75–77]. A particular advantage of using coupled resonators quoted by these works is the amplification of quality factor possible in coupled resonator array filters over single resonator filters. Furthermore, coupled resonators have also been used as vibration amplitude amplifier [78]. To realize this, arrays of 8 resonators are used and vibration amplification is noticed when the energy is heavily localised to one of the resonators due to the disorder in the system.

The ever increasing competition in the field has led to rapid increase in the development of research acumen in mode-localised devices and as the field grows, the potential of mode-localised MEMS devices is revealed.

2.2 Theory

Several different approaches have been previously studied and implemented to model mode localisation. The Classical Perturbation Method and Modified Perturbation Methods were used to predict modes of weakly and strongly coupled M-DoF systems for decades. Although these methods remain pertinent in modelling the mechanical behaviour of such systems, they are less useful when building an integrated model for practical applications. MEMS devices require models that capture both the mechanical and the electrical behaviour (including electronic interfaces). Thus, it is essential that the models used for MEMS devices can encapsulate the fluidity between the mechanical and electrical domains. Furthermore, since the focus in this work is on MEMS sensors, the models need to be able to predict key metrics of the MEMS-based sensor such as scale factor and noise figures.

In this section, three different models are assessed in the context of the mode-localised resonator system. First, an eigenanalysis is considered for the basic dynamics of the curve *veering* phenomenon and the trend of the amplitude ratio variation with stiffness perturbations. For simple systems, eigenanalysis remains the simplest method to predict the eigenvalues and eigenvectors of a coupled system upon the application of a perturbation. Next, the transfer function method of modelling is described. By reducing the mechanical dynamics of the resonators to a transfer function, individual amplitudes of vibration of the two resonators can be predicted at various perturbation states. This method is instrumental in predicting noise processes that occur in mode-localised resonators. Finally, a Butterworth Van-Dyke (BVD) electrical model of the resonators is derived so that they can be incorporated in a system with readout electronics and a closed-loop oscillator circuit to sustain their oscillations. A

combination of these three modelling approaches is proposed to predict the behaviour of a practical MEMS sensor.

2.2.1 Eigenvalue solution

Mode localisation in its simplest form is seen in an unforced 2-DoF mass-spring system coupled with a weak spring (as seen in Fig. 2.1). The two masses represent the intrinsic masses of the two resonators and springs represent their corresponding stiffness. They are both assumed to be similar (i.e. $m_1 = m_2 = m$ and $k_1 = k_2 = k$). The coupling spring is assumed to be far weaker than the springs of the resonators themselves ($k_c \ll k$). The disorder is applied to the system by tuning the stiffness of one of the resonators and is represented by Δk on one of the springs. It is to be noted that in this work, Δk acts as a proxy for a measurand when being implemented into a sensor. The equations of motion of the unforced system can be outlined as follows:

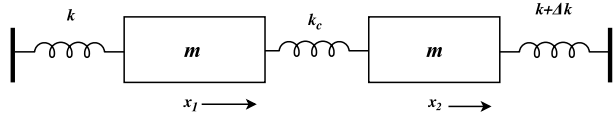


Fig. 2.1 Lumped unforced spring-mass model of 2-DoF coupled system

$$m\ddot{x}_1 + kx_1 + k_c(x_1 - x_2) = 0 \quad (2.1a)$$

$$m\ddot{x}_2 + (k + \Delta k)x_2 + k_c(x_2 - x_1) = 0 \quad (2.1b)$$

The eigenvalues can be solved for by arranging the system of equations into a matrix form:

$$\begin{bmatrix} m & 0 \\ 0 & m \end{bmatrix} \begin{bmatrix} \ddot{x}_1 \\ \ddot{x}_2 \end{bmatrix} + \begin{bmatrix} k + k_c & -k_c \\ -k_c & k + \Delta k + k_c \end{bmatrix} \begin{bmatrix} x_1 \\ x_2 \end{bmatrix} = \begin{bmatrix} 0 \\ 0 \end{bmatrix} \quad (2.2)$$

Assuming harmonic displacement, $[x_1 \ x_2]^T = u_n e^{(i\omega t)}$ ($n = 1, 2$) and $\Delta k = 0$ for the unperturbed case, the matrix can be simplified to:

$$\begin{bmatrix} -\omega^2 m + k + k_c & -k_c \\ -k_c & -\omega^2 m + k + k_c \end{bmatrix} \begin{bmatrix} x_1 \\ x_2 \end{bmatrix} = \begin{bmatrix} 0 \\ 0 \end{bmatrix} \quad (2.3)$$

The eigenvalues of the system can be found by equating the determinant of the system to zero.

$$\begin{vmatrix} -\omega^2 m + k + k_c & -k_c \\ -k_c & -\omega^2 m + k + k_c \end{vmatrix} = 0 \quad (2.4)$$

From there, the two eigenvalues of the unperturbed system can be calculated as follows:

$$\omega_1^2 = \frac{k}{m}; \quad \omega_2^2 = \frac{k+2k_c}{m}; \quad (2.5)$$

The eigenvalue for the in-phase mode is independent of the coupling stiffness since the two masses are moving in the same direction. However, in the anti-phase mode, the coupler impacts the dynamics of the system and shifts the eigenvalue by a factor proportional to itself. If the two masses were not coupled, the eigenvalue of the two subsystems would be identical (having their natural fundamental mode shape) and dependent on their individual mass and stiffness. However, due to the coupler, the eigenvalue of the anti-phase mode occurs either after or before the in-phase mode depending on whether the two masses are connected with positive (mechanical) or negative (electrical) coupling respectively.

The eigenvalues are then substituted into Eq. 2.3 and the unperturbed normalised eigenvectors can be calculated as:

$$u_{01} = \frac{1}{\sqrt{2}} [1; 1]; \quad u_{02} = \frac{1}{\sqrt{2}} [1; -1]; \quad (2.6)$$

For the unperturbed state, the two modes are: the two masses moving in-phase with each other and the two masses moving out-of-phase with each other. In a 2-DoF system, the amplitude ratio (AR) is defined as the ratio of the two resonator amplitudes when the system is operated in either of those modes. In the unperturbed case, the amplitude ratios of the two modes are as follows:

$$AR_{01} = 1 \quad AR_{02} = -1 \quad (2.7)$$

The modal amplitudes provide a good scalar representation of the localisation of vibrational energy between the two resonators. In the unperturbed state, the system is symmetric and the vibration energy is equally distributed. Therefore, the mode shapes are symmetric, corresponding to an amplitude ratio of 1. As the system is perturbed from its symmetry with a positive Δk , it should be noticed that the vibrational energy is confined to one of the resonators in the mode of operation whereas, with a negative Δk , energy is confined to the

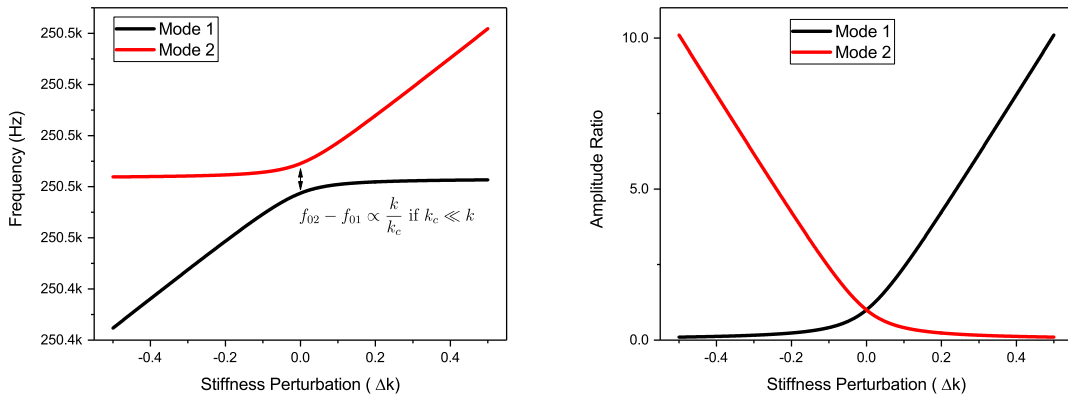
other resonator. This is seen when the same eigenvalue problem (in Eq. 2.3) is solved with a non-zero perturbation term added to the second spring-mass system.

$$\begin{vmatrix} -\omega^2 m + k + k_c & -k_c \\ -k_c & -\omega^2 m + k + \Delta k + k_c \end{vmatrix} = 0 \quad (2.8)$$

Again, the eigenvalues and eigenvectors of the system can be found by equating the determinant to zero:

$$\omega_i^2 = \frac{2k + 2k_c + \Delta k \pm \sqrt{\Delta k^2 + 4k_c^2}}{2m} \quad (i = 1, 2) \quad (2.9)$$

$$u_1 = \frac{x_{i2}}{x_{i1}} = \frac{\Delta k \mp \sqrt{\Delta k^2 + 4k_c^2}}{2k_c} \quad (i = 1, 2) \quad (2.10)$$



(a) Eigenvalue variation with stiffness perturbation.
(b) Amplitude ratio variation with stiffness perturbations.

Fig. 2.2 Analytical representation of the two output metrics in the two modes of 2-DoF coupled resonator system.

The above relations are plotted in Fig. 2.2. The values of $k = 1080$ N/m, $k_c = 0.05$ N/m, -0.5 N/m $< \Delta k < 0.5$ N/m and $m = 4.36 \times 10^{-10}$ Kg are chosen to provide a representative set of parameters corresponding to the resonators used in the experiments. Fig. 2.2a shows the variation of the eigenvalues of the two modes upon applying stiffness perturbations. The eigenvalue for the unperturbed case represents the symmetrical case where the two eigenvalues are separated by a factor proportional to $\frac{k_c}{k}$. This can be derived from taking the difference of the two eigenvalues:

$$\begin{aligned}
\omega_{0,2}^2(\Delta k = 0) - \omega_{0,1}^2(\Delta k = 0) &= \frac{k + 2k_c}{m} - \frac{k}{m} \\
\implies (\omega_{0,2} + \omega_{0,1})(\omega_{0,2} - \omega_{0,1}) &= 2 \frac{k_c}{m} \\
\implies 2\omega_{0,1}(\omega_{0,2} - \omega_{0,1}) &= 2 \frac{k_c}{k} \omega_{0,1}^2 \\
\implies \frac{(\omega_{0,2} - \omega_{0,1})}{\omega_{0,1}} &= \frac{k_c}{k}
\end{aligned} \tag{2.11}$$

From that symmetrical case, a negative perturbation in stiffness results in the *veering* of mode 1 away from mode 2 and *vice versa* for positive perturbation. It is interesting to note that the two eigenvalues never intersect each other. This phenomenon is known as mode *veering* and it is seen in conjunction with mode localisation as predicted by Pierre [39].

Fig. 2.2b shows the relation between the magnitude of amplitude ratio and the applied stiffness perturbation. The symmetric case shows the amplitude ratio of the two resonators for mode 1 and mode 2 to be equal to 1. As mentioned before, this operating point signifies the case where the vibration energy is shared equally between the two modes. With a negative perturbation from the symmetric case, the amplitude ratio of mode 2 increases while that on mode 1 reduces, showing that vibration energy is now localised to mode 2. For a positive perturbation from the symmetric case, the reverse is noticed with vibration energy localised to mode 1. This localisation effect can be used for sensing purposes where the output metric is the amplitude ratio and the input stiffness perturbations can be caused due to a measurand such as acceleration, displacement or charge.

The advantage of mode localisation for sensor design is evident when the comparisons of the sensitivities of the modal ratio shift and the frequency shift are made in the same device. Analytically, the two sensitivities around the symmetrical case simplify to:

$$S_{AR} = \left| \frac{u_i - u_{0i}}{u_{0i}} \right| = \left| \frac{\Delta k}{k_c} \right| \tag{2.12a}$$

$$S_\omega = \left| \frac{\omega_i - \omega_{0i}}{\omega_{0i}} \right| = \left| \frac{\Delta k}{2k} \right| \tag{2.12b}$$

Eq. 2.12 shows that if the condition of $|k_c| < \frac{k}{2}$ is fulfilled in the system, amplitude ratio measurements trump the resonant frequency shift measurement in terms of their relative sensitivity to stiffness perturbations. In designing mode-localised sensors, two kinds of coupling exist – mechanical, where the two resonators are coupled mechanically and electrical, where

the two resonators are coupled capacitively using electro-elastic coupling. In both cases, practical values of the coupling constant in the order of $10^{-2} - 10^{-3}$ times smaller than the stiffness of the resonators can be readily achieved. This enables a 2-3 orders of magnitude increase in sensitivity in comparison to the eigenvalue shift sensing method.

2.2.2 Transfer function solution

A transfer function solution of the mode-localised system needs to be obtained to integrate the mechanical and electrical behaviour in a unified system level model. This method allows for simulating the complex noise processes within the system and the trends of the individual vibration amplitude variation to input perturbations. The model for a 2-DoF system can setup by considering the forced spring-mass-damper system in Fig. 2.3 as a system of equations.

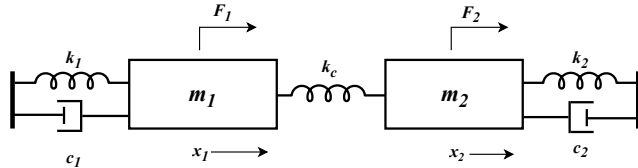


Fig. 2.3 Lumped spring-mass-damper model of 2-DoF coupled system

The equations of motion of the two resonator system can be expressed as follows:

$$m_1 \ddot{x}_1 + c_1 \dot{x}_1 + k_1 x_1 + k_c(x_1 - x_2) = F_1 \quad (2.13a)$$

$$m_2 \ddot{x}_2 + c_2 \dot{x}_2 + k_2 x_2 + k_c(x_2 - x_1) = F_2 \quad (2.13b)$$

In the Laplace domain, these equations are expressed as:

$$m_1 s^2 x_1(s) + c_1 s x_1(s) + k_1 + k_c x_1(s) = F_1 + k_c x_2(s) \quad (2.14a)$$

$$m_2 s^2 x_2(s) + c_2 s x_2(s) + (k_2 + k_c) x_2(s) = F_2 + k_c x_1(s) \quad (2.14b)$$

This can be simplified to

$$H_1(s) x_1(s) = F_1(s) - k_c x_2(s) \quad (2.15a)$$

$$H_2(s) x_2(s) = F_2(s) - k_c x_1(s) \quad (2.15b)$$

where

$$H_1(s) = m_1 s^2 + c_1 s + (k_1 + k_c) \quad (2.16a)$$

$$H_2(s) = m_2 s^2 + c_2 s + (k_2 + k_c) \quad (2.16b)$$

Using Cramer's rule, the displacement of each resonator in response to each one of the forces can be derived as follows:

$$\begin{bmatrix} H_1(s) & k_c \\ k_c & H_2(s) \end{bmatrix} \begin{bmatrix} x_1 \\ x_2 \end{bmatrix} = \begin{bmatrix} F_1 \\ F_2 \end{bmatrix} \quad (2.17)$$

$$x_1 = \frac{\begin{vmatrix} F_1 & k_c \\ F_2 & H_2(s) \end{vmatrix}}{\begin{vmatrix} H_1(s) & k_c \\ k_c & H_2(s) \end{vmatrix}}; x_2 = \frac{\begin{vmatrix} H_1(s) & F_1 \\ k_c & F_2 \end{vmatrix}}{\begin{vmatrix} H_1(s) & k_c \\ k_c & H_2(s) \end{vmatrix}}; \quad (2.18)$$

$$x_1 = \frac{F_1 H_2(s) - k_c F_2}{H_1(s) H_2(s) - k_c^2}; x_2 = \frac{F_2 H_1(s) - k_c F_1}{H_1(s) H_2(s) - k_c^2}; \quad (2.19)$$

Using Eq. 2.19, the transfer function of the displacement of resonator i due to force on the j th resonator can be described as

$$x_i = \sum_{j=1}^2 H_{ij} F_j \quad (2.20)$$

where transfer functions (H_{ij}) for various inputs and outputs can be described as follows:

$$\begin{aligned} H_{11} &= \frac{H_2(s)}{H_1(s) H_2(s) - k_c^2}; H_{12} = \frac{-k_c}{H_1(s) H_2(s) - k_c^2}; \\ H_{21} &= \frac{-k_c}{H_1(s) H_2(s) - k_c^2}; H_{22} = \frac{H_1(s)}{H_1(s) H_2(s) - k_c^2}; \end{aligned} \quad (2.21)$$

This analysis can be used to simulate the response of the individual amplitude of vibration of the two resonator system upon the application of stiffness perturbations. Ideally, the transfer function and the eigenvalue method of calculating the amplitude ratio should result in the same curve. However, since a finite quality factor is used in the transfer function method, there is a slight variation between the damped transfer function solution and the undamped eigenvalue method. Practically, the system can be excited either by using a Double Ended Drive (DED) method, where forcing is applied on both resonators or, by using a Single Ended Drive (SED) where forcing is only applied on one of the resonators while the second resonator is driven synchronously through the coupler. The expression of the individual amplitudes under SED can be shown by using only one of the force terms (F_1 or F_2) in Eq.

2.19 and setting the other to be equal to zero. This produces a slightly different amplitude variation profile as compared to that produced by DED as shown in Fig. 2.4a.

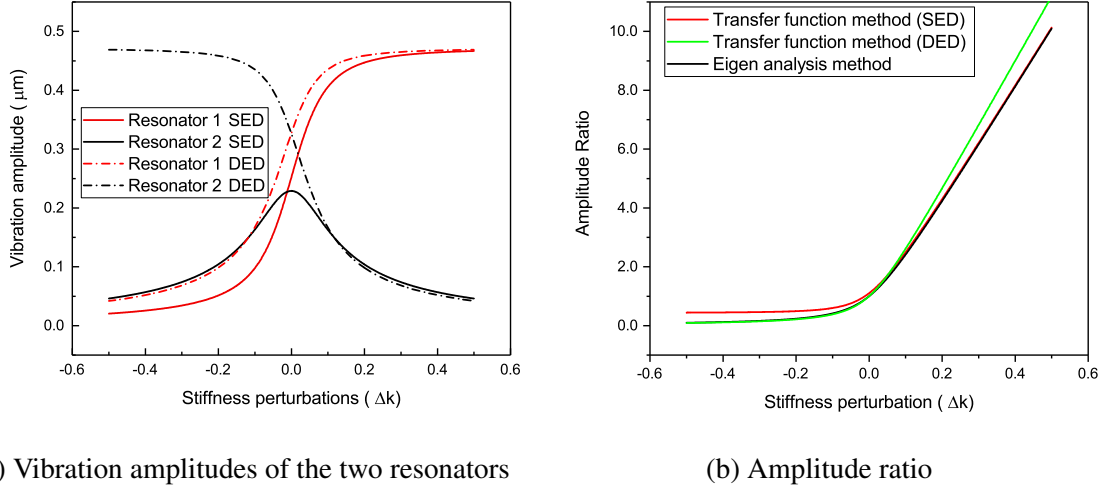


Fig. 2.4 Comparison between amplitude and amplitude ratio output metrics variations with stiffness perturbations in Single Ended Drive (SED) and Double Ended Drive (DED).

Furthermore, SED and DED influence the profile of the amplitude ratio variation profile with the application of stiffness perturbations. Fig. 2.4b shows the amplitude ratio profile of SED, DED and the analysis of the unforced system using the eigenanalysis approach are compared to each other. Either of the SED and DED methods can be employed. However, in the test structures fabricated for the experiments performed in this thesis, the DED is impractical due to the shortage of electrical ports for applying stiffness perturbations. Thus, throughout this work, only SED is used and the sensitivity plots shown in this work will reflect this behaviour.

2.2.3 Butterworth Van-Dyke (BVD) model

An equivalent electrical circuit model for the MEMS will translate the mechanical parameters of spring, mass, and damper into equivalent electrical counterparts of capacitance, inductor, and resistance respectively. This will aid simulations of the MEMS device and front end electronics in the electrical domain. Electronic circuits are usually simulated using SPICE (Simulation Program with integrated Circuit Emphasis) based simulation softwares. Having a BVD model of the resonator system helps simulate the practical integration of the resonators with the front-end electronics that use transimpedance amplifiers (TIA) and band pass filters (BPF). A model of a 1-DoF resonator system is presented in Fig. 2.5 representing the RLC

circuit for the MEMS device with the various parasitic capacitances leading to leakage currents included.

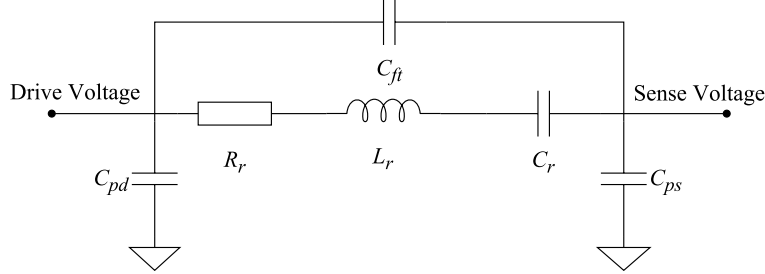


Fig. 2.5 BVD model of a 1-DoF resonator system.

Individual spring, mass, and damper values of the resonator can be converted from mechanical domain to electrical domain as follows:

$$L_r = \frac{m_{eff}}{\eta^2} \quad (2.22)$$

$$C_r = \frac{\eta^2}{k_{eff}} \quad (2.23)$$

$$R_r = \frac{\sqrt{k_{eff}m_{eff}}}{Q\eta^2} \quad (2.24)$$

where, m_{eff} is the effective mass of the resonator, k_{eff} is the effective stiffness of the resonators, Q is the quality factor of the resonator that is related to the damping constant, and η is the electro-mechanical transduction coefficient. For a symmetric capacitive transduction system, the electro-mechanical coupling coefficient depends on the area of the electrode (A_{elec}), transduction gap (g_{elec}), drive voltage (V_D), and the permittivity (ϵ) of the operating medium. It can be modelled to be:

$$\eta = \epsilon \frac{A_{elec}}{g_{elec}^2} V_D \quad (2.25)$$

Additional parasitic capacitances are added in the form of C_{ft} , C_{pd} and C_{ps} as feedthrough capacitance from the drive port to the sense port through the resonator body, parasitics from the drive and sense pads to the grounded substrate respectively. Generally, the effect of C_{ft} is a more significant than C_{pd} and C_{ps} [79] and therefore, for this simulation, C_{pd} and C_{ps} are ignored. The circuit shown in Fig. 2.5 is simulated in LTSPICE software with representative values of motional parameters $R_r = 0.1 \text{ M}\Omega$, $L_r = 500 \text{ H}$, $C_r = 1 \text{ fF}$ and $C_{ft} = 100 \text{ fF}$. Using

dimensions of the capacitive actuation similar to the experimental values shown in Tab 2.1, and a transduction voltage of 20 V, the equivalent mechanical parameters can be calculated from Eqs. 2.22-2.25 as $k_{eff} = 82 \text{ N/m}$, $m_{eff} = 41 \text{ ng}$, and $Q = 7000$. The frequency response of the two different scenarios are shown in Fig. 2.6b.

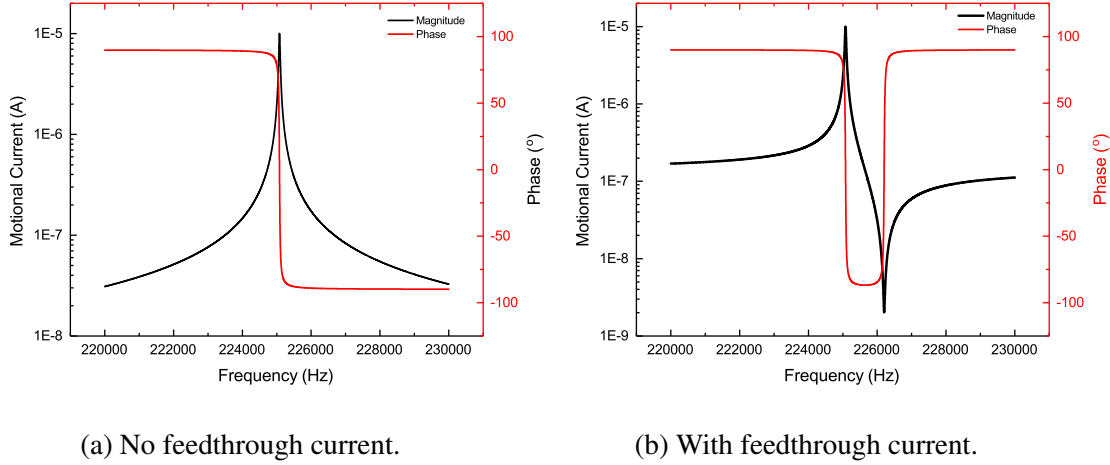


Fig. 2.6 Simulated frequency response from the 1-DoF BVD model.

As seen in Fig. 2.6b, the feedthrough current distorts the frequency response curve of the resonator by contributing an anti-resonance. The direction of the feedthrough current determines whether the anti-resonance occurs before or after the resonance peak. Although small amount of feedthrough current is to be expected in the physical systems, badly designed devices could have high amounts of feedthrough capacitances. This could potentially distort the phase and amplitude of the resonator and effect the design of oscillator systems, or accurate amplitude/frequency measurements.

This simple system can be converted into a coupled mode-localised resonator topology by adding the components for the second resonator and a coupling capacitance. The coupling capacitance must be small to ensure that the two resonator systems are weakly coupled. A circuit including the two parasitic capacitances is shown in Fig. 2.7.

The system of mode-localised resonators is simulated again in LTSPICE with test values of $R_{1r} = R_{2r} = 0.1 \text{ M}\Omega$, $L_{1r} = L_{2r} = 500 \text{ H}$, $C_{1r} = C_{2r} = 1 \text{ fF}$, $C_c = 1 \text{ pF}$, and $C_{ft} = 100 \text{ fF}$. The frequency response of the system is shown at the symmetric condition ($C_{2p} = 0 \text{ F}$) and the asymmetric condition ($C_{2p} = 200 \text{ fF}$) in Fig. 2.8. Using dimensions of the capacitive actuation similar to the experimental values shown in Tab 2.1, and a transduction voltage of 20 V, the equivalent mechanical parameters can be calculated from Eqs. 2.22-2.25 as $k_{eff} = 82 \text{ N/m}$, $k_c = 0.082 \text{ N/m}$, $\Delta k = 0.4 \text{ N/m}$, $m_{eff} = 41 \text{ ng}$, and $Q = 7000$. The arrow

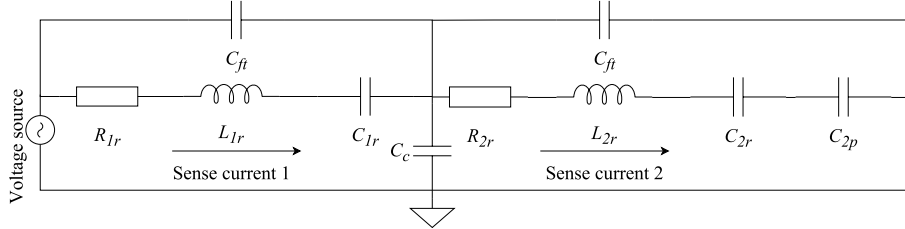


Fig. 2.7 BVD model of a 2-DoF resonator system.

indicates the measured motional current which is the representative current produced by the resonator when it is resonating at its natural frequency. The first mode is described to be the in-phase mode and the second as the anti-phase mode due to the phase conditions seen at the output of each resonator. Localisation is clearly seen in the motional current measurement of each resonator between the symmetrical (Fig. 2.8a) and asymmetrical state (Fig. 2.8b). The effects of modal overlap and feedthrough currents clearly affect the amplitude measurements and are further addressed in detail.

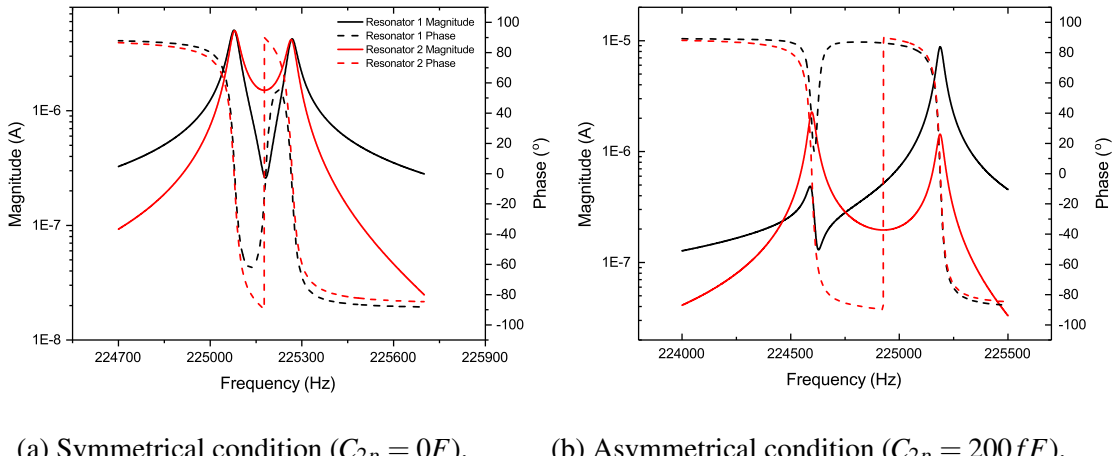


Fig. 2.8 Frequency response of the coupled resonator system

Modal overlap

A salient feature seen in Fig. 2.8a is that the two modes of vibration are on the verge of overlapping with each other due to the limited quality factor of the resonators. Modal overlap is detrimental to the closed-loop applications of the coupled resonators and needs to be avoided. The modal overlap depends directly on the difference between the natural frequency of the two modes (ω_{01} and ω_{02}) and the quality factor of the two resonators in question. As

seen in Fig. 2.8a, that the closest the two eigenfrequencies approach each other is in the symmetrical case, or the *veering zone*. So if the two eigenvalues are distinguishable at the *veering point*, they should be distinguishable at any other point along the symmetry breaking conditions. The key condition to be fulfilled for this is:

$$\omega_{02} - \omega_{01} \geq \frac{\Delta\omega_{01}}{2} + \frac{\Delta\omega_{02}}{2} \quad (2.26)$$

Where $\Delta\omega$ is the width of each modal spectrum that is dependent on the quality factor. Now, if the quality factors of both these modes are assumed to be similar and the two frequencies are close enough so that $\omega_{01} \approx \omega_{02}$, Eq. 2.26 can be approximated to be:

$$\omega_{02} - \omega_{01} \geq \frac{\omega_{01}}{Q} \quad (2.27)$$

Hence, there is a direct relationship between the modal overlap and the quality factor. This means that the quality factor of the resonators needs to be high enough for low modal overlap. One of the dominant causes of quality factor reduction in capacitive devices is the presence of fluid damping. In order to reduce fluid damping, these devices need to be either operated in a vacuum chamber or sealed in hermetic packaging for practical applications. If low Q factor devices need to be used, feedback control can be used to introduce stable negative damping to avoid expensive packaging [80].

Feedthrough current

Another feature seen in Fig. 2.8 is the detrimental effect of feedthrough on the frequency response of the resonators. As the system is transduced in a SED, the feedthrough in the driven resonator is much higher than in the other. In this case, the feedthrough current limits the dynamic range of the sensor if it exceeds the motional current. Furthermore, in such a case, the phase conditions required for the oscillation loop by the Barkhausen conditions are not met. To ensure that the dynamic range is not limited, high feedthrough currents are not desirable. Some ways to reduce parasitic capacitance are to have the drive and sense pads far from each other with sufficient separation between parallel metallic traces for drive and sense purposes. Additionally, once the sensor is mounted on to a chip carrier and a printed circuit board (PCB) is used for the motional current readout, the electrical feedthrough from the traces on the PCB will also add to the parasitic capacitance. To reduce those parasitics, the sense signal tracks should be isolated from the drive signal traces and the channels measuring the two motional currents should be kept on separate sides of the PCB.

2.3 Experiment

The simulations outlined here capture the dynamics of the coupled resonator system. A representative experiment is now shown to validate the results of the simulation and to understand the issues underlining mode localisation in coupled resonators from a practical standpoint.

The device used for this experiment is an electrically coupled Double Ended Tuning Fork (DETF) resonator system. It is manufactured using SOIMUMPS® process, a commercial foundry process using silicon-on-insulator (SOI) wafers by MEMSCAP Inc. Durham, NC, USA. The device parameters and key experimental quantities are outlined in Tab. 2.1.

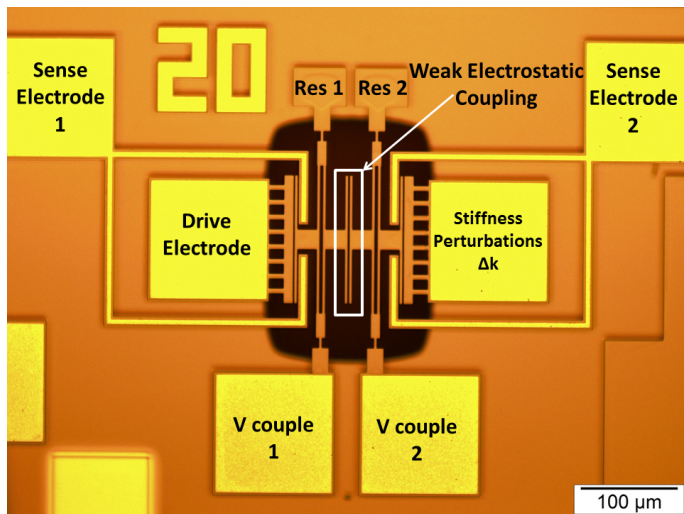


Fig. 2.9 Micrograph of an electrically coupled DETF resonator system

Table 2.1 Device parameters

Parameter	Dimensions
Beam Length	350 μm
Beam Width	6 μm
Electrode Length	260 μm
Electrode Width	6 μm
Device Layer Thickness	25 μm
Proof Mass (2 for each DETF)	40 $\mu\text{m} \times 40 \mu\text{m}$
Electrode Gaps	2 μm
Computed Resonator Stiffness (k)	1080 N/m
Computed Resonator Mass (m)	0.45 μg
Computed Resonance Frequency (f_0)	245 kHz
Experimental Quality factor (Q)	10000

In this experiment, only an open-loop characterisation is carried out with a SED configuration. A SED is chosen due to the restrictions on the number of electrodes available on the device. A Zurich Instruments HF2LI is used as the signal generator and as a two channel frequency response analyser. The coupling stiffness is realised by applying DC voltages on the two resonator bodies. In this case, V_{DC1} is set to 0 V whereas V_{DC2} is set to 10 V to realise a coupling voltage of $V_c = 10$ V. Resonator 1 is always defined as the resonator that is being driven directly by the HF2LI and Resonator 2 as the resonator that is driven through the coupler to which perturbations are being added. Perturbations are added to Resonator 2 in the form of a voltage on the perturbation electrode. This voltage is converted into a negative perturbation due to the presence of the capacitor between the resonator electrode plate and the perturbation electrode [23].

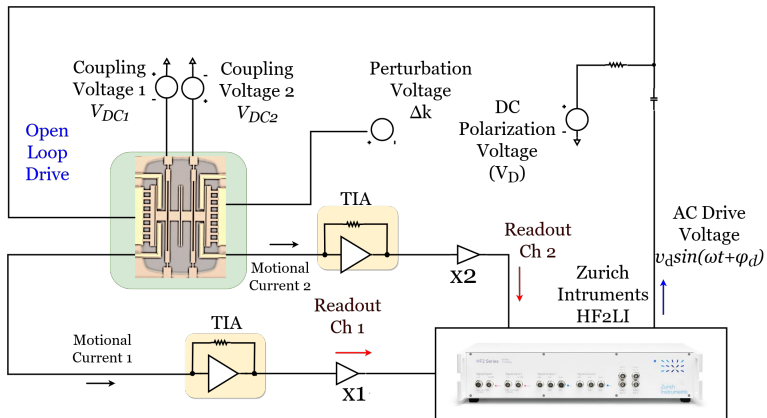


Fig. 2.10 Experimental setup of the open-loop readout circuit

The AC drive voltage from the HF2LI is passed through a Bias-T (a three port method of setting a DC bias point at the sense node of the sensor without disturbing the AC component of sense current) with a DC polarising voltage of 20 V. The motional current from both resonators is first passed through a transimpedance amplifier (Analog Devices ADA4817) to convert it to a voltage and then through a buffer before being recorded by the frequency response analyser of the HF2LI. A Bias-T is also used on the output node with a DC voltage of 60 V for a good transduction of the motional sense current.

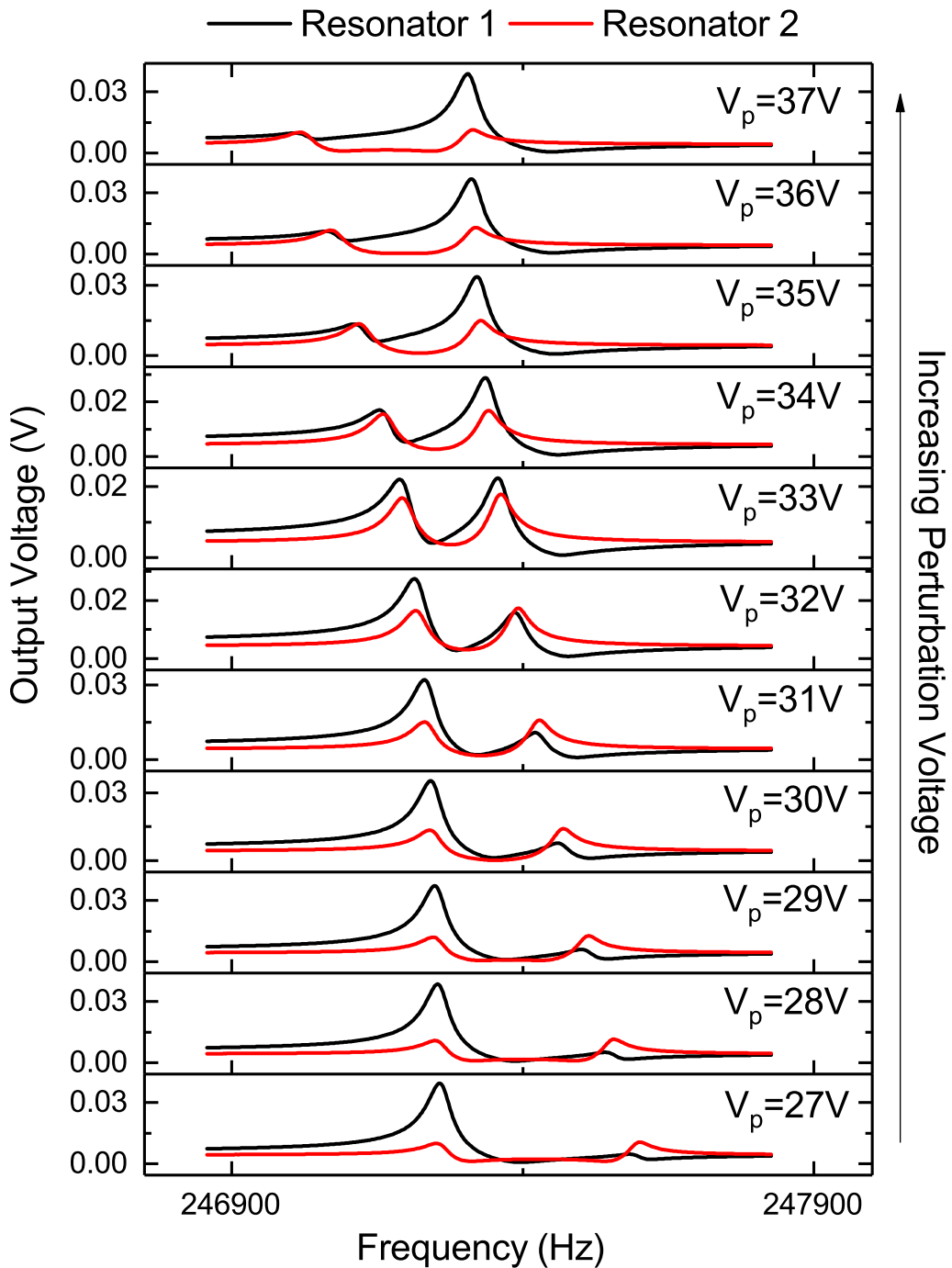


Fig. 2.11 Open-loop frequency response curves of the two resonators at different states of symmetry due to applying perturbation voltage.

2.4 Results

2.4.1 Open-loop frequency response

The frequency is swept around the vicinity of the resonant frequencies using the HF2LI and the response of each channel is recorded. The stiffness of Resonator 2 is changed by increasing the perturbation voltage resulting in vibration mode localisation. The results are plotted in Fig. 2.11 with 11 different perturbation voltages highlighting the energy transfer that occurs between the two modes as well as the two resonators in the same mode. It is to be noted that the resonators are not perfectly matched due to fabrication tolerances and accordingly need a high voltage to be brought to the symmetrical state (in this case ~ 33 V). It can be clearly seen that when the perturbation voltage is increased, amplitude of mode 1 (in-phase mode) of Resonator 1 decreases whereas that of mode 2 (anti-phase mode) of the same resonator increases. As expected of the SED configuration, the amplitude of Resonator 2, on the other hand, increases for both modes together until the symmetric condition (achieved ~ 33 V) and before reducing again. In this case, the feedthrough current is quite low and allows for a wide range of operation between amplitude ratios of 1 to 4 for mode 1 and amplitude ratios of 0.5 to 3.5 for mode 2. Any further change in the symmetry results in the motional current of one of the resonators to be comparable to the feedthrough current and therefore rendering it impractical to be used for sensing purposes. In practice, either mode can be used in a sensing context but for this study, mode 2 (anti-phase mode) will be considered.

Fig. 2.12a illustrates the frequency and amplitude at the peaks of each of the modes of the frequency response curves shown in Fig. 2.11 plotted with respect to the applied perturbations. The resonant frequencies of the two modes plotted this way leads to the *veering* plot which has been described widely in coupled systems. As the perturbations are added, it is seen that the two resonant frequencies come close to each other until the *veering* zone at which point they veer away from each other. The *veering* zone is described as the region in the plot with the smallest difference between the two resonant frequencies. This is an important value since it allows us to estimate the real coupling stiffness that is being generated by the coupling voltage applied to the system. The theoretical estimation of the coupling voltage in the test device can be derived by equating the mechanical and electrical forces in a capacitive plate as:

$$k_{c,analytical} = -\frac{\epsilon_0 A_{cap}}{g_{elec}^3} V_c^2 = -0.72 \text{ N/m} \quad (2.28)$$

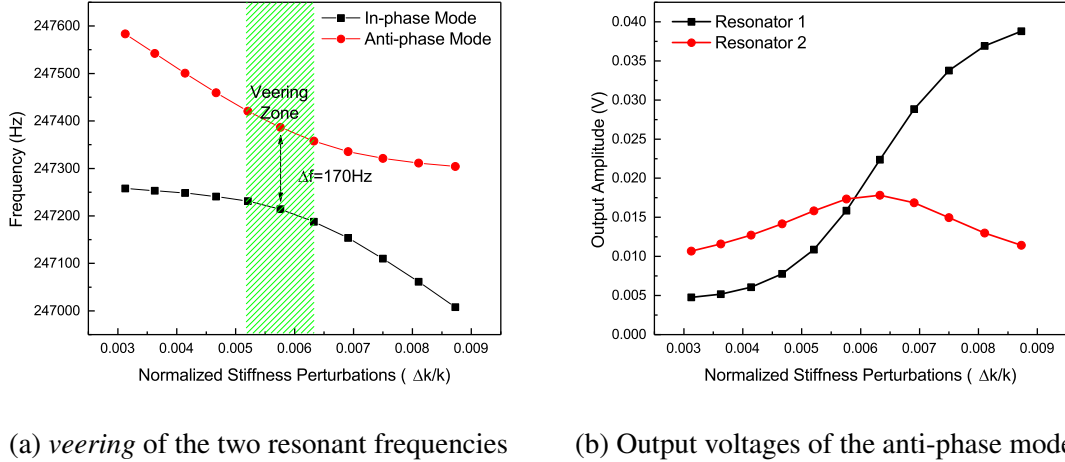


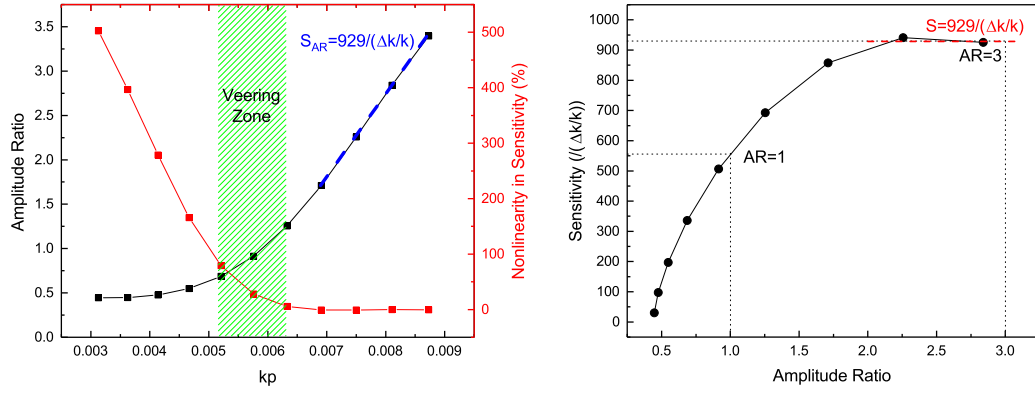
Fig. 2.12 Eigenfrequencies of the in-phase and anti-phase modes and amplitudes of the anti-phase mode varying across different perturbation stiffness.

Furthermore, the experimental calculation of the coupling stiffness (k_c) can be estimated by taking a frequency difference of the two resonant frequencies in the symmetric condition as is seen at the *veering* zone (as shown in Eq. 2.11). The frequency difference around *veering* is seen to be 170 Hz and the resonant frequency is seen to be 247 kHz. The stiffness (k) is calculated to be 1080 N/m and through this relation, the experimental k_c is estimated to be -0.743 N/m . This is quite close to the calculated k_c and it can be concluded that the fabrication tolerances are minimal. This method of calculating coupling stiffness is useful in mechanically coupled devices where the theoretical estimation of the coupling stiffness is complex.

Fig. 2.12b displays the output voltages of the two resonators of the anti-phase mode (mode 2). These can be regarded to be synonymous with the vibration amplitudes. As expected of the SED configuration, the amplitude of the driven resonator (Resonator 1) increases with the increase in perturbations whereas that of Resonator 2 increases to the symmetrical condition and then decreases with the further increase in perturbations. Since the *veering* zone is representative of a symmetric resonator system, it is expected to see an amplitude ratio of 1 there. In ideal systems, the *veering* would occur at $\Delta k/k = 0$. However, here it occurs at $\Delta k/k = 0.006$ which can be associated to the fabrication tolerances that lead to the production of an asymmetric system of resonators.

2.4.2 Amplitude ratio and sensitivity

The amplitude ratio (AR) can then be calculated for each of these perturbation values by taking the ratio of the amplitude of the Resonator 1 and Resonator 2. The result of this is plotted in Fig. 2.13a against input stiffness perturbations.



(a) Amplitude ratio of mode 2 varying across added stiffness perturbations. (b) Localised sensitivity variation across the different operating amplitude ratios.

Fig. 2.13 Amplitude ratio variation with input perturbation stiffness and the localised sensitivity to input perturbation.

Three main regions can be highlighted in this plot – the *veering* region (around $AR \sim 1$), the region where $AR > 1$ and the region where $AR < 1$. The region where $AR > 1$ is where the energy gets localised to the driven resonator (in this case Resonator 1) and the variation of amplitude ratio with respect to stiffness perturbations is linear. The *veering* region is where the two resonators are matched in stiffness and the energy tends to be equally distributed between the two resonators. The amplitude ratio here tends to vary nonlinearly with input stiffness perturbations. The region of $AR < 1$ is where the vibration amplitudes of both resonators are low and from the perspective of the signal to noise ratio is not an ideal operating region. Thus, this region is not considered for analysis.

Fig. 2.13a shows the nonlinearity in the variation of amplitude ratio is also plotted in reference to the constant sensitivity of the system at $AR > 1$ (in this case $929/(\Delta k/k)$). The nonlinearity in the scale factor is very small at high amplitude ratios and gradually increases as the amplitude ratio decreases. It is generally expected of sensors to have a linear variation in the output metric resulting in a constant scale factor. If a constant scale factor is paramount, operating at a higher amplitude ratios might be considered. However, there are many advantages to working around the *veering* zone (especially with optimising the

noise) that will be discussed in later chapters. Hence, a plot showing the local sensitivity is illustrated in Fig. 2.13b to aid the understanding of how the sensitivity changes with the operating amplitude ratio. The sensitivity at large amplitude ratios shows an asymptotic behaviour which is consistent with Fig. 2.13a. The sensitivity at *veering* ($AR \sim 1$) is a lot lower than that at higher amplitude ratios and analytically is half of the sensitivity at the constant sensitivity region. The sensitivity below $AR \sim 1$ reduces further until it is no longer viable for use as a sensor due to the low signal to noise ratio, low sensitivity and low linearity of the amplitude ratio variation. Although it is desirable to operate in the constant sensitivity region, operating around the *veering* is not a great hindrance. The system can be run in a feedback loop to keep the resonator system operating around a particular amplitude ratio or the sensitivity can be calibrated so that the nonlinear variation in sensitivity is no longer an issue.

The process of finding an optimum operating amplitude ratio requires much thought and will differ depending the specifications needed for the sensor. Since the mode-localised sensor is versatile, it can be operated at different amplitude ratios for various applications. Optimum operating points will be detailed in later chapters from the perspective of sensitivity, resolution, bandwidth, and building an oscillator.

Summary

This chapter discusses the basic operation of weakly coupled mode-localised resonator with an emphasis on establishing the dynamics of a coupled resonator system from a modelling and experimental perspective. Various modelling techniques reveal different aspects about the dynamics of the coupled resonator topology. A simple eigenanalysis is helpful in understanding the variation of the amplitude ratio and eigenfrequencies with input stiffness perturbations as a measurand. The transfer function approach is useful to model the variation of the amplitude of each resonator, and for estimating the noise in each resonator (discussed later in Chapter 5). The BVD model allows us to understand the electrical aspect of sensing the two resonator amplitudes and highlights potential issues with the feedthrough current. From the experimental open-loop analysis, frequency *veering* is observed in the frequency response curves and is critical in experimentally estimating the coupling stiffness. The amplitude ratio variation trend with input stiffness perturbation is intrinsically nonlinear at low amplitude ratios (around $AR \sim 1$) whereas it becomes linear at higher amplitude ratios. Localised sensitivity around a chosen amplitude ratio is important to characterise to facilitate the operation of the sensor at different amplitude ratios depending on the application. Future

chapters focus more on the choice of particular operating amplitude ratios and coupling stiffness for a variety of applications.

Chapter 3

Designing a Mode-localised Sensor

The path to building an integrated mode-localised sensor requires the incorporation of the mechanical sensor components with the front-end electronics and a self-sustaining oscillator. This chapter describes the necessary considerations for building a practical mode-localised sensor. For the scope of this study, the sensor modules comprising of weakly coupled MEMS resonators, front-end electronics including low noise TIA and a band pass filter, and a self-oscillating loop are considered. The design process of each of these components is detailed with explanations on the rationale behind them.

3.1 Mechanical design summary

The core of the sensor is the micromechanical resonator system that is manufactured using a silicon-on-insulator (SOI) process. The fabrication process is outlined in Appendix A.

The device considered for the test structure is an electrically coupled MEMS resonator system. Due to the high quality factor and low anchor losses, a DETF configuration was chosen for the experiments over simple clamped-clamped beam resonator. Before fabrication, an analytical model of the DETF resonator was created to aid with the design process (detailed in Appendix B). The two DETF resonators are coupled using an electrostatic coupling instead of a mechanical coupling. Since the coupling stiffness can be tuned simply by controlling the voltage between the two resonators [23], electrostatic coupling offers the flexibility needed in test structures for a variety of experiments. Furthermore, electrostatic coupling can offer lower absolute values of coupling spring constant than mechanical coupling [23] for realising highly sensitive mode-localised sensors.

The resonator needs to be compatible with the front-end electronics and the oscillator topology. The dimensions of the DETF are governed by several conditions that must be met

from the perspective of oscillator choice, power handling of the resonator, and transduction method.

Oscillator requirement

A direct feedback oscillator is chosen in this implementation of a closed-loop sensor. This topology is chosen due to its simplicity and is apt for the first implementation of an oscillator for mode-localised sensor. More complex oscillators can be proposed in the future to optimise different aspects of the sensor. The direct feedback oscillator works best when the resonator has a high power handling ability, a low resonant frequency, and low feedthrough current.

Power handling

The power handling ability is a measure of the energy stored in the resonator. This ability reduces when the size of the resonators is decreased. Since the direct feedback oscillator requires a greater power handling ability, narrow beams are avoided when designing the DETF resonators. The aspect ratio of the length to width of the resonator is set to 100:1 by the manufacturing process. This guides the design of the length of the resonators. Furthermore, to avoid stiction issues with fabrication, long beams are avoided. All these factors are considered when designing the DETF resonators.

Transduction method

Electromechanical transduction in SOI resonators is done capacitively. The most common kinds of capacitive transduction employ either a parallel plate capacitor or a comb-drive capacitor. A parallel plate capacitor allows for greater transduction force but is inherently nonlinear in its operation; whereas comb-drive transduction offers lower drive force but is linear in its behaviour. The higher the drive force, the larger the amplitude of vibration, and higher the motional current. However, if the drive force is too small, the motional current of the resonator would be too low, and the signal to noise ratio would be affected. Therefore, a parallel plate configuration with a large sensing electrode and a small transduction gap is desired since it increases the motional current being sensed.

These are some of the main factors that need to be considered in the process of designing the micromechanical resonator system. Significant optimisation needs to be performed to tune these parameters and some compromises need to be made in arriving at the final design. These optimisations are done using finite element modelling (FEM) using COMSOL®. The

details of the COMSOL® simulation including the mode shapes, eigenfrequencies and the sensitivity estimations of the device are shown in Appendix C.

The dimensions of the device were derived from previous operating designs that showed resonant frequencies and quality factors consistent with the requirements for this work. These were confirmed using FEM simulations as shown in Appendix C. An optical micrograph of the device is shown in Fig. 3.1 and the dimensions are described in Table 3.1.

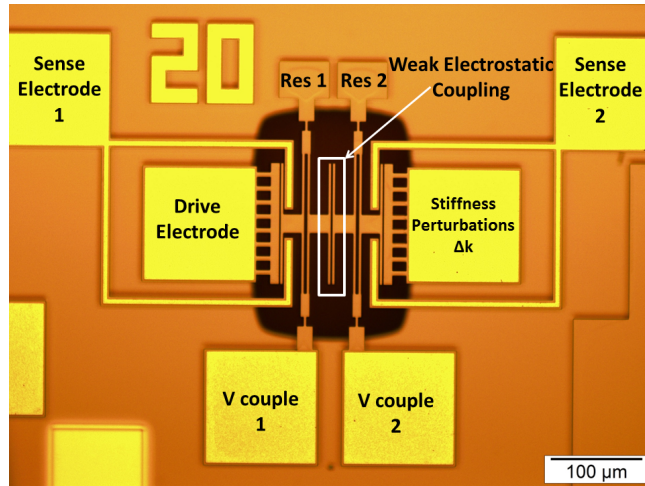


Fig. 3.1 Optical micrograph of the device.

Table 3.1 Device parameters

Parameter	Dimensions
Beam Length	350 μm
Beam Width	6 μm
Electrode Length	260 μm
Electrode Width	6 μm
Device Layer Thickness	25 μm
Proof Mass (2 for each DETF)	40 $\mu\text{m} \times 40 \mu\text{m}$
Electrode Gaps	2 μm
Computed Resonator Stiffness (k)	1080 N/m
Computed Resonator Mass (m)	0.45 μg
Computed Resonance Frequency (f_0)	245 kHz

3.2 Electrical circuit design

The interface circuit is closely tied with the design of the MEMS resonator. A key component of the front-end electronics includes the circuitry that converts the motional current of the

resonator into voltage using a trans-impedance amplifier (TIA) and then a band pass filter (BPF) to reduce the broad band noise in amplitude measurements. Additionally, to sustain the oscillation of the resonators, an oscillator needs to be designed to conclude the integration of all the components needed for a mode-localised sensor.

3.2.1 Interface circuit

The interface circuitry is used for preliminary experimental analysis about the various characteristics of the resonators and sensors. In this process, the resonant frequencies, amplitude of the modes and quality factors of the devices are measured. The design and simulation results of the TIA and the BPF are detailed further.

TIA configuration

A dual stage charge amplifier circuit using ADA4817-1 and OPA656 for the first and second stage operation amplifiers is chosen as the TIA. A schematic of such a circuit is shown in Fig. 3.2. In the schematic, the resonator is illustrated as a current source; the parasitic capacitance due to bond wires and packaging is chosen to be 10pF; the gain resistor is chosen to be $1\text{G}\Omega$; and the parasitic capacitance between the pads of the gain resistor is chosen to be 150fF .

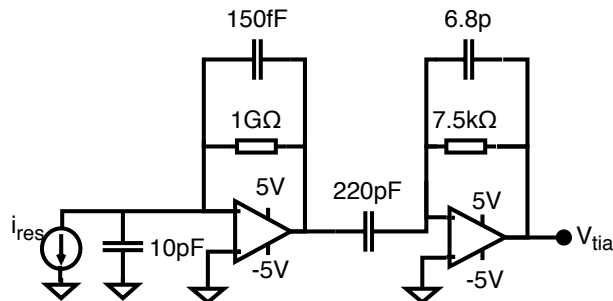


Fig. 3.2 Dual charge amplifier TIA using ADA4817-1 and OPA656

Using SPICE simulation, the circuit above can be simulated for its noise performance and its gain values. Fig. 3.3 shows the results of the simulation for the TIA circuit. The resonators in this work have a resonant frequency in the range of 250 kHz which has been marked as the operating region. A charge amplifier is chosen for the TIA configuration for the high gain and the low noise it offers as compared to conventional TIA. High gain allows for higher output voltages without the need for high drive voltages that could lead to nonlinear effects in the resonator. Furthermore, high output voltages are crucial in amplitude measurements since the signal to noise ratio in the case of an electronic noise dominant system is entirely

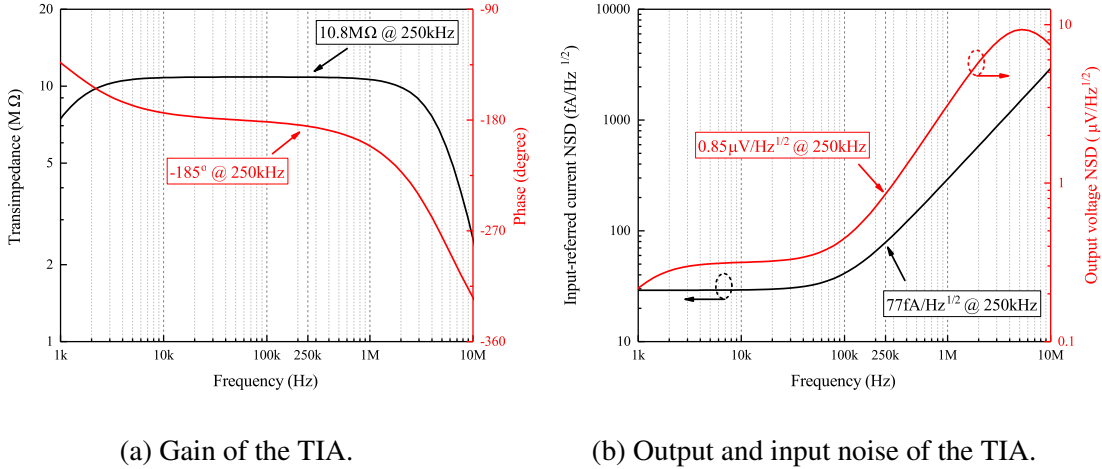


Fig. 3.3 Simulated properties output noise, gain and, input-referred noise of the charge amplifier TIA configuration.

dependent on the magnitude of the sense voltage. The first stage maximises the gain; but, the charge amplifier does not have a flat gain or phase around the frequency of interest. Thus, the second stage of a differentiator is added to shift the phase by -180° and flatten the gain around the operating region. The gain and phase response of the TIA is shown in Fig. 3.3a. The noise of the circuit is also simulated and the results are plotted in Fig. 3.3b. The output noise describes the voltage noise seen at the output of the TIA. The input-referred noise is acquired by dividing the output noise with the gain of the amplifier. This metric gauges the equivalent current noise that is added to the motional current before the amplifier stage. The output noise is seen to be $0.85 \mu\text{V}/\sqrt{\text{Hz}}$ whereas due to the high gain the input-referred current noise is only $77 \text{ fA}/\sqrt{\text{Hz}}$.

The current noise in Fig. 3.3b decreases at lower frequencies with a corner frequency around 100kHz. If the resonant frequency of the device was below that corner, the noise could be reduced by 5 times. Therefore, this TIA configuration is best suited for operating at under 100 kHz. However, it provides the best noise performance for the range of operation and the bandwidth required for this implementation. Future breakthroughs in the TIA technology could potentially improve the noise floor, leading to higher resolution measurements.

Band pass filter

Band pass filters are quintessential in amplitude measurements to restrict the amplitude noise. A simple second order band pass filter as shown in Fig. 3.4 is implemented to allow for a small bandwidth around the resonant frequency with sharp cut-off. The frequency

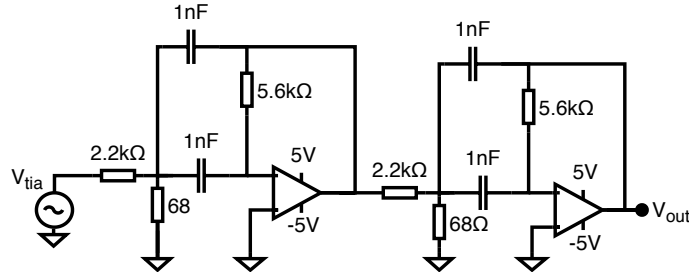


Fig. 3.4 A second order band pass filter using ADA4898 OPAMP

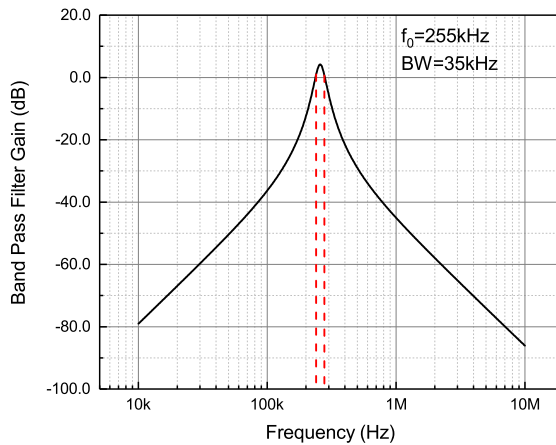


Fig. 3.5 Gain and bandwidth of the TIA

response of the band pass filter is shown in Fig. 3.5. The center frequency of 255 kHz is achieved with the closest available commercial resistor and capacitor values; besides, a bandwidth of 35 kHz is chosen to have a quasi-flat gain in the operation range while ensuring the out-of-band components are heavily suppressed.

The noise models and the properties of the interface circuitry used in SPICE simulations are helpful in the initial design of the electronics. However, they need to be experimentally verified for their accuracy. Therefore, an experiment is conducted after assembling the electronics for the noise and gain of the interface electronics. A wide frequency band is chosen for gain measurement (shown in Fig. 3.6a) to capture the effect of the band pass filter. A filter bandwidth of 40 kHz is measured around a center frequency of 250 kHz. The gain measured from the interface circuit is almost double of what was seen from the model of the TIA. This can be attributed to the variation in the parasitic capacitance around the pads of the gain resistor and variability of the real components from the ideal ones used in the model.

There is also a difference in the gain of the two channels and this is attributed to the variation in the parts used for the two channels.

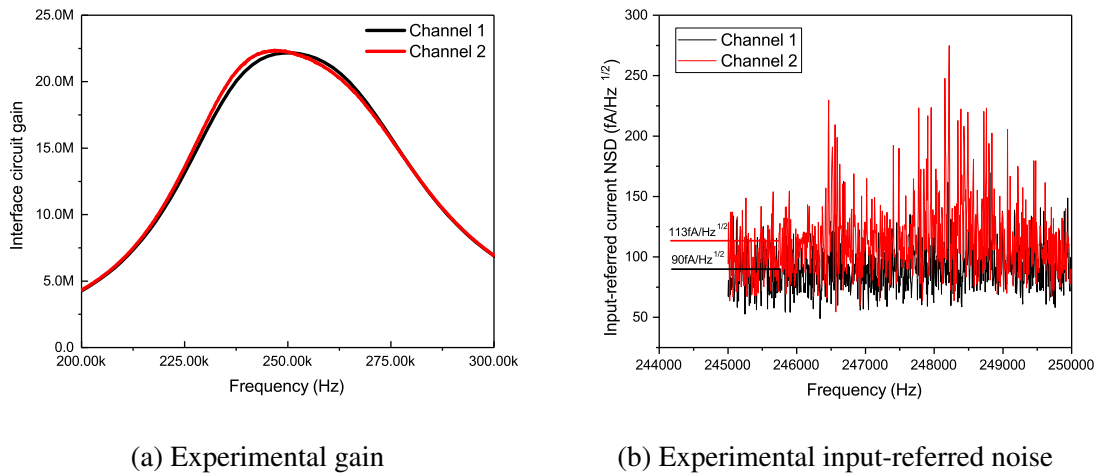


Fig. 3.6 Experimental characterization of the gain and noise of the interface cirucit.

The experimental noise of the interface circuitry is shown in Fig. 3.6b. The noise band between 245 kHz and 250 kHz is chosen as the operating region. The noise in the two channels differs from the SPICE model by about 30%. However, the model only captures the noise from the TIA and not the noise introduced by the band pass filter as well. There is also a difference of 20% between the two channels that can be attributed to the error in the component values used in both the channels.

These experimental results prove that the models used in the SPICE simulations were accurate for providing insight into the behaviour of the interface circuit. They were instrumental in simulating all of the circuitry presented in this work.

3.2.2 Closed-loop circuit

To develop a self sustaining loop, the main criteria to be fulfilled is the Barkhausen criteria [81]. Fig. 3.7 shows the role the feedback control loop plays in sustaining oscillations from the resonator system. The resonators and the amplifier form the open-loop pathway and have already been described in the previous section.

Barkhausen criteria suggests that for oscillations to be sustained the following two conditions must be met:

- The gain of the open-loop and feedback network must be greater than or equal to 1 ($\alpha(j\omega) \times \beta(j\omega) \geq 1$).

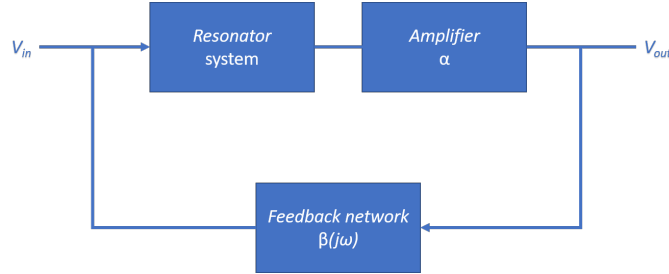


Fig. 3.7 Control loop including the resonator, amplifier and the feedback network.

- The phase lag in the loop must be a multiple of 2π

The feedback network includes a soft limiter gain control instead of the conventional amplitude gain control. This allows for a gain control that reduces nonlinear effects including higher order harmonics. In addition to that, a phase shifter is included in the loop to tune the phase to fulfill the Barkhausen criteria. This oscillator is apt for operating the sensor in the region where the output amplitude of the feedback resonator remains constant across the operating region. If Resonator 1 is used in the control loop, then the operation region is limited to high amplitude ratios ($AR > 5$). Contrarily, if Resonator 2 is used in the control loop, then the operation region is limited to the *veering* range ($0.9 < AR < 1.5$) since amplitude of Resonator 2 in SED remains relatively constant in that region. Therefore, the operation region is confined to where the amplitude being controlled is constant across stiffness perturbations as seen in Fig. 2.4a. To implement an oscillator at a greater range of working region, a phase locked loop (PLL) should be preferred instead of a direct feedback oscillator topology.

Soft limiter gain control

A schematic of the soft limited circuit employed for the amplitude gain control is shown in Fig. 3.8. The soft limiter has two diodes to limit the positive and negative parts of the amplitude of sine wave. When the output voltage (V_{out}) is small, the two diodes are off. The soft limiter behaves as a simple voltage amplifier with a gain of $-\frac{R_2}{R_1}$. When starting the oscillations up, the noise in the system gets amplified and drives the resonators to continuously get higher and higher amplitudes at resonance in this operating region. When the amplitude becomes comparable to V_{lim} (with the positive threshold of V_L+ and a negative threshold of V_L-), the diodes start to conduct. The thresholds of these voltages can be defined with respect to the forward voltage of the diode (V_f) and the reference voltage as follows:

$$V_{L+} = \frac{R_6}{R_5} 5V + \left(1 + \frac{R_6}{R_5}\right) V_f \quad (3.1a)$$

$$V_{L-} = -\frac{R_4}{R_3}5V - \left(1 + \frac{R_4}{R_3}\right)V_f \quad (3.1b)$$

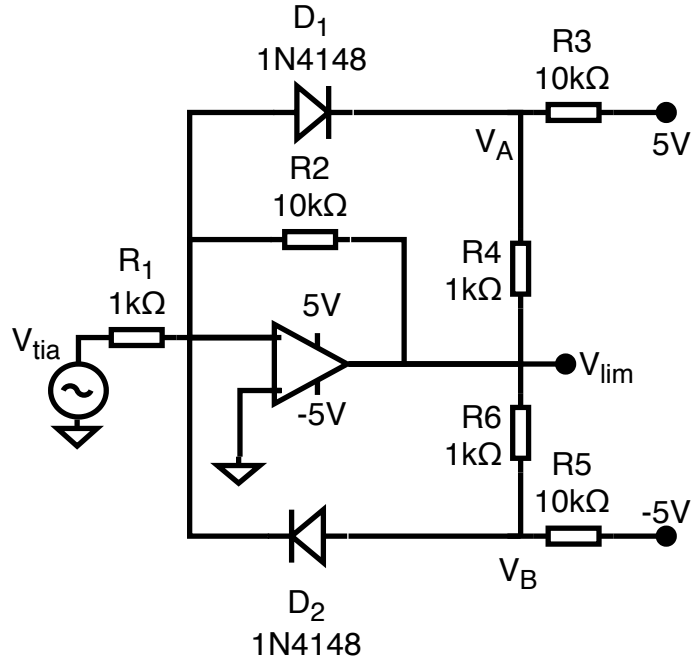


Fig. 3.8 Soft limiter circuit

When the threshold is reached and the input voltage tries to increase further, more current is injected into diodes D_1 and D_2 whereas, V_A and V_B stay at the forward voltage of the diode (V_f and $-V_f$). The current through R_5 and R_3 remains constant and the diode current flows through R_6 and R_4 thus, reducing the gain in this region to:

$$G_{L+} = -\frac{R_2||R_6}{R_1} \quad (3.2a)$$

$$G_{L-} = -\frac{R_2||R_4}{R_1} \quad (3.2b)$$

These two regions are described in Fig. 3.9. Notice that increasing the value of the feedback resistor R_2 increases the gain in the linear region but does not impact the limits V_{L+} and V_{L-} .

The full circuit implementation with the values for the components are shown in Fig. 3.8. The values are chosen after setting the gain of the TIA to achieve an output voltage of 200 mV. Using a diode 1N4148 with a forward voltage of 0.7 V, and the reference voltage of ± 5 V, the voltage is limited to $1.27 V_{pk}$. The drive voltage feeding into the resonator needs to be

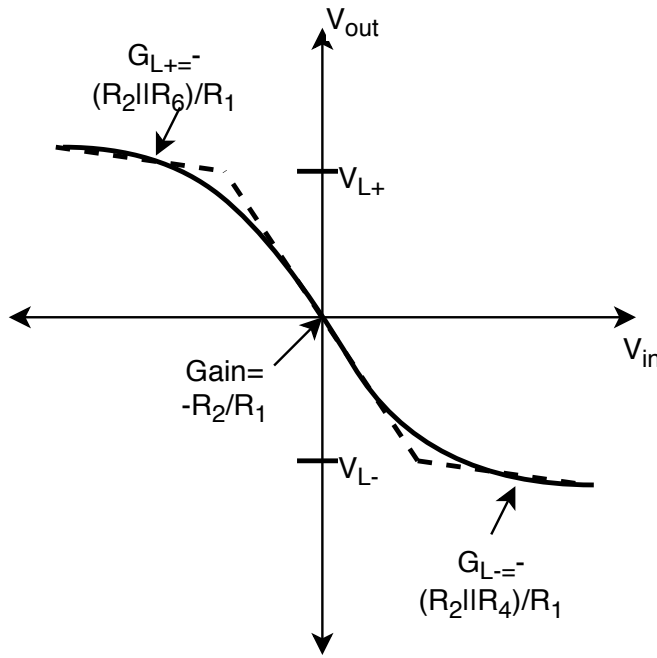


Fig. 3.9 Soft limiter operation

much lower for linear operation so a voltage divider is introduced at the drive port to reduce this voltage by a factor to 10 before driving the resonator.

Phase shifter

A phase shifter is used to maintain the Barkhausen criteria of having a zero phase in the loop. An example of a simple phase shifter is implemented as the schematic in Fig. 3.10 suggests.

Because the nodes of the two input terminals in an operational amplifier are at the same voltage, the transfer function of the voltage from input to output node can be determined as $H(j\omega) = \frac{1-j\omega RC}{1+j\omega RC}$. The gain of the operation amplifier is defined by R_3 and R_1 and since they are equal, the amplifier has unity gain. The phase of the operational amplifier is defined as:

$$\phi(\omega) = \arctan(-\omega RC) - \arctan(\omega RC) = -2 \arctan(\omega RC) \quad (3.3)$$

Assuming that the capacitor (C_1) is going to remain constant, the phase needs to be adjusted by adjusting R_2 . Knowing the amount of phase that needs to be changed, a resistor R_2 can be chosen as follows:

$$R = \frac{-\tan(\frac{\phi}{2})}{C_1 \omega} \quad (3.4)$$

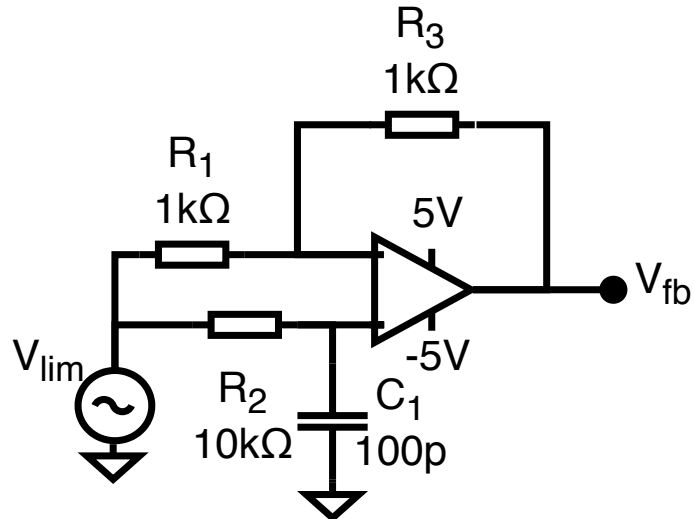


Fig. 3.10 Phase shifter circuit

The phase lag in the circuit can be simulated but since the circuit components tend to vary from their nominal values, it is prudent to experimentally determine R_2 at the prescribed operating range. The circuit components in Fig. 3.10 are chosen for operation at 250 kHz to induce a phase lag of 60 °.

The fully integrated mode-localised sensor is realised on a printed circuit board (PCB). A picture of this is shown in Fig. 3.11.

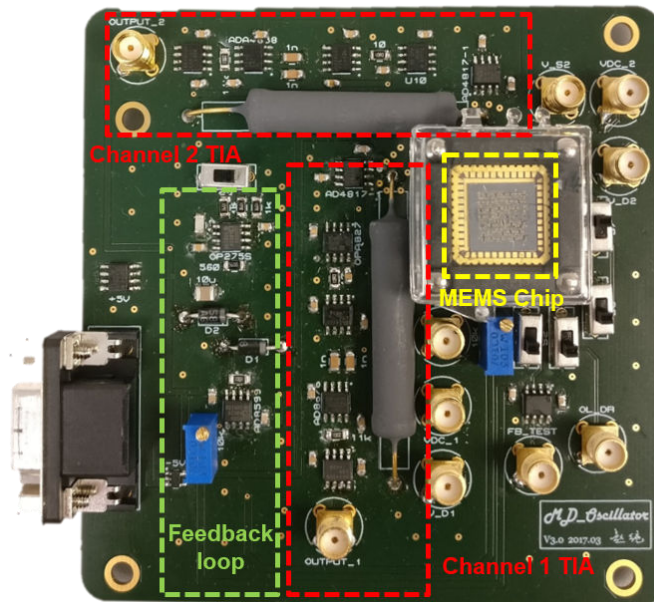


Fig. 3.11 Mode-localised sensor integrated with the electronics on a PCB

3.2.3 Closed-loop implementation using lock-in amplifiers

The Zurich Instruments MFLI and HF2LI are off-the-shelf lock-in amplifiers with built in PLL controller that can close the loop on the resonator system. By doing so, the PLL locks to the oscillation frequency to fulfill a particular phase condition. The MFLI is a single channel system lock-in amplifier while the HF2LI offers a dual channel lock-in amplifier option. Both systems calculate the control values using the model of the resonator with a particular resonant frequency and quality factor. A set of PI values are created using this model which contribute towards sustaining oscillations by minimising phase error between sense and drive signal. An added advantage is that the phase of the drive signal can be changed to facilitate nonlinear frequency analysis by mapping unstable regions. This system is instrumental in prototyping and is detailed in many of the experiments outlined in the thesis.

Unlike the direct feedback oscillator outlined previously, this method can be applied to close the loop in a greater range of amplitude ratios. This is made possible as it does not require the signal amplitude to be constant in the operating region. Either the output voltage of Resonator 1 or 2 can be used in the loop for a large operating conditions. However, it should be noted that the low amplitudes of vibration (<10 mV) increase the noise in the system and limit the resolution of the sensor. Ultimately, the phase conditions being fulfilled by the PLL will determine the resonator in the loop. Resonator 1 output shows the same phase with respect to the drive voltage in both the in-phase mode and the anti-phase mode; contrarily, Resonator 2 shows a phase difference of π between the two modes. Thus, Resonator 2 is preferred because of the unique phase conditions it fulfils for either mode of operation across a range of operating amplitude ratios.

3.3 Experiment

The experimental setup is shown in Fig. 3.12. The two resonators are weakly coupled with negative stiffness by applying a DC voltage across the gap between the resonators. The two sense electrodes were biased at the same DC Voltage and were used to sense the vibration amplitudes (X_1 and X_2) of the resonators. A negative stiffness perturbation relative to Resonator 1 was applied on the perturbation electrode in the form of voltage difference for sensitivity measurements. The direct feedback oscillator topology is employed to sustain the oscillations of the MEMS device.

The oscillator for the sensor was created using cascade drive configuration. The loop was closed using the output current of Resonator 1. This motional current was first converted

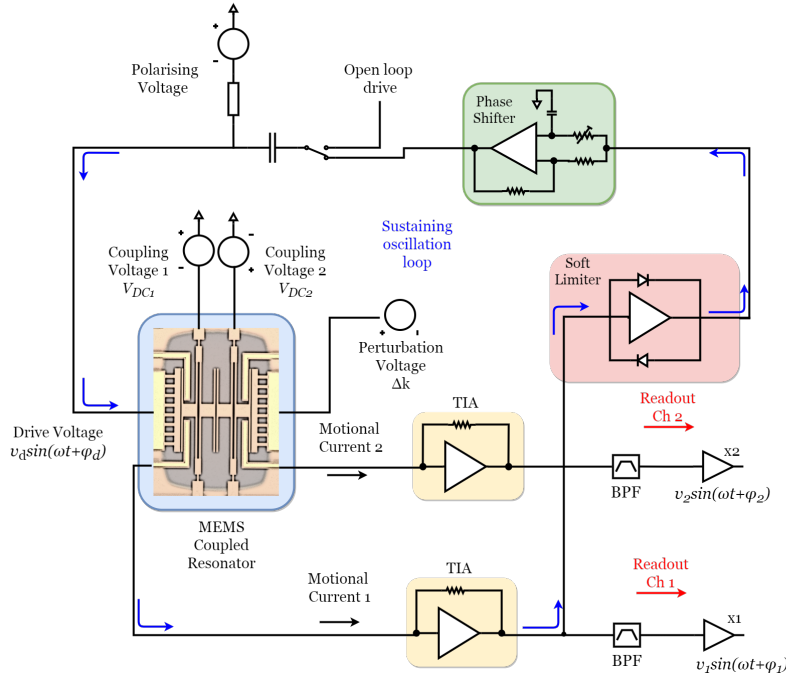


Fig. 3.12 Schematic of the experimental setup.

into voltage through a transimpedance amplifier (TIA), then passed through a soft limiter circuit, and a phase shifter to satisfy the Barkhausen criteria. Resonator 1 was driven with a combination of a DC polarising voltage and an AC excitation voltage and Resonator 2 was driven synchronously through the coupling.

3.3.1 Sensitivity analysis

To achieve high sensitivity, V_{DC1} was set to 0 V and V_{DC2} was set to 5 V thereby applying a coupling voltage of 5 V. The voltage difference for the drive and sense transduction is maintained at 35 V to maintain equal drive and sense polarisation voltages. Stiffness perturbations were applied to Resonator 2 by applying a voltage to the perturbations electrode. The perturbation voltage were swept from -5 V to -15 V with increments of 2 V. The amplitudes and frequency were first measured in open-loop setup with the Zurich Instruments lock-in amplifier, and then in closed-loop with digital multimeters (Keithley) and frequency counters (Keithley) respectively. Each measurement was averaged over a period of 1 min. The results are plotted in Fig. 3.13.

Fig. 3.13 shows the sensitivity of various output variables in both open-loop and closed-loop configurations. Since the operation point of this sensor is away from the *veering zone*, the amplitude of Resonator 1 stays relatively constant while that of Resonator 2 increases

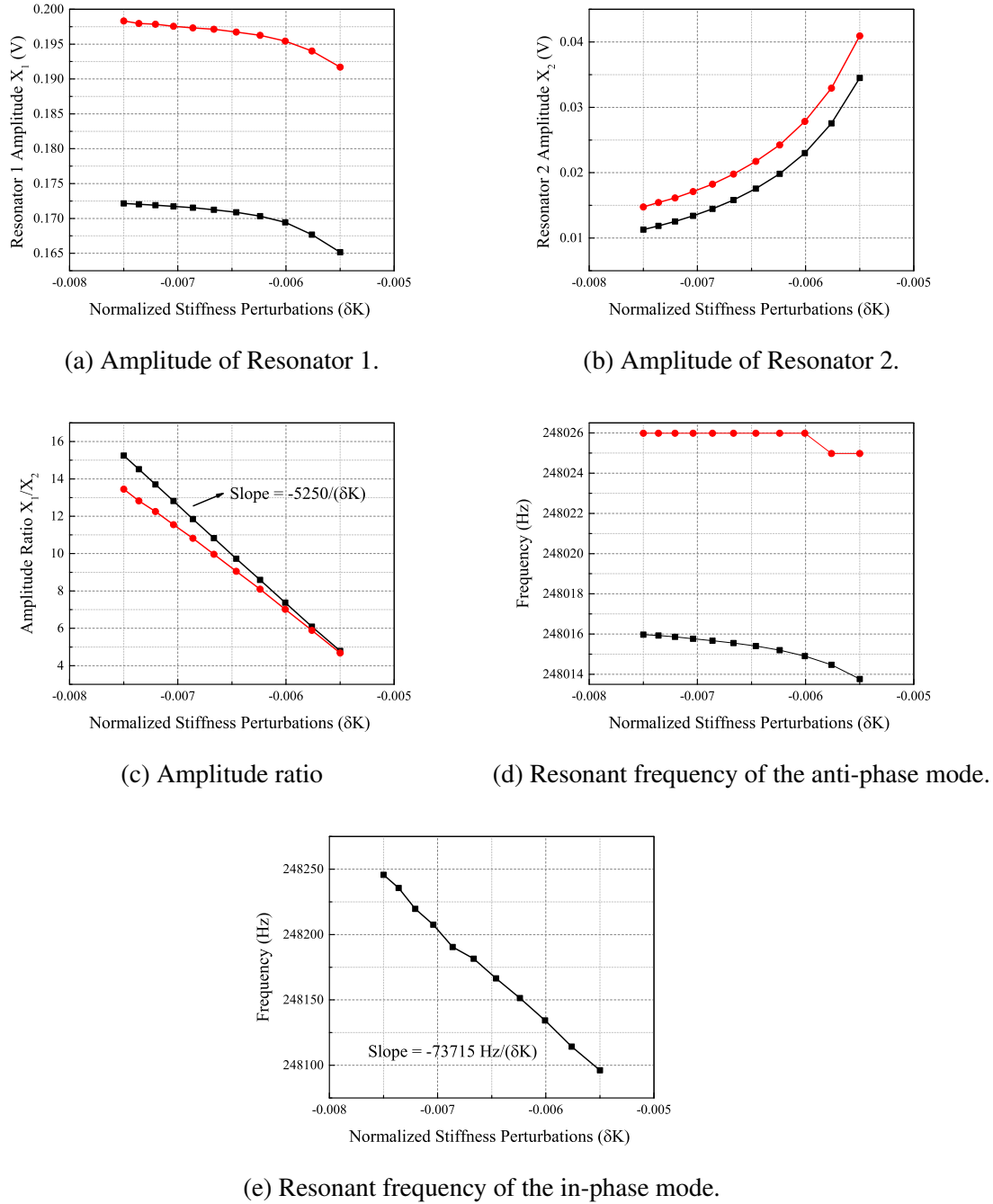


Fig. 3.13 Sensitivity of various output metrics to stiffness perturbations in closed-loop (Black) and in open-loop (Red) configurations

with increased stiffness perturbations. Additionally, the observed change in amplitude ratio over stiffness perturbations is linear while the frequency shift for this mode is almost negligible due to the operating regime. The difference in the values of the open-loop and closed-loop measurements can be attributed to different loading conditions observed over the measuring devices. Furthermore, due to the low resolution of the open-loop measurements, the frequency trend is not consistent with closed-loop measurements.

The sensitivity of the amplitude ratio in terms of normalised stiffness perturbation, $\delta K = \Delta K / K$, is calculated as:

$$S_{AR} = \frac{\partial AR}{\partial (\delta K)} = -5250/\delta K \quad (3.5)$$

The frequency shift in this operating region is insensitive to input stiffness perturbation in comparison to other operating regions. It does not represent the maximum sensitivity achieved with frequency shift sensing in this device. Due to the choice of the feedback oscillator, the operating region is limited to the mode where the amplitude of Resonator 1 is insensitive to stiffness perturbations. A by-product of this condition with electrically coupled devices is that the frequency of the anti-phase mode (the mode being measured) remains approximately constant. This is seen in Fig. 3.13d where the closed-loop frequency changes by only 2 Hz over the range of the stiffness perturbations. However, in this operating region, the sensitivity of the in-phase mode is maximum. Due to the symmetry of the system, the in-phase mode stability can be assumed to be similar to the anti-phase mode stability. To achieve the highest input-referred bias instability, the sensitivity of the in-phase mode (shown in Fig. 3.13e) is used for calculations of input-referred stability.

Fig. 3.13e shows the measured open-loop sensitivity of the frequency shift of mode 2 in the same operation region. The slope describes the sensitivity with respect to normalised stiffness perturbation, δK , and it is calculated as:

$$S_f = \frac{\partial f}{\partial (\delta K)} = -73715 \text{ Hz}/\delta K \quad (3.6)$$

3.3.2 Stability analysis

To investigate the long-term stability of the system, the sensor was placed in the closed-loop configuration with the DC perturbation voltage set to -10 V while amplitude and frequency data was collected for 12 hours. The Allan deviation of the amplitude ratio and the frequency data was then calculated to indicate the stability of the two output metrics. Fig. 3.14a shows the absolute stability of the amplitude ratio measurements. The trend of the curve shows

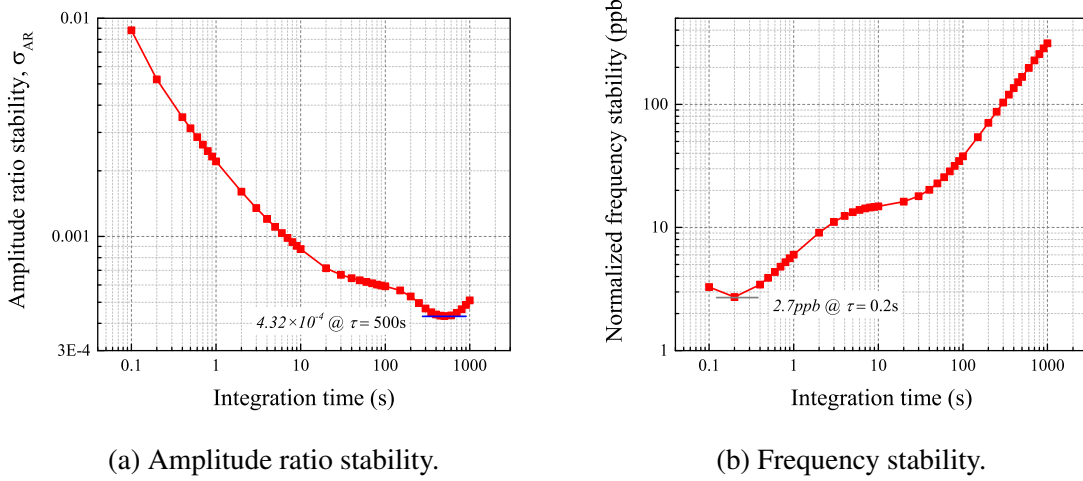


Fig. 3.14 Modified Allan variance of the measured a) amplitude ratio and b) frequency stability.

that the amplitude ratio output metric is more stable at higher integration times with the best stability (σ_{AR}) of 4.32×10^{-4} achieved at 500 s. In comparison, Fig. 3.14b plots the Allan deviation of the output frequency data. In this case, the trend of the curve shows that the stability decreases with larger integration times signifying a poor long-term stability. Nonetheless, a best stability (σ_f) of 0.6 mHz (2.7ppb) is achieved at 0.2 s integration time.

Although output stability is an important metric, the input-referred stability governs the resolution of the sensor. In terms of normalised stiffness perturbation, $\sigma_{\delta K}$, the input-referred stability signifies the minimum normalised perturbation that can be sensed by the mode-localised system. This can be calculated for amplitude ratio and frequency as follows:

$$\sigma_{\delta K, AR} = \frac{\sigma_{AR}}{S_{AR}} \quad (3.7)$$

$$\sigma_{\delta K, f} = \frac{\sigma_f}{S_f} \quad (3.8)$$

Using the above relation, the input-referred stability of both the amplitude ratio and the frequency shift are compared in Fig. 3.15. The trend of the output stability is retained in the input-referred stability as well. Normalised perturbations δK can be resolved very well by frequency as an output metric for shorter integration times. The turnover point (in this case at $\tau = 100\text{s}$) signifies the integration time after which, the amplitude ratio measurements provide better stability than frequency measurements.

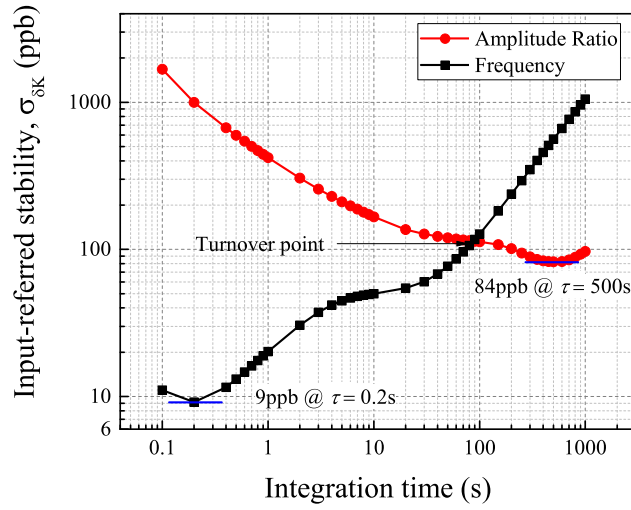


Fig. 3.15 Experimental Input-referred stability.

3.3.3 Bandwidth

The bandwidth of the mode-localised sensor in the closed-loop setup has been characterised by applying alternating perturbations. A square wave with maximum and minimum amplitudes of -5 V and -10 V was applied to the perturbation electrode at various frequencies. The frequency was swept from 0.1 Hz to 10 Hz with appropriate steps in between them. Similar to the sensitivity test, the amplitudes and the frequency were measured and recorded.

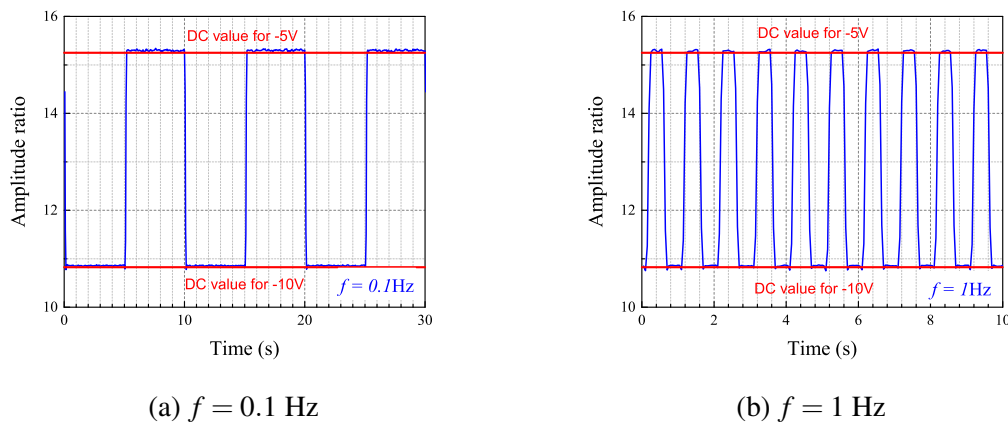


Fig. 3.16 Real-time monitoring of the amplitude ratio for different input perturbation frequencies (a) $f = 0.1$ Hz and (b) $f = 1$ Hz. The DC values of amplitude ratio for those particular perturbation voltages are shown in red.

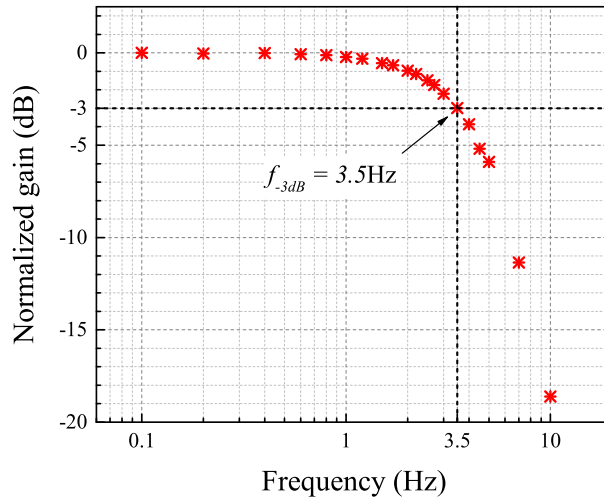


Fig. 3.17 Measured amplitude ratio, normalised to DC amplitude ratio, at different frequencies of perturbation.

The real time response of the amplitude ratio to such perturbation is shown in Fig. 3.16. The two examples show the switching between the perturbation stages of -5 V and -10 V at 0.1 Hz and 1 Hz . The amplitude ratio at both these frequencies track the DC values of -5 V and -10 V indicating that these frequencies are well within the bandwidth of the sensor.

Upon further increasing the frequency of perturbations, it is seen that the amplitude ratio values change from the DC values seen above. To calculate the bandwidth of the sensor, the RMS value of the amplitude ratio is taken for different perturbation frequencies. This gain is normalised to the DC gain and plotted in decibels in Fig. 3.17. The 3dB bandwidth of the system under test as shown in the figure is 3.5 Hz which is representative of the maximum frequency of perturbation that can be sensed by this system without losing information about the perturbations. Theoretically, the bandwidth of the system should be equal or close to the mechanical bandwidth of the resonator (29.3 Hz) but the limiting factor to achieving it can be attributed to the oscillator and electrical circuit. This oscillator has been designed for near DC perturbation frequency and is not optimised for higher frequency perturbations; but future work on oscillators for mode-localised systems can result in the system working at higher frequency perturbations.

Summary

In this chapter, the design of an integrated mode-localised sensor is shown with a detailed description of the mechanical device design and the open-loop readout circuit including a transimpedance amplifier and a band pass filter. Furthermore, a closed-loop implementation is developed with a direct feedback topology and a PLL topology with Zurich Instruments lock-in amplifier. The sensitivity, stability and bandwidth of the sensor were all characterised using the direct feedback closed-loop topology. The stability results show that the input-referred stability of the amplitude ratio output is better than the frequency shift output at large integration times (in this case at $\tau > 100$ s).

This work also demonstrates the potential practical benefits of the amplitude ratio sensing over the conventional frequency shift sensing. However, there are many parameters that affect the stability of the measured amplitude and those need to be studied thoroughly to improve the stability of the system in both short and long integration times. The next chapters discuss some of these factors that affect the resolution of the mode-localised resonators.

Chapter 4

Practical Limits to Common Mode Rejection in Weakly Coupled Resonators

Common mode rejection is the ability of a sensor to reject effects caused by undesirable sources that couple into the output metric being sensed. In silicon MEMS resonant sensors such as accelerometers and gyroscopes, long-term stability in the output metric is highly desirable. Differential frequency output in resonant accelerometers can reject common mode changes in the ambient temperature that lead to frequency drifts in frequency measurement. Amplitude ratio measurement in mode-localised sensors also provides such common mode rejection that makes it superior to frequency shift-based sensing. This chapter delves into the details of understanding the different mechanisms that play a role in defining the practical limits to common mode rejection of temperature fluctuations in both electrically coupled and mechanically coupled mode-localised resonators.

4.1 Temperature fluctuations and MEMS resonators

One of the key issues affecting resonant silicon MEMS devices is the high temperature coefficient (T_{CF}) of the resonant frequency. This effect is primarily caused due to the intrinsic temperature sensitivity of (Young's Modulus) of silicon. In the context of resonant sensors, high T_{CF} results in undesirable frequency drifts in devices that restrict them from achieving good long-term stabilities.

Several technical approaches have been researched to address this issue. Two widely used methods are – oven control of the device [82–85], and temperature compensation of the device by either using passive [86, 87] or active methods [88, 89]. Oven control involves controlling the temperature in the vicinity of the MEMS chip so that the chip temperature

is nominally independent of ambient conditions. Though some implementations of this method [83, 82] have shown high thermal stabilities, the bulky nature of the setup and the associated high power consumption undercut the advantages that MEMS devices offer with the miniaturisation.

Temperature compensation involves the correction of the response of the frequency measurement to temperature by using a calibrated dummy resonator with a known T_{CF} to sense the temperature. Once the temperature variations are accurately measured, they can be used to compensate for the fluctuations seen in the frequency output of the device using external circuitry [88, 89]. This requires additional electronic circuitry that consumes power and an independent measure of the temperature that is impractical for many low power applications. A passive method that is used in inertial sensors [57, 90, 8] is a differential frequency output where two identical resonators are used to measure inertial forces and a difference of the frequency output leads to rejection of common mode effects including temperature. However, due to fabrication tolerances, the T_{CFS} of the two resonators may not be perfectly matched leading to an imperfect cancellation of temperature fluctuations.

On the other hand, an eigenstate or amplitude ratio shift metric in mode-localised weakly coupled MEMS resonators has shown exceptional common mode rejection capabilities to the first order when exposed to temperature or pressure changes in comparison to the frequency-based readout [24, 25, 91]. Additionally, it also provides an increase in the sensitivity to input measurand by 2-3 orders of magnitude in comparison to the conventional frequency shift method of sensing [23, 32, 28, 92]. Typically, a temperature coefficient for frequency-based readout of approximately $-30 \text{ ppm}/^\circ\text{C}$ has been measured that is dominated by temperature induced variation in elastic modulus of silicon. Thus, the promise of an output metric rejecting temperature variations is highly desirable for sensor applications.

In this chapter, a detailed investigation of the common mode rejection in weakly coupled mode-localised resonators is presented. Previous work on this topic focuses on a study confined to electrically coupled resonators biased to a particular working range [24] or to a study restricted to a mechanically coupled resonator operating at one vibration mode [93]. However, no coherent study has been done encompassing both modes, large range of amplitude ratio operating points, and different coupling topologies. Furthermore, it has been established and shown that the amplitude ratio measurement demonstrates greater common mode rejection capabilities than a frequency shift output but, an apt comparison has not been made to a differential frequency shift output which is the convention with resonant sensors. This study fills these gaps in the current state-of-the-art and sheds light on all the important

factors impacting the common mode rejection capabilities of amplitude ratio readout metric in mode-localised resonators.

4.2 Theory

In order to evaluate the limits to common mode rejection of amplitude ratio output metric in mode-localised resonators, it is necessary to understand the different variables that affect the amplitude ratio and frequency shift output metric. The three output metrics chosen for this analysis are amplitude ratio in a coupled resonator system, frequency shift in a coupled resonator system, and a differential frequency in uncoupled identical resonators representing the current state-of-the-art. The temperature dependence of the variables that affect these output metrics need to be studied with a discussion on the degree to which they affect each of the output metrics. To aid the comparison with the same metrics, the analysis is limited to common mode rejection in sensors. Furthermore, the measurand chosen for this analysis is a perturbation in stiffness (Δk) since it effects both the frequency and the amplitude ratio output metric.

4.2.1 Temperature dependence of output metrics

Mode localisation in its most basic form can be represented by a 2-DoF lumped spring-mass model. The two springs (k_1) and masses (m_1) are assumed to be the same. They are coupled together with a weak coupling spring (k_c). A perturbation in stiffness (Δk) is added to one of the resonators to perturb the system from a state of symmetry. The analysis is done on an undamped system. Thus, c_1 and c_2 are neglected. A detailed work on the variability of the quality factor should be done in the future with special importance given to the type of damping that dominates in different coupled systems. This causes a shift in the eigenstate of the resonators proportional to the measurand and this is represented as the ratio of the two amplitudes of vibration of the resonators.

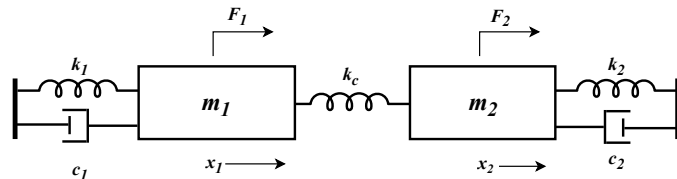


Fig. 4.1 A coupled resonator configuration used for amplitude ratio measurements

Frequency shift in mode-localised resonators

The eigenfrequencies of the two modes of the coupled resonator system have already been derived previously in Chapter 2.2.1 and can be written as:

$$\omega_i^2 = \frac{2k + \varepsilon_k + 2k_c + \Delta k \pm \sqrt{(\Delta k + \varepsilon_k)^2 + 4k_c^2}}{2m} \quad (i = 1, 2) \quad (4.1)$$

It is to be noted that the two resonators are assumed to be different in stiffness (k and $k + \varepsilon_k$) due to fabrication tolerances. Eq. 4.1 shows that frequency of a mode-localised resonator has the following temperature (T) dependent components:

$$\omega_i(T) = \omega_{i0} + \left(\omega_i \left(\frac{\partial k}{\partial T} \right) + \omega_i \left(\frac{\partial k_c}{\partial T} \right) + \omega_i \left(\frac{\partial \varepsilon_k}{\partial T} \right) + \omega_i \left(\frac{\partial \Delta k}{\partial T} \right) \right) \Delta T \quad (i = 1, 2) \quad (4.2)$$

Amplitude ratio in mode-localised resonators

Similarly, the expression for the amplitude ratio is also derived from Chapter 2.2.1. Thus, amplitude ratios of the two modes can be expressed as:

$$AR_i = \frac{\Delta k + \varepsilon_k \mp \sqrt{(\Delta k + \varepsilon_k)^2 + 4k_c^2}}{2m} \quad (i = 1, 2) \quad (4.3)$$

It is also important to note that the fabrication imperfections (ε_k) in this case can be merged with the stiffness perturbations (Δk) term since the fabrication tolerances can be tuned electrostatically without affecting the drive or sense transduction. Therefore, Δk can be used as a sole representative of the measurand. Considering all these factors, the temperature dependent features of amplitude ratio measurements in mode-localised sensors are:

$$AR_i(T) = AR_0 + \left(AR_i \left(\frac{\partial k_c}{\partial T} \right) + AR_i \left(\frac{\partial \Delta k}{\partial T} \right) \right) \Delta T \quad (i = 1, 2) \quad (4.4)$$

Differential frequency shift in two uncoupled resonators

It is necessary to make comparisons to a differential frequency output from two single resonator systems, representing the current state-of-the-art in resonant sensors. Thus, an expression is derived for a frequency difference readout metric in two separate but similar resonator devices undergoing a differential change in the measurand (i.e. Δk). Fig. 4.2 shows the lumped spring mass damper model for two uncoupled resonators that can be used for frequency difference measurements.

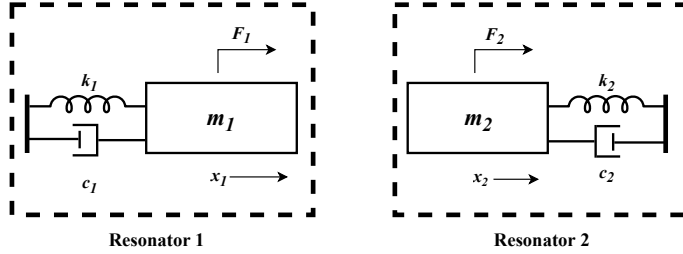


Fig. 4.2 Uncoupled resonators for differential frequency measurement

$$\omega_1^2 = \frac{k_1 + \Delta k}{m}; \omega_2^2 = \frac{k_2 - \Delta k}{m} \quad (4.5)$$

where the frequencies of the two resonators are expressed as ω_1 and ω_2 . The two masses are assumed to be equal when resonating and any variation in it with temperature is assumed to be negligible. The stiffness of the two resonators are assumed to be different to include the cumulative effect of manufacturing tolerances. They can be reduced to k and $k + \varepsilon_k$ to simplify the expression by including a term (ε_k) to represent fabrication tolerances. The frequency difference as an output metric can be achieved from subtracting the expressions in Eq. 4.5:

$$\omega_1 - \omega_2 = \omega_d = \sqrt{\frac{k + \Delta k}{m}} - \sqrt{\frac{k + \varepsilon_k - \Delta k}{m}} \quad (4.6)$$

Any variation in k with temperature is rejected in this output metric too. But, it can be noticed in Eq. 4.6 that the frequency difference output includes the ε_k term that ultimately is the limit of common mode rejection. Even in this case, the fabrication tolerances can be compensated by electrostatically tuning the resonators. But this generally hampers the drive or sense transduction and requires continuous tuning [94, 90]. Thus, for the purposes of this analysis, it is assumed that the fabrication tolerances are uncompensated and vary with temperature. Therefore, the variables with temperature dependence in this output metric are:

$$\omega_d(T) = \omega_{d0} + \left(\frac{\partial \varepsilon_k}{\partial T} + \frac{\partial \Delta k}{\partial T} \right) \Delta T \quad (4.7)$$

Although it might seem from an initial inspection that the amplitude ratio output metric has similar number of temperature dependent terms in it, the mechanisms that cause this temperature dependence are different in both these output metrics. Thus, it is prudent to understand these mechanisms and their variation with temperature to highlight their individual advantages.

4.2.2 Variables with temperature dependence

The above section provided insight into the variables that affect the three output metrics under question. These variables are discussed in detail here with emphasis on the various mechanisms causing these changes in the different systems and output metrics.

Resonator stiffness (k)

The resonator stiffness is dependent on material parameters such as Young's modulus and density, and structural properties. The Young's Modulus of single-crystal silicon varies with temperature at $\approx -60\text{ppm}/^\circ\text{C}$ [95] and affects the stiffness of the resonator. The thermal expansion coefficient of single-crystal silicon is $\approx 2.6\text{ppm}/^\circ\text{C}$ [96]. This induces a change in the structural dimensions of the resonator with a variation in temperature which, in turn affects the stiffness of the resonator. The temperature dependence of the resonator stiffness affects only individual resonator frequencies. A differential frequency or an amplitude ratio output eliminates common mode effects of the Young's modulus changes since both resonators would be part of the same wafer with the same crystal orientation.

Stiffness mismatch (ϵ_k)

When the resonators are non-identical due to fabrication tolerances, it leads to a stiffness mismatch in the resonators (ϵ_k). Thus, due to their geometrical imperfections, the resonators exhibit different responses to a change in temperature. This mismatch in the variation of stiffness with temperature forms the fundamental limit to the common mode rejection capabilities of an output metric. Tuning this mismatch in a differential frequency output metric using the electrostatic spring softening effect has been shown [97]. Varying the voltage on either the drive, sense electrode or the body of the resonator can lead to tuning the stiffness mismatch between the two resonators. The caveat here is that changing the voltage also varies the transduction factor which is undesirable for sensor applications. An additional port can also be designed for the sole purpose of tuning, but this would encroach on valuable space around the transduction of the resonator. Mode-localised resonators enjoy the mode shape extending between the two coupled resonators and rely on a sensing mechanism based on the stiffness mismatch. Thus, electrical tuning voltages do not change the transduction capabilities. Therefore, they have a less direct effect on the common mode rejection abilities of the amplitude ratio output metric.

Coupling stiffness (k_c)

The variation of the coupling stiffness in mode-localised resonators affects the amplitude ratio as well as the frequency output metric. Thermal effects will affect the coupling stiffness in different ways depending on whether it is realised using a mechanical beam or electrical capacitive coupling. In a mechanically coupled device, the coupling stiffness is susceptible to changes in the material's Young's modulus. Additionally, any thermal expansions of the beam will lead to stresses developing around the point of connection with the resonator. In electrical coupling, there is no physical connection between the resonators. Hence, the effect of temperature on the output metric is mainly due to thermal expansion effects modifying the capacitive gaps. It is to be noted that the thermal expansion coefficient is smaller than the Young's modulus change by about an order of magnitude and thus it is prudent to expect a proportional variation in the effectiveness of the common mode rejection between electrical coupling and mechanical coupling in these devices.

Stiffness perturbations (Δk)

It should be noted that in analysing the thermal effects on the output metrics, the stiffness perturbations include only the added perturbations for sensing purposes and not the stiffness mismatch that is caused due to fabrication tolerances. There are two main ways of applying perturbations to a capacitively transduced resonator system: one, by using the capacitive gaps next to the resonators, and the other through axial stress application. In the experiments carried out in this work, electrostatic spring softening effect using a capacitive gap has been used. Thus, the magnitude of these perturbations will change with temperature due to the thermal expansion of electrodes. This will lead to the capacitive gaps changing, therefore, resulting in the change of stiffness perturbations added. This effect is much smaller than the change in the other variables such as the coupling stiffness, resonator stiffness, or even stiffness mismatch. Thus, it does not contribute greatly to the variation of the output metrics.

If the perturbations were added axially with the help of force amplification levers as used in resonant accelerometers [8], the perturbations would result from stress on the resonators. These stresses could have a much greater variation with temperature. However, for the sake of this analysis, only electrostatic sources of perturbations are considered.

These are some of the main temperature dependent variables that affect the three output metrics under study. The experimental results are analysed by referring to the mechanisms affecting each of these variables and ultimately each of the output metrics.

4.3 Experiment

The experiments in this study are designed to test the effectiveness of the common mode rejection that the three output metrics offer. The experiments include only changes to the temperature as the pressure is kept constant in the system. Two systems are chosen for this experiment – a system of mechanically coupled resonators and a system of electrically coupled resonators. These two devices allow for the comparison between the coupling mechanism and highlight the differences in the temperature dependence of these two coupling mechanisms. The electrically coupled resonators can also be used to emulate two uncoupled resonators by applying the same voltage on both resonators ($V_c = 0$ V) thereby allowing for differential frequency measurements.

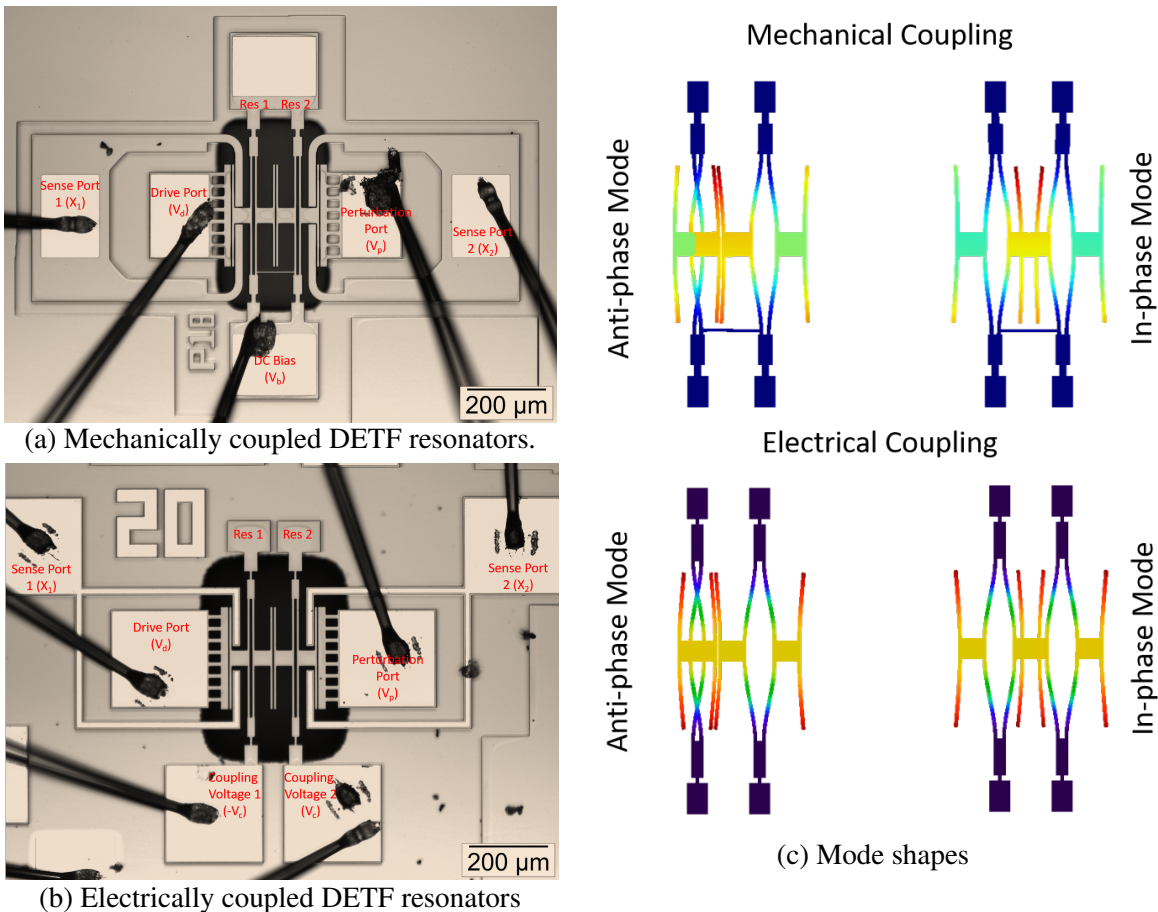


Fig. 4.3 Micrographs and mode shapes of the two device structures under test.

The devices used for the experiment consist of a system of double ended tuning fork (DETF) resonators coupled using electrical coupling and another, coupled using a mechanical beam. They are fabricated using a SOIMUMPS process by MEMSCAP Inc. Fig. 4.3a shows

the optical micrograph of the electrical coupled resonators and Fig. 4.3b shows that of a mechanically coupled device. The design of these devices are not a core part of this work as they existed prior to the commencement of this work. To make accurate experimental comparisons, the device parameters of both resonators are kept as close as possible. Table 4.1 summarises some of the key device parameters of both devices. Furthermore, the mode shapes of the two devices in their in-phase and anti-phase modes are shown in Fig. 4.3c. It is to be noted that the in-phase and anti-phase mode refer to the motion of the DETF element with respect to each other. The tines of the individual DETF elements of both the modes of operation are moving out-of-phase with each other to increase the quality factor of the device under test.

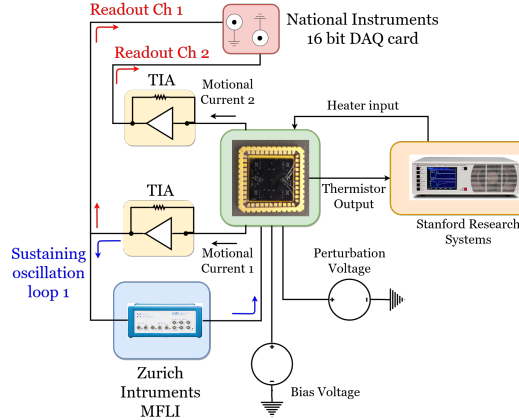
Table 4.1 Device parameters

Parameter	Electrically coupled device	Mechanically coupled device
Resonator Beam Length	350 μm	350 μm
Resonator Beam Width	6 μm	6 μm
Coupling Beam width	-	4 μm
Coupling Beam Length	-	150 μm
Device Layer Thickness	25 μm	25 μm
Proof Mass	0.6 μg	0.6 μg
Q factor	17000	19000
Resonant Frequency	251 kHz	252 kHz

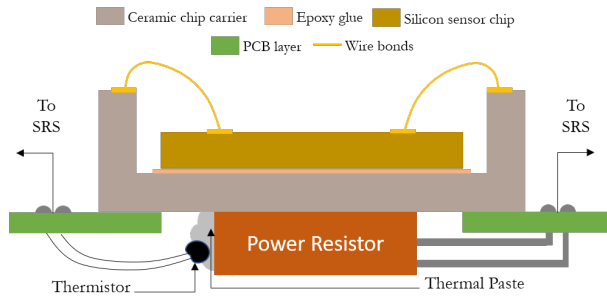
The measurement setup is divided in two parts: the oscillation circuit to sustain the closed-loop oscillations of the resonators and the temperature control systems to regulate the local temperature control of the MEMS chip.

The oscillation circuit (shown in Fig. 4.4a) comprises two transimpedance amplifiers to convert the motional current of resonator into a voltage that can be easily recorded. Oscillations are sustained using the phase locked loop (PLL) function of the Zurich Instruments MFLI using the output voltage of the driven resonator – Resonator 1 (As seen in Fig. 4.3). Resonator 2 is driven through the coupler in a cascade configuration. Both output voltages are measured and recorded simultaneously using the National Instruments data acquisition (DAQ) card. For the electrically coupled resonator, coupling is realised by applying -7 V on Resonator 1 and 7 V on Resonator 2. A drive bias voltage (V_d) of 22 V is used while the sense ports are set to 0 V each. For the mechanically coupled resonators, a V_d of -20 V and V_b of 20 V is used and the sense ports are set to 0 V . Perturbation voltages (V_p) are varied to tune the amplitude ratio from the perturbation port in both devices. The experiments are

carried out in a custom vacuum chamber at a pressure of 20 mTorr to avoid operating at pressures where fluid damping dominates.



(a) Circuit level schematic of the experimental setup.



(b) Illustration of the chip level temperature control setup

Fig. 4.4 The measurement and temperature control setup.

The heating is realised at the chip scale only. A cross section of the setup is shown in Fig. 4.4b. A $20\ \Omega$ power resistor is used as the heating element and it is put in contact with the ceramic chip carrier. A thermistor is placed close to the bottom face of the chip carrier and is attached to the power resistor using thermal paste. The thermal paste ensures that the temperature in the vicinity of the thermistor is evenly distributed and the heat from the resistor gets transferred efficiently to the thermistor. A Stanford Research Systems (SRS) temperature controller is used to accurately control the temperature of the device using the built-in PID feature to a $10\text{ m}^\circ\text{C}$ stability. It is to be noted that there will be a gradient of temperature from the heater to the chip but since the heated area is only $1\text{ cm} \times 1\text{ cm}$, a settling down time of 1 hr for each temperature step is chosen to spread the temperature evenly across the chip. An alternative option would be to place the thermistor at the top of

the chip; however, it is undesirable to expose the bonded wires and the electrical interface to the thermal paste.

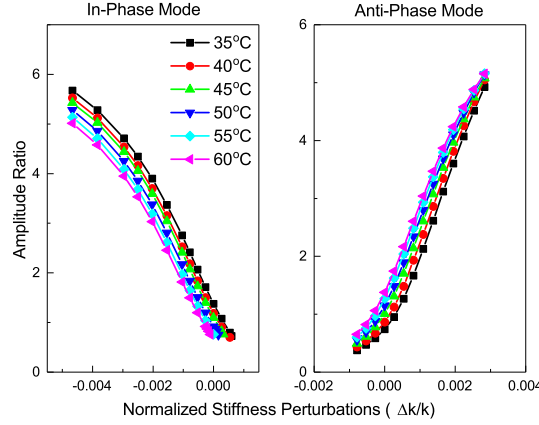
4.4 Results

The results section is divided into the temperature dependent experiments conducted on the electrically coupled device, mechanically coupled device, and a differential frequency measurement done on two uncoupled DETF devices.

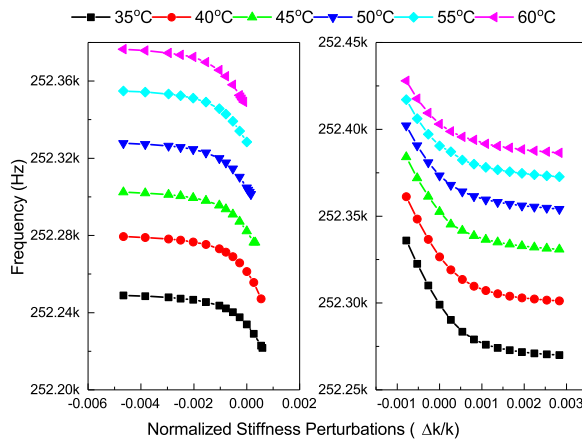
4.4.1 Mechanically coupled device

The mechanically coupled device used for the experiment is shown in Fig. 4.3b. It consists of two DETF resonators coupled using a mechanical beam. A bias voltage of 20 V is applied on the body to aid the transduction process. The resonators are set into oscillation in the in-phase mode with a drive voltage of 10 mV while ensuring that they are operating in the linear regime. The temperature is stabilised to 35 °C using the SRS temperature controller. Once the temperature is stabilised to 10 m°C, the perturbation voltage is varied to see the amplitude ratio change from 1 to 5. The amplitude ratio and the frequency is noted and then the experiment is repeated for temperatures upto 60 °C with steps of 5 °C. Then similar steps are taken to repeat the experiment in the anti-phase mode. The results are plotted in Fig. 4.5. It is to be noted here that the initial mismatch between the resonators is 0.54 N/m for the mechanically coupled device.

The amplitude ratio of both the in-phase and the anti-phase mode undergo variations with the change in temperature as seen in Fig. 4.5a. This can be expected of mechanically coupled resonators since the coupler is dependent on the T_{CF} of the elastic constant of silicon. Any change in the coupling stiffness, directly results in changes in the amplitude ratio. A peculiar observation is related to Fig. 4.5b where the frequency of the mechanically coupled resonators appears to have a positive variation with temperature. The material properties of silicon call for a frequency dependence to temperature of approximately $-30\text{ppm}/^\circ\text{C}$, but a positive variation points to secondary effects such as stress mechanisms dominating the temperature dependence of frequency [98]. Stress build up is caused due to thermal expansion at the anchor and coupling points of the resonator system which, can lead to resonance frequency shift [99]. On the resonators, stress mechanisms would lead to a change in frequency while the same on the coupler would be the major contributor to changes in amplitude ratio.



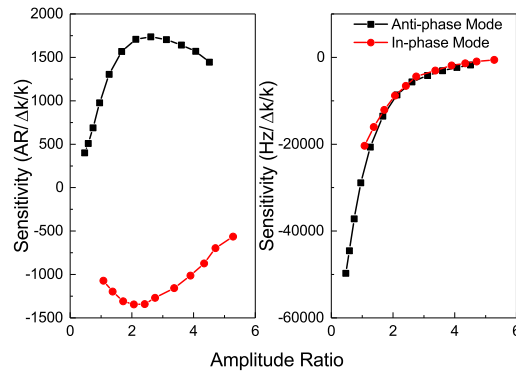
(a) Amplitude ratio variation with temperature and stiffness perturbations of the in-phase and the anti-phase mode.



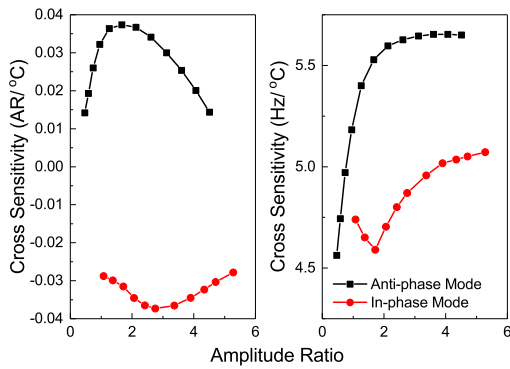
(b) Frequency variation with temperature and stiffness perturbations of the in-phase and the anti-phase mode.

Fig. 4.5 Temperature and stiffness perturbation dependent variation in amplitude ratio and frequency in mechanical coupled resonators.

The sensitivity to stiffness perturbations of amplitude ratio in both the in-phase and the anti-phase modes of the mechanically coupled resonator is shown in Fig. 4.6a. It is expected that the sensitivity of amplitude ratio output metric to measurand would increase with the amplitude ratios and then plateau at higher amplitude ratios. Meanwhile, the sensitivity of the frequency output is expected to decrease with the increase in amplitude ratio and plateau at higher amplitude ratios. In this particular case, the sensitivity of amplitude ratio



(a) Sensitivity to stiffness perturbations of amplitude ratio and frequency output metrics.



(b) Sensitivity to change in temperature of amplitude ratio and frequency output metrics.

Fig. 4.6 Sensitivity analysis of the mechanically coupled resonators.

to stiffness perturbations has a parabolic feature where the sensitivity increases to about an amplitude ratio of 2 and then decreases with further increase in amplitude ratio. To investigate this feature, finite element modelling using COMSOL[®] is carried out on the mechanically coupled device and is detailed in Appendix C. The results indicate that this feature is a by-product of the structural design but does not impact its temperature immunity or the conclusions drawn in this study.

The cross sensitivity (sensitivity of the output metric to temperature) of both the amplitude ratio and the frequency output metric is shown in Fig. 4.6b. As mentioned in the theory section, there are two key mechanisms that effect the cross sensitivity of the output metrics – the variation of the Elastic Young's Modulus (E) of silicon and thermal expansion coefficient

(α) of silicon. The frequency output metric is dependent on the variation of E_{si} of the resonator, E_{si} and α_{si} of the coupler, and α_{si} increasing the capacitive gap, resulting in stiffness change in (k), (k_c) and (Δk) respectively. Thus, the trend of the cross sensitivity curve follows that of the sensitivity curve across different amplitude ratio operating points. Fig. 4.6b suggests that for both modes of vibration, there is an average temperature coefficient of about 5 Hz/ $^{\circ}\text{C}$ (20 ppm/ $^{\circ}\text{C}$). These two observations lead to the conclusion that the frequency is affected by two superimposing factors that simultaneously vary (k), (k_c) and (Δk). The amplitude ratio output metric is dependent on the variation of E_{si} and α_{si} in the coupling beam and the α_{si} increasing the capacitive gap to impact the stiffness perturbations. Thus, even the cross sensitivity of the amplitude ratio output metric follows the same trend as the sensitivity of amplitude ratio to stiffness perturbations.

All these stiffness variations can be amalgamated into a net stiffness perturbation due to temperature variations and this can be used to create a normalised representation of the common mode rejection. Thus, a Figure of Merit (FOM) is created by dividing the cross sensitivity of the output metric to temperature by the sensitivity of the output metric to the measurand. This FOM represents the input-referred change in the normalised stiffness perturbation of each output metric to a change in the temperature (measured in $\Delta k/k/\text{ }^{\circ}\text{C}$) or (ppm/ $^{\circ}\text{C}$). Thus, it is an apt quantity to judge the appropriate variation in the measurand that is inflicted by temperature fluctuations in each output metric. Therefore, a lower FOM results in better rejection of temperature fluctuations of the output metric.

$$\text{FOM} = \frac{\text{Sensitivity of output metric to temperature}}{\text{Sensitivity of output metric to measurand}} \quad (4.8)$$

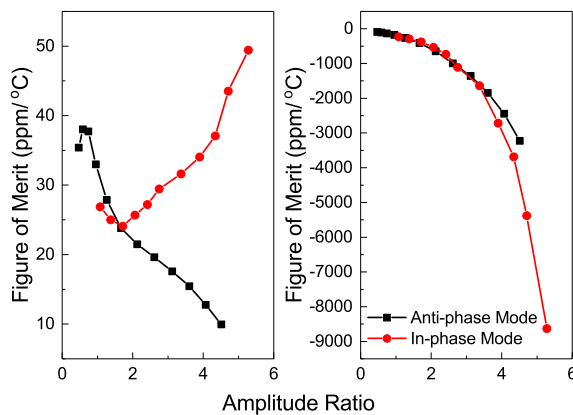


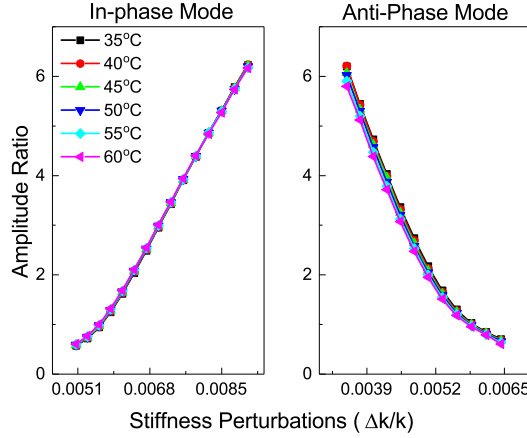
Fig. 4.7 Figure of merit for amplitude ratio and frequency output metrics.

The FOM is calculated and plotted with respect to the various amplitude ratio operating points in Fig. 4.7. A two orders of magnitude improvement of the amplitude ratio over frequency output metric is seen. This is caused by the different stiffness parameters affecting the two output metrics separately. Amplitude ratio is affected by the changes in coupler and the stiffness perturbations parameter, which leads to opposing changes in the amplitude ratio of the two modes. Thus, the FOM of the amplitude ratio in the two modes shows opposing slopes. Since the frequency output is dependent on the same two parameters as the amplitude ratio in addition to the stiffness of the resonators (k), the FOM is orders of magnitude worse than that of amplitude ratio. This also highlights the magnitude of contribution of each stiffness parameter to variation in the output metric. Clearly, any variation in the stiffness of the resonator impacts the output metric more than the variation in the coupler and capacitive gap variation. Thus, it can be concluded that the amplitude ratio output metric is superior to the frequency shift output metric in terms of rejecting temperature-based effects. Unfortunately, it is impossible to implement a differential frequency output with a mechanically coupled device so no comparisons are made of the amplitude ratio output metric with a differential frequency output metric. This comparison is made in the electrically coupled device with the same dimensions.

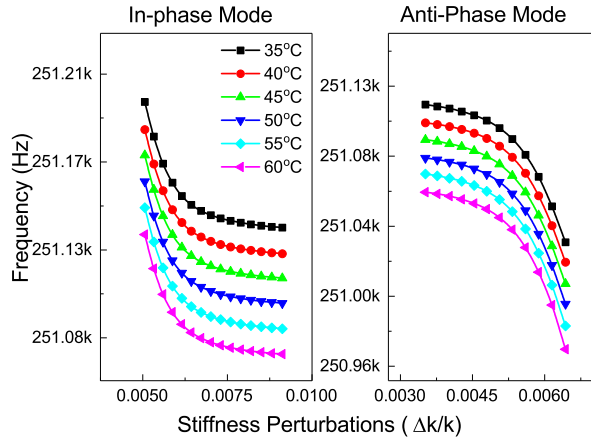
4.4.2 Electrically coupled device

Electrically coupled resonators are driven into closed-loop oscillation with a 10 mV drive voltage to ensure a linear frequency response. A coupling voltage of 14 V is chosen to ensure the same magnitude of coupling stiffness as its mechanical counterpart. This is done by inspecting the frequency difference between the two modes in the two devices and calculating the coupling stiffness accordingly [23, 28]. It is to be noted here that the initial mismatch between the resonators is 6.4 N/m for the electrically coupled device. The temperature is first set to 35 °C which is the minimum temperature that is controllable to 10 m°C precision. The perturbation voltage is added on the perturbation port to vary the amplitude ratio from 1 to 5. The temperature is then increased in steps of 5 °C and the same perturbation voltages are applied on the port while noting the amplitude ratio and frequency at each of those voltages. The results are plotted in Fig. 4.8 for the amplitude ratio and the frequency of both the in-phase and the anti-phase modes with respect to changes in the temperature.

It is evident on inspection that in comparison to the mechanically coupled device, the amplitude ratio output in the electrically coupled device is less sensitive to temperature variations. This can be attributed to the absence of the mechanical coupling beam that



(a) Amplitude ratio variation with temperature and stiffness perturbations of the in-phase and the anti-phase mode.



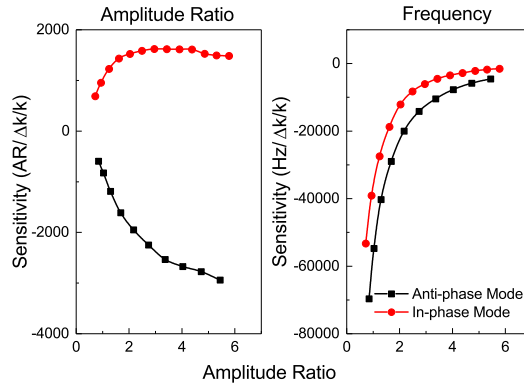
(b) Frequency variation with temperature and stiffness perturbations of the in-phase and the anti-phase mode.

Fig. 4.8 Temperature and stiffness perturbation variation in electrically coupled resonators.

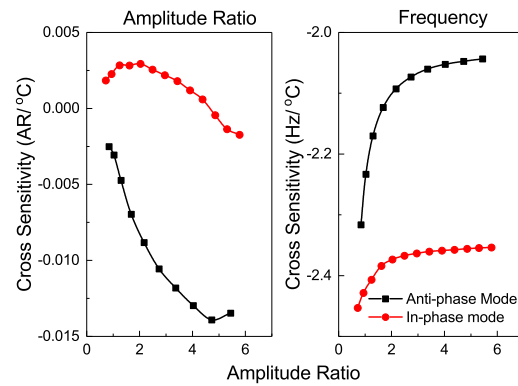
causes greater variation in the coupling stiffness in comparison to its electrical counterpart. The frequency variation with temperature is more in character with the negative T_{CF} that is associated with silicon resonators. The absence of the coupling beam can also reduce stress accumulation around the anchor points.

The sensitivity of the electrically coupled resonators to input stiffness perturbations is plotted against various amplitude ratio operating regions in Fig. 4.9a. As expected, the sensitivity of amplitude ratio increases and plateaus at higher amplitude ratios. In contrast, the sensitivity of the frequency reduces and plateaus with the increase in amplitude ratios. There is no sensitivity reduction in the amplitude ratio output at higher amplitude ratios

similar to that seen in mechanically coupled device. This feature is also consistent with COMSOL® simulation in Appendix C.



(a) Sensitivity to stiffness perturbations of amplitude ratio and frequency output metrics.



(b) Sensitivity to change in temperature of amplitude ratio and frequency output metrics.

Fig. 4.9 Sensitivity and FOM analysis of the electrically coupled resonators.

The temperature sensitivity of the frequency output of the electrically coupled resonators mirrors that of its mechanically coupled counterpart. However, since the E_{si} of the coupling beam does not play a role here, the cross sensitivity is approximately half of that seen in the mechanically coupled device. The amplitude ratio is only affected by thermal expansion of the capacitive gaps and thus shows a much lower temperature coefficient. The anti-phase mode follows the same trend as the sensitivity to stiffness perturbation curve in Fig. 4.9a. Thus, the change can be attributed to addition of effective stiffness perturbation in the form of thermal expansion of capacitive gaps. However, the in-phase mode shows a different trend

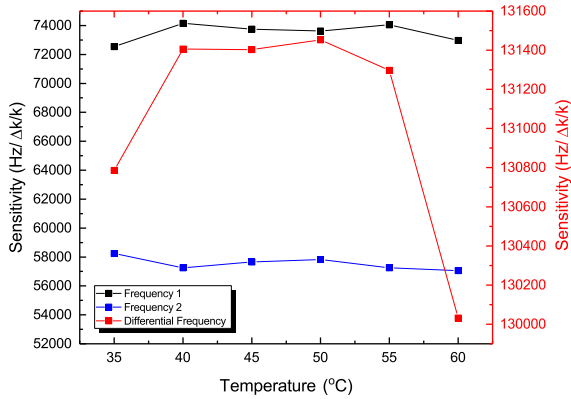
and has a temperature sensitivity crossing 0 AR/ $^{\circ}\text{C}$. This portrays an effective cancellation of the thermal effects sourced from the thermal expansion of various capacitive gaps.

Taking the comparison one step further, it is important to compare the amplitude ratio output metric with the differential frequency output. Unlike in the mechanically coupled device, it is quite straightforward to implement a differential frequency output in the electrically coupled device. To implement this, the two resonators are decoupled by applying 12 V on both resonators (effective 0 V applied between the two resonators). They now behave as two uncoupled resonator systems that can be individually put into closed-loop oscillations. After inducing closed-loop oscillations, the temperature is increased with steps of 5 $^{\circ}\text{C}$ as done with the electrically coupled resonators. The sensitivity to stiffness perturbation is tested by varying the voltage on the body of the two resonators from 11 V to 13 V. The variation of the individual frequencies and the frequency difference to stiffness perturbations and temperature are plotted in Fig. 4.10.

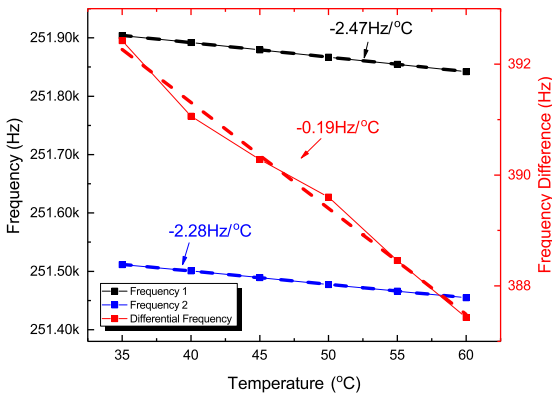
To mimic the response of a differential frequency measurement where the sensitivity to a measurand is increased by ≈ 2 times, the sensitivities in this case are added instead of being subtracted. This is reflected in Fig. 4.10a where the sensitivity to stiffness perturbation of the differential frequency output is an addition of the individual frequency sensitivities. The sensitivity to temperature of the individual resonator frequencies shown in Fig. 4.10b reflects that the two resonators have similar T_{CF} . The sensitivity of the differential frequency to temperature is a difference of the individual frequency sensitivities to temperature. The difference in sensitivities in the two resonators is expected since (due to manufacturing tolerances), their physical properties differ and thus lead to these variations in sensitivities.

The observations made from both these experiments are represented in the figure of merit plot in Fig. 4.11. The amplitude ratio clearly shows about 2-3 orders of magnitude better figure of merit than the frequency output metric thus, showing benefits over the individual frequency shift output metric. As an additional reference, the FOM of the differential frequency output calculated from the results in Fig. 4.10 has been added to compare it to the FOM of the amplitude ratio. In this particular device, the amplitude ratio shows a similar FOM to a differential frequency output although the mechanisms that lead to this are quite different. The differential frequency output metric is affected by the issues of mismatch in physical properties of the resonators from fabrication tolerances while the amplitude ratio output metric is affected by the thermal expansion of the capacitive gaps leading to a change in coupling stiffness and perturbations applied.

From a direct comparison of the FOM of the mechanically coupled device (Fig. 4.7) and the electrically coupled device (Fig. 4.11) with identical device parameters and coupling



(a) Variation of frequency outputs with stiffness perturbations.



(b) Variation of frequency output with temperature.

Fig. 4.10 Differential frequency sensitivity and cross sensitivity.

strength, it is evident the electrically coupled device offers up 10 times greater immunity to temperature fluctuations than the mechanically coupled device. Within the electrically coupled device, it is seen that the in-phase mode (refer to Fig. 4.3c) offers greater rejection; even crossing the 0 AR/°C threshold. It leads to the conclusion that there is a possibility of cancelling the effects of thermal expansion of the gaps and ensuring that the temperature sensitivity is negligible. It should be noted here that the variation of the bias with respect to temperature has been considered very small in comparison to the variation of the coupling stiffness with temperature. A detailed study on the temperature dependence of the bias will

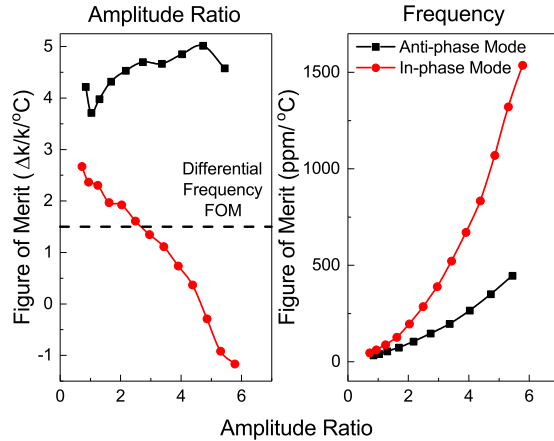


Fig. 4.11 Figure of merit for amplitude ratio and frequency output metrics in electrically coupled device.

shed more light into the residual temperature dependence seen in the electrically coupled device.

The advantages of using amplitude ratio output metric in mode-localised coupled resonators (especially electrically coupled) over differential frequency output metric in similar resonators is twofold – (1) the same FOM can be achieved with the use of a single oscillator circuit as compared to two separate ones used in differential frequency output, and (2) the stiffness mismatch due to fabrication tolerances can be better integrated into an amplitude ratio output metric in mode-localised resonators than a differential frequency output metric in two separate resonators.

Summary

The ability of amplitude ratio and frequency shift output metrics to reject temperature fluctuations in weakly coupled mode-localised resonators is discussed in this work with particular emphasis on the limiting mechanisms. The mechanically coupled resonator displays worse common mode rejection than its electrically coupled counterpart due to the additional temperature dependent E_{si} of the coupling beam. Furthermore, amplitude ratio output metric in an electrically coupled device and a differential frequency readout metric are compared in the same device. The results show similar common mode rejection capabilities in the two methods but point towards a dependence on different physical mechanisms. It is also demonstrated that it is possible to cancel the effects of the thermal expansion on capacitive gaps that affect the amplitude ratio metric in electrically coupled devices to yield

a AR_{TCF} of 0. This result greatly enhances the possible applications that lie ahead for the amplitude ratio output metric in mode-localised devices in the form of sensor design.

Further study is needed on a detailed derivation of the procedure to cancel thermal effects as seen in the in-phase mode of the electrically coupled devices. Additionally, a theoretical framework encompassing the contributions of the various factors outlined in this study would be beneficial in validating the cause for the variation in the T_{CF} variation in the amplitude ratio output metric between mechanically and electrically coupled devices. Furthermore, since electrically coupled devices are less robust in applications for inertial sensors such as accelerometers (discussed in Chapter 7), a new output metric should be developed to further the common mode rejection capabilities of the mechanically coupled mode-localised device. One option is to use a differential amplitude ratio readout metric using two systems of coupled resonators to reduce the impact of temperature fluctuations on the coupler. This new output metric will be used in Chapter 7 in a custom designed mechanically coupled mode-localised accelerometer. The benefits of this new output metric will be discussed there.

Chapter 5

Noise Analysis

Understanding the governing sources of noise and their impact on the output metric of a sensor is critical for predicting the ultimate resolution that it can achieve. Noise can originate from various sources such as from the mechanical sensor, interface electronics, and the measurement setup. Thus, these noise sources must be estimated and quantified in order to optimise the resolution of the sensor. In this chapter, the key noise sources plaguing the amplitude ratio output metric are identified. Then, models are used to estimate and predict the impact they have on the output metric of a weakly coupled resonator. Finally, experimental results are shown to validate the model and suggest an optimum operating point while employing an amplitude ratio output metric in mode-localised devices.

5.1 Sources of noise

Noise processes in MEMS resonators have been studied in depth over the years [100–102]. Conventionally, a periodic signal of frequency ω_0 and amplitude V_0 with additive amplitude and phase noise is represented with the following notation:

$$v(t) = [V_0 + \alpha_N(t)]\cos(2\pi\omega_0 t + \phi_N(t)) \quad (5.1)$$

The representation in Eq. 5.1 refers to a signal that is corrupted with an amplitude noise $\alpha_N(t)$ and phase noise $\phi_N(t)$. It is assumed in this notation that the noise components are much smaller than the signal components. Both the amplitude and phase noise are affected by different noise processes operative in the MEMS system. In applications where the MEMS resonator is employed as a reference oscillator, the key noise metric is phase noise. However, when using MEMS resonators for sensor application, the key metric is generally frequency

or amplitude noise. Since amplitude ratio employs the amplitude of the resonators as the primary output metric, this chapter will focus on amplitude noise more than phase/frequency noise. It is to be noted however, that when measuring using a closed-loop configuration, the phase noise of the external oscillator will be a key metric in the performance of the sensor. However, it is not trivial to estimate or predict it. Therefore, for the scope of this study, only the noise sources from the sensor and the readout electronics are considered and oscillator noise is not discussed in detail.

5.1.1 Thermo-mechanical noise

Thermo-mechanical noise is often a measure of the fundamental intrinsic limit of in micromechanical resonators [103, 104]. It arises from the interaction of the resonating MEMS sensor with the molecular agitation of the fluid surrounding the structure and in classical physics is known to be caused due to Brownian motion [105]. Since this noise mechanism arises from the dynamic equilibrium between the resonator and the ambient environment around the resonator, it can be represented as a force (\bar{F}_n^2) exerted on the resonator system due to thermal agitation of the molecules in this environment. The transfer function analysis will be used in this section to estimate the amplitude noise of the coupled system. It employs the same transfer function method described in Chapter 2.2.2 but the forcing is replaced with that of thermal origin (\bar{F}_n^2). Before estimating the thermo-mechanical noise, it is important to derive an expression for this forcing term.

To formulate an expression for this thermal forcing, Equipartition theory [106, 107] is used. Equipartition theory suggests that when a mechanical system is in thermal equilibrium with its ambient surroundings, each mode of the mechanical system will have an average energy equal to half of the product between the Boltzmann's constant (k_B) and the ambient temperature (T) at equilibrium. It is sufficient to do a single degree of freedom analysis to derive the expression for the thermal forcing while making the assumption that in a M-DoF system, each DoF will be affected by the same thermal forcing. The energy stored in any mechanical system is proportional to its mean squared displacement. Hence, equating these terms leads to [108, 109]:

$$\frac{1}{2}k_B T = \frac{1}{2}k\bar{x}_j^2 \quad (5.2)$$

In Equation 5.2, \bar{x}_j^2 represents the mean squared displacement of the j^{th} resonator due to the thermal forcing ($\bar{F}_{n,m}^2$). Therefore, it can be expressed as a response of the transfer function $H_j(i\omega)$ of the mechanical resonator system to input forcing:

$$\overline{x_j^2}(i\omega) = |H_j(i\omega)|^2 \overline{F_{n,m}^2} \quad (5.3)$$

The transfer function of each individual (j^{th}) resonator can be expressed in terms of the stiffness (k), mass (m), and damping (c) of the resonator as follows:

$$H_j(i\omega) = \frac{1}{-\omega^2 m_j + i\omega c_j + k_j} \quad (5.4)$$

Thus, the mean square fluctuation ($\overline{x_j^2}(t)$) of the j^{th} resonator can be simplified to [110]:

$$\begin{aligned} \overline{x_j^2}(t) &= \frac{1}{2\pi} \int_0^\infty |H_j(i\omega)|^2 \overline{F_{n,m}^2} d\omega \\ &= \frac{1}{2\pi} \int_0^\infty \left| \frac{1}{-\omega^2 m_j + i\omega c_j + k_j} \right|^2 \overline{F_{n,m}^2} d\omega \\ &= \frac{1}{2\pi} \int_0^\infty \frac{1}{(k_j - \omega^2 m_j)^2 + (\omega c_j)^2} \overline{F_{n,m}^2} d\omega \end{aligned} \quad (5.5)$$

This integral can be simplified by assuming that the resonator has a high mechanical quality factor leading to the majority of the energy in the resonator to be concentrated around the resonant frequency (ω_0). Also to be noted is that $\overline{F_{n,m}^2}$ is white noise with a constant spectral density ($S_{F,m}$) evaluated over a 1 Hz bandwidth. Therefore, a solution can be obtained as below [110]:

$$\begin{aligned} \overline{x_j^2}(t) &= \frac{\overline{F_{n,m}^2}}{2\pi} \int_0^\infty \frac{1}{(k_j - \omega^2 m_j)^2 + (\omega c_j)^2} d\omega \\ &= \frac{\overline{F_{n,m}^2}}{2\pi} \frac{\pi}{2\omega_0^2 c_j m_j} \end{aligned} \quad (5.6)$$

Using the results in Eq. 5.6 and substituting in Eq. 5.2, the expression for the thermal forcing term can be found:

$$\begin{aligned} \frac{1}{2} k_B T &= \frac{\overline{F_{n,m}^2}}{8\pi} \frac{\pi k_j}{\omega_0^2 c_j m_j} \\ \implies \overline{F_{n,m}^2} &= 4k_B T c_j \end{aligned} \quad (5.7)$$

The thermal forcing ($\overline{F_{n,m}^2}$) can be used to derive the thermo-mechanical component of the resonator noise by using the transfer function model that was developed in Chapter 2.2.2. Assuming the noise sources for the resonators are uncorrelated, the noise spectrum of the resonator displacement can be expressed as:

$$\begin{aligned}\overline{x_{1,m}^2} &= |H_{11}|^2 \overline{F_{1,m}^2} + |H_{12}|^2 \overline{F_{2,m}^2} \\ \overline{x_{2,m}^2} &= |H_{21}|^2 \overline{F_{1,m}^2} + |H_{22}|^2 \overline{F_{2,m}^2}\end{aligned}\quad (5.8)$$

In Eq. 5.8, $\overline{F_{1,m}^2} = \overline{F_{2,m}^2} = \overline{F_{n,m}^2} = 4k_B T c_j$ which is the thermal noise power forcing. The transfer functions (H_{jk}) mentioned in Chapter 2.2.2 are defined to be the transfer functions for j^{th} resonator due to the forcing on the k^{th} resonator. The relevant expressions are:

$$\begin{aligned}|H_{11}|^2 &= \left| \frac{H_2(s)}{H_1(s)H_2(s) - k_c^2} \right|^2; |H_{12}|^2 = \left| \frac{-k_c}{H_1(s)H_2(s) - k_c^2} \right|^2; \\ |H_{21}|^2 &= \left| \frac{-k_c}{H_1(s)H_2(s) - k_c^2} \right|^2; |H_{22}|^2 = \left| \frac{H_1(s)}{H_1(s)H_2(s) - k_c^2} \right|^2;\end{aligned}\quad (5.9)$$

Therefore, an expression for the amplitude noise power can be achieved from Eq. 5.8 and 5.9.

$$\begin{aligned}\overline{x_{1,m}^2} &= \left| \frac{H_2(s)}{H_1(s)H_2(s) - k_c^2} \right|^2 \overline{F_{1,m}^2} + \left| \frac{-k_c}{H_1(s)H_2(s) - k_c^2} \right|^2 \overline{F_{2,m}^2} \\ \overline{x_{2,m}^2} &= \left| \frac{-k_c}{H_1(s)H_2(s) - k_c^2} \right|^2 \overline{F_{1,m}^2} + \left| \frac{H_1(s)}{H_1(s)H_2(s) - k_c^2} \right|^2 \overline{F_{2,m}^2}\end{aligned}\quad (5.10)$$

In Eq. 5.10, the individual resonator transfer functions are defined as $H_1(s) = ms^2 + sc + k + k_c$ and $H_2(s) = ms^2 + sc + k + k_c + \Delta k$. Using Eq. 5.8, the thermo-mechanical noise in the two resonators ($\overline{x_{1,m}^2}$ and $\overline{x_{2,m}^2}$) can be calculated. Fig. 5.1 shows the spectrum of amplitude noise density ($x_{j,m} = \sqrt{\overline{x_{j,m}^2}}$ where $j = 1, 2$) as a response to the thermal forcing when the two resonators are matched in stiffness. The parameters used for this simulation are as follows: $Q = 10000$; $k = 1080$ N/m; $m = 0.445$ μg ; $k_c = -1$ N/m; and $\Delta k = 0$. Note that a negative coupling stiffness is used to best emulate the electrostatic coupling achieved in the experiment later in the chapter.

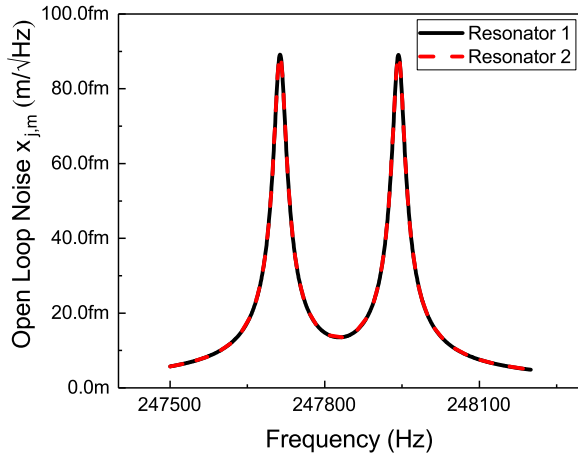


Fig. 5.1 Simulated open-loop noise response

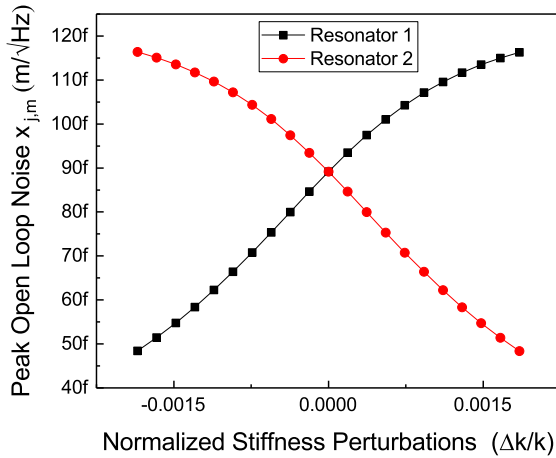


Fig. 5.2 Peak open-loop noise when perturbations are added on Resonator 2

As seen from Fig. 5.1, the thermo-mechanical noise in both resonators is identical when the resonators are identical. In order to predict the noise at different levels of asymmetry, perturbations in stiffness (Δk) are added to the system. This perturbs the resonator system away from symmetry and results in localisation of energy. The RMS noise at the resonance is referred in this case as the peak noise amplitude. These are recorded for one mode and are plotted in Fig. 5.2. Due to the symmetry in the system, the second mode will have a similar trend with reversed behaviour from the two resonators.

5.1.2 Electronic noise

The noise from the electronic sources can be divided into two parts – the noise from the pre-amplifier circuit and the noise from the voltage sources used for biasing the MEMS device. The difference in the two parts arises in how they shape the noise of the system. The noise from the pre-amplifier results in a wide band current noise that is added onto the motional current from the MEMS device and is regarded to be white in nature. However, the noise from the voltage sources results in a capacitive forcing on the resonator much like the thermo-mechanical noise discussed previously and, hence, is shaped by the resonator. These two sources are discussed in detail from an analytical and experimental perspective.

Pre-amplifier noise

The derivation of the electrical noise due to the pre-amplifier in each of the channels is fairly straightforward. It has no relation with the intrinsic noise of the resonators themselves and is assumed to be independent of the MEMS device. The noise is generated in the electrical pathway of the motional current and all the electrical components in the channel add to the noise. It will be dependent on the noise specifications of the components used. For this application, the input-referred current noise will be considered as the specific variable to optimise since it gives a good indication of the equivalent noise of the amplifier circuit that directly affects the motional current.

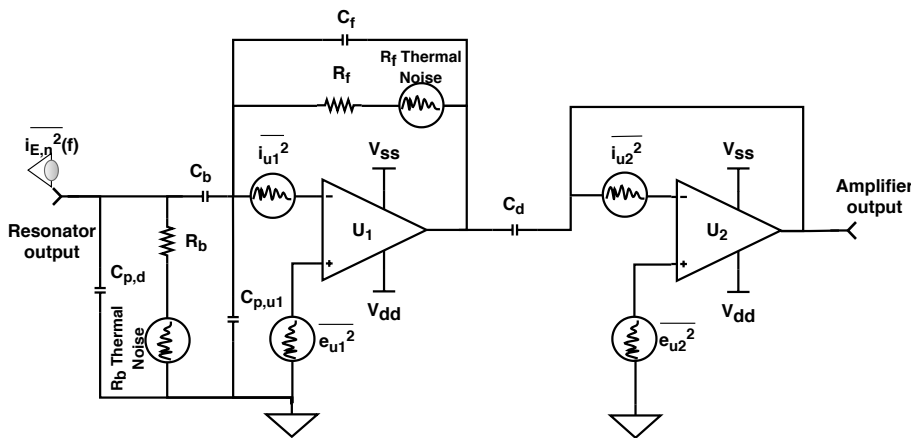


Fig. 5.3 A transimpedance amplifier topology, with the main noise sources included schematically.

The readout circuitry consists of the transimpedance amplifier (TIA) and a buffer amplifier. The TIA converts the motional current from the MEMS resonator to voltage and the buffer amplifier decouples the loading conditions from the output voltage. An ultra-low-noise single

stage TIA structure (as shown in Fig. 5.3) is used [111]. A bias-T consisting of R_b and C_b are used to DC bias the sense electrode of the MEMS resonator (MEMS input port in Fig. 5.3). R_f and C_f provide the feedback network for the first stage charge amplifier with U_1 . $C_{p,d}$ and $C_{p,u1}$ acting as the parasitic capacitance of the device and the amplifier U_1 , respectively. A capacitor C_d is used at the output of the first stage to decouple the DC component at the output of U_1 . U_2 in this case consists of an ultra-low noise operational amplifier that is used as a buffer. Since the input parasitic capacitance of U_2 is generally much smaller than C_d , it is neglected. It is to be noted that unlike the 2-stage TIA described in Chapter 3, this TIA consists only of a single stage charge amplifier. This configuration is chosen since it reduces the total noise in the output channel.

The current noise at the input node, $\overline{i_{E,n}^2}$, can be expressed by [112]:

$$\begin{aligned}\overline{i_{E,n}^2} &= (\overline{i_{u1}^2}) + (\overline{e_{u1}^2}) [2\pi f(C_f + C_{p,d} + C_{p,u1})]^2 \\ &+ (\overline{e_{u1}^2}) \left[\left(\frac{1}{R_b} \right)^2 + \left(\frac{1}{R_f} \right)^2 \right] \\ &+ \left[\left(\frac{C_f}{C_d} \right)^2 + \left(\frac{1}{2\pi f R_f C_d} \right)^2 \right] \times [(\overline{i_{u2}^2}) + (\overline{e_{u2}^2})(2\pi f C_d)^2] \\ &+ \frac{4kT}{R_b} + 4kT R_f \left[\left(\frac{1}{R_f} \right)^2 + (2\pi f C_f)^2 \right]\end{aligned}\quad (5.11)$$

It should be pointed out that near the operating region, $1/2\pi f C_f \ll R_f$. Additionally, due to the high gain of the first stage, the noise contribution from the second stage can be negligible. Therefore, the total current noise at the input node can be approximated as:

$$\begin{aligned}\overline{i_{E,n}^2} &\approx (\overline{i_{u1}^2}) + (\overline{e_{u1}^2}) [2\pi f(C_f + C_{p,d} + C_{p,u1})]^2 \\ &+ (\overline{e_{u1}^2}) \left(\frac{1}{R_b} \right)^2 + \frac{4kT}{R_b}\end{aligned}\quad (5.12)$$

To optimise the noise current, R_b should be maximised, whereas $\overline{i_{u1}^2}$, $\overline{e_{u1}^2}$, C_f , $C_{p,d}$ and $C_{p,u1}$ should be minimised. However, R_b is directly proportional to the charge-up time of the circuit due to the bias-T. Therefore, for a reasonable balance between the noise and the charge-up time, $20\text{M}\Omega$ is chosen as the value of R_b . Input current noise, $\overline{i_{u1}^2}$, input voltage noise, $\overline{e_{u1}^2}$ and input parasitic capacitance, $C_{p,u1}$, are the key specifications for the U_1 op-amp. Therefore, ADA4817 (Analog Devices, Inc.) is chosen for its optimal noise performance

Table 5.1 Circuit parameters

Parameter	Value
U_1	ADA 4817
U_2	ADA 4899
e_{u1}	4 nV/ $\sqrt{\text{Hz}}$
i_{u1}	2.5 fA/ $\sqrt{\text{Hz}}$
R_f	1 G Ω
C_f	0.1 pF
$C_{p,d}$	10 pF
$C_{p,u1}$	1.3 pF
R_b	20 M Ω

near the operating frequency of 250 kHz. Furthermore, a device parasitic capacitance of $C_{p,d}=10$ pF is assumed, and a $C_f=0.1$ pF (smallest for discrete capacitance) is chosen. The various values used in the circuit are summarised in Tab. 5.1.

Using the above values and plugging them into Eq. 5.12, an input-referred RMS noise ($i_{E,n} = \sqrt{i_{E,n}^2}$) can be calculated around an operating region of 250kHz as 77 fA/ $\sqrt{\text{Hz}}$.

Noise from voltage sources

The noise generated by the voltage sources used for transduction, biasing, and perturbations act on the resonator as a force. Unlike the noise from the pre-amplifier, this noise is shaped by the resonator. The force in this case is generated due to the capacitive nature of transduction and coupling. A simple schematic capturing this mechanism on a resonator and electrode is shown in Fig. 5.4

The power of the forcing due to the electronic noise from the DC sources ($\overline{F_{dcn}^2}$) can be calculated using the force relation between two capacitive plates:

$$\overline{F_{dcn}^2} = \left| -\frac{\epsilon_0 A_{cap}}{d_{cap}^2} V_{dc} \right|^2 \overline{V_{dcn}^2} \quad (5.13)$$

The forcing shown in Eq. 5.13 is sourced from a single DC voltage supply. There are several of these DC supplies used in the practical implementation of the electrical coupled DETF device. Noise in each of these sources will result in an equivalent forcing on the resonator. To understand the various sources of noise generated due to the DC voltage sources, a schematic of a coupled DETF resonator system connected to all the voltage sources is

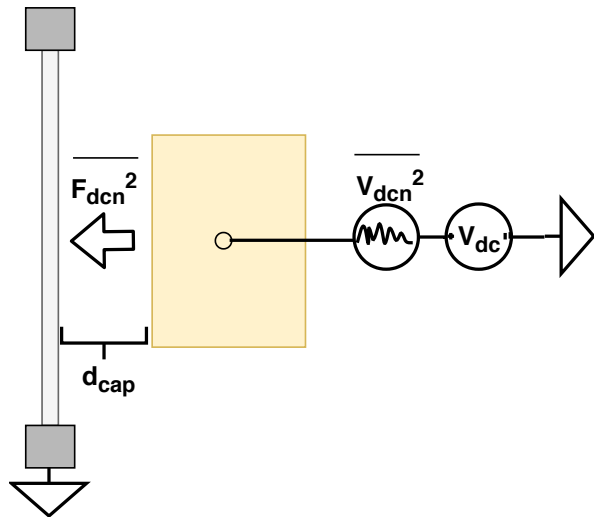


Fig. 5.4 Schematic of forcing generated by the DC voltage sources

shown in Fig. 5.5. The noise of each source is connected in series with the respective source, representing a noisy DC signal that is supplied to the resonators.

V_{c1} and V_{c2} refer to the voltages applied on the body of the resonators to generate a negative coupling stiffness. The noise associated with these two sources are V_{c1n} and V_{c2n} . V_d refers to the DC bias voltage applied to the drive electrode along with V_{ac} through the use of a Bias-T (comprising of C_d and R_d). V_{dn} is the DC noise associated with the drive DC bias voltage. V_p refers to the perturbation voltages used to perturb the coupled system from symmetrical condition and its corresponding noise source is labelled V_{pd} . Lastly, V_{s1} and V_{s2} are the sense voltages applied through a Bias-T to increase the transduction of the motional current seen by the TIA. R_b and C_b are the same as shown in Fig. 5.3 with their own noise sources but they are not portrayed here. V_{s1n} and V_{s2n} are the two noise sources associated with this sense transduction voltages.

The noise forcing ($\overline{F_{dcn}^2}$) due to the electronic noise from the voltage sources is dependent on the area of the capacitor (A_{cap}), distance between the plates (d_{cap}) and the voltage (both DC and AC). The noise of each of the DC voltage source was measured using the noise measurement feature of the Zurich Instruments MFLI and the noise floor is stated in Tab. 5.2. The supply voltages corresponding to these noise measurements are also stated next to the noise measure. These particular voltages are chosen to mimic the experimental conditions discussed later. Hence, these noise measures are valid only at these particular voltages.

Since different voltage sources were used in the experiments, the noise figures vary across the various voltages used. High sense voltages (V_{s1} and V_{s2}) transduce the resonator noise favourably in the experimental section. The perturbation voltage (V_p) is changed throughout

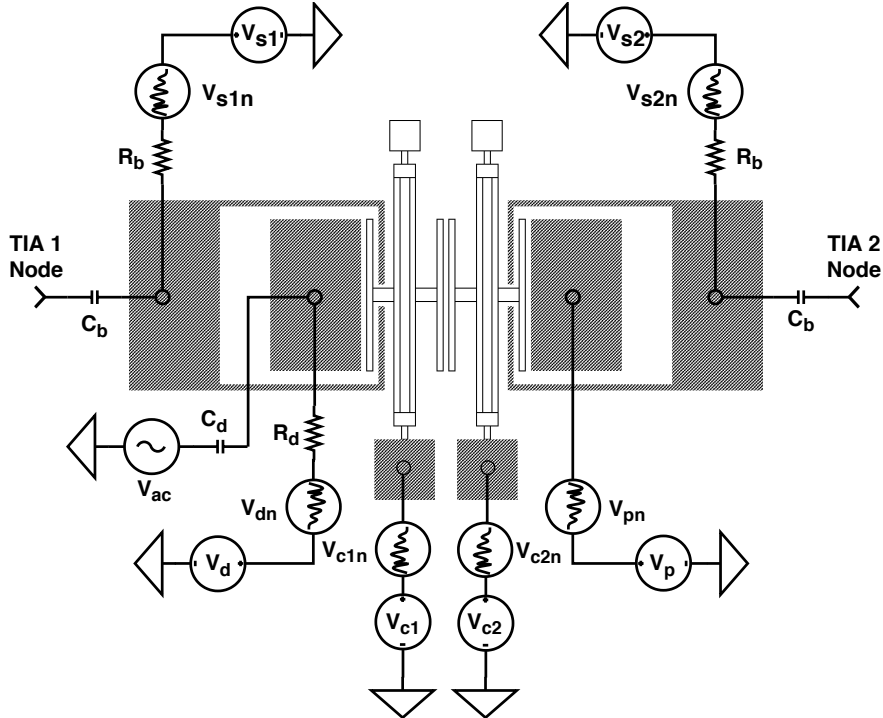


Fig. 5.5 Schematic of two coupled resonators with the different DC sources and the noise associated with each source.

Table 5.2 Noise values for DC sources

Parameter	Noise	DC Voltage
V_{s1n}	$100 \text{ nV}/\sqrt{\text{Hz}}$	60V
V_{s2n}	$100 \text{ nV}/\sqrt{\text{Hz}}$	60V
V_{dn}	$500 \text{ nV}/\sqrt{\text{Hz}}$	20V
V_{pn}	$400 \text{ nV}/\sqrt{\text{Hz}}$	25V
V_{c1n}	$20 \text{ nV}/\sqrt{\text{Hz}}$	14V
V_{c2n}	-	0V

the experiment and this could lead to changes in the noise forcing. However, for the sake of simplicity, the changes in the perturbation voltages are assumed to be much smaller than the absolute perturbation voltage applied. The coupling stiffness is generated by applying 14V on the first resonator and grounding the second one. Therefore, no noise measure is provided for V_{c2n} .

The forces from the noise sources mentioned in Tab. 5.2 are calculated using Eq. 5.13 and added in quadrature with the thermo-mechanical forcing calculated (F_{1m} and F_{2m}) in Eq.

5.7 to achieve the net noise forcing on each of the resonators. The total noise forcing ($\overline{F_{jn}^2}$ where $j = 1, 2$) being experienced by each of the resonators can be summarised as follows:

$$\overline{F_{1n}^2} = \overline{F_{1m}^2} + \overline{F_{s1n}^2} + \overline{F_{dn}^2} + \overline{F_{cn}^2} \quad (5.14a)$$

$$\overline{F_{2n}^2} = \overline{F_{2m}^2} + \overline{F_{s2n}^2} + \overline{F_{pn}^2} + \overline{F_{cn}^2} \quad (5.14b)$$

As discussed, the noise forcing on each resonator is sourced from the various noise sources supplying DC voltages to them. $\overline{F_{s1n}^2}$ and $\overline{F_{s2n}^2}$ are the sourced from the sense bias voltages applied to transduce the sense voltages on each resonator. $\overline{F_{dn}^2}$ describes the forcing applied on the drive resonator due to the drive voltage bias. $\overline{F_{pn}^2}$ includes the forcing applied on the second resonator due to the perturbation voltage. Lastly, $\overline{F_{cn}^2}$ is the forcing applied on both the resonators due to the coupling voltage when realising an electrostatic coupling.

To calculate the total effect of noise on the system, the forcing in Eq. 5.8 needs to be replaced with the forcing in Eq. 5.14 to calculate the net displacement spectrum from the resonator transfer functions (which are mentioned in Eq. 5.10) .

$$\begin{aligned} \overline{x_{1n}^2} &= \left| \frac{H_2(s)}{H_1(s)H_2(s) - k_c^2} \right|^2 \overline{F_{1n}^2} + \left| \frac{-k_c}{H_1(s)H_2(s) - k_c^2} \right|^2 \overline{F_{2n}^2} \\ \overline{x_{2n}^2} &= \left| \frac{-k_c}{H_1(s)H_2(s) - k_c^2} \right|^2 \overline{F_{1n}^2} + \left| \frac{H_1(s)}{H_1(s)H_2(s) - k_c^2} \right|^2 \overline{F_{2n}^2} \end{aligned} \quad (5.15)$$

Then, this displacement noise needs to be converted into current noise through the capacitive transduction equation using the sense transduction voltages (V_{s1} and V_{s2}), the frequency being transduced in radians (ω_0), the area of the capacitor (A_{cap}), and the plate gap (d_{cap}):

$$\overline{i_{1n}^2} = \left(-\frac{\epsilon_0 A_{cap}}{d_{cap}^2} V_{s1} \omega_0 \right)^2 \overline{x_{1n}^2} \quad (5.16a)$$

$$\overline{i_{2n}^2} = \left(-\frac{\epsilon_0 A_{cap}}{d_{cap}^2} V_{s2} \omega_0 \right)^2 \overline{x_{2n}^2} \quad (5.16b)$$

Finally, the electronic noise from the pre-amplifier calculated in Chapter 5.1.2 is added to this current noise in quadrature:

$$\overline{i_{1t}^2} = \overline{i_{1n}^2} + \overline{i_{En}^2} \quad (5.17a)$$

$$\overline{i_{2t}^2} = \overline{i_{2n}^2} + \overline{i_{En}^2} \quad (5.17b)$$

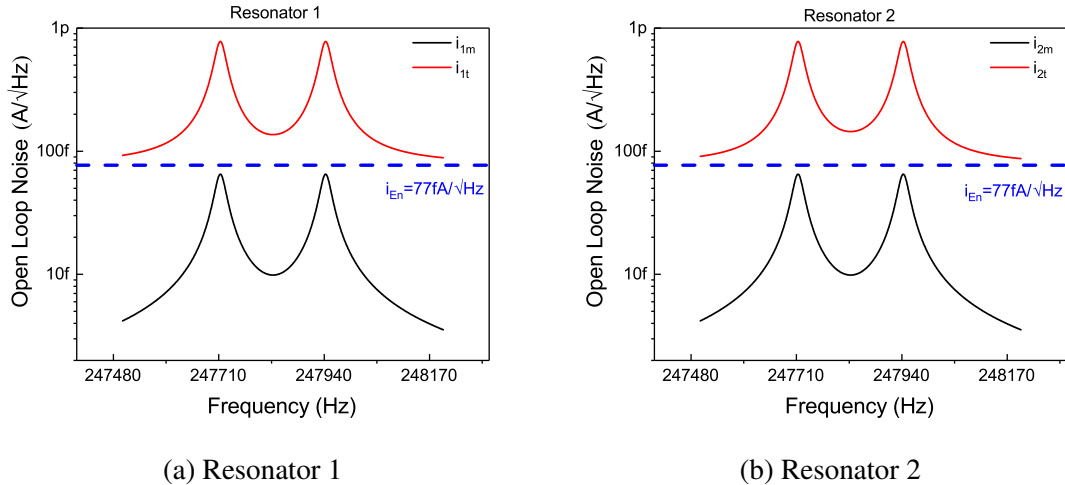


Fig. 5.6 Noise comparisons in the two resonators with different noise forcings compared to the electronic pre-amplifier noise floor.

The spectrum of total amplitude noise calculated using Eqs. 5.15-5.17 is shown in Fig. 5.6 in red. The noise due to only thermo-mechanical noise forcing as seen in Fig. 5.1 is converted into current noise using Eq. 5.16 transduced by the same voltages as mentioned in Tab. 5.1 and plotted in black. The wide band electronic pre-amplifier noise is shown in blue. The red curve summarises the total resonator noise that should be observed experimentally if the noise sources mentioned in this section are all considered. These are the major sources of noise plaguing the mode-localised resonator when measuring amplitude ratio as an output metric. In this system, the noise contribution from thermo-mechanical forcing is only 8% of the total noise forcing applied on the resonator. Therefore, such a system exhibiting these noise properties cannot be characterised purely as a thermo-mechanical noise dominant system. The effect of the noisy DC sources are considerable and eclipse the thermal forcing in this case. As this noise is shaped by the resonator, it will be referred to in this work as resonator noise. Resonator noise shows similar characteristics as thermo-mechanical noise and can be useful in predicting the behaviour of mode-localised resonators when they are purely limited by it.

5.1.3 Amplitude ratio noise

Now that the individual amplitude noise of the resonators have been estimated, the noise of the output metric or in this case amplitude ratio noise needs to be determined. It is imperative that the amplitude ratio be derived from the noise in each channel. To do so, the noise is compared to a statistical variance ($\overline{\cdot^2} = \sigma^2(\cdot)$) around a mean of a particular output metric. Thus, the variance of the amplitude ratio can be calculated by estimating the variance and mean of each channel. A detailed derivation of this calculation is shown in Appendix D. The results of that derivation are highlighted here.

The variance of a ratio can be deduced as:

$$\sigma_{X/Y}^2 = \frac{\mu_X^2}{\mu_Y^2} \left[\frac{\sigma_X^2}{\mu_X^2} + \frac{\sigma_Y^2}{\mu_Y^2} - 2 \frac{\text{Cov}(X, Y)}{\mu_X \mu_Y} \right] \quad (5.18)$$

This relation can then be adapted to the coupled resonator system by equating the variables X and Y to the motional current i_1 and i_2 . Hence, Eq. 5.18 can be remodelled to be:

$$\overline{AR^2} = \sqrt{\frac{\mu_{i1}^2}{\mu_{i2}^2} \left[\frac{\overline{i_{1t}^2}}{\mu_{i1}^2} + \frac{\overline{i_{2t}^2}}{\mu_{i2}^2} - 2 \frac{\text{Cov}(i_1, i_2)}{\mu_{i1} \mu_{i2}} \right]} \quad (5.19)$$

Furthermore, the $\text{Cov}(i_1, i_2)$ can be shown to be negligible when considering the noise sources pertaining to this study (see Appendix D for the full derivation). Therefore, Eq. 5.19 can be simplified to the following relation that can estimate the the amplitude ratio noise ($\overline{AR^2}$) by including the relations between the individual motional currents i_1 and i_2 and their respective total noise values $\overline{i_{1t}^2}$ and $\overline{i_{2t}^2}$:

$$\overline{AR^2} = \frac{\mu_{i1}^2}{\mu_{i2}^2} \left[\frac{\overline{i_{1t}^2}}{\mu_{i1}^2} + \frac{\overline{i_{2t}^2}}{\mu_{i2}^2} \right] \quad (5.20)$$

A further analysis can be undertaken to estimate the input-referred noise when measuring amplitude ratio output metric. The input-referred noise refers to the minimum measurand that is able to be measured given the noise in an output metric. It is achieved by dividing the amplitude ratio noise ($AR_n = \sqrt{\overline{AR^2}}$) by the sensitivity of amplitude ratio to input measurand (in this case it is the normalised stiffness perturbation or $\frac{\Delta k}{k}$).

$$\left(\frac{\Delta k}{k} \right)_n = \frac{AR_n}{\frac{\partial AR}{\partial \Delta k/k}} \quad (5.21)$$

The sensitivity can be found to be a function of amplitude ratio (AR) and coupling stiffness (k_c) with the following relation [113]:

$$\frac{\partial AR}{\Delta k/k} = \frac{AR}{(AR + \frac{1}{AR})k_c} k \quad (5.22)$$

Using this model, the input-referred amplitude ratio noise can be predicted and optimised with respect to the various operating conditions such as the stiffness mismatch, the coupling stiffness, and the quality factor.

5.2 Optimising amplitude ratio noise

In practical operation of the sensor, either the output metric in the sensing frequency range is dominated by resonator noise or by the electronic pre-amplifier noise. To understand the different variables affecting the amplitude ratio noise, it is prudent understand how the system behaves when one of these sources is dominant.

5.2.1 Electrical noise dominant system

The theory and modelling done in this subsection are derived from my own work in [113] in which I was equally contributing author. In an electrical noise dominant system, the current amplifier noise ($\overline{i_{En}^2}$) tends to dominate the noise from the resonator. To analyse the impact that this noise has on amplitude ratio noise, the current noise is converted into vibration amplitude noise $\overline{x_{En}^2}$. Since the two channels use similar electronic pathways, the noise in both the channels is assumed to be same. The amplitude ratio noise when operating at the resonant frequency of the coupled system can be estimated to be:

$$\frac{\overline{AR^2}}{\overline{AR^2}} = \frac{\overline{i_{En}^2}}{\overline{X_1^2}} + \frac{\overline{i_{En}^2}}{\overline{X_2^2}} \quad (5.23)$$

The aim of optimising the amplitude ratio noise is to investigate an optimum with respect to operating amplitude ratio (AR) and coupling stiffness (k_c). Therefore, it is important to write the relation in Eq. 5.23 purely in those terms and some important constants. The resonant frequency for the two modes of the weakly coupled resonators has been derived in Chapter 2.9 to be:

$$\omega_i^2 = \frac{2k + 2k_c + \Delta k \mp \sqrt{\Delta k^2 + 4k_c^2}}{2m} \quad (5.24)$$

Using this expression for the resonant frequency and the transfer function approach for a single ended drive configuration, the individual resonator amplitudes when driven at a force (F_d) can be expressed to be [113]:

$$|X_1| = \left| \left(\frac{H_2}{H_1(\omega_0)H_2(\omega_0) - k_c^2} \right) F_d \right| = \frac{1}{2} \left| \frac{\Delta k + \sqrt{\Delta k^2 + 4k_c^2} + 2jc\omega_0}{-c^2\omega_0^2 + jc\omega_0\sqrt{\Delta k^2 + 4k_c^2}} \right| |F_d| \quad (5.25a)$$

$$|X_2| = \left| \left(\frac{-k_c}{H_1(\omega_0)H_2(\omega_0) - k_c^2} \right) F_d \right| = \left| \frac{k_c}{-c^2\omega_0^2 + jc\omega_0\sqrt{\Delta k^2 + 4k_c^2}} \right| |F_d| \quad (5.25b)$$

Since, the amplitudes of the resonators at their resonant frequency (ω_0) are considered for the noise analysis, $|X(\omega_0)| = |X|$ in the amplitude ratio calculations. Accordingly, the amplitude ratio (AR) can be expressed as:

$$|AR| = \left| \frac{X_1}{X_2} \right| = \left| \frac{\Delta k + \sqrt{\Delta k^2 + 4k_c^2} + 2jc\omega_0}{2k_c} \right| \quad (5.26)$$

Assuming no modal overlap ($k_c > \frac{2k}{Q}$), the terms containing the damping term can be ignored for simplicity. Furthermore, using some simple arithmetic on Eq. 5.26, the following relations can be derived to simplify the equation in terms of the amplitude ratio:

$$\frac{\Delta k}{k_c} = \left(\frac{AR^2 - 1}{AR} \right) \quad (5.27a)$$

$$\frac{\sqrt{\Delta k^2 + 4k_c^2}}{k_c} = \left(\frac{AR^2 + 1}{AR} \right) \quad (5.27b)$$

Using the above relations, the expression for the two amplitudes can be written in terms of AR , k_c , k , Q and F_d as:

$$|X_1| = \left| \frac{Q}{k + k_c} \frac{AR^2}{AR^2 + 1} \right| |F_d| \quad (5.28a)$$

$$|X_2| = \left| \frac{Q}{k + k_c} \frac{AR}{AR^2 + 1} \right| |F_d| \quad (5.28b)$$

Substituting the value of $|X_1|$ and $|X_2|$ in Eq. 5.23, amplitude ratio noise (AR_n) can be estimated to be:

$$AR_n = x_{En} \left| \frac{k + k_c}{F_d Q} \right| \frac{(AR^2 + 1)^{\frac{3}{2}}}{AR} \quad (5.29)$$

Note the change from noise power to noise amplitude ($x_{En} = \sqrt{x_{En}^2}$). Since the input-referred noise is of interest, Eq. 5.29 needs to be divided by the sensitivity to stiffness perturbations as shown in Eqs. 5.21 and 5.22. Thus, the input-referred amplitude ratio noise assuming $k_c \ll k$ can be expressed as:

$$\left(\frac{\Delta k}{k} \right)_n = \frac{AR_n}{\frac{\partial AR}{\Delta k/k}} = x_{En} \left| \frac{k + k_c}{F_d Q} \right| \frac{(AR^2 + 1)^{\frac{3}{2}}}{AR} \frac{AR^2 + 1}{AR^2} \frac{k_c}{k} = x_{En} \left| \frac{k_c}{F_d Q} \right| \frac{(AR^2 + 1)^{\frac{5}{2}}}{AR^3} \quad (5.30)$$

This relation shows that the input-referred amplitude ratio noise in an electrical noise dominant system is dependent directly on the coupling stiffness (k_c) and the electrical noise (x_{En}); whereas, it is inversely dependent on the drive force (F_d) and Quality factor of the resonator (Q). Since x_{En} , F_d and Q are all constant in a system, the coupling stiffness (k_c) is a very important tuning variable (especially in an electrically coupled device) to reduce the input-referred amplitude ratio noise. The dependence of the noise on amplitude ratio is complex. Therefore, the minimum of the function can be obtained by equating its derivative to zero ($\frac{\partial(\Delta k/k)_n}{\partial AR}(AR) = 0$) in order to find its roots. This leads to the result where the input-referred noise is minimized at $AR = \sqrt{1.5} = 1.22$. Therefore, in a system dominated with electrical noise from the amplifier, it is beneficial to work at an amplitude ratio of 1.22 to achieve the best sensing resolution.

To simulate this behaviour, values as close to the experimental system are chosen. The drive force ($F_d = 2 \times 10^9$ N) representative of linear operation and a quality factor of 10000 are selected. Three different k_c values of -0.8 N/m, -1 N/m, and -1.2 N/m are used to show the variation of the noise with coupling stiffness. The amplitude ratio is swept between 0.5 and 3 to investigate optimal operating points. A representative amplitude noise of the pre-amplifier noise corresponding to ($x_{En} = 100$ fm/ $\sqrt{\text{Hz}}$) is used. The results of the simulation are shown in Fig. 5.7.

As the figure suggests, the input-referred noise varies with both the coupling stiffness and the amplitude ratio with the minimum occurring at an amplitude ratio of 1.22. Furthermore, Eq. 5.30 dictates that the noise decreases with a decrease in k_c . However, it is worth noting that there is a lower limit to k_c that is determined by the modal overlap assumption. Therefore,

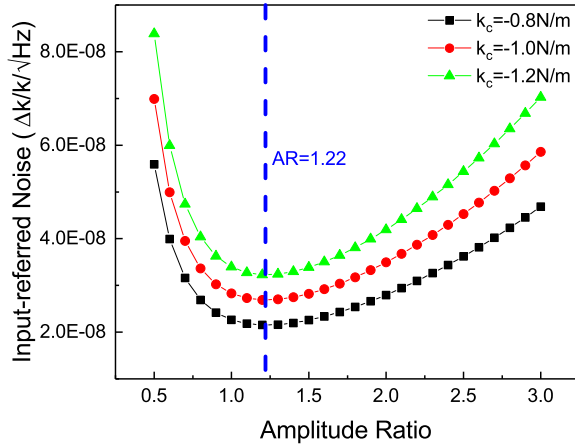


Fig. 5.7 Input-referred noise when electrical pre-amplifier noise dominates in the sensing region.

for optimum operation, k_c can be reduced as far as $k_c \geq \frac{k}{Q}$ but cannot be reduced further since it would deter the appropriate working of the coupled system as a sensor.

5.2.2 Resonator noise dominant system

In a resonator noise dominant system, the noise can no longer be considered to be constant across different amplitude ratios or across both channels. Hence, to derive an expression for such a system, the transfer function method needs to be employed. The expression for the amplitude ratio remains similar except for the noise in each of the resonators, which is now shaped by the resonator:

$$\frac{\overline{AR^2}}{\overline{AR^2}} = \frac{\overline{x_{1m}^2}}{\overline{X_1^2}} + \frac{\overline{x_{2m}^2}}{\overline{X_2^2}} \quad (5.31)$$

The expression for the resonator noise (that includes thermo-mechanical and voltage source noise) has been derived previously in Eq 5.15 using the transfer function method. A similar method has also been used to derive expressions for the vibration amplitudes of individual resonators (in Eq. 5.25a and 5.25b). The expression for amplitude ratio noise in Eq. 5.31 can be similarly setup as:

$$\frac{\overline{AR^2}}{\overline{AR^2}} = \frac{|H_{11}|^2 \overline{F_{1n}^2} + |H_{12}|^2 \overline{F_{2n}^2}}{|H_{11}|^2 F_d^2} + \frac{|H_{21}|^2 \overline{F_{1n}^2} + |H_{22}|^2 \overline{F_{2n}^2}}{|H_{21}|^2 F_d^2} \quad (5.32)$$

In Eq. 5.32, $\overline{F_{1n}^2}$ and $\overline{F_{2n}^2}$ are the two noise forcing on the resonators and can be assumed to be equal ($\overline{F_n^2}$). F_d is the drive forcing on resonator 1 when the system is operating in the linear regime. By substituting the individual resonator transfer functions ($H_1(j\omega)$ and $H_2(j\omega)$) into Eq. 5.32, the expression for amplitude ratio noise can be reduced to:

$$\begin{aligned}\frac{\overline{AR^2}}{AR^2} &= \frac{|H_2(j\omega_0)|^2 \overline{F_n^2} + |k_c|^2 \overline{F_n^2}}{|H_2(j\omega_0)|^2 F_d^2} + \frac{|H_1(j\omega_0)|^2 \overline{F_n^2} + |k_c|^2 \overline{F_n^2}}{|k_c|^2 F_d^2} \\ &= \left(\frac{\overline{F_n^2}}{F_d^2} \right) \left(2 + \frac{k_c^2}{|H_2(j\omega_0)|^2} + \frac{|H_1(j\omega_0)|^2}{k_c^2} \right)\end{aligned}\quad (5.33)$$

The transfer functions have been previously achieved to be $H_1(j\omega) = -m\omega^2 + jc\omega + k + k_c$ and $H_2(j\omega) = -m\omega^2 + jc\omega + k + k_c + \Delta k$. These two expressions need to be defined in terms of amplitude ratio. To achieve that, the expression for the resonant frequency as shown in Eq. 5.24 is plugged in for the mode of interest and then the relations in Eq. 5.27a and 5.27b are used:

$$|H_1(j\omega_0)| = \left| \frac{-\Delta k + \sqrt{\Delta k^2 + 4k_c^2} + 2jc\omega_0}{2} \right| = \left| \frac{k_c}{AR} + jc\omega_0 \right| \quad (5.34a)$$

$$|H_2(j\omega_0)| = \left| \frac{\Delta k + \sqrt{\Delta k^2 + 4k_c^2} + 2jc\omega_0}{2} \right| = \left| k_c AR + jc\omega_0 \right| \quad (5.34b)$$

Substituting Eqs. 5.34a and 5.34b into Eq. 5.33, and assuming low modal overlap due to a high quality factor ($jc\omega_0 \approx 0$), the expression for amplitude ratio noise can be reduced to:

$$\begin{aligned}AR_n &= \sqrt{AR^2 \left(\frac{\overline{F_n^2}}{F_d^2} \right) \left(2 + \frac{1}{AR^2} + \frac{1}{AR^2} \right)} \\ &= \left(\frac{F_n}{F_d} \right) \sqrt{2(AR^2 + 1)}\end{aligned}\quad (5.35)$$

As previously done with the electronic noise, it is important to achieve an expression for the input-referred noise. For that, the expression in Eq. 5.35 needs to be divided by the sensitivity to input stiffness perturbations highlighted in Eqs. 5.21 and 5.22. This way, the input-referred noise in a resonator noise dominant system can be derived to be:

$$\left(\frac{\Delta k}{k}\right)_n = \left(\frac{F_n}{F_d}\right) \frac{k_c}{k} \sqrt{2(AR^2 + 1)} \frac{AR^2 + 1}{AR^2} = \sqrt{2} \left(\frac{F_n}{F_d}\right) \frac{k_c}{k} \frac{(AR^2 + 1)^{\frac{3}{2}}}{AR^2} \quad (5.36)$$

Thus, in a system dominated by resonator noise, the input-referred amplitude ratio noise is once again directly proportional to the coupling stiffness (k_c) and the noise forcing (F_n) and inversely proportional to the drive force (F_d). The noise forcing is in turn dependent on the ambient temperature and the Q factor of the system. However, F_d and F_n are constant in a system during operation and the main factors that can be tuned are the coupling stiffness and the amplitude ratio. Similar to a system that is dominated by electronic noise, the coupling stiffness can be reduced to reduce the input-referred noise. Again the lower limit to this would be defined by $k_c \geq \frac{k}{Q}$ to avoid modal overlap. To find the minimum of the function, its differential is solved for its roots by equating it to zero ($\frac{\partial(\Delta k/k)_n}{\partial AR}(AR) = 0$). In this case, the function has a minimum at $AR = \sqrt{2} = 1.41$. It should be noted that this is also the case for thermo-mechanical noise which is shaped in the same manner by the resonator.

The expression is again used to plot the input-referred noise with respect to different amplitude ratios and three different coupling stiffness. A noise forcing ($F_n = 150$ fN/ $\sqrt{\text{Hz}}$) is used which is representative of the total forcing from thermal and electronic sources. The drive force ($F_d = 2 \times 10^9$ N) representative of linear operation, a resonator stiffness (k) of 1080 N/m, and a quality factor of 10000 are chosen. Three different k_c values of -0.8 N/m, -1 N/m, and -1.2 N/m to show the variation of the noise with coupling stiffness. The amplitude ratio is swept between 0.5 and 3 to investigate optimal operating points. The results are plotted in Fig. 5.8.

As seen from Fig. 5.8, the input-referred noise has a minimum at $AR = \sqrt{2}$ and decreases with a decrease in the coupling stiffness. Although the trend of the noise is similar to that of a system dominated by electronic noise, it is worth noting that the minimums with respect to amplitude ratios are different. It is to be noted that the noise forcing considered here is the noise amplitude at the resonant frequency. If the noise away from resonant frequency needs to be estimated (even at the 3dB point), the expression for the minimum in Eq. 5.36 could vary. However, the analytical solutions point to the conclusion that the choice of operating point will depend on which noise (electronic pre-amplifier or the resonator noise) governs.

Although the analytical solutions show that different minimums for the input-referred amplitude ratio noise exist for the two dominant noise mechanisms, the minimum can be considered more of a range than a particular amplitude ratio point. Especially in the case of the resonator noise dominant case, if the noise drive force (F_n) is not equal on both resonators,

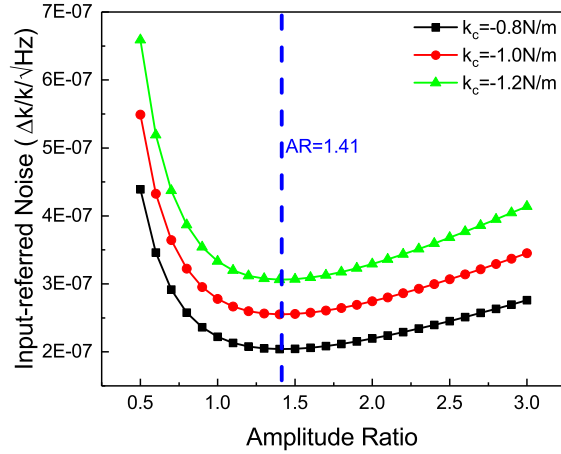


Fig. 5.8 Input-referred noise when resonator noise dominates in the sensing region.

the minimum tends to move towards the amplitude ratio $\sqrt{1.5}$. In the ideal case that the two noise forcings are equal (as assumed in this case) and the pre-amplifier noise is much lower than the resonator noise, the input-referred noise would have a minimum at amplitude ratio $\sqrt{2}$. However, in practice, equal noise forcing is not achievable and more often than not, the minimum tends to be broadly distributed in between $\sqrt{1.5}$ and $\sqrt{2}$ when implementing single ended drive configuration. It would be different for a double ended drive which is beyond the scope of this work. The more important result is that the input-referred noise reduces with a reduction of coupling stiffness. Therefore, this result has more impact on the ultimate resolution of the sensor than operating the sensor between an amplitude ratio of $\sqrt{1.5}$ and $\sqrt{2}$.

5.3 Experiment

Modelling and predicting the ultimate limit of amplitude ratio sensing using mode-localised sensors has been the topic of several studies so far [73, 33, 74]. Many studies have also tried to experimentally determine the amplitude ratio noise by measuring the noise of each resonator output and estimating the amplitude ratio noise from those noise channels [72, 30, 114]. Although these are helpful ways of estimating the noise of the amplitude ratio output metric, they all make certain assumptions about the relation between the amplitude ratio noise and the noise in individual resonators. The theory shown in this chapter also is a way of estimating the noise of the amplitude ratio noise from the noise in each resonator

channel. However, the most accurate way of describing the amplitude ratio noise is by experimentally analysing the ratio of the two resonator amplitudes taken directly rather than analysing the noise in each channel separately. This way, the true noise in the output metric is determined experimentally rather than through analytical estimates. It also allows for direct optimisations to be made with respect to the resolution of the amplitude ratio output metric. They can then be used to validate the results of the optimisations achieved via analytical studies.

Therefore, an experiment is designed around the electrostatically coupled resonator topology as shown in Fig. 5.9.

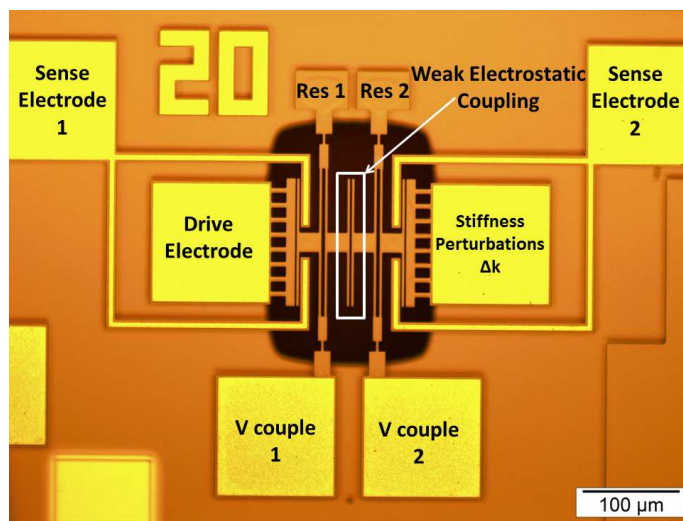


Fig. 5.9 Optical micrograph of the electrostatically coupled resonators

Device Parameters

The device used for the experiment consists of a system of electrically coupled DETF resonators as shown in Chapter 3.1. It is re-illustrated in Fig. 6.5.

Measurement setup

A schematic of the measurement setup is shown in Fig. 5.10. The coupling in the device is realised using the two voltages (V_{DC1}) and (V_{DC2}) that are applied on the resonators' body. For this experiment, (V_{DC1}) is grounded at 0 V and (V_{DC2}) is changed from 12 V to 16 V to apply different coupling stiffness. The AC drive voltage (10 mV) is applied from the Zurich Instruments MFLI and is passed through a Bias-T with a DC voltage (V_B) of 20 V ensure a high transduction force while keeping the resonator operating in the linear regime.

Perturbation voltage is applied on Resonator 2 to vary the operating amplitude ratio from $AR = 0.8$ to $AR = 2$. The motional currents from both resonators are then passed through a transimpedance amplifier with a gain $\approx 2 \text{ M}\Omega$ to convert the motional current into a voltage. To aid the sense transduction, a bias voltage (V_s) of 60 V is applied on the sense node using a Bias-T. This is done only to have a higher transduction to sense the resonator noise of the device. For operation as a sensor, it is not necessary to have such a high V_s .

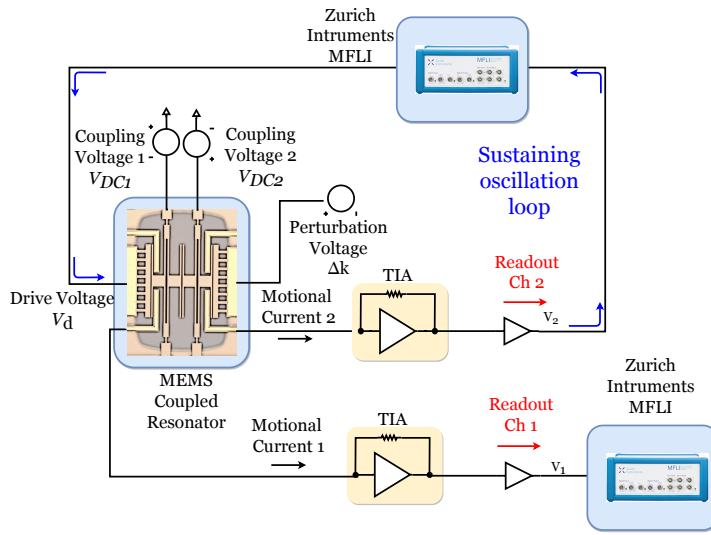


Fig. 5.10 Experimental setup to realise a closed-loop measurement.

To realise a closed-loop measurement, the Phase Locked Loop (PLL) function of the MFLI is used to lock onto the resonant frequency of the coupled resonator using the output voltage (V_2) as an input. The other output voltage is read out in an open-loop configuration using another MFLI in a lock in configuration. The clocks of the two MFLIs are synchronised and an external signal generator is used to provide a trigger for both MFLIs so that the measurements are taken at the same time.

5.4 Results

The results section is divided into two parts – an open-loop noise measurement and a closed-loop noise measurement. Both measurements reveal different noise processes occurring in the system and are important to analyse in depth.

5.4.1 Open-loop noise measurement

To measure the open-loop noise of the system, the AC drive voltage (V_d) is turned off while keeping all the other DC voltages on. The noise measurement option in the MFLI is used to measure the noise with a 1 Hz bandwidth around the resonant frequency of the resonators. The results are plotted in Fig. 5.11a and 5.11b. To prove that the noise measured is due to the two modes of the coupled system, an open-loop sweep is also done with a 10 mV AC drive voltage (V_d). This sweep results in the resonance occurring at the same frequency as seen during the noise sweep. This confirms that the noise peaks measured are originating from the resonator.

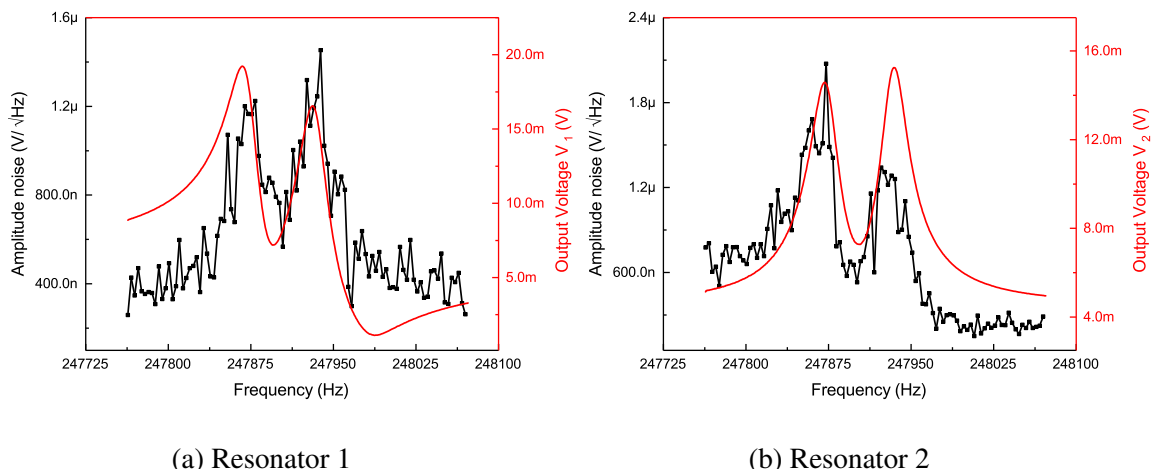


Fig. 5.11 Measured open-loop noise in each channel superimposed with the output voltage at the same perturbation voltage.

The noise profile seen in Fig. 5.11 suggests that the electronic noise due to the amplifiers and the readout circuitry is around $400 \text{ nV}/\sqrt{\text{Hz}}$ and forms the noise floor for amplitude measurements in both channels. There is a slight discrepancy in the two channels and that can be attributed to the variation in the electronic parts used between the two channels.

The noise peaks shown in the plot can be attributed to the result of the forcing from thermo-mechanical sources and the DC voltage sources. It can be concluded from these plots that the system is dominated by resonator noise. Due to the fact that the resonator noise profile is visible in the open-loop noise sweep suggests that in closed-loop operation, the noise close to resonance will also be dominated by resonator noise.

5.4.2 Closed-loop noise measurement

Open-loop noise sweeps cannot be used to accurately describe the amplitude ratio noise since they do not reflect the amplitude ratio noise in closed-loop operation. Furthermore, the noise in open-loop can describe only the noise in individual channels and not the noise in the actual output metric – amplitude ratio. Thus, they cannot be used as a representative noise figure for the amplitude ratio output metric. The accurate way of measuring amplitude ratio noise would be to (a) measure the two output voltages during closed-loop operation, (b) take the ratio of the two output voltages corresponding to the same time, (c) perform Fast Fourier Transform (FFT) on the data to get the noise spectral density (NSD) of the amplitude ratio.

In order to achieve the NSD of the amplitude ratio, the resonators are set into closed-loop oscillations using the PLL function of the Zurich Instruments MFLI as shown in Fig. 5.10. The oscillator is locked to the in-phase mode of resonators. The filter bandwidth of the PLL is set to 500 Hz and the measurement sampling frequency is chosen to be 1 kHz to capture all the frequency components within the range of 500 Hz. The measurement of the amplitude is done using the lock-in feature of the MFLI and the two MFLIs are synchronised with an external trigger in the form of a signal generator applying a frequency of 1 kHz. The coupling voltage of 16 V and a perturbation voltage of 9.5 V are set to achieve an amplitude ratio ~ 1 . The measurement of each channel is taken for 5 minutes synchronously. An FFT is then performed on the data which is shown in Fig. 5.12a and 5.12b.

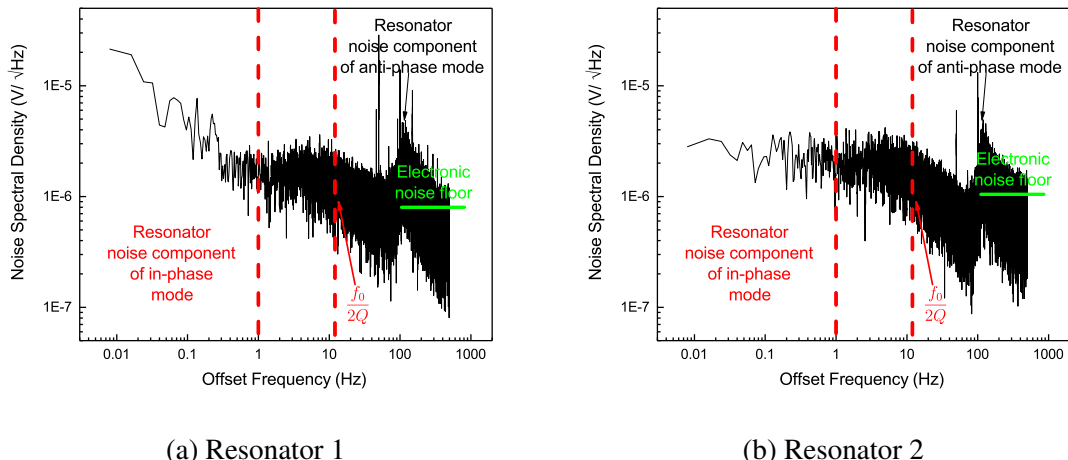


Fig. 5.12 Noise spectral density of the output amplitudes of the two resonators with the different noise areas highlighted.

The NSD of the closed-loop amplitude measurements can be thought of as a representative noise profile achieved by offsetting the open-loop noise to the respective frequency of the

mode being sensed. The noise close to carrier (until 12 Hz) shows the resonator noise dominating. As discussed previously, this is representative of the noise sourced from thermo-mechanical origins and the DC voltage sources. The resonator noise of the anti-phase mode is also visible here but, it is not trivial to decompose the various noise factors affecting this mode. Thus, it is not going to be part of this analysis. Beyond this, the electronic noise of the amplifier is also visible at frequencies above 400 Hz. This noise is going to form the noise floor for each channel and is assumed to be of white nature beyond 400 Hz. The bandwidth of the sensor is limited to the position of the non-driven mode (anti-phase mode in this case) to avoid modal coupling. This means that in the sensing region (0-100 Hz), resonator noise dominates as predicted from the open-loop noise sweep.

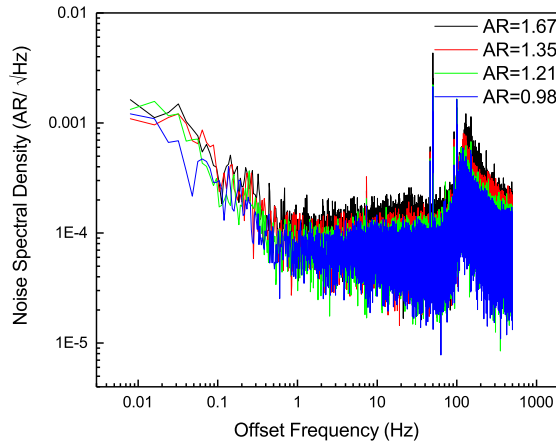


Fig. 5.13 Noise spectral density of the amplitude ratio output metric at different operating amplitude ratios.

To get the NSD of the amplitude ratio output metric, a ratio of the two output voltages measured is taken and FFT is performed on this ratio metric data. By applying perturbations to the system, the amplitude ratio operating points are changed. The results of this FFT for four different operating amplitude ratios is shown in Fig. 5.13.

Overlaying the NSD at different amplitude ratio shows the variation of the amplitude ratio noise with the different operating amplitude ratios. For the purposes of this analysis, the noise only until 100 Hz would be considered due to the bandwidth of the sensor. The noise before 1 Hz is dominated by the noise of the oscillator which is non-trivial to predict. The noise in a 10 Hz bandwidth between 1Hz and 11 Hz is integrated and averaged to achieve the RMS noise. This frequency range is chosen to avoid including high frequency noise that is coupled in from the mains and the environment to skew the resulting noise figure.

Furthermore, the resonator noise is maximum within the bandwidth of the resonators (in this case 12 Hz) so by using this frequency range, the impact of the resonator noise on amplitude ratio noise is captured.

In order to achieve an input-referred noise, the sensitivity of the amplitude ratio to stiffness perturbations must be experimentally characterised for all the operating points and coupling stiffness. This data is captured in Fig. 5.14. The sensitivity increases with increasing amplitude ratio operating points; it also increases with a decrease in the coupling stiffness (represented here by a decrease in coupling voltage).

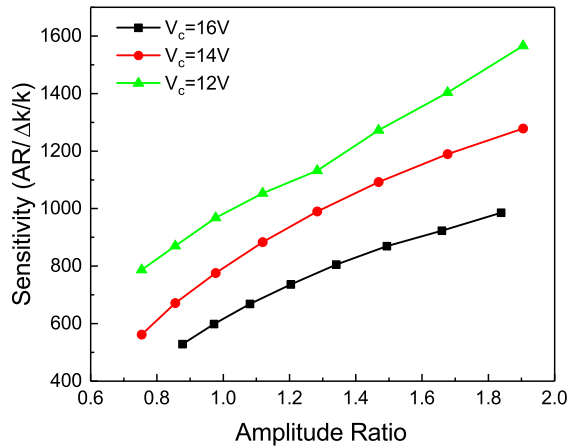


Fig. 5.14 Localised sensitivity of amplitude ratio to input stiffness perturbations at different operating amplitude ratios.

The amplitude ratio noise is averaged in the respective frequency range of interest at different amplitude ratio operating points ranging from AR=0.8 to AR=2. The input-referred noise is then calculated by dividing the amplitude ratio noise by the experimental local sensitivity at each of those amplitude ratios and coupling voltages. The averaged input-referred noise are plotted in Fig. 5.15.

There is a clear minimum in the input-referred noise with respect to the amplitude ratio operating point much like the simulation predicted. As expected, this minimum is quite broad in between $\sqrt{1.5}$ and $\sqrt{2}$. Similar to the discussion in the theoretical section (refer to Fig. 5.8), the minimum of the input-referred noise with respect to amplitude ratio operating point in a resonator noise dominant system is dependent on the noise forcing on the two resonators being equal. It is not practically possible to achieve symmetric noise forcing due to different voltage sources being used in the experiment and this causes the minimum to shift away from $AR = \sqrt{2}$. More importantly, the noise tends to reduce with the reduction in

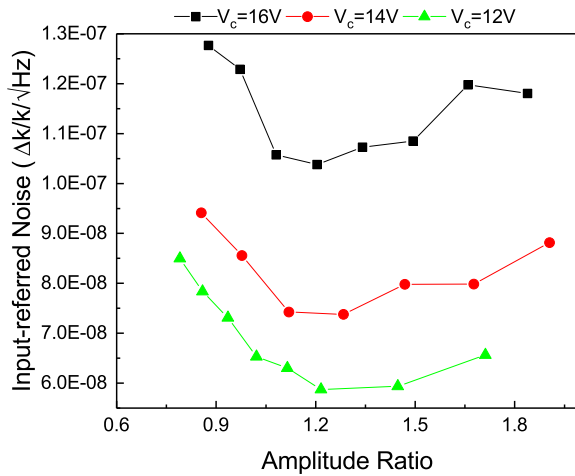


Fig. 5.15 Input-referred noise plotted against various amplitude ratios and coupling voltages.

the coupling voltage. This shows that a reduction in the coupling stiffness is key in reducing the input-referred amplitude ratio noise and therefore leading to better sensing resolution.

It is to be noted that the thermo-mechanical noise limit of the resonator is not reached in this experiment. As mentioned, earlier, the noise in the DC voltage sources are shaped by the resonator much like the shaping of the thermo-mechanical noise. Thus, conclusions about the optimisations done on the resonator noise can be applied to a system that is solely limited by thermo-mechanical noise. The key findings of the optimum amplitude ratio and coupling operating points would hold for a system limited by thermo-mechanical noise. Future systems that have better electronic noise performance would benefit from this study and optimisation techniques used here can be employed to achieve optimum sensing resolution.

Summary

A complete analysis of the amplitude ratio noise in weakly coupled resonators is carried out in this chapter. Various noise sources that could affect the coupled system are discussed and their effect on the noise in each resonator is predicted using a transfer function method. Using the noise in each resonator amplitude, the input-referred amplitude ratio noise is predicted with emphasis on optimising the noise in resonator noise dominant system and in the electronic noise dominant system. Analytical calculations show that in the ideal case, the optimum operating amplitude ratio to minimise input-referred electronic noise floor is $AR = \sqrt{1.5}$ and that to minimise resonator noise is $AR = \sqrt{2}$ in a single ended drive configuration. This paves the way for applications where the system can be put into a

control loop at a particular operating amplitude ratio (where the noise is minimum) and the control effort is measured so as to achieve the best resolution from mode localised devices. Furthermore, these solutions predict that the input-referred noise reduces with the reduction of the coupling stiffness.

The results of the simulations were bolstered with experimental validation of the model with the help of an electrically coupled resonator system. Various coupling stiffness and amplitude ratio operating points were chosen and the amplitude ratio noise at each of those operating conditions was measured. The input-referred noise was calculated and plotted to confirm the results of the simulations. The experiment on the whole agreed with the simulations validating the key observation that the system showed a reduction in noise with a reduction in the coupling stiffness. This result is paramount in creating high Q factor devices with a low coupling stiffness to improve the ultimate achievable resolution of amplitude ratio output metric in weakly coupled mode-localised sensors. The next steps on this topic would revolve around comparing the fundamental limits of the amplitude ratio noise to the noise of the frequency shift output metric.

Chapter 6

Nonlinear Characterisation of Mode-localised Sensor

To date, mode-localised sensors have not been characterised in the nonlinear domain at high vibration amplitudes. Nonlinear models of mode localisation are complex, and their solutions are difficult to obtain analytically. Furthermore, high vibration amplitudes lead to an amplitude-frequency (*a-f*) dependency that affects the closed-loop stability of the oscillator [115]. Nonetheless, there are several advantages of operating the sensor in high vibration amplitudes. In a system dominated by the electrical noise of readout electronics, high vibration amplitudes allow for a greater output signal that result in high signal to noise ratio (SNR). This could potentially lead to higher resolution amplitude measurements for amplitude ratio sensing [66]. This chapter develops a model to predict the dynamics of the coupled resonator system in the nonlinear domain. Using the modelling and experimental results, it investigates the possibility of the improving the noise floor of amplitude ratio as an output metric by operating the sensor at its bifurcation points.

6.1 Nonlinearity in MEMS resonators

Conventionally, MEMS/NEMS resonators are operated in the linear regime. The increasing need for high performance sensors with high resolution has saturated design optimisations revolving around improving sensitivity, signal-to-noise ratio (SNR) and quality factors. Of these parameters, in the context of a sensor, SNR plays a crucial role in determining the ultimate sensing resolution. Thus, SNR is an important factor to improve.

If the noise in the system remains constant, the SNR can be enhanced by either increasing the sense transduction factor or increasing the drive force to the resonant structure. Since

the transduction factor is limited by design conditions such as manufacturing constraints and the supply voltage for the system, optimising the transduction factor for a given process offers only limited options. Furthermore, increasing the drive force will make the resonator amplitude grow until it is limited by nonlinear effects. In order to increase the linear range of operation, the concept of nonlinearity cancellation was proposed [116]. This approach can be employed to cancel the mechanical sources of nonlinearity arising from the geometric stiffening of the resonator using the electrical nonlinearities arising from voltage bias across parallel plate electrodes. However, since this approach requires precise control over tuning of the voltage, it is not practical for use in sensor applications.

Operating the nonlinear regime is generally considered detrimental to stability of the oscillator due to the presence of amplitude to frequency (*a-f*) effect [117]. However, in the community of MEMS/NEMS resonators, it has been demonstrated theoretically and experimentally by various groups that nonlinear effects can be useful for noise reduction in frequency and amplitude measurements [118–125]. In particular, operating at the top and bottom bifurcation points has shown better phase noise filtering effects because of the frequency-phase plot having a zero slope at those points. This has resulted in better frequency stability at those points [120].

Energy localisation in coupled nonlinear systems has been studied previously [126–128] whilst, its applications in the context of sensing have not been significantly pursued. Recently, operating actively coupled devices in the nonlinear regime through injection locking mechanisms has shown to provide an enhanced locking range [129]. However, one of the drawbacks of operating beyond the critical Duffing amplitude is stated to be the reduced sensitivity to stiffness perturbations that is critical for sensing applications[130].

High resolution amplitude ratio measurements in a mode-localised sensor require not only a reduction of phase and frequency noise but also an optimisation of the amplitude noise. Previous work has shown [123, 124] that working at the nonlinear bifurcation points of both single and coupled resonators leads to an increased amplitude SNR. On the other hand, the long-term stability of the amplitude readout is affected due to higher order noise (f^{-n} where $n \geq 2$) mixing in the nonlinear regime. Furthermore, the tuning of electrostatic coupling has also been shown to induce a nonlinearity cancellation regime. This can be useful in achieving higher SNR without introducing higher order noise mixing [128].

This work amalgamates the concepts of utilising the nonlinear bifurcation points and the energy localisation phenomena within a weakly coupled nonlinear resonator to demonstrate a proof-of-concept sensor. It is important to note that the region just beyond the critical Duffing amplitude is considered here. This ensures that non-trivial effects such as stress build up on

the mechanical resonators and higher order nonlinear effects do not undercut the key benefit of improvement in signal-to-noise ratio.

In this chapter, a theoretical study is first conducted on a nonlinear single resonator system which is then expanded to include a coupled resonator topology. Features such as the suppression of amplitude ratio output metric in the nonlinear domain are predicted. Experiments are used to characterise the amplitude ratio output metric in the nonlinear domain at different operating points and modes. These results are then compared to the linear operation of the sensor. Next, it is shown that the resolution of the amplitude ratio output metric can be enhanced by operating at the top and bottom bifurcation points in a regime beyond the critical Duffing amplitude. Discrepancies between theory and experiment are explained with discussions on wider impact of the results to other MEMS devices.

6.2 Nonlinear model of a single resonator

Before modelling a nonlinear coupled resonator topology, it is pertinent to understand the effects of nonlinearity on a resonator. To that end, a model of a single resonator with nonlinear stiffness is used with a lumped spring-mass-damper diagram as seen in Fig. 6.1 where k_n is the nonlinear spring, c is the linear damper, m is the mass and F is forcing applied to the system.

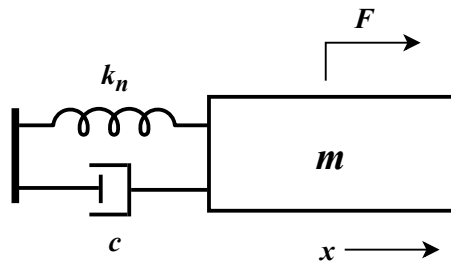


Fig. 6.1 Lumped spring-mass-damped model of a single nonlinear resonator.

The primary effect of nonlinearity on the resonator is noticed in the frequency response of the system. One way of analyzing this effect is through the method of harmonic balance to achieve both the backbone curve of the system (for an undamped system) and the frequency response curve (for a damped system). For simplicity, the damper is assumed to be linear although further analysis can be performed on a system with nonlinear damping as well.

Backbone function

A 1-DoF equation of motion for an undamped nonlinear resonator with cubic stiffness nonlinearity (assuming that the quadratic stiffness nonlinearity is negligible due to the symmetry of the device) is as below [69]:

$$\ddot{x} + \omega_n^2 x + \beta x^3 = 0 \quad (6.1)$$

where, $\omega_n^2 = \frac{k}{m}$ is the natural frequency of the resonator and β is the cubic nonlinearity term. The harmonic solution for this equation takes the general form of $x = X_R \cos(\omega t)$. Substituting this solution into Eq. 6.1, yields:

$$(\omega_n^2 - \omega^2)X_R \cos(\omega t) + \beta(X_R \cos(\omega t))^3 = 0 \quad (6.2)$$

Using the trigonometric relation $\cos(\omega t)^3 = 0.75 \cos(\omega t) + 0.25 \cos(3\omega t)$ gives:

$$(\omega_n^2 - \omega^2)X_R \cos(\omega t) + \beta X_R^3 (0.75 \cos(\omega t) + 0.25 \cos(3\omega t)) = 0 \quad (6.3)$$

Ignoring the higher harmonics and keeping only the components at the natural frequency, harmonic balance can be applied to the system of equations:

$$(\omega_n^2 - \omega^2)X_R \cos(\omega t) + \beta X_R^3 (0.75 \cos(\omega t)) = 0 \quad (6.4a)$$

$$\omega^2 = \omega_n^2 + 0.75\beta X_R^2 \quad (6.4b)$$

Eq. 6.4b describes the relation between the frequency and amplitude of the resonator at its resonant frequency. This is called the backbone function. For a linear system, this is a straight line; for a nonlinear system, it generally bends forward or backward depending on the type of nonlinearity. If the system is dominated by nonlinearity from mechanical sources, the backbone curve bends forward whereas if it is dominated by nonlinearity from electrical sources, the curve bends backward.

Frequency response curve

The frequency response of the system is also important for the analysis of nonlinear systems. The frequency response is achieved for a forced damped resonator system outlined below:

$$\ddot{x} + 2\zeta\omega_n\dot{x} + \omega_n^2 x + \beta x^3 = 0 \quad (6.5)$$

Assuming a harmonic solution of $x = X_R \cos(\omega t)$ and substituting this relation into Eq. 6.5:

$$(\omega_n^2 - \omega^2)X_R \cos(\omega t) + \beta X_R^3(0.75 \cos(\omega t) + 0.25 \cos(3\omega t)) + 2\zeta \omega_n \omega X_R \sin(\omega t) = F(\sin(\omega t) \cos(\phi) + \cos(\omega t) \sin(\phi)) \quad (6.6)$$

Equating the $\cos(\omega t)$ and $\sin(\omega t)$ terms, and ignoring the higher order terms, yields:

$$(\omega_n^2 - \omega^2)X_R + \beta X_R^3(0.75 \cos(\omega t)) \approx F \cos(\phi) \quad (6.7a)$$

$$2\zeta \omega_n \omega X_R \approx F \sin(\phi) \quad (6.7b)$$

Squaring and adding Eq. 6.7 produces:

$$X_R^2 \left[\left(\omega_n^2 - \omega^2 + 0.75\beta X_R^2 \right)^2 + 4\zeta^2 \omega_n^2 \omega^2 \right] \approx F^2 \quad (6.8)$$

This leads to the amplitude dependent transfer function and phase relation:

$$\frac{X_R}{F} = \frac{1}{\left[\left(\omega_n^2 - \omega^2 + 0.75\beta X_R^2 \right)^2 + 4\zeta^2 \omega_n^2 \omega^2 \right]^{1/2}} \quad (6.9a)$$

$$\phi = \arctan \left(\frac{2\zeta \omega_n \omega X_R}{\omega_n^2 - \omega^2 + 0.75\beta X_R^2} \right) \quad (6.9b)$$

Eq. 6.9 shows a clear amplitude-frequency (*a-f*) relation which is plotted in Fig. 6.2. The parameters that control this *a-f* effect are β (which is the nonlinear spring constant that is dependent on the structural and material properties), the damping constant ζ (which is dependent on energy dissipation mechanisms such as fluid damping, anchor losses, *etc.*), and the drive force (F) that is dependent on the AC drive voltage and the DC bias polarising voltage. To achieve a linear response of the system, β can be either set to zero in the simulation or the drive force can be set to be small. By doing so, the linear frequency response is captured on the left side of Fig. 6.2. There is no *a-f* effect here and there is only one solution of phase and amplitude for each frequency of vibration. If now the drive voltage is increased and β is given a positive value, a spring hardening effect results in a positive *a-f* effect and there are multiple solutions to both the amplitude and phase for each frequency.

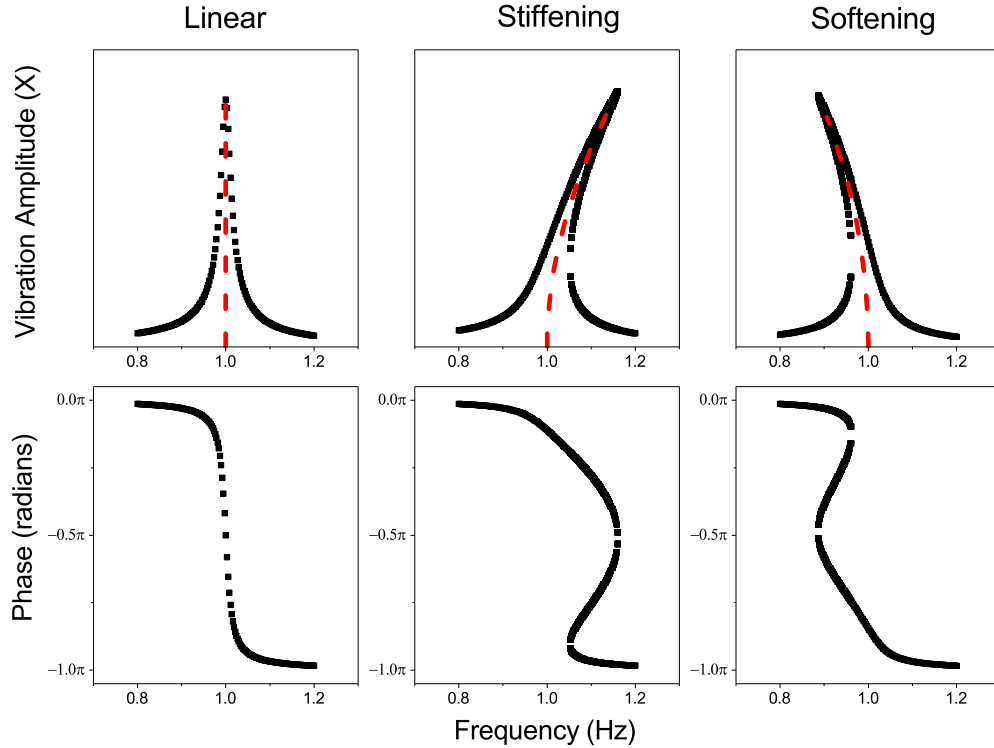


Fig. 6.2 Simulated frequency response (black dotted) and backbone curve (red dashed) for linear and nonlinear resonator.

Contrarily, if β is given a negative value, a spring softening effect is seen where there is a negative $a-f$ effect and again, there are multiple solutions to both the amplitude and phase for each frequency. A backbone function is also shown in Fig. 6.2 which shows only the $a-f$ effect and does not consider the damping constant.

The backbone curve and the frequency response curve can be used to capture different effects of the nonlinear system. The back-bone curve sufficiently captures the frequency-drive force relation. However, if modelling the vibration amplitude of the resonator is paramount, a frequency response curve is necessary.

6.3 Nonlinear model of coupled resonator system

After understanding the various ways in which nonlinearity affects a single resonator, the study can be expanded to include the effect of nonlinearity in a coupled 2-DoF system. To develop an analytical model, a lumped model of the system is shown in Fig. 6.3. The two masses (m) and linear dampers (c) are assumed to be the same for both resonators. Nonlinear

springs for the two resonators are defined as $k_{n1} = k(1 + k_3x^2)$ and $k_{n2} = k(1 + k_3x^2) + \Delta k(1 + \Delta k_3x^2)$. To mimic experimental conditions, perturbations are applied capacitively on the second spring (k_{n2}) only. A negative nonlinear coupling spring is defined as $k_{nc} = k_c(1 + k_{c3}x^2)$ as realised through a capacitive coupling. The dynamics of the system is approximated by the equations:

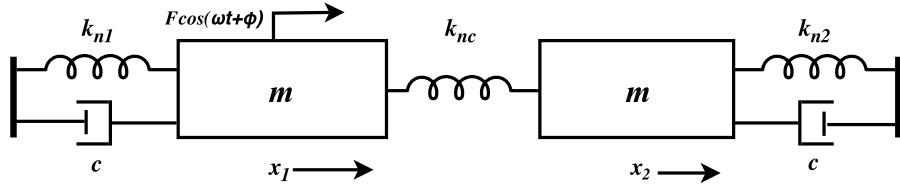


Fig. 6.3 Lumped spring-mass-damped system with nonlinear springs.

$$m\ddot{x}_1 + c\dot{x}_1 + (k + k_c)x_1 - k_c x_2 + kk_3x_1^3 + k_c k_{c3}(x_1 - x_2)^3 = F \cos(\omega t + \phi) \quad (6.10a)$$

$$m\ddot{x}_2 + c\dot{x}_2 + (k + k_c + \Delta k)x_2 - k_c x_1 + kk_3x_2^3 + \Delta k \Delta k_3 x_2^3 + k_c k_{c3}(x_2 - x_1)^3 = 0 \quad (6.10b)$$

Assuming a harmonic response at the resonant frequency, the amplitudes of the two resonators can be written as $x_1 = A \cos(\omega t)$ and $x_2 = B \cos(\omega t + \gamma)$. For the purposes of simulating the system closest to the experimental mode under consideration, the phase difference (γ) between the two resonators is assumed to be π . This assumption is valid for all operating amplitude ratios – near *veering* and far from *veering*. Furthermore, harmonic balance is used to separate the contribution of the nonlinear terms to ω and 3ω as $(A \cos(\omega t))^3 = A^3(0.75 \cos(\omega t) + 0.25 \cos(3\omega t))$. Only the terms of ω are considered while ignoring the higher order terms. Eq. 6.10 can be reduced to:

$$-\omega^2mA + (k + k_c)A + k_cB + 0.75kk_3A^3 + 0.75k_c k_{c3}(A + B)^3 = F \cos(\phi) \quad (6.11a)$$

$$\omega^2mB - (k + k_c + \Delta k)B - k_cA - 0.75kk_3B^3 - 0.75\Delta k \Delta k_3 B^3 - 0.75k_c k_{c3}(B + A)^3 = 0 \quad (6.11b)$$

$$\omega cA = F \sin(\phi) \quad (6.11c)$$

Eq. 6.11c can be substituted into 6.11a and 6.11b and using MATLAB[®], the system can be solved for a range of $0.4 < \phi < 2.8$. This range of ϕ is chosen to cover the required

frequency response range of interest. The drive voltage is swept from 10 mV to 80 mV to emulate the shift from linear to nonlinear domain. The results, plotted in Fig. 6.4 show the frequency response functions with the two bifurcation points and the unstable region between them clearly discerned. The simulated values mirror the experimental values for $k = 1080 \text{ N/m}$, $k_c = -0.46 \text{ N/m}$, $m = 3.7 \times 10^{-10} \text{ kg}$, $Q = 10000$. The nonlinear parameters are $k_3 = 2.1306 \times 10^{10} \text{ m}^{-2}$, $k_{c3} = 5 \times 10^{11} \text{ m}^{-2}$ and Δk_3 is calculated on a case by case basis depending on the perturbation voltage applied using the nonlinear parallel plate capacitor equation. Furthermore, the two output metrics are plotted against the phase to show that the bifurcation points occur at points that fulfill $\frac{\partial f}{\partial \phi} = 0$ and $\frac{\partial AR}{\partial \phi} = 0$, where f is the resonant frequency of the device and AR is the amplitude ratio of the mode of operation.

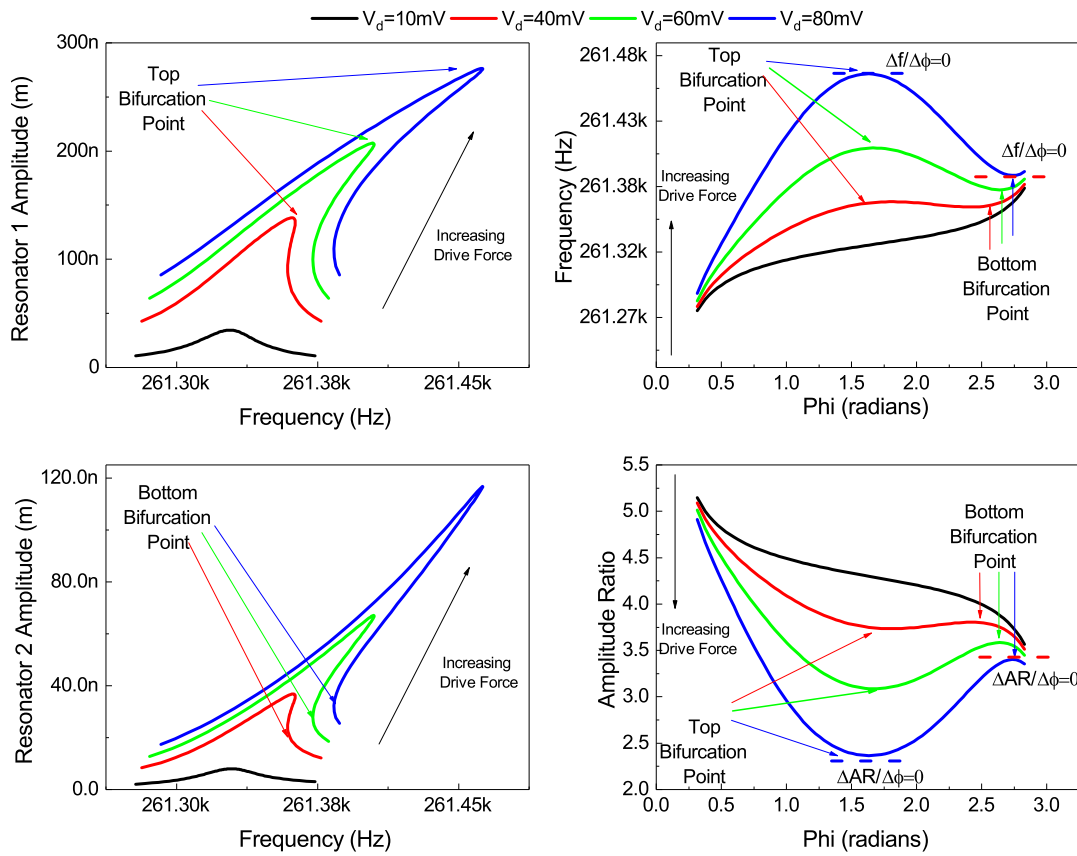


Fig. 6.4 (Left) Simulated frequency response functions of the two resonators showing the *a-f* effect and (right) the frequency-phase and the amplitude ratio-phase plots showing the points where the two bifurcation points occur.

Some interesting features can be noticed in Fig. 6.4. The plots to the left show the simulated frequency response curves of the two resonators at various increasing drive voltages. The nonlinearity from the mechanical sources (e.g. resonator) dominate in the scenario and a positive $a-f$ effect is seen. With the onset of nonlinearity at $V_d = 40$ mV, the amplitude of Resonator 1 at the top bifurcation point (TBP) increases proportionally with the drive voltage indicative of the weak nonlinearity region. However, it is seen that the amplitude of Resonator 2 at the TBP does not follow the same proportion. This feature is further discussed later in the chapter with experimental data. The plots on the right show the $\phi - f$ and $\phi - AR$ relation to find operating points where their slope is zero. As expected, both output metric shows a zero slope with phase at the top and bottom bifurcation points. This further bolsters the argument for operating at these points from the perspective of lowering phase noise. These observations are validated by experimental results shown next.

6.4 Experiment

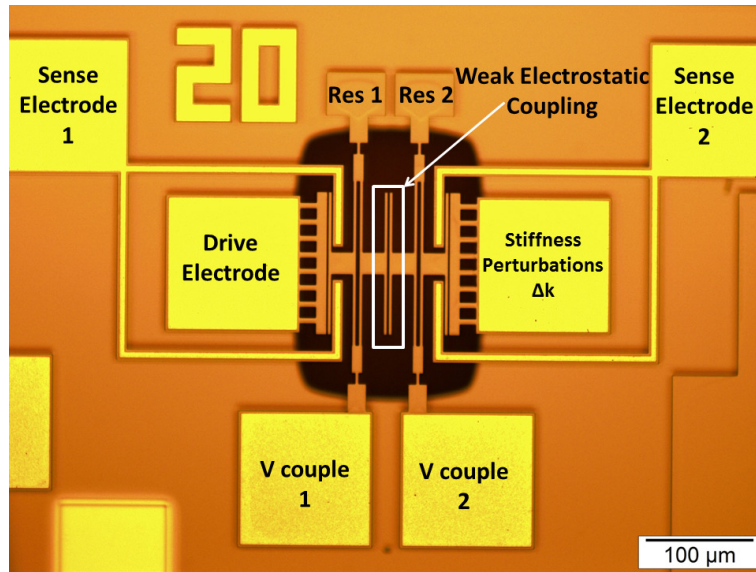


Fig. 6.5 Optical micrograph of the device.

The device used for the experiment consists of a system of electrically coupled DETF resonators as shown in Chapter 3.1. It is re-illustrated in Fig. 6.5. A schematic of the measurement setup is shown in Fig. 6.6. The DETF resonators are electrically coupled by applying two different DC voltages on each of their bodies. The resonators are driven in a cascade configuration where the first resonator is driven capacitively by an AC voltage

from a commercially available lock-in amplifier (Zurich Instruments HF2LI) and the second resonator is driven synchronously (i.e. resonance occurs at the same frequency) through the coupler. The motional current from each of the resonator channels is converted to voltage by an off-the-shelf transimpedance amplifier (TIA) and then through a band pass filter (BPF) to remove the broadband amplitude noise. In this study, a closed-loop configuration is utilised for the characterisations, where the resonance tracking is realised through the built-in PLL/PID features of the HF2LI. The in-phase mode is chosen for the operating mode at a resonant frequency of $\approx 250\text{kHz}$.

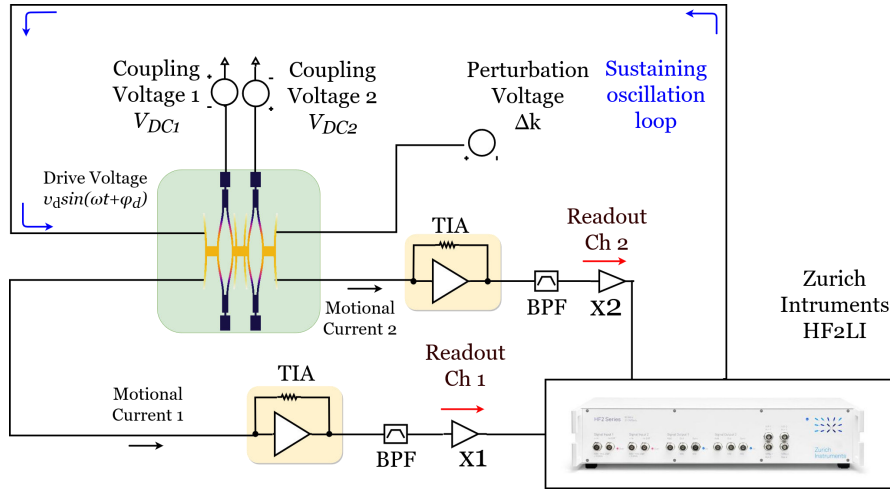


Fig. 6.6 Circuit level schematic of the experimental setup.

6.5 Results

First, the nonlinear frequency response curves are mapped in a closed-loop configuration to identify the bifurcation points. Then, the performance of the sensor is tested at these points to verify the reduction of amplitude ratio noise as predicted [131]. Finally, key specifications of the sensor such as the sensitivity and noise floor are studied with the purpose of improving the sensing resolution.

6.5.1 Instability mapping

Nonlinear oscillations produce regions of multiple amplitudes of vibration for a given frequency as seen from the simulation in Fig. 6.4. This can be called as the unstable region of the frequency response function and is generally visible as the amplitude of the drive

signal is increased. The AC drive signal is increased from 10 mV (representing linear frequency response) to 80 mV to transition into the nonlinear regime beyond the critical Duffing amplitude. Once the critical Duffing amplitude is reached, a PID controller is used to tune the phase of the drive signal to map the different unstable regions in a closed-loop configuration. In doing so, the two bifurcation points – top bifurcation point (TBP) and the bottom bifurcation point (BBP) are identified for each drive voltage (see Fig. 6.7). The top bifurcation point (TBP) is defined as the bifurcation point with a higher amplitude while the bottom bifurcation point (BBP) is defined as the bifurcation point with lower amplitude. TBP and BBP occur synchronously at the same drive frequency for both resonators.

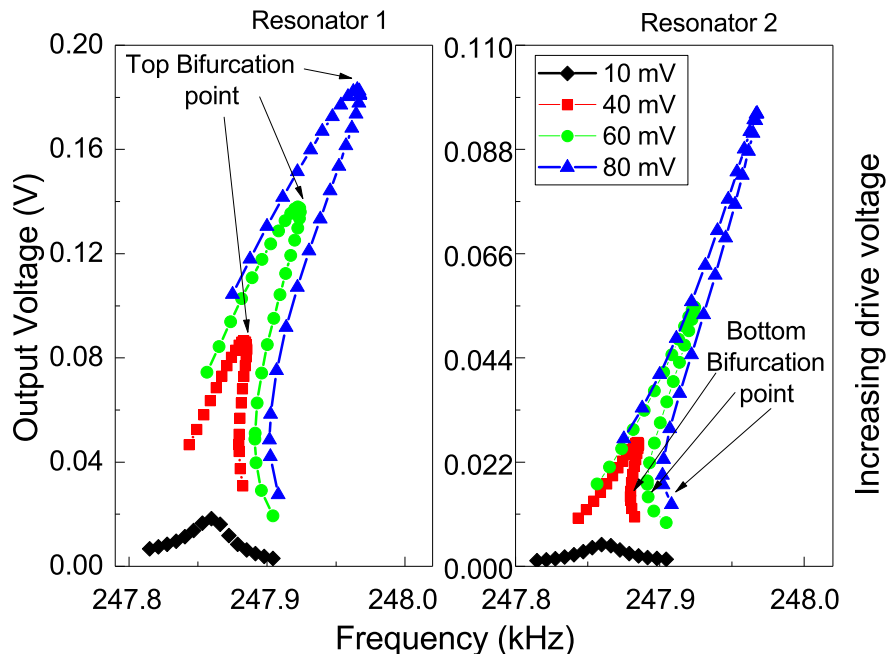


Fig. 6.7 Instability region mapping for the two resonators for each drive voltage. The linear response (at 10 mV drive level) is shown in black.

Another way to view the results of the instability mapping is to plot the amplitude ratio and the frequency as a function of the phase of the drive signal. This is plotted in Fig. 6.8. The figure shows both $\frac{\partial AR}{\partial \phi}$ and $\frac{\partial F}{\partial \phi}$ decrease with the increase in drive amplitude at TBP and BBP. Therefore, at both TBP and BBP, the amplitude ratio noise due to phase fluctuations is reduced as predicted by the simulation in Fig. 6.4. Hence, these points will be the focus for this study.

To understand the nonlinear behaviour of the coupled resonator system at other operating amplitude ratios, stiffness perturbations are added on Resonator 2 to tune the symmetry of

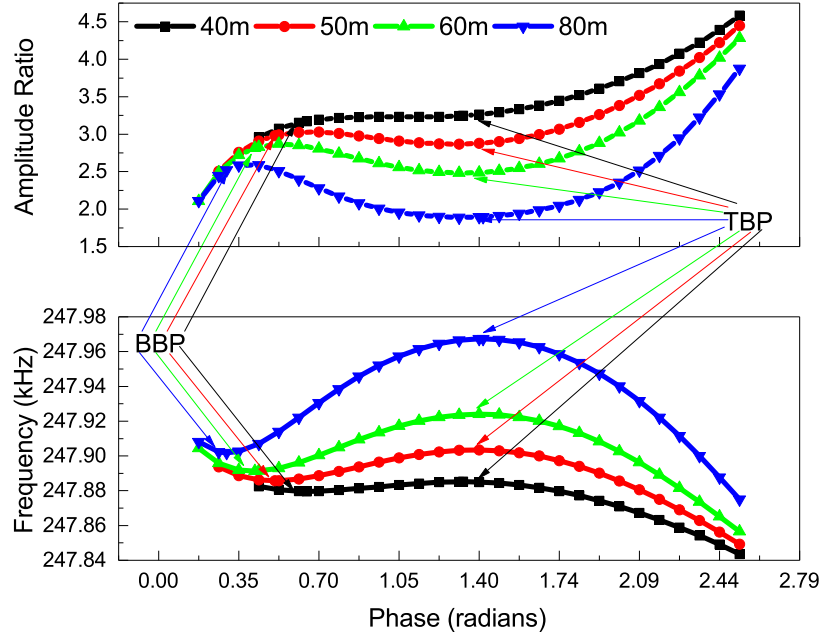


Fig. 6.8 Experimental amplitude ratio-phase and frequency-phase plots showing the Bottom Bifurcation Point (BBP) and the Top Bifurcation Point (TBP).

the resonators. The drive voltage is then increased from 20 mV to 120 mV to encompass nonlinear drive regimes with increasing levels of Duffing nonlinear behaviour. The two bifurcation points are chosen as operating points and the change in amplitude ratio at those points at different perturbations is recorded. The amplitude ratio and the frequency shift are shown in Fig. 6.9.

The first observation that can be made from Fig. 6.9 is that the bottom bifurcation from many amplitude ratios close to *veering* does not exist for drive voltages 50 mV and 80 mV. This leads to the hypothesis that the *a-f* effect in coupled nonlinear resonators is dependent on the operating amplitude ratio at a particular drive voltage. Another manifestation of this phenomenon is that the amplitude ratio and frequency of both bifurcation points do not vary much around the *veering* region but vary greatly away from the *veering* region. This is seen in Fig. 6.9 where the amplitude ratio and the frequency at both bifurcation points are immune to drive power variations at $AR \sim 1$ but change significantly at $AR \gg 1$.

Fig. 6.9 also shows that amplitude ratio at both TBP and BBP reduce with increasing drive voltage away from *veering*. A reduction in amplitude ratio can be due to either a disproportionate decrease in the amplitude of driven resonator (Resonator 1) or a disproportionate increase in the amplitude of the non-driven resonator (Resonator 2). To understand this trend,

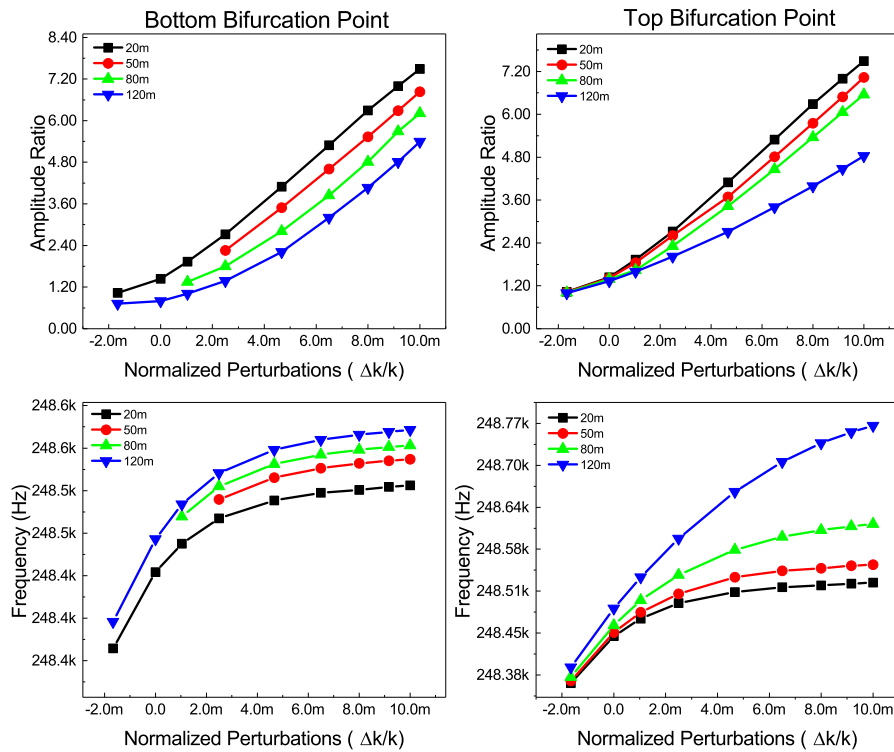


Fig. 6.9 Comparison of amplitude ratio at different drive voltages across a range of stiffness perturbations.

a table with the output voltages at a linear operating amplitude ratio of 4 is plotted. This amplitude ratio is chosen since both BBP and TBP occur at this point across the different drive amplitudes. Tab. 6.1 summarises these results.

It is seen that at the BBP, the amplitude ratio reduces due to disproportionate reduction in the amplitude of the driven resonator (Resonator 1). This can be explained by the phenomenon of gain compression which is described as the energy transfer between the first order harmonics and the third order harmonics at large amplitudes of vibration. Due to the occurrence of third order harmonic in the Duffing equation, energy is transferred to higher frequency terms from the fundamental frequency, resulting in reduction of the vibration amplitude at the fundamental frequency.

At the TBP, however, the amplitude ratio reduces due to a disproportionate increase in the amplitude of Resonator 2. As the amplitude of Resonator 1 increases, so does the force applied on Resonator 2 since it is driven in cascade configuration. This leads to a greater nonlinear force being applied on Resonator 2 through the coupler. Furthermore, the coupling gap between the resonators cannot be assumed to be constant at high vibration amplitudes. This also contributes to the increase in the effective forcing on Resonator 2. Therefore,

Table 6.1 Amplitude ratio at TBP and BBP at different drive voltages

(a) Bottom Bifurcation Point

Drive amplitude (mV)	Resonator 1 (V)	Resonator 2 (V)	Amplitude Ratio
20 (Linear)	0.36	0.08	4.09
50	0.65	0.18	3.48
80	0.51	0.18	2.81
120	0.41	.18	2.21

(b) Top Bifurcation Point

Drive amplitude (mV)	Resonator 1 (V)	Resonator 2 (V)	Amplitude Ratio
20 (Linear)	0.36	0.08	4.09
50	0.85	0.23	3.68
80	1.71	0.50	3.42
120	2.79	1.02	2.71

these two phenomena increase the amplitude of that resonator in a disproportionate manner, resulting in the reduction of the amplitude ratio at the TBP.

6.5.2 Sensitivity analysis

Once the bifurcation points for each drive voltage have been identified, the sensitivity of the system at the TBP and BBP to input stiffness perturbations are studied by applying a small DC perturbation voltage on Resonator 2 [24]. Three operating regions are chosen with amplitude ratios ranging from 1 to 8 to cover a wide range of operating points of the sensor. The sensitivity results are plotted in Fig. 6.10 for both TBP and BBP. The simulated values (dashed lines) for the sensitivity are also plotted using the results from the solution to Eq. 6.11. The sensitivities shown as error bars are a representation of the range of experimental sensitivities that are measured for that span of amplitude ratios. The amplitude ratio at both TBP and BBP decrease with an increase in drive amplitude but there is a clear difference in the degree of this reduction between two bifurcation points. A certain reduction in sensitivity is expected with a reduction in amplitude ratio in mode-localised sensors. This is due to their inherent property as mentioned earlier in Chapter 2. At the BBP, the sensitivity reduces with the increase in drive voltage and is consistent with the reduction expected with a reduction in

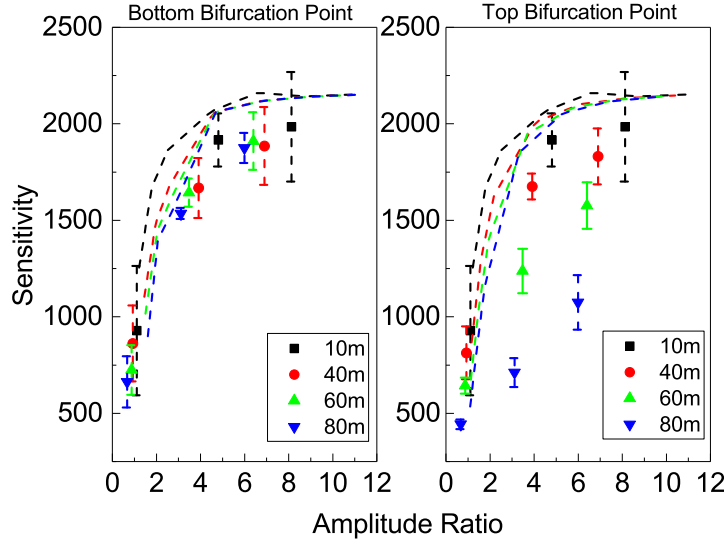


Fig. 6.10 Sensitivity of the system to input stiffness perturbations at the top bifurcation point (TBP) and bottom bifurcation point (BBP) with dashed lines signifying the simulated results.

amplitude ratio. Thus, when the sensitivity is plotted with respect to amplitude ratio, there is no deviation from the expected sensitivity curve.

However, this is not the case at the TBP where there is a disproportionate decrease in sensitivity with the increase in amplitude ratio. This feature can be explained by the presence of higher order nonlinearity in the coupler and electrostatic stiffness perturbations that become considerable at high vibration amplitudes. These effects lead to changes in the effective coupling and the added stiffness perturbations. They can be seen in the expression of these nonlinear couplers and stiffness perturbations associated with capacitive coupling and transduction deduced to the second order by the series expansion of the electrostatic force created by a capacitor.

$$F_{cap} = -\frac{V_{DC}^2}{2} \frac{\partial C}{\partial x} \quad (6.12a)$$

$$C = \frac{\epsilon_0 A_e}{g - x} \quad (6.12b)$$

Here, the V_{DC} represents the DC voltage difference between the two capacitive plates; x represents the generalised displacement of the plates; g is the initial gap between the plates and A_e is the capacitive face area.

$$k_c = -\frac{V_{couple}^2}{2} \frac{\partial^2 C}{\partial(x_1 - x_2)^2} = -\frac{V_{couple}^2 \epsilon_0 A_e}{g^3} \left(1 - \frac{3}{2g}(x_1 - x_2) + \frac{2}{g^2}(x_1 - x_2)^2\right) \quad (6.13a)$$

$$k_p = -\frac{V_p^2}{2} \frac{\partial^2 C}{\partial(x_2)^2} = -\frac{V_p^2 \epsilon_0 A_e}{g^3} \left(1 - \frac{3}{2g}(x_2) + \frac{2}{g^2}(x_2)^2\right) \quad (6.13b)$$

The higher order terms of both these spring constants leads to variations in the effective coupling and perturbations which results in the change in sensitivity. This explains how the simulations of the sensitivity of amplitude ratio to stiffness perturbations agree with the experiments for the BBP but show a discrepancy for the TBP. Since the second order harmonics are ignored in the simulation due to convergence issues, the behaviour at the TBP is not represented accurately in the simulations.

6.5.3 Noise floor

Next, the noise floor improvement due to operating in the nonlinear domain is experimentally investigated. To measure the broadband noise floor of the amplitude ratio output, the amplitudes of the two resonators are measured at a high sampling rate (2000 samples/s) for 5 minutes. The ratio of the two amplitudes is computed and a FFT is performed on this data. The noise floor for each of the drive voltages is compared for the three operating regions with increasing amplitude ratios, and is shown in Fig. 6.11. It should be noted that in addition to the 50 Hz peaks (as well as its higher order harmonics, e.g. 100 Hz, 150 Hz etc.), the thermo-mechanical noise of the in-phase mode is visible on the plot. Similar observations of thermo-mechanical noise of spurious peaks have been spotted in the phase noise plots in coupled opto-electronic oscillators [132]. Furthermore, these peaks have been shown to comprise other sources of additive noise as well [33]. This effect is worthy of a separate analysis and, therefore, are beyond the scope of this study. Additionally, for measuring the amplitudes of vibration, a bandwidth of 500 Hz on the Zurich Instruments PLL has been chosen and it is represented in the noise roll off seen at that frequency.

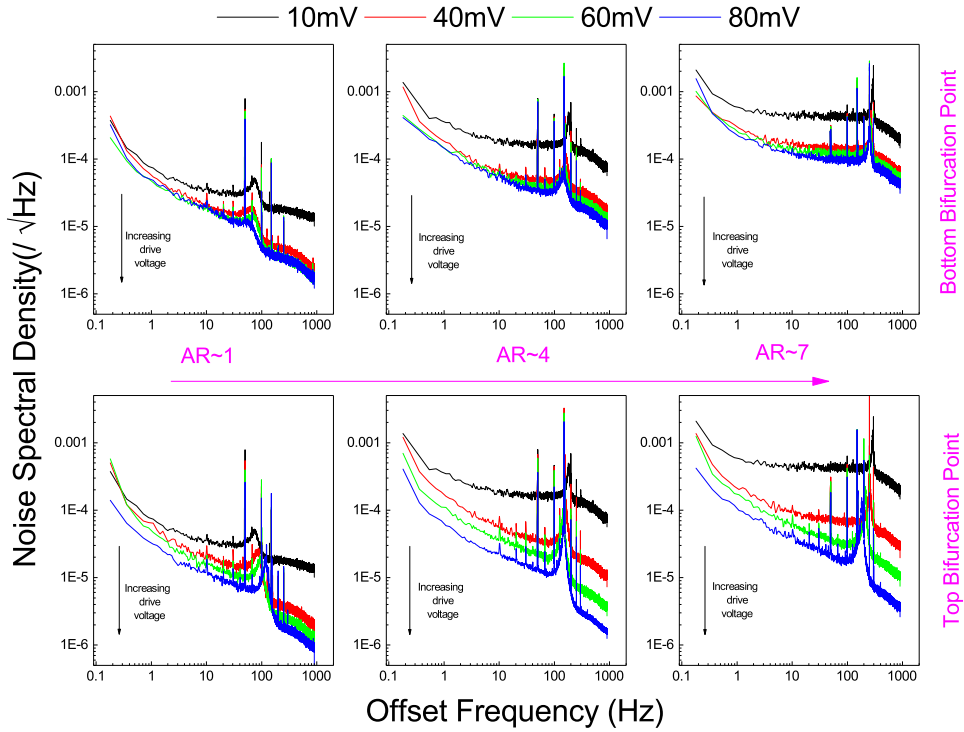


Fig. 6.11 Output noise spectral density for the BBP and TBP for different drive power and different operating regions (i.e. different amplitude ratios).

To understand the observations from Fig. 6.11, it is important to revisit the expression for the calculation of amplitude ratio noise power, $\sigma^2(x_1/x_2)$, expressed as a function of the individual resonator amplitude noise power ($\sigma^2(x_1)$ and $\sigma^2(x_2)$) [133]:

$$\frac{\sigma^2(x_1/x_2)}{[\mu(x_1)]^2/[\mu(x_2)]^2} = \frac{\sigma^2(x_1)}{[\mu(x_1)]^2} + \frac{\sigma^2(x_2)}{[\mu(x_2)]^2} - 2 \frac{\text{Cov}(x_1, x_2)}{\mu(x_1)\mu(x_2)} \quad (6.14)$$

In Fig. 6.11, due to the more pronounced increase in the amplitudes of vibration, the SNR ($\frac{[\mu(x_i)]^2}{\sigma^2(x_i)}$, $(i = 1, 2)$) is better for each resonator amplitude at the TBP than BBP. This leads to a better noise floor of the amplitude ratio output metric at the TBP as compare to BBP. At both bifurcation points, the noise floor improves as the amplitude ratio, $\frac{\mu(x_1)}{\mu(x_2)}$ decreases. This is in agreement with the conclusions drawn in Chapter 5. Since the amplitude of vibrations ($\mu(x_i)^2$, $(i = 1, 2)$) are insensitive to drive voltage at the BBP, the improvement of the output noise floor with an increase in drive voltage (after the bifurcation occurs) is minimal. This is also confirmed in the $AR - \phi$ plot in Fig. 6.8 where the region around the BBP sees very little change in amplitude ratio as compared to that at the TBP. This leads to a greater improvement in the noise floor at the TBP as compared to the BBP when the drive voltage is increased in the nonlinear regime.

A further comparison is made by averaging the noise floor around 30 Hz offset frequency for all the above cases and plotting it against their amplitude ratio in Fig. 6.12. 30 Hz is chosen here because most of the FFTs show the noise floor around that frequency and also it excludes the thermo-mechanical noise peaks that start to appear at later offset frequencies. The trend of the output noise spectrum (in Fig. 6.12a) clearly shows an improvement in the noise floor by increasing the drive voltage at both bifurcation points. Consistent with the observation in the noise floor plots, it is seen that the improvement is incremental at the TBP as compared to the BBP where the noise floor remains consistent throughout this nonlinear operating regime.

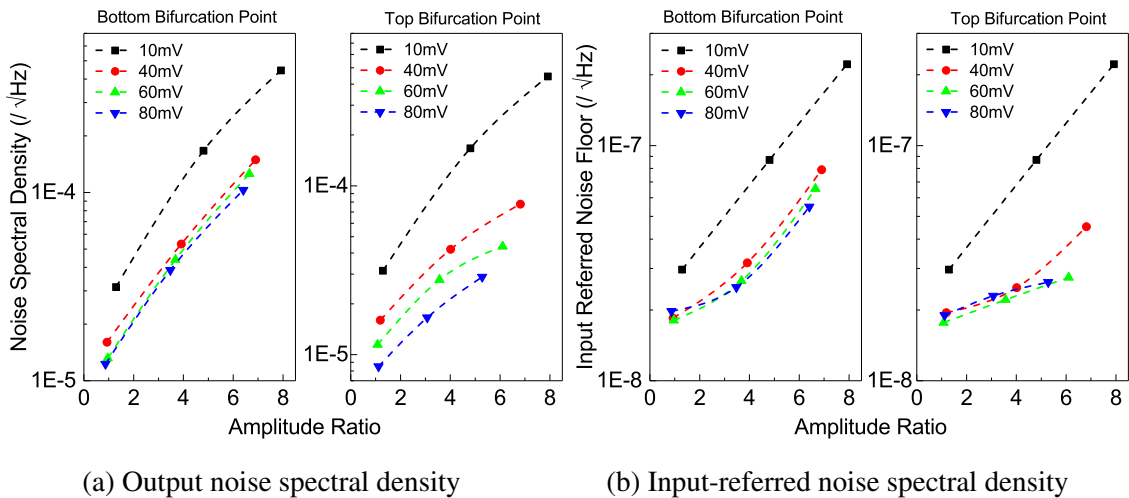


Fig. 6.12 Averaged noise around 30 Hz compared for the various different drive voltages at the TBP and BBP.

The input-referred noise is then calculated by dividing the output noise floor AR_n by the sensitivity at each operating point S_{AR} , $(\frac{\Delta k}{k})_n = \frac{AR_n}{S_{AR}}$. Fig. 6.12b compares the trend of the input-referred noise spectral density around 30 Hz offset frequency. The trend of the input-referred noise floor changes significantly from the trend seen in the output noise. Since the sensitivity at the top bifurcation point (as shown in Fig. 6.10) decreases with the increased drive voltage, the input-referred noise at that point is affected by this decrease in sensitivity. Therefore, it no longer shows an incremental improvement in the noise floor with an increase in drive voltage. The noise increases at higher amplitude ratio operating point which is expected from the system that is dominated by electronic noise. On the other hand, the input-referred noise at the bottom bifurcation point preserves its trend similar to the output noise due to a relatively small change in the sensitivity with an increase in drive

voltage. Similar to the TBP, the noise at the BBP also increases with an increase in amplitude ratio.

An interesting feature that is observed in the input-referred noise floor is that at the amplitude ratio of 1 (nearly symmetric resonators), the improvement of the noise floor with an increase in drive voltage is minimal for both bifurcation points. This shows the advantage of working around the *veering* region. Although the sensitivity of the system is lower there, the input-referred noise floor is the best and the most insensitive to changes in drive voltage [125]. Away from *veering*, however, the improvement in the noise floor compared to the linear drive is better at the TBP than at the BBP. Ultimately, an improvement of 2 times in input-referred noise floor, or resolution, in comparison to its linear counterpart at both bifurcation points has been achieved around *veering* and an improvement of 4 times at the top bifurcation point away from *veering*. This is likely due to the higher SNR and additional noise filtering properties at the bifurcation points. A minimum of $18 \text{ ppb}/\text{Hz}^{1/2}$ has been achieved in this work demonstrating an improvement relative to operation in the linear regime ($30 \text{ ppb}/\text{Hz}^{1/2}$) for this system.

It is to be noted that the results presented here apply to devices using electrical coupling only since the sensitivity reduction is a direct consequence of the second order term of the coupler. It is additionally beneficial for the improvement of the SNR to operate at the TBP in a device where there is no significant reduction in sensitivity at that point. For example, the dynamics in a mechanically coupled system would be different since the coupling would no longer be governed by nonlinear capacitive behaviour but be dependent on the nonlinear response of the mechanical coupling beam. This might not adversely affect its sensitivity. Nonetheless, for operation as a sensor, it is recommended that the mode-localised resonators be driven just beyond the critical amplitude to see improvements in the SNR of the amplitude ratio output metric. This is to ensure that unwanted effects associated with stress build-up or higher order nonlinear behaviours are not observed in the output. As long as the mode-localised system is operated in the weak nonlinear regime, the noise and sensitivity observations in a resonator system showing softening or stiffening nonlinearities should not differ.

Summary

The nonlinear dynamics of a mode-localised resonator system are studied in this chapter. Operation at higher drive amplitudes leads to higher signal-to-noise ratio in an electrical noise dominant system but increases the nonlinearity in the system. Instead of using nonlinearity cancellation techniques, operation at the bifurcation points is studied in view of the potential

for enhanced amplitude ratio noise filtering. Modelling is done to understand the behaviour of the coupled resonators when exposed to large amplitudes of vibration across different amplitude ratio operating points. It is seen that amplitude ratio reduction takes place at both bifurcation points but to a greater extent at the top bifurcation point due to gain suppression. The sensitivity also reduces with an increase in the drive voltage at both bifurcation points. However, the top bifurcation point sees a disproportionately large reduction in sensitivity to what is predicted by the gain suppression. This is attributed to the presence of second order nonlinearities from the electrical coupling. Nonetheless, the noise floor is seen to improve despite this reduction in sensitivity.

It has been shown in the previous chapter that in a system dominated by electronic noise, the noise floor can be optimised at an amplitude ratio of $\sqrt{1.5}$. Ideally, operating at the TBP at an amplitude ratio of $\sqrt{1.5}$ improves the noise floor due to the higher signal-to-noise ratio as compared to the linear case. Unfortunately, in this system operating at that amplitude ratio led to a reduction in sensitivity. Hence, similar experiments carried out on a mechanically coupled device would allow for greater improvement in the noise floor in the nonlinear operating regime of the mode-localised resonators.

Chapter 7

Mode-localised Accelerometer

Accelerometers are sensors that detect dynamic acceleration as a measurand. They have become one of the most widely implemented inertial sensors for consumer applications in mobile phones and automobiles. They also have industrial applications such as in modal analysis, and noise vibration and shock testing. Additionally, they have also been used for geophysical measurements (e.g. seismic sensors for geological imaging). In this chapter, a prototype of mode-localised MEMS accelerometer is presented that shows the potential of matching the performance of the commercial accelerometers in the field of seismic monitoring. The resolution optimisation techniques presented in the previous chapters are applied on a mode-localised accelerometer (MLAXL) to show state-of-the-art sensing resolution.

7.1 Review of MEMS accelerometers

MEMS accelerometers have become a common commercial commodity for inertial measurements. Their size, ability to be batch-fabricated, and their low cost have given MEMS sensors a great advantage over their competitors [134]. This has led to them displacing their larger size alternatives in the field of consumer electronics [135–137] and auto mobiles [138–142]. These devices have flooded the market and have given great impetus to the MEMS industry. But, the performance of these sensors is mostly in the low to mid-range with stabilities in the region of the 10^{-3} g (mg) where g is one unit of gravitational acceleration or 9.8 m/s². Although these sensors are powerful for their applications, most of them do not meet the resolution, long-term stability, robustness, or bandwidth requirements for high performance applications (μ g) such as in defense, oil and gas industry, and seismic monitoring.

With the advent of new fabrication technologies, MEMS accelerometers employing a variety of different principles have been introduced. However, they all revolve around two basic principles of acceleration detection – measurement of the displacement of a proof mass relative to a reference frame or measurement of the inertial force experienced by a proof mass due to input acceleration. Some accelerometers employing displacement sensing principle are capacitive [143–148], tunnelling [149, 150], and optical [151–153] based and some employing force sensing are piezo-resistive [154–156], piezo-electric [157, 158], and resonant [57, 90, 8] based approaches. The main mechanisms implemented for high performance accelerometers currently in the market are either capacitive-based [159] or resonant-based [160]. This is because although accelerometers using other mechanisms provide better noise performance (optical and tunnelling), or a wide range of input acceleration and frequency response (piezo-electric and piezo-resistive), they have key drawbacks such as minimisation difficulties (optical and piezo-electric), low frequency noise (tunnelling), and high temperature sensitivity (piezo-resistive) that make them unsuitable for current commercial applications. Thus, the two ubiquitous accelerometers that employ the capacitive and resonant approaches are discussed in detail with a special mention of optical accelerometers due to the exceptionally high resolution it offers.

Optical accelerometers

The optical method of transduction in accelerometers has shown to consistently result in high resolution and performance [151, 152] as compared to other transduction methods. These accelerometers generally employ a laser interferometry to accurately detect changes in the displacement of the proof mass. Since the transduction method does not use electronic components in the readout path, the noise in the system is defined by the thermal noise of the sensor and the laser. Since both of these are orders of magnitude lower than the noise of analogue electronics, optical transduction enables for extremely high resolution measurements. Generally, optical accelerometers are fabricated using MEMS technology but the transduction method including a laser makes the integrated sensor very bulky and impractical for field applications. Nonetheless, works have shown noise floors of $17 \text{ ng}/\sqrt{\text{Hz}}$ [151] and $40 \text{ ng}/\sqrt{\text{Hz}}$ [152]. In the coming years, this technology has the great potential in the field for gravimetric or seismic applications but for now, other technologies that offer similar performances in a compact package are preferred.

Capacitive accelerometers

One of the simplest designs employing a displacement-based sensing is the capacitive accelerometer architecture. This sensor architecture consists of a proof mass that moves relative to a support frame upon the presence of an external acceleration. A capacitive transducer (usually comb-drive) present on the moving mass is used to measure a change in the capacitance relative to the stator frame with the help of simple circuitry. Key advantages of this method of sensing is the resistance to temperature fluctuations offered and the low noise floors achieved. Recent work on capacitive MEMS accelerometers [161–163] resulted in impressive noise floors of $100 \text{ ng}/\sqrt{\text{Hz}}$ but their limitations lie in the small dynamic range of sensing they offer (usually in the mg region). Additionally, they are plagued by $1/f$ noise that reduce their ability to measure low frequency accelerations to few hertz. The small dynamic range is due to the need for a force feedback loop that keeps the proof mass from moving since, large accelerations will lead to the mass collapsing into the frame. Furthermore, a large proof mass needs to be implemented with compliant suspensions to achieve large sensitivities. This inherently effects the maximum achievable bandwidth in these devices. Most recently, a capacitive accelerometer [148] with a bandwidth between 0.1 Hz-10 Hz, a noise floor of $0.25 \text{ ng}/\sqrt{\text{Hz}}$ and able to withstand high shock ($>1000\text{g}$) was reported. This has been the highest performance reported to date and was implemented with a force feedback loop. Their results showed that the sensor was able to measure the earth's tidal wave patterns. Although it shows brilliant noise performance, this device does not have a large bandwidth to be used ubiquitously for a large range of applications.

Resonant accelerometers

On the other side of the spectrum, resonant accelerometers are part of a family of designs employing force sensing mechanism. The core of this sensing principle is a resonator coupled to a proof mass that is driven at its resonant frequency. An inertial force acting on a proof mass due to an external acceleration is coupled into the resonator, thus changing its resonant frequency [90, 57]. This method requires an oscillator design that accurately tracks the resonant frequency of the resonator. It is particularly useful in offering large dynamic range (upto kHz) since the sensitivity does not scale down with the size of the proof mass the same way as in capacitive accelerometers. Furthermore, it does not experience the same issue with low frequency noise since the resonator frequency of the sensing element is usually in the kHz region. It has been proven to offer good noise performance without sacrificing the

dynamic range or the bandwidth of the sensor [57, 90, 8] monolithically in single axis [164], two axes [165], and three axes [166].

One of the main drawbacks for using the resonant sensing approach is the temperature dependence of the resonant frequency of the resonator that can lead to drifts in the output frequency. To tackle this issue, several designs [167, 21] have incorporated a passive temperature compensation using differential frequency readout scheme. In this scheme, the frequencies of two identical resonators are subtracted to double the inertial signal and cancel the first order temperature effects [168, 10]. However, this method is limited again by fabrication tolerances which result in unequal temperature-based drift between the two resonators [57]. Yet, recent work on these sensors reported stabilities on the order of 100 ng [169, 8] with a prospect of bettering the resolution with the advent of low noise amplifier circuits and better fabrication technologies. The main issue at hand is the need for more temperature compensation techniques due to the high temperature coefficient of these resonators ($-30 \text{ ppm}^{\circ}\text{C}$). Although many architectures do exist where external ovenisation [170, 114, 171] based on the oven controlled crystal oscillator (OCXO) has been used, they creates the need for bulky circuitry and oven technologies that renders the advantages of the MEMS technology irrelevant. This shows that there is a need for a mode-localised resonant accelerometer (MLRXL) to provide similar noise performance but without the need for complex and bulky temperature compensation techniques. Therefore, the MLRXL is an ideal candidate for an accelerometer with a high measurement bandwidth, high sensitivity while providing greater rejection to temperature fluctuations, thus, allowing for high resolution measurements of slowly varying acceleration.

Mode-localised accelerometers

There have been several reported versions of mode-localised accelerometer that employ two [28], three [71, 32], and four [72] DoF resonator systems. However, all of that work has been based on open-loop characterisations and do not quote any information on the bias stability, noise floor, or bandwidth of the sensor. Recent work [172] from the same group showed the implementation of an oscillator based on previous implementation of a simple feedback circuit [69]. A bias stability of 1.4 mg was achieved at integration time of 100 s and a noise floor of $7.6 \mu\text{g}/\sqrt{\text{Hz}}$ was reported by the group. However, the noise floor calculations were not conclusive since they included the noise outside of the sensor bandwidth. The noise outside the sensor's bandwidth is lower than the noise in the sensing bandwidth and therefore is a misleading quotation of noise floor. A further implementation of a three degree of freedom system [173] was shown to provide a bias stability of 157

μg. Although a breakthrough for MLRXL resolution, this resolution was not sufficient to compete with the current off-the-shelf accelerometers in the market.

In this work, a differential mode-localised resonator system is proposed and implemented that can show similar, if not better resolution compared to off-the-shelf accelerometers. The system is able to offer high performance in its noise floor, stability, common mode rejection, and tunable bandwidth which opens the doors for a wide range of potential applications from low frequency tidal wave sensing to high frequency seismic activity sensing. A theoretical analysis of the differential mode-localised accelerometer is presented since it employs a new amplitude ratio difference output metric. As discussed in Chapter 4, mechanically coupled devices offer lower common mode rejection than electrically coupled devices because of the variability in the coupler with temperature and pressure. Since there are two coupled systems in this case, the couplers in the two systems will undergo similar variations in common mode variables. Therefore, using the difference of the two amplitude ratios offers additional common mode rejection in mechanical coupled devices. A characterisation of the scale factor, bias stability, noise floor, bandwidth, and the record of a seismic event is shown as measured by the sensor. An analysis of the noise factors affecting the current resolution is provided along with a discussion on the long-term stability of the sensor.

7.2 Theory

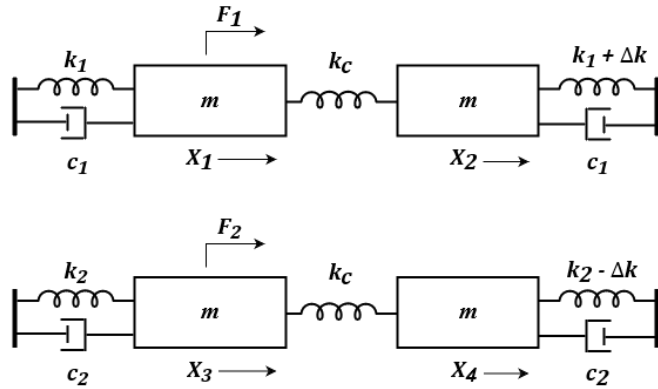


Fig. 7.1 Lumped model of the differential 2-DoF coupled system

Mode localisation in its most basic form can be represented by a 2-DoF lumped spring-mass model. The two springs (k_1) and masses (m_1) are assumed to be the same and are coupled together with a weak coupling spring (k_c). A perturbation in stiffness (Δk) is added to one of the resonators to perturb the system from a state of symmetry. This causes a shift

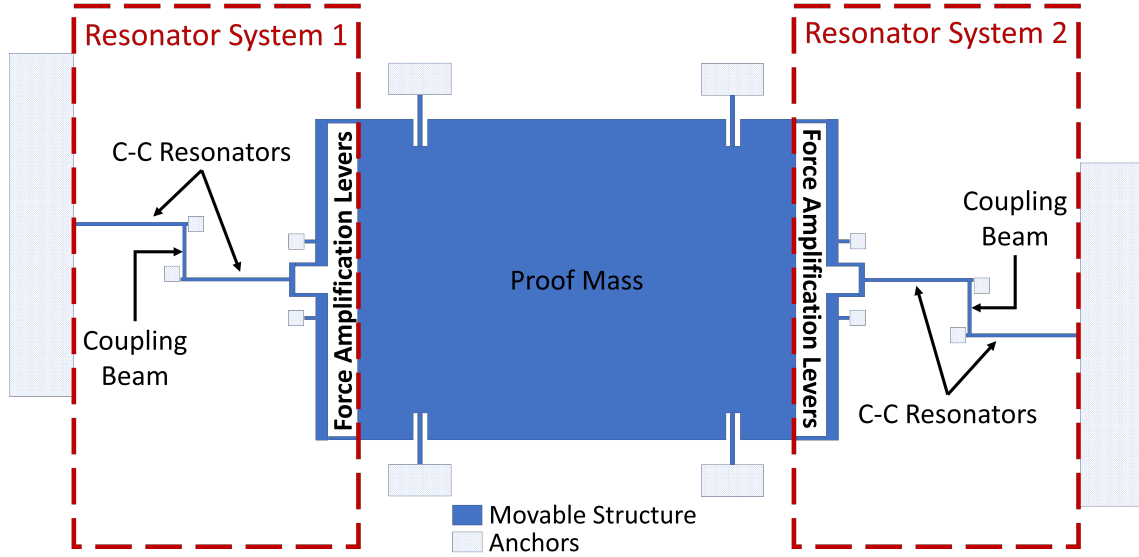


Fig. 7.2 A schematic of the differential mode-localised accelerometer

in the eigenstate of the resonators proportional to the measurand and this is represented as the ratio of the two amplitudes of vibration of the resonators. However, since a differential configuration is chosen for this sensor, another system of coupled resonators with springs (k_2), masses (m_2), and coupling spring (k_c) experiencing a negative change in perturbation ($-\Delta k$) is added to the model. The two resonator systems need to be considered as two separate coupled systems but both experiencing a differential axial perturbation in stiffness that is proportional to input acceleration. It is to be noted that the amplitude ratio difference measurements are most effective when the operating amplitude ratio of both the systems are matched. A lumped spring-mass-damper model representing this is shown in Fig 7.1 and the schematic of the accelerometer is shown in Fig. 7.2.

To solve for eigenvalues and eigenvectors, the two systems are assumed to be undamped and unforced. Thus, the equation of motion can be acquired as:

$$\begin{bmatrix} m_1 & 0 \\ 0 & m_1 \end{bmatrix} \begin{bmatrix} \ddot{X}_1 \\ \ddot{X}_2 \end{bmatrix} + \begin{bmatrix} k_1 + k_c & -k_c \\ -k_c & k_1 + k_c + \Delta k \end{bmatrix} \begin{bmatrix} X_1 \\ X_2 \end{bmatrix} = \begin{bmatrix} 0 \\ 0 \end{bmatrix} \quad (7.1a)$$

$$\begin{bmatrix} m_2 & 0 \\ 0 & m_2 \end{bmatrix} \begin{bmatrix} \ddot{X}_3 \\ \ddot{X}_4 \end{bmatrix} + \begin{bmatrix} k_2 + k_c & -k_c \\ -k_c & k_2 + k_c - \Delta k \end{bmatrix} \begin{bmatrix} X_3 \\ X_4 \end{bmatrix} = \begin{bmatrix} 0 \\ 0 \end{bmatrix} \quad (7.1b)$$

Solving these systems of matrices leads to the eigenvalue and eigenvectors as:

$$\omega_{1,2}^2 = \frac{2(k_1 + k_c) - \Delta k \mp \sqrt{\Delta k^2 + 4k_c^2}}{2m} \quad (7.2a)$$

$$u_{1,2} = \frac{-\Delta k \pm \sqrt{\Delta k^2 + 4k_c^2}}{2k_c} \quad (7.2b)$$

$$\omega_{3,4}^2 = \frac{2(k_2 + k_c) + \Delta k \mp \sqrt{\Delta k^2 + 4k_c^2}}{2m} \quad (7.2c)$$

$$u_{3,4} = \frac{\Delta k \pm \sqrt{\Delta k^2 + 4k_c^2}}{2k_c} \quad (7.2d)$$

ω_1, ω_3 correspond to the eigenfrequency of the in-phase mode and u_1, u_3 correspond to the eigenstate or in this case amplitude ratio of the in-phase mode of the two resonator systems. Similarly, ω_2, ω_4 and u_1, u_3 correspond to the anti-phase mode of the two resonator systems. For a differential amplitude ratio measurement, the difference between the two eigenstates corresponding to either of the modes is derived to be:

$$|u_1 - u_3| = |u_2 - u_4| = \frac{\Delta k}{k_c} \quad (7.3)$$

Thus, the sensitivity of the amplitude ratio difference (ARD) to input stiffness perturbation at *veering* (when $\Delta k = 0$) can be modelled as:

$$\frac{\partial |u_1 - u_3|}{\partial \Delta k} = \frac{\partial |u_2 - u_4|}{\partial \Delta k} = \frac{1}{k_c} \quad (7.4)$$

Both the amplitude ratio and its sensitivity to stiffness perturbations is simulated and plotted in Fig. 7.3. The two amplitude ratios meet at an *equilibrium point* (χ) corresponding to an amplitude ratio 1. As the figure suggests, the sensitivity enhancement of the differential amplitude ratio is maximum in the operating region around this equilibrium point and thus, it is preferable to work around that region. Furthermore, the amplitude ratio difference provides a constant sensitivity around this point. This is a very important result since amplitude ratio measurements in mode-localised accelerometers have been plagued with high nonlinearity of sensitivity around the *veering* zone [32, 28]. Using an amplitude ratio difference as an output metric allows for greater linearity of operating around the *veering* zone where the system provides the best noise floor [113].

The equilibrium point can be tuned electrostatically by applying perturbation voltages on either one of the systems. The results of a simulation showing the change of sensitivity in this case is shown in Fig. 7.4 plotted against the individual amplitude ratios of the two

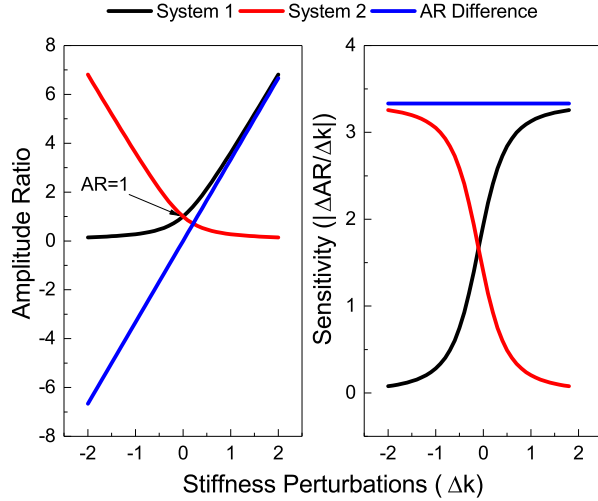


Fig. 7.3 Simulation showing the variation and the sensitivity of the two individual amplitude ratios and their difference across different perturbations at equilibrium point of $AR=1$

systems. The sensitivity of the amplitude ratio is dependent on both the amplitude ratios and reaches a maximum at the various equilibrium points (marked in red) in each case. Even though the sensitivity increases around the equilibrium points at higher amplitude ratios, the sensitivity of the system is no longer constant there. Only when the equilibrium point is at $AR \sim 1$, is the sensitivity constant in the amplitude ratio difference across all amplitude ratios. Thus, it is still preferable to work around the *veering* zone for higher linearity of the output metric. In this work, all results are done at the equilibrium points with the amplitude ratios of both the systems matching each other to 3 decimal places.

7.3 Experiment

The sensor consists of two systems of coupled clamped-clamped beam resonators that are placed on either side of a proof mass so that each system of resonators experiences differential change in acceleration. The design and fabrication of the sensor is not part of my work. However, the rationale behind the design is pertinent to this work. Thus, The design of the different parts of the sensor are discussed in detail in Appendix E. Tab. 7.1, has been prepared to include all key parameters as a summary of the design considerations. The sensor is fabricated using a custom process by SILEX Microsystems AB where they are vacuum sealed using fusion bonding. An optical micrograph of the sensor is shown in Fig. 7.5.

A schematic of the measurement setup is shown in Fig. 7.6. The device layer and the substrate are both biased at 10 V to avoid any deformations of the proof mass. The resonator

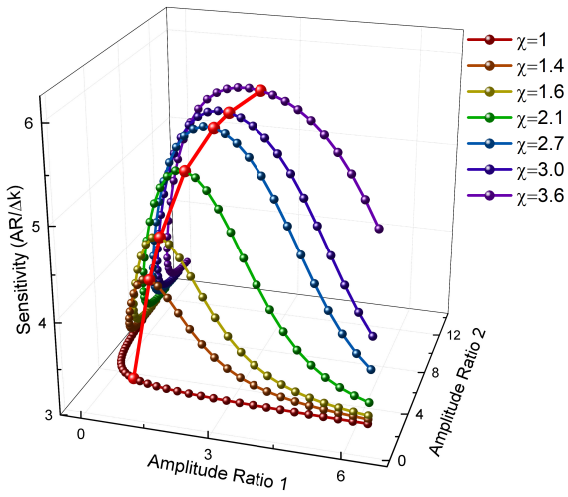


Fig. 7.4 3-dimensional plot showing the variation of the amplitude ratio sensitivity at different individual amplitude ratios.

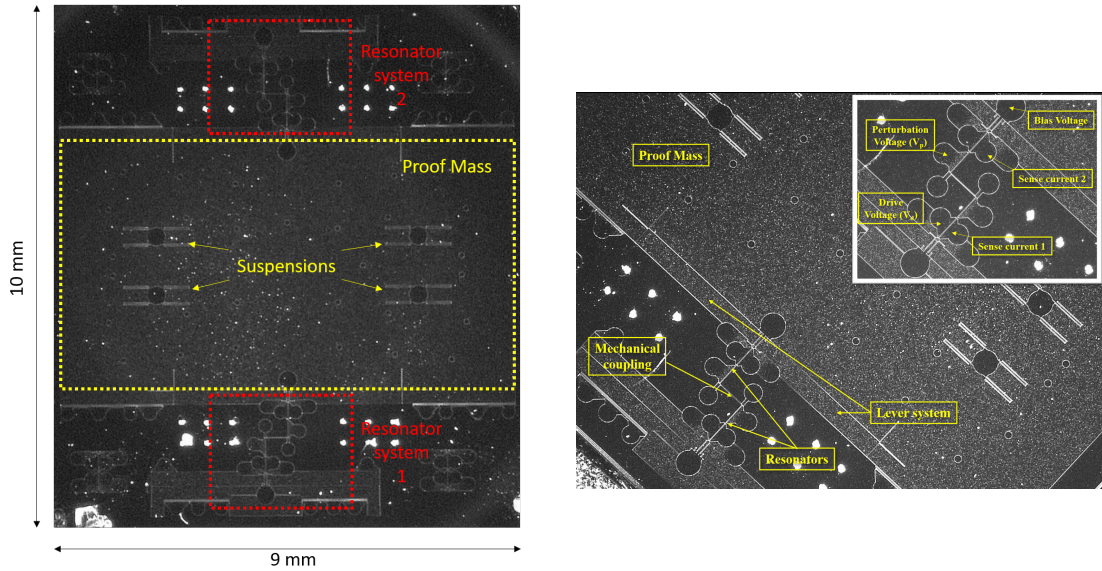


Fig. 7.5 Optical micrograph of the accelerometer.

systems on either side of the proof mass are driven individually by two commercially available lock-in amplifiers (Zurich Instruments MFLI). A single resonator system is driven in a cascade configuration where the first resonator is driven capacitively and the second resonator is driven synchronously through the coupler. The motional current from each resonator channel is passed through a custom transimpedance amplifier (TIA) and is fed back to the lock-in amplifiers to realise a closed-loop tracking of the amplitude and frequency. MFLIs are used for to achieve resonance tracking in this study; however, more details

Table 7.1 Device parameters

Parameter	Dimensions
Resonator beam length	700 μm
Resonator beam Width	7 μm
Coupling beam width	4 μm
Coupling beam length	400 μm
Device layer thickness	40 μm
Computed resonator stiffness	108.4 N/m
Computed resonator mass	$1.75 \times 10^{-10}\text{Kg}$
Computed resonant frequency	125.2 kHz
Estimated coupling stiffness	0.27 N/m
Computed suspension stiffness	374 N/m
Computed proof mass	$4.6 \times 10^{-6}\text{Kg}$
Computed resonant frequency of proof mass	1443 Hz
Computed effective lever amplification factor	9.5

on realising an oscillator topology for mode-localised resonators can be found elsewhere [69, 91]. To synchronise the measurement of all four channels, they are all fed into a National Instruments Data Acquisition card that reads all the amplitudes and frequencies synchronously.

The resonators are tuned electrostatically by applying perturbation voltage to bias the resonators at different levels of symmetry. The coupling strength is characterised experimentally to be 0.3 N/m by calculating the frequency difference between the first flexural modes [28, 23, 24] (see Appendix E for calculations). A quality factor of 60000 is realised for the first flexural mode at the operating frequency of 130 kHz. All experiments are carried out at room temperature without the use of any external temperature control.

7.4 Results

Experiments are performed on the designed accelerometer on its scale factor, bias stability, noise floor, and bandwidth in closed-loop configuration. As an example of its application in seismology, seismic activity measured while conducting experiments is also shown with data from a reference seismometer in the British Geological Survey network.

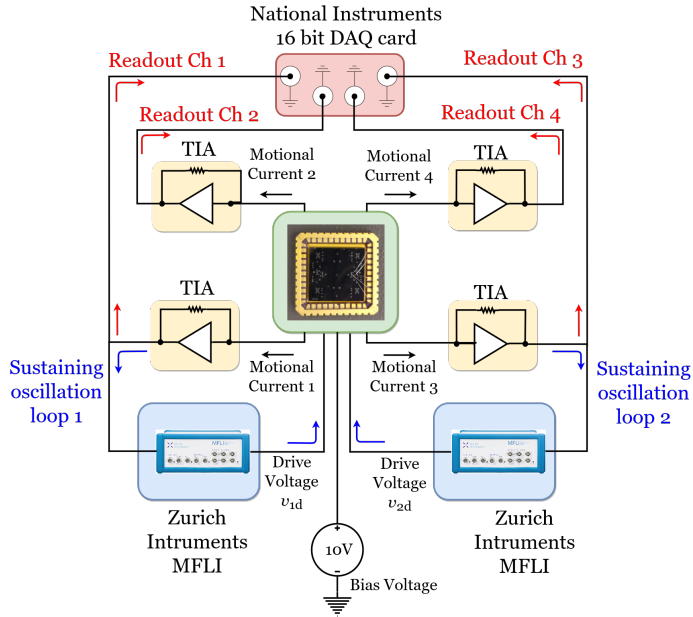
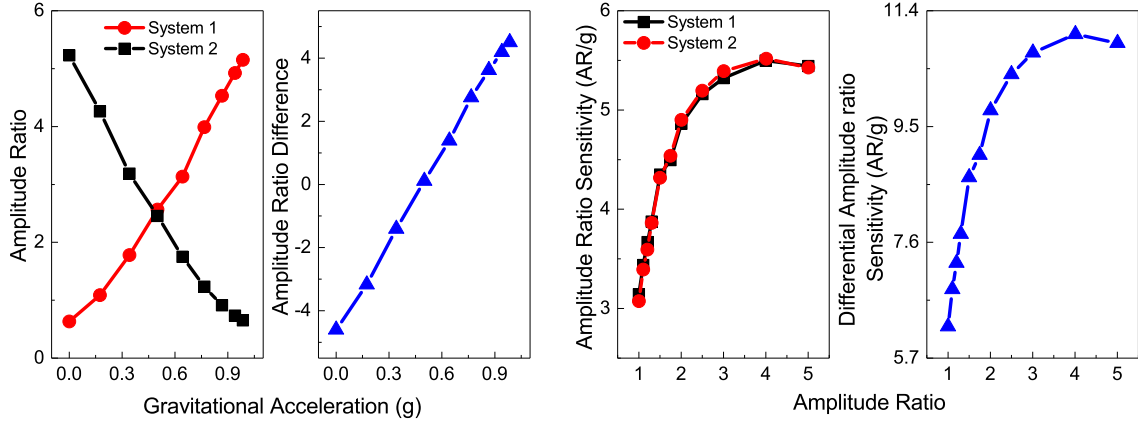


Fig. 7.6 Circuit level schematic of the experimental setup.

7.4.1 Scale factor

The scale factor analysis is done with the help of a tilt table that applies gravitational acceleration from 0-1 g depending on the tilt angle. 10 V of bias voltage was applied, and continuous resonance tracking was achieved using the Zurich Instruments MFLIs. The amplitude ratios of both systems were recorded at various tilt angles ranging from $0^\circ - 90^\circ$.

These results are plotted against the respective change in gravitational acceleration in Fig. 7.7a. In this case, it is seen that the equilibrium point (point where the amplitude ratios of the two coupled systems meet) is at an amplitude ratio of 2.5. This can be modified by individually tuning the two systems using electrostatic perturbations [23]. The localised sensitivities at different equilibrium points is measured using the tilt test and the results are shown in Fig. 7.7b. Each of the points in Fig. 7.7b refers to a different equilibrium point where the tilt test is repeated. As the equilibrium point is changed, the sensitivity of the differential amplitude ratio follows that of the individual amplitude ratios thus being consistently double of the sensitivity of individual systems. This trend of sensitivity is consistent with the simulation results shown in Fig. 7.4.



(a) Change in ARs (left) and ARD (right) upon change in tilt angle
(b) Sensitivity of ARs and ARD at different equilibrium points

Fig. 7.7 Model of the differential mode-localised accelerometer.

7.4.2 Noise floor

The noise floor is calculated by measuring the two amplitude ratios simultaneously and performing a power spectral density (PSD) analysis on the data. The sampling rate is set to 100 Hz and the measurements are taken for 5 minutes at each different equilibrium point. The noise spectral density (NSD) is achieved by taking the square-root of the PSD data. An example of the NSD for each value of the amplitude ratio compared to that of the differential amplitude ratio is shown in Fig. 7.8 (left). There is a peak around 10 Hz which can be attributed to the environmental noise in the laboratory. The noise floor is seen after this peak until the Nyquist frequency which in this case is 50 Hz. This noise floor is averaged for equilibrium points ranging from amplitude ratio 1 to 5 and plotted in Fig. 7.8 (right). A similar analysis of optimisation of individual amplitude ratios has been carried out on electrically coupled resonators [113] but this is the first to be done on a differential amplitude ratio as an output metric. It regards the noise in individual channels as a variance around a mean value and calculates the noise in the amplitude ratio as an output metric [133]:

$$\frac{\sigma^2(AR)}{[\mu(AR)]^2} = \frac{\sigma^2(x_1)}{[\mu(x_1)]^2} + \frac{\sigma^2(x_2)}{[\mu(x_2)]^2} - 2\frac{\text{Cov}(x_1, x_2)}{\mu(x_1)\mu(x_2)} \quad (7.5)$$

The noise in the individual channels can be assumed to be uncorrelated as the system is dominated by electronic amplifier noise. Thus, the component of $\text{Cov}(x_1, x_2) = 0$. The response of the individual amplitude ratio noise with respect to different operating amplitude

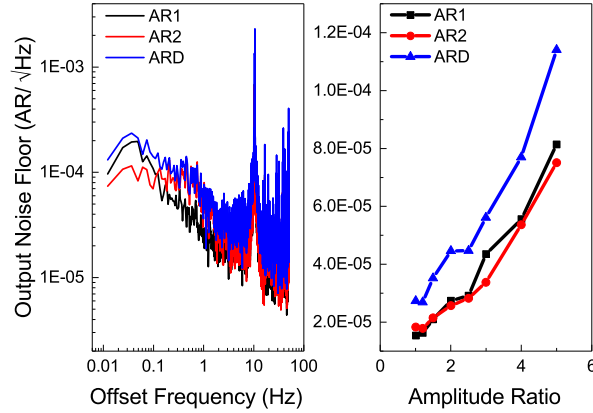


Fig. 7.8 Noise of the output metrics at AR=1 (left) and comparison of noise floor at different ARs

ratio points in the work [113] is similar to that achieved in Fig 7.8 (right). Using the Bienaymé formula [174], the noise in the amplitude ratio difference can be estimated as:

$$\sigma^2(AR_1 - AR_2) = \sigma^2(AR_1) + \sigma^2(AR_2) \quad (7.6)$$

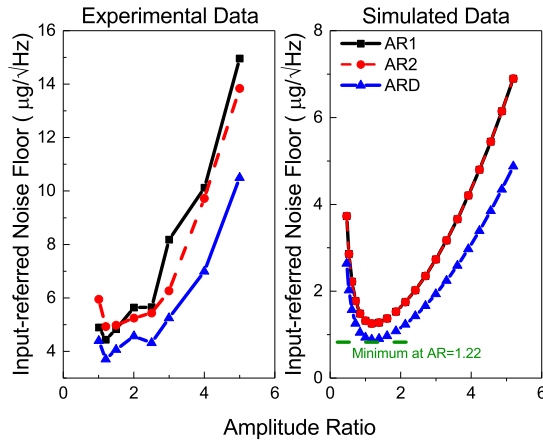


Fig. 7.9 Input-referred noise floor compared at different ARs

Thus, assuming that the sensor is being operated at an equilibrium point where both amplitude ratios are similar, the noise floor of the differential amplitude ratio is $\sqrt{2}$ times worse than the noise floor of individual amplitude ratio. However, since the sensitivity is improved by 2 times by using a differential amplitude ratio, the input-referred noise floor ($(AR_1 - AR_2)_n / (\partial(AR_1 - AR_2) / \partial(g))$) is improved by a factor of $\sqrt{2}$. This is seen in Fig.

7.9 where the input-referred noise floor (minimum amount of change in g that the sensor can capture) is plotted against various different equilibrium amplitude ratio points. The differential amplitude ratio tracks a similar trend as the individual amplitude ratio metrics but is consistently better by a factor of $\sqrt{2}$. Furthermore, a simulation is done using Equations 7.5 and 7.6, assuming an individual amplitude electronic noise floor of $100 \text{ nV}/\sqrt{\text{Hz}}$ operated at the equilibrium amplitude ratios. The trend of the amplitude ratio noise of both the systems as well as the noise of the amplitude ratio difference is similar in the experimental and simulated data. The minimum of the input-referred noise floor in both the simulation and experiment is around the amplitude ratio of $1.22(\sqrt{1.5})$ for individual amplitude ratios [113]. A similar minimum is seen for differential amplitude ratio as an output metric. In this case the best noise floor of $3 \mu\text{g}/\sqrt{\text{Hz}}$ is achieved at an amplitude ratio equilibrium point of 1.22. To achieve optimum resolution, 1.22 is chosen as an operating equilibrium amplitude ratio point.

It is important to understand the contributions of noise from various sources in achieving these noise floors. Therefore, FFT measurements are made on the output of each channel at the operating amplitude ratio of 1.22 using the MFLI under four different conditions – (1) closed-loop with the PLL function of the MFLI (total noise), (2) open-loop with the bias voltage and perturbation voltage on (noise of the resonator and amplifier), (3) amplifier circuit on but external bias and perturbation voltages off (amplifier noise), and (4) amplifier circuit and voltages off (measurement noise). These noise values for one of the resonator channels is plotted in Fig. 7.10 along with a theoretical estimation of the thermo-mechanical noise of the resonator as shown in Chapter 5.

The noise from the electrical sources and the oscillator are the most dominant as suggested by Fig. 7.10. This includes the noise from the amplifier and the electrical sources such as the voltage source supplying the bias and perturbation voltages. The oscillator noise close to the carrier is generally non-deterministic and is intrinsic to all oscillators. There are two second order low pass filters that are used with a cut-off frequency of 1 Hz on the bias voltage and the perturbation voltages to filter high frequency noise and that is seen in the open-loop noise profile. Usually for a low noise measurement, these sources would be replaced with batteries to ensure that no noise from the mains transfers into the resonators. Since most measurements were done in the lab environment, flexibility with tuning operating conditions was required and so no batteries were used.

When these sources are switched off, the amplifier noise can be measured. The results show that the noise in individual channels can be reduced by almost an order of magnitude if these sources were turned off and replaced with batteries. This is very promising since it

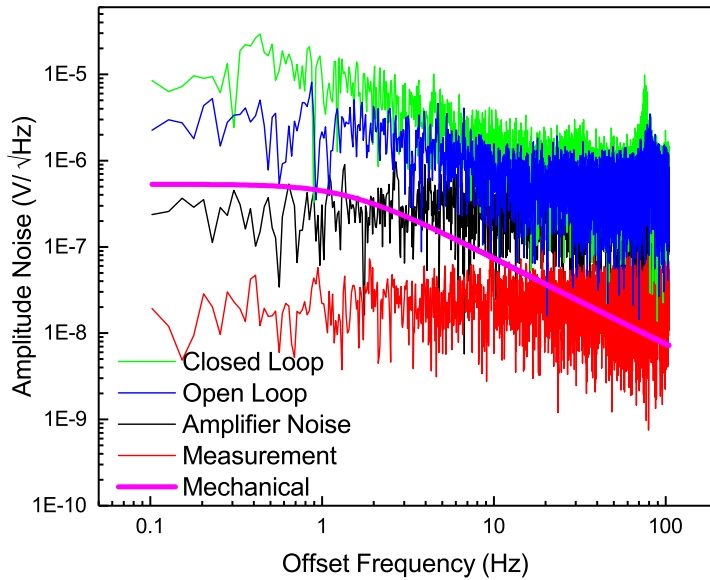


Fig. 7.10 Different amplitude noise sources dissected.

means that there is potentially room to improve the resolution. Furthermore, it is seen that the calculated thermo-mechanical noise of the resonators also is at the same vicinity of the amplifier noise which goes to show that the same simple circuitry can be used for further enhancement in resolution of these devices. The last limit on the plot is the measurement noise of the MFLI to show that the noise sources measured are from their respective sources and not from the MFLI itself.

Using these noise sources in individual channels, the noise in the amplitude ratio difference output metric can be compared as in Fig. 7.11. As seen from the individual channels, the noise in the differential amplitude ratio in the current setup is dominated by the electronic noise of the amplifier and the voltage sources. As a comparison, the theoretical thermo-mechanical noise limit is shown, and this signifies that there is a potential improvement in the noise floor by at least two orders of magnitude if the electronic noise was reduced. This improvement would put the resolution of the mode-localised sensor comparable to other resonant resonant accelerometers employing frequency shift output [169, 167] to date which is in the order of $100 \text{ ng}/\sqrt{\text{Hz}}$ between 0.1 Hz and 100 Hz. Applications such as monitoring the slow varying tidal waves is a realistic possibility with the help of better electronic amplifiers and low noise sources for bias and perturbation voltages.

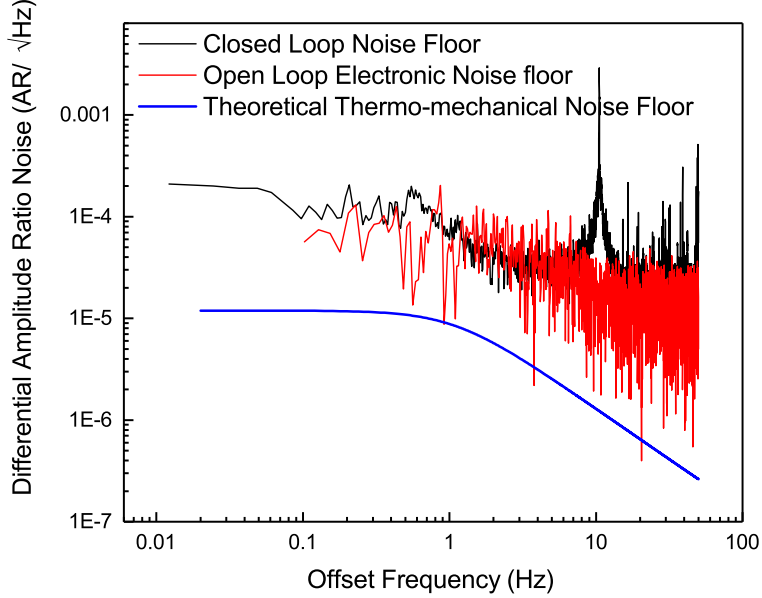
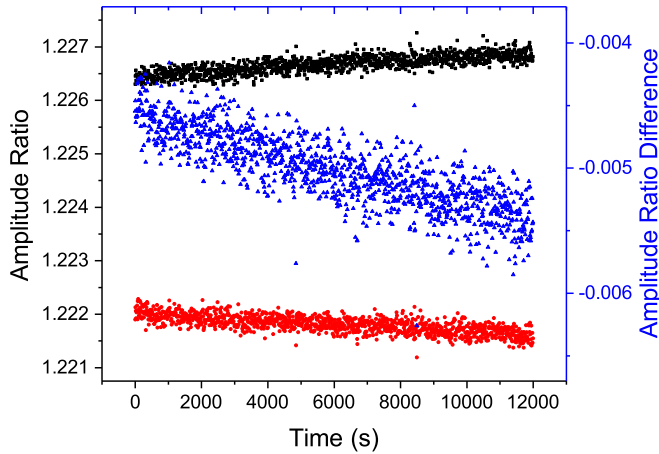


Fig. 7.11 Differential amplitude ratio noise sources.

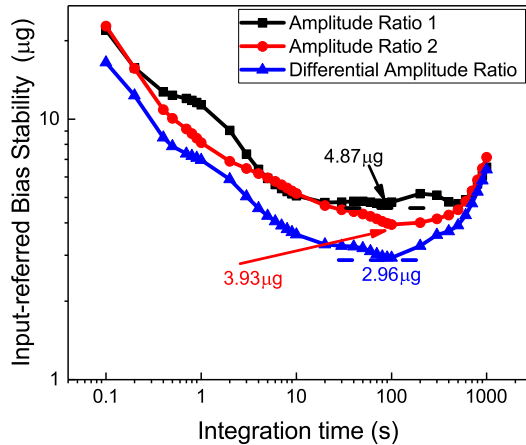
7.4.3 Bias stability

To calculate the bias stability of the sensor, the amplitude ratios of both sensors are logged for a period of 4 hours at a sampling rate of 10 Hz (raw data shown in Fig. 7.12a) and the Modified Allan variance of the data set is taken. The resulting curve is then divided by the scale factor for each of the output metrics to achieve input-referred stability which is shown in Fig. 7.12b.

Both the individual amplitude ratio and the differential amplitude ratio outputs show similar trends where due to the noise in the amplitude ratios integrating over time the long-term Allan variance curve gets better. A bias stability of $2.96 \mu\text{g}$ is achieved at an integration time of 100 s from the differential amplitude ratio output. This is better in comparison to the individual amplitude ratio outputs which have an individual bias stability of $3.93 \mu\text{g}$ and $4.87 \mu\text{g}$ respectively. All three of these bias stabilities are unprecedented and represent a significant improvement over results reported by other groups by two orders of magnitude [173] and are better than our previous work by a factor of 2 [91]. One effect to be noticed is that the Allan variance curve for both the individual amplitude ratio and the differential amplitude ratio start to increase after the integration time of 200 s. These effects could be attributed to residual temperature effects and micro-tilt of the chip due to limitations in the test setup.



(a) Amplitude ratio raw data.



(b) Bias stability comparison between the individual amplitude ratio and the differential amplitude ratio.

Fig. 7.12 Bias stability characterisation of the MLRXL.

7.4.4 Bandwidth

The bandwidth characterisation is carried out on a single coupled system instead of using a differential configuration since both of them are tuned to the same amplitude ratio (1.22) when in operation and both are equivalent in physical properties. An open-loop frequency sweep is done to investigate the resonant frequency of the proof mass. Using the MFLI, an AC excitation signal is applied on the comb-drive electrodes of the proof mass and the output current is passed through a TIA and analysed on the MFLI. The results are shown in Fig.

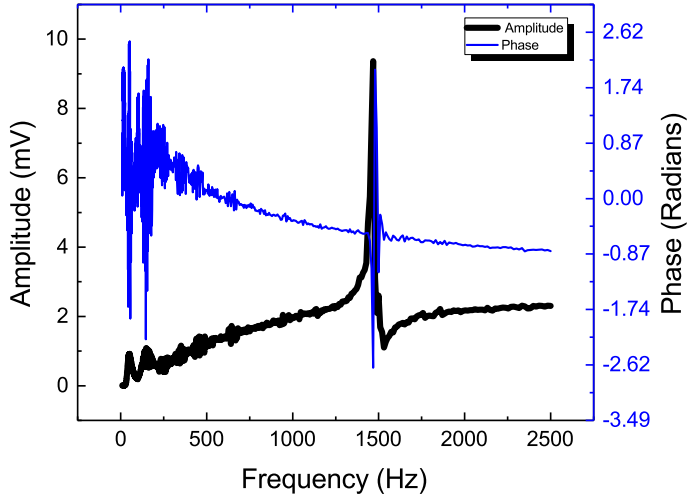


Fig. 7.13 Open-loop characterisation of the proof mass.

7.13. The resonance of the proof mass is at 1500 Hz with a quality factor of 900. This shows the limit that is posed by the proof mass on the maximum frequency of acceleration that can be measured.

Next a dynamic test is done on the proof mass by inducing dynamic acceleration through applying a sinusoidal signal to actuate the proof mass. To do this, an AC actuation signal of peak amplitude 500 mVpp is applied on the comb-drive actuators of the proof mass. The frequency of this AC excitation is swept from 1 Hz to 2000 Hz. The amplitude ratio is then measured for a period of 5 minutes at each actuation frequency and the FFT is taken to show the amplitude ratio component at the excitation frequency. These components are plotted against the actuation frequency to reveal the effective bandwidth of the sensor (as seen in Fig. 7.14). The effective bandwidth in this case is described to be the excitation frequency at which the gain is within 1% of that compared to the DC component. As seen in the results, the effective bandwidth is reduced below the expected 1500 Hz, due to a resonance occurring at 350 Hz. This is attributed to the fact that the anti-phase mode of the coupled resonators is exactly 350 Hz away from the operating in-phase mode causing for mode coupling. This leads to an amplified response when the input acceleration matches this frequency difference. Thus, although the proof mass limits the ultimate bandwidth achievable, the effective bandwidth is set by the frequency difference between the two modes of the resonators. This opens the investigation into a tunable bandwidth based on the operating amplitude ratio of the mode-localised accelerometer. The resonators are therefore tuned to

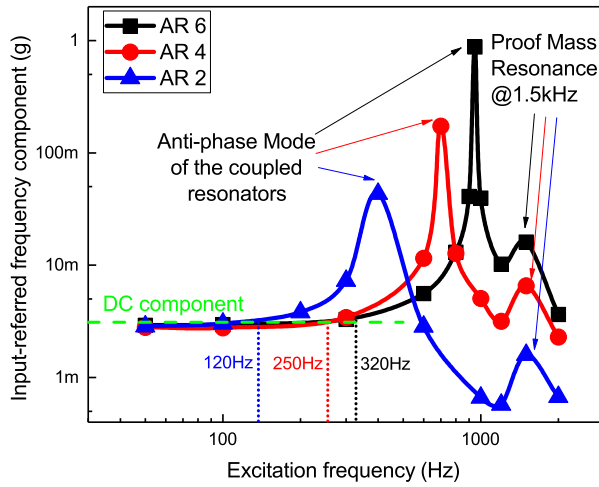


Fig. 7.14 Bandwidth analysis done at different amplitude ratios.

three different amplitude ratios – 2, 4 and 6 and the same experiment is repeated to investigate the bandwidth of the resonator at these amplitude ratios.

As hypothesized, Fig. 7.14 shows the anti-phase mode moving away from the measurement mode with the increase in amplitude ratio. Tab. 7.2 summarises this effect at the three different amplitude ratio operating points. Thus, the effective bandwidth also increases with the increase in amplitude ratio. This phenomenon creates a trade-off between the bandwidth and the operating amplitude ratio and in turn the resolution of the sensor. It has been established that the mode-localised resonators provide the best resolution whilst operating at an amplitude ratio of 1.22 in an electronic noise dominant system. The user would need to understand that if the sensor is operated at that amplitude ratio, it would limit the sensor's bandwidth. On the contrary, if the resonator is operated at higher amplitude ratios, the bandwidth would be improved but at the cost of a worse resolution. Another factor that would affect the bandwidth is the coupling stiffness since that directly influences the frequency difference between the two modes around *veering*. Lower coupling strengths allow for higher sensitivities and therefore a gateway to better resolutions but at the cost of lower bandwidth. This design trade-off must be considered in determining the optimal coupling strength for a specific device application.

Although a smaller bandwidth might seem disadvantageous for working at amplitude ratios close to *veering*, it adds to the filtering of the background seismic noise in addition to the filtering provided by the proof mass itself. Thus, for applications where large bandwidth

Table 7.2 Relationship between frequency difference between two modes and the bandwidth of the sensor.

Amplitude ratio	In-phase mode	Anti-phase mode	Frequency difference	Bandwidth
2	126272 Hz	126659 Hz	387 Hz	120 Hz
4	126323 Hz	127033 Hz	710 Hz	250 Hz
6	126338 Hz	127298 Hz	960 Hz	320 Hz

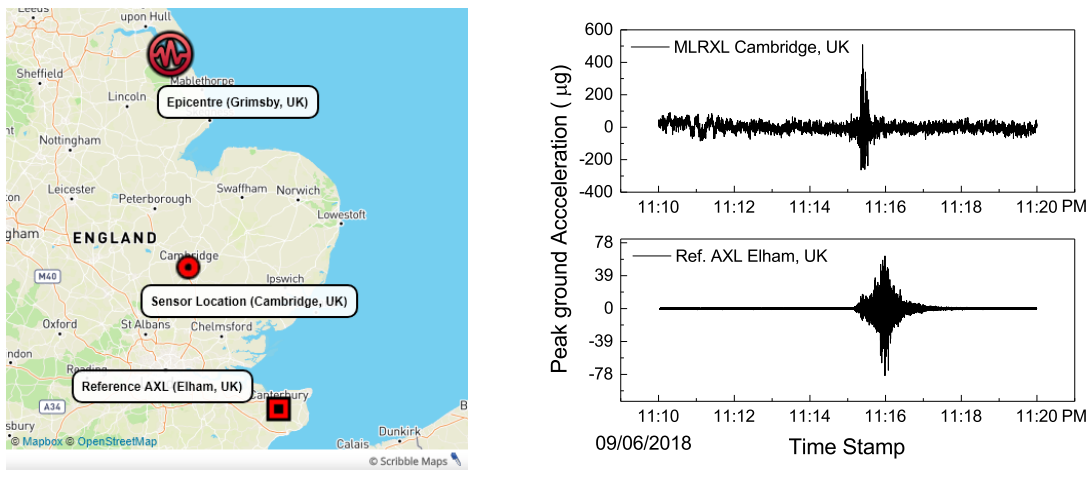
of measurement is not essential but an ultra high resolution is desired, operating around *veering* can be very beneficial. On the other hand, for applications for monitoring seismic activity where large bandwidth is preferred over resolution, operating at higher amplitude ratios is prescribed.

7.4.5 Seismic measurement

MEMS based seismometers are greatly advantageous because of their size and ability to be batch fabricated. Special high performance applications such as in geological monitoring of seismic activity requires sensors to be portable without sacrificing performance. Keeping this in mind, evidence is provided to show the potential of using MLRXL as a seismometer.

The seismic measurement was recorded of an earthquake of 3.8 magnitude on the Richter scale in Grimsby, UK on the 9th June, 2018 at about 23:15 BST. The sensor was being used to carry out long-term measurements when the earthquake was captured. The raw data with the time stamp is shown in Fig. 7.15b along with a comparison from a reference accelerometer at Elham, UK installed by the British Geological Survey. A 10 minute window around the earthquake is shown where both the mode-localised accelerometer (MLRXL) and reference accelerometer picked up signatures of the earthquake.

Since the sensor was positioned in a horizontal direction (oriented in the E-W direction), the horizontal component of the earthquake propagation waves is recorded. It is seen that the peak ground acceleration is higher by an order of magnitude in the MLRXL and this is due its proximity to the earthquake by 200 km. The time delay between the two measurements is also explained by the longer distance the waves must travel to the reference AXL as compared to the MLRXL. It is to be noted that the MLRXL was setup to measure the long-term stability of the sensor with a oscillator bandwidth of 10 Hz. Therefore, the MLRXL shows a damped response as compared to the Reference AXL that is solely setup for measuring seismic



(a) Location of the Earthquake

(b) Data from the mode-localised accelerometer.

Fig. 7.15 Data from the earthquake in Grimsby, UK on 9th June, 2018.

data. Furthermore, due to the lower sampling rate, many of the high frequency components have not been captured. However, from the bandwidth measurement, the sensor is able to effectively pick up frequency components up to 200 Hz and thus has the potential to be used as a seismic-grade accelerometer.

Summary

A prototype of a mode-localised accelerometer is presented in this chapter with detailed descriptions on the design, theory, and experimental observations of differential amplitude ratio output metric. The advantages of the new output metric in bettering the sensitivity (by 2 times) and the resolution (by $\sqrt{2}$ times) is shown. Although an unprecedented $2.96 \mu\text{g}$ stability and $3 \mu\text{g}/\sqrt{\text{Hz}}$ were achieved with this work to sense seismic activity, the resolution needs to be improved by at least an order of magnitude for these sensors to benchmark to state-of-the-art capacitive MEMS and geophone technology. The theoretical estimation of the thermo-mechanical noise and the experimental characterisation of the other electronic noise sources currently limiting the amplitude detection resolution suggest that the voltage sources for bias and perturbations are the main inhibitors of the resolution. Batteries as voltage sources could be an alternative to eliminate the noise due to the voltage sources. Beyond that, to reach closer to the thermo-mechanical noise floor, the amplifier noise will need to be reduced further by using ultra-low noise TIAs. The true advantage of the mode-localised accelerometer is its ability to provide ultra-stable long-term measurements. A robust setup needs to be designed to ensure no micro-tilting of the sensor occurs. Since the resonators

reject first order changes in temperature and pressure variations, operating at the mechanical noise limit would aid in measuring gravitational effects that vary on the order of 100 s or longer time scales.

From a design perspective, the resolution can also be improved by increasing the scale factor of the sensor. This can be either done by making weaker coupling springs or increasing the size of the proof mass. A weaker coupler would increase the sensitivity of the resonator system but would also amplify the effect of mismatch of the resonators at fabrication on the uncompensated amplitude ratio output metric. For example, if the coupling beam width is reduced by half, and a mismatch of $\pm 0.5 \mu\text{m}$ in the fabrication tolerances in the two coupled resonators could lead to an initial uncompensated amplitude ratio of 40 instead of currently 10. Although this will not change the voltage that needs to be applied to tune this mismatch, it does increase in the mismatch of physical properties such as temperature-based amplitude drifts between the two resonators. Since the mismatch in stiffness is due to the fabrication process, unless the fabrication process becomes more accurate, the mismatch will exist and perturbation voltages will need to be applied to tune the operating amplitude ratio. The proof mass, on the other hand, is limited by the size of the die. But, if the width and length of the size are to stay the constant from a fabrication point of view, one way to increase the proof mass would be to increase the thickness of the proof mass. A demonstration of a capacitive accelerometer derived from this method was able to separate the sensing elements that were fabricated on a thinner layer and inertial elements that included an additional thick substrate to increase the effective mass [175]. This way, the proof mass can be increased without compromising the overall width of the sensor.

If the sensitivity needs to be improved in the same device, there is another interesting phenomenon that can be used which has been observed in opto-mechanics community. Parametric pump [176], essentially uses an external AC source as a perturbation to couple the in-phase and anti-phase mode. If the AC source matches the frequency that is equal or close to the frequency difference between the two modes, it leads to a modal coupling, and a component of the in-phase mode mixes with the pump frequency to appear close to the anti-phase mode and *vice versa*. This in turn leads to a pseudo-reduction in the coupling stiffness and increase in sensitivity. More on this can be found in the future work section (Chapter 8.1). Since this can be implemented without any structural changes to the design, this approach can be implemented on the same accelerometer design.

Chapter 8

Conclusion

This work has deepened the understanding of the practical limitations imposed on mode-localised sensors in terms of noise, sensitivity, common mode rejection, and bandwidth. It has further quantified these metrics in the context of a high-resolution accelerometer. By doing so, the work has paved the way for ultra-high resolution mode-localised sensing by providing analytical and experimental evidence from a practical point of view.

The understanding of the physics behind these sensors is of utmost importance to predict its performance. To that effect, the simulations performed on the coupled 2-DoF in the form of a transfer function analysis, finite element modelling, and harmonic balance of the nonlinear system provided valuable insight into predicting the intrinsic noise in amplitude ratio measurements, their behaviour when exposed to temperature variations, and large vibration amplitudes respectively. They provided the freedom to optimise sensitivity, noise, temperature variability, and nonlinear behaviour without the need for a physical system. This enabled the prediction of the performance of the coupled resonator system as a sensor.

The implementation of an oscillator for a mode-localised sensor shown in this work was the first of its kind and paved the way to further study the practicality of using mode-localised sensors. The demonstration of a closed-loop configuration for the coupled resonator system enabled faster characterisation of the sensitivity since the oscillator was able to follow the resonance with the application of perturbations. Thus, the two amplitudes were able to be measured instantaneously in comparison to constantly performing open-loop frequency sweeps. Furthermore, it allowed for the true measurement of stability, noise floor, and bandwidth of the sensor which are key in understanding and optimising the resolution of the mode-localised sensor.

Experimental characterisations on electrically and mechanically coupled devices at different operating temperatures highlighted the variability in the common mode rejection

offered by these mode-localised devices. The results suggest that the electrically coupled device offers almost an order of magnitude better rejection than their mechanical counterpart. Furthermore, the superiority of the amplitude ratio over differential frequency output metric was emphasised by the comparison between the two output metrics in the same electrically coupled device. Amplitude ratio offered the same level of rejection as the differential frequency output without the need for an additional oscillator.

The detailed noise analysis performed in this thesis delineated major sources of noise that affect mode-localised sensors. The modelling of the noise using the transfer function method enabled an accurate prediction of the variation of the amplitude noise in the resonator noise and electrical noise dominant scenarios. The amplitude ratio noise was predicted from the individual amplitude noise by assuming them to be a variance around a mean vibration amplitude. The simulations predicted that optimisations could be made by operating at different amplitude ratios and coupling stiffnesses. The experiment was able to confirm this prediction with lower coupling stiffnesses leading to lower input-referred noise floors across all amplitude ratio operating regions. Furthermore, the optimum amplitude ratio to minimise noise was shown to be between $\sqrt{1.5}$ and $\sqrt{2}$ depending on the dominant noise mechanism and drive configuration.

Nonlinearity has always been a deterrent to the practical implementation of MEMS sensors. Thus, characterising the mode-localised sensor in the nonlinear domain accentuated the advantages of working in this domain in relation with improving the amplitude noise floor in an electronic noise dominant system. Amplitude ratio showed some interesting behaviours at the top and bottom bifurcation points mainly due to gain compression and electrical coupling that led to a reduction in sensitivity at the top bifurcation point. Despite this detrimental feature, the noise floor was seen to better by 4 times in comparison to its linear counterpart. Being able to utilise nonlinear effect in such a sensor can lead to great optimisations from a phase noise filtering and amplitude ratio noise floor improvements that can prove to be instrumental in enabling ultra-high resolution measurements.

Finally, a mode-localised accelerometer was implemented to show the potential of the weakly coupled resonators to be used as a physical sensor. With the introduction of a differential amplitude ratio output metric, superior common mode rejection was achieved even with a mechanically coupled resonator system. A stability of $3 \mu\text{g}$ and a noise floor of $3 \mu\text{g}/\sqrt{\text{Hz}}$ was achieved. The key factors limiting the resolution were identified as the electronic noise sourced from the large perturbation voltage needed to bias the system at symmetry. More work can be carried out to either reduce this perturbation voltage noise or increase the sensitivity through a larger proof mass to achieve better resolutions.

These contributions have furthered the understanding of the community on mode localisation in weakly coupled resonators and advanced the ultimate goal of implementing physical sensors with exceptional long-term stability and resolution.

8.1 Future work

Although many aspects of mode localisation are presented and discussed in this work, there is much potential to be harvested from this concept in the field of sensing. Some of these are proposed for future directions that can be taken to guide this field.

Mass sensing

An interesting application of mode-localised sensors could be their use for mass sensing. The sensitivity enhancement that amplitude ratio sensing offers over frequency shift sensing could be of immense help in sensing ultra-fine particulate matters (PM10). A possible implementation is shown in Fig. 8.1. It is to be noted that this particular proposed implementation would be done using piezoelectric transduction rather than the capacitive method discussed in this work. This is to ensure good quality factors (100 - 1000) when operating in air.

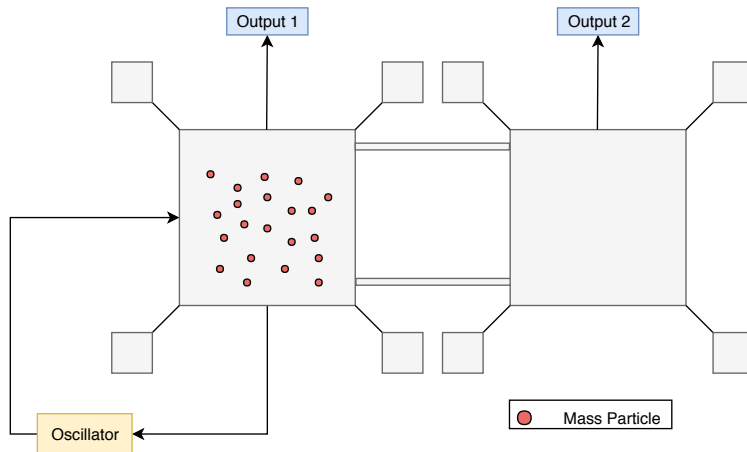


Fig. 8.1 Prototype mass sensor design.

This is a simple implementation of a 2-DOF mode-localised mass sensor. The mass particles in this case are selectively deposited on one of the resonators to change the symmetry of the system. As the perturbations can be applied to the system in the form of a stiffness or a mass change, energy localisation still takes place with the deposition of mass. A similar oscillator as proposed in this thesis can be applied to the system to sustain closed-loop

oscillations. Additionally, similar front-end electronics with the TIA configuration can be utilised.

Parametric pump

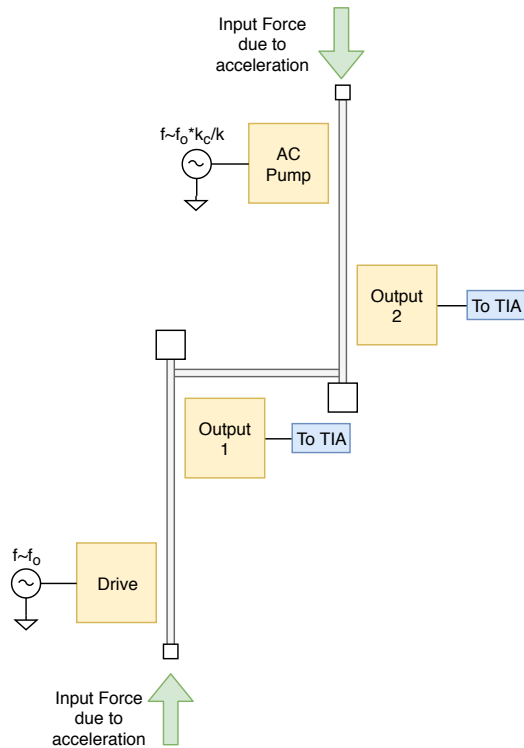


Fig. 8.2 Parametric pump design for accelerometers.

Another promising phenomenon that can be explored, especially for application as accelerometer is the use of parametric pump [176] to boost the effective sensitivity of the mode-localised accelerometer. It is desirable to use mechanical coupling over electrical coupling in an accelerometer design due to the constraints from a robustness perspective. This provides a floor on the strength of the coupling stiffness from a sensitivity perspective alone and restricts any tuning of the coupling stiffness. However, one way to tune the sensitivity in a mechanically coupled device is to use an AC pump as perturbation instead of the conventional DC perturbations. If the frequency of the pump is near the frequency difference between the two modes ($f_{pump} \approx f_0 \frac{k_e}{k}$), it induces modal coupling in the system. This leads to a component of the in-phase mode appearing near the anti-phase mode and *vice versa*. Here, increasing the amplitude of the pump can increase the coupling and *vice versa*. This way, the effective coupling and sensitivity can be tuned as required and can be

potentially increased by 2-3 orders of magnitude depending on the frequency of the pump chosen [177]. An illustration of the proposed setup is shown in Fig. 8.2.

The setup is similar to what is seen in a conventional mode-localised accelerometer with the exception of the pump being applied at the perturbation electrode. In this illustration an accelerometer undergoing perturbation due to acceleration on both the resonators is shown but the concept would work with one of them undergoing perturbation as well. In this work, the mode-localised accelerometer in linear operation was showing sensitivities of 6 AR/g but with the pump, sensitivities of upto 1000 AR/g have been shown [177]. This would help bring down the noise floor significantly to the region of ultra-high resolution acceleration measurements. Furthermore, the noise contribution from the perturbation voltage is reduced since the tuning of the amplitude ratios is now done using an AC signal. This concept is the next step that needs to be taken to reach the performance levels of other resonant frequency shift-based accelerometers showing sub 20 ng stability [178].

8.2 Contribution of the author

The work presented in this thesis has been published, in part in international peer reviewed journals and proceedings in international conferences as outlined below.

8.2.1 Articles in international peer reviewed journals

- M. Pandit, C. Zhao, G. Sobreviela, and A. A. Seshia, "Practical Limits to Common Mode Rejection in mode-localized Weakly Coupled Resonators", in *IEEE Sensors Journal*, **In print**.
- M. Pandit, C. Zhao, G. Sobreviela, X. Zou and A. A. Seshia, "A High Resolution Differential Mode-localized MEMS Accelerometer", in *Journal of Microelectromechanical Systems*, **In print**.
- M. Pandit, C. Zhao, G. Sobreviela, S. Du, X. Zou and A. A. Seshia, "Utilizing Energy Localization in Weakly Coupled Nonlinear Resonators for Sensing Applications", in *Journal of Microelectromechanical Systems*, vol. 28, no. 2, pp. 182-188, Apr. 2019.
- M. Pandit, C. Zhao, G. Sobreviela, A. Mustafazade, S. Du, X. Zou and A. A. Seshia, "Closed-loop Characterization of Noise and Stability in a Mode-localized Resonant MEMS Sensor", in *Transactions in Ultrasonics Ferroelectronics and Frequency Control (TUFFC)*, vol. 66, no. 1, pp. 170-180, Jan. 2019.

- C. Zhao, M. Pandit, G. Sobreviela, A. Mustafazade, S. Du, X. Zou and A. A. Seshia, "On the Optimization of Resonant MEMS Sensors Utilizing Vibration Mode Localization", in *Appl. Phy. Lett.*, vol. 112, no. 19, p.194103, May 2018.

8.2.2 Proceedings in international conferences

- M. Pandit, C. Zhao, G. Sobreviela, X. Zou, and A. A. Seshia, " Seismic Recording Using A Mode Localized MEMS Accelerometer", *2019 20th International Conference on Solid-State Sensors, Actuators and Microsystems and Eurosensors XXXIII* , Berlin, Germany, 2019,pp. 2150-2153.
- M. Pandit, C. Zhao, G. Sobreviela, and A. A. Seshia, " Immunity to Temperature Fluctuations in Weakly Coupled MEMS Resonators", *2018 IEEE SENSORS*, New Delhi, 2018, pp. 1-4.
- M. Pandit, C. Zhao, G. Sobreviela, A. Mustafazade and A. A. Seshia, " Coupled Non-linear MEMS Resonators for Sensing", *2018 IEEE International Frequency Control Symposium (IFCS)*, Olympic Valley, CA, 2018, pp. 1-4.
- M. Pandit, C. Zhao, G. Sobreviela, A. Mustafazade, X. Zou and A. A. Seshia, " A Mode-localized MEMS accelerometer with $7\mu\text{g}$ bias stability", *2018 IEEE Micro Electro Mechanical Systems (MEMS)*, Belfast, January 2018, pp. 968-971
- M. Pandit, C. Zhao, G. Sobreviela, A. Mustafazade and A. A. Seshia, " Reduction of amplitude ratio dependence on drive level in mode-localized resonant MEMS sensors", *2017 IEEE SENSORS*, Glasgow, October 2017, pp. 1-3.
- M. Pandit, C. Zhao, G. Sobreviela, A. Mustafazade and A. A. Seshia, " Nonlinear cancellation in weakly coupled MEMS resonators", *2017 Joint Conference of the European Frequency and Time Forum and IEEE International Frequency Control Symposium (EFTF/IFCS)*, Besançon, July 2017, pp. 16-19.
- M. Pandit, C. Zhao, G. Sobreviela, A. Mustafazade and A. A. Seshia, " Closed-loop tracking of amplitude and frequency in a mode-localized resonant MEMS sensor", *2017 Joint Conference of the European Frequency and Time Forum and IEEE International Frequency Control Symposium (EFTF/IFCS)*, Besançon, July 2017, pp. 510-513.

Nominated for best paper award

References

- [1] H. C. Nathanson, W. E. Newell, R. A. Wickstrom, and J. R. Davis. The resonant gate transistor. *IEEE Transactions on Electron Devices*, 14(3):117–133, March 1967.
- [2] J. N. Nilchi, R. Liu, and C. T. . Nguyen. High cx/co 13nm-capacitive-gap transduced disk resonator. In *2017 IEEE 30th International Conference on Micro Electro Mechanical Systems (MEMS)*, pages 924–927, Jan 2017.
- [3] Rob N Candler, Matthew A Hopcroft, Bongsang Kim, Woo-Tae Park, Renata Mela-mud, Manu Agarwal, Gary Yama, Aaron Partridge, Markus Lutz, and Thomas W Kenny. Long-term and accelerated life testing of a novel single-wafer vacuum encapsulation for mems resonators. *Journal of Microelectromechanical Systems*, 15(6):1446–1456, 2006.
- [4] Bongsang Kim, Rob N Candler, Matthew A Hopcroft, Manu Agarwal, Woo-Tae Park, and Thomas W Kenny. Frequency stability of wafer-scale film encapsulated silicon based mems resonators. *Sensors and Actuators A: Physical*, 136(1):125–131, 2007.
- [5] Yunhan Chen, Dongsuk D Shin, Ian B Flader, and Thomas W Kenny. Tri-mode operation of highly doped silicon resonators for temperature compensated timing references. In *Micro Electro Mechanical Systems (MEMS), 2017 IEEE 30th International Conference on*, pages 1158–1161. IEEE, 2017.
- [6] Clark T-C Nguyen. Mems technology for timing and frequency control. *IEEE transactions on ultrasonics, ferroelectrics, and frequency control*, 54(2), 2007.
- [7] Songbin Gong and Gianluca Piazza. Design and analysis of lithium–niobate-based high electromechanical coupling rf-mems resonators for wideband filtering. *IEEE Transactions on Microwave Theory and Techniques*, 61(1):403–414, 2013.
- [8] X. Zou, P. Thiruvenkatanathan, and A. A. Seshia. A Seismic-Grade Resonant MEMS Accelerometer. *Journal of Microelectromechanical Systems*, 23(4):768–770, August 2014.
- [9] Giacomo Langfelder, Alessandro Caspani, and Alessandro Tocchio. Design criteria of low-power oscillators for consumer-grade mems resonant sensors. *IEEE Transactions on Industrial Electronics*, 61(1):567–574, 2014.
- [10] S. A. Zotov, B. R. Simon, A. A. Trusov, and A. M. Shkel. High Quality Factor Resonant MEMS Accelerometer With Continuous Thermal Compensation. *IEEE Sensors Journal*, 15(9):5045–5052, September 2015.

- [11] Yixiang Wang, Hong Ding, Xianhao Le, Wen Wang, and Jin Xie. A mems piezoelectric in-plane resonant accelerometer based on aluminum nitride with two-stage microleverage mechanism. *Sensors and Actuators A: Physical*, 254:126–133, 2017.
- [12] M Li, EJ Ng, VA Hong, CH Ahn, Y Yang, TW Kenny, and DA Horsley. Lorentz force magnetometer using a micromechanical oscillator. *Applied Physics Letters*, 103(17):173504, 2013.
- [13] Yu Hui, Tianxiang Nan, Nian X Sun, and Matteo Rinaldi. High resolution magnetometer based on a high frequency magnetoelectric mems-cmos oscillator. *Journal of Microelectromechanical Systems*, 24(1):134–143, 2015.
- [14] Jenna L Fu, Roozbeh Tabrizian, and Farrokh Ayazi. Dual-mode aln-on-silicon micromechanical resonators for temperature sensing. *IEEE Transactions on Electron Devices*, 61(2):591–597, 2014.
- [15] Roozbeh Tabrizian and Farrokh Ayazi. Dual-mode vertical membrane resonant pressure sensor. In *Micro Electro Mechanical Systems (MEMS), 2014 IEEE 27th International Conference on*, pages 120–123. IEEE, 2014.
- [16] Enrico Rubiola. *Phase noise and frequency stability in oscillators*. Cambridge University Press, 2008.
- [17] James C Salvia, Renata Melamud, Saurabh A Chandorkar, Scott F Lord, and Thomas W Kenny. Real-time temperature compensation of mems oscillators using an integrated micro-oven and a phase-locked loop. *Journal of Microelectromechanical Systems*, 19(1):192–201, 2010.
- [18] Igor P Prikhodko, Alexander A Trusov, and Andrei M Shkel. Compensation of drifts in high-q mems gyroscopes using temperature self-sensing. *Sensors and Actuators A: Physical*, 201:517–524, 2013.
- [19] Roy H OlssonIII, Kenneth E Wojciechowski, Michael S Baker, Melanie R Tuck, and James G Fleming. Post-cmos-compatible aluminum nitride resonant mems accelerometers. *Journal of Microelectromechanical Systems*, 18(3):671–678, 2009.
- [20] Alessandro Tocchio, Alessandro Caspani, and Giacomo Langfelder. Mechanical and electronic amplitude-limiting techniques in a mems resonant accelerometer. *IEEE Sensors Journal*, 12(6):1719–1725, 2012.
- [21] Seonho Seok, Sangkyung Seong, Byeungleul Lee, Jeongheon Kim, and Kukjin Chun. A high performance mixed micromachined differential resonant accelerometer. In *2002 IEEE SENSORS*, volume 2, pages 1058–1063 vol.2, June 2002.
- [22] Matthew Spletzer, Arvind Raman, Alexander Q. Wu, Xianfan Xu, and Ron Reifenberger. Ultrasensitive mass sensing using mode localization in coupled microcantilevers. *Applied Physics Letters*, 88(25):254102, June 2006.
- [23] P. Thiruvengatathan, Jize Yan, J. Woodhouse, and A.A. Seshia. Enhancing Parametric Sensitivity in Electrically Coupled MEMS Resonators. *Journal of Microelectromechanical Systems*, 18(5):1077–1086, October 2009.

- [24] Pradyumna Thiruvenkatanathan, Jize Yan, and Ashwin A Seshia. Differential amplification of structural perturbations in weakly coupled mems resonators. *IEEE transactions on ultrasonics, ferroelectrics, and frequency control*, 57(3), 2010.
- [25] Hemin Zhang, Jiming Zhong, Weizheng Yuan, Jing Yang, and Honglong Chang. Ambient pressure drift rejection of mode-localized resonant sensors. In *Micro Electro Mechanical Systems (MEMS), 2017 IEEE 30th International Conference on*, pages 1095–1098. IEEE, 2017.
- [26] Philip W Anderson. Absence of diffusion in certain random lattices. *Physical review*, 109(5):1492, 1958.
- [27] Chun Zhao, Graham S Wood, Jianbing Xie, Honglong Chang, Suan Hui Pu, and Michael Kraft. A comparative study of output metrics for an mems resonant sensor consisting of three weakly coupled resonators. *Journal of Microelectromechanical Systems*, 25(4):626–636, 2016.
- [28] H. Zhang, B. Li, W. Yuan, M. Kraft, and H. Chang. An Acceleration Sensing Method Based on the Mode Localization of Weakly Coupled Resonators. *Journal of Microelectromechanical Systems*, 25(2):286–296, April 2016.
- [29] P. Thiruvenkatanathan and A.A. Seshia. Mode-Localized Displacement Sensing. *Journal of Microelectromechanical Systems*, 21(5):1016–1018, October 2012.
- [30] H. Zhang, J. Huang, W. Yuan, and H. Chang. A High-Sensitivity Micromechanical Electrometer Based on Mode Localization of Two Degree-of-Freedom Weakly Coupled Resonators. *Journal of Microelectromechanical Systems*, 25(5):937–946, October 2016.
- [31] Graham S Wood, Chun Zhao, Suan Hui Pu, Stuart A Boden, Ibrahim Sari, and Michael Kraft. Mass sensor utilising the mode-localisation effect in an electrostatically-coupled mems resonator pair fabricated using an soi process. *Microelectronic Engineering*, 159:169–173, 2016.
- [32] Chun Zhao, Graham S Wood, Jianbing Xie, Honglong Chang, Suan Hui Pu, and Michael Kraft. A force sensor based on three weakly coupled resonators with ultrahigh sensitivity. *Sensors and Actuators A: Physical*, 232:151–162, 2015.
- [33] J. Juillard, P. Prache, P. M. Ferreira, and N. Barniol. Impact of output metric on the resolution of mode-localized MEMS resonant sensors. In *2017 Joint Conference of the European Frequency and Time Forum and IEEE International Frequency Control Symposium (EFTF/IFCS)*, pages 506–509, July 2017.
- [34] P. Thiruvenkatanathan, J. Yan, J. Woodhouse, A. Aziz, and A. A. Seshia. Ultrasensitive mode-localized mass sensor with electrically tunable parametric sensitivity. *Applied Physics Letters*, 96(8):081913, February 2010.
- [35] P. W. Anderson. Absence of Diffusion in Certain Random Lattices. *Physical Review*, 109(5):1492–1505, March 1958.
- [36] P. W. Anderson. Local moments and localized states. *Reviews of Modern Physics*, 50(2):191–201, April 1978.

- [37] C. H. Hodges and J. Woodhouse. Confinement of vibration by structural irregularity. *The Journal of the Acoustical Society of America*, 69(S1):S109–S109, May 1981.
- [38] C. H. Hodges and J. Woodhouse. Vibration isolation from irregularity in a nearly periodic structure: Theory and measurements. *The Journal of the Acoustical Society of America*, 74(3):894–905, September 1983.
- [39] C. Pierre and E. H. Dowell. Localization of vibrations by structural irregularity. *Journal of Sound and Vibration*, 114(3):549–564, May 1987.
- [40] Christophe Pierre and Philip D. Cha. Strong mode localization in nearly periodic disordered structures. *AIAA Journal*, 27(2):227–241, 1989.
- [41] Arthur W. Leissa. On a curve veering aberration. *Zeitschrift für angewandte Mathematik und Physik ZAMP*, 25(1):99–111, June 1973.
- [42] J. R. Kuttler and V. G. Sigillito. On curve veering. *Journal of Sound Vibration*, 75:585–588, April 1981.
- [43] C. Pierre. Mode localization and eigenvalue loci veering phenomena in disordered structures. *Journal of Sound and Vibration*, 126(3):485–502, November 1988.
- [44] Jonathan Luke Du Bois, Sondipon Adhikari, and Nick A. J. Lieven. Eigenvalue curve veering in stressed structures: An experimental study. *Journal of Sound and Vibration*, 322(4–5):1117–1124, May 2009.
- [45] J. A. Kenyon, J. H. Griffin, and N. E. Kim. Sensitivity of Tuned Bladed Disk Response to Frequency Veering. *Journal of Engineering for Gas Turbines and Power*, 127(4):835, 2005.
- [46] J. Laine and D. Mougenot. A high-sensitivity MEMS-based accelerometer. *The Leading Edge*, 33(11):1234–1242, November 2014.
- [47] Bongsang Kim, R. N. Candler, M. Hopcroft, M. Agarwal, Woo-Tae Park, and T. W. Kenny. Frequency stability of wafer-scale encapsulated MEMS resonators. In *The 13th International Conference on Solid-State Sensors, Actuators and Microsystems, 2005. Digest of Technical Papers. TRANSDUCERS '05.*, volume 2, pages 1965–1968 Vol. 2, June 2005.
- [48] V. Kaajakari, T. Mattila, A. Oja, J. Kiihamaki, and H. Seppa. Square-extensional mode single-crystal silicon micromechanical resonator for low-phase-noise oscillator applications. *IEEE Electron Device Letters*, 25(4):173–175, April 2004.
- [49] C. T. C. Nguyen and R. T. Howe. An integrated CMOS micromechanical resonator high-Q oscillator. *IEEE Journal of Solid-State Circuits*, 34(4):440–455, April 1999.
- [50] M. J. Mescher, R. Lutwak, and M. Varghese. An ultra-low-power physics package for a chip-scale atomic clock. In *The 13th International Conference on Solid-State Sensors, Actuators and Microsystems, 2005. Digest of Technical Papers. TRANSDUCERS '05.*, volume 1, pages 311–316 Vol. 1, June 2005.

- [51] Kun Wang and C. T. C. Nguyen. High-order medium frequency micromechanical electronic filters. *Journal of Microelectromechanical Systems*, 8(4):534–556, December 1999.
- [52] Sheng-Shian Li, Yu-Wei Lin, Zeying Ren, and C. T. C. Nguyen. Self-switching vibrating micromechanical filter bank. In *Proceedings of the 2005 IEEE International Frequency Control Symposium and Exposition, 2005.*, pages 7 pp.–, August 2005.
- [53] M. Villarroya, J. Verd, J. Teva, G. Abadal, F. Perez, J. Esteve, and N. Barniol. Cantilever based MEMS for multiple mass sensing. In *Research in Microelectronics and Electronics, 2005 PhD*, volume 1, pages 197–200 vol.1, July 2005.
- [54] G. Hagleitner, D. Lange, O. Brand, A. Hierlemann, and H. Baltes. A single-chip CMOS resonant beam gas sensor. In *2001 IEEE International Solid-State Circuits Conference. Digest of Technical Papers. ISSCC (Cat. No.01CH37177)*, pages 246–247, February 2001.
- [55] B. V. Amini, S. Pourkamali, and F. Ayazi. A high resolution, stictionless, CMOS compatible SOI accelerometer with a low noise, low power, 0.25 μ m CMOS interface. In *17th IEEE International Conference on Micro Electro Mechanical Systems. Maastricht MEMS 2004 Technical Digest*, pages 572–575, 2004.
- [56] B. V. Amini, S. Pourkamali, and F. Ayazi. A 2.5v 14-bit Sigma; Delta; CMOS-SOI capacitive accelerometer. In *2004 IEEE International Solid-State Circuits Conference (IEEE Cat. No.04CH37519)*, pages 314–530 Vol.1, February 2004.
- [57] A. A. Seshia, M. Palaniapan, T. A. Roessig, R. T. Howe, R. W. Gooch, T. R. Schimert, and S. Montague. A vacuum packaged surface micromachined resonant accelerometer. *Journal of Microelectromechanical Systems*, 11(6):784–793, December 2002.
- [58] A. A. Seshia, R. T. Howe, and S. Montague. An integrated microelectromechanical resonant output gyroscope. In *Technical Digest. MEMS 2002 IEEE International Conference. Fifteenth IEEE International Conference on Micro Electro Mechanical Systems (Cat. No.02CH37266)*, pages 722–726, January 2002.
- [59] S. A. Bhave, J. I. Seeger, Xuesong Jiang, B. E. Boser, R. T. Howe, and J. Yasaitis. An integrated, vertical-drive, in-plane-sense microgyroscope. In *TRANSDUCERS, Solid-State Sensors, Actuators and Microsystems, 12th International Conference on, 2003*, volume 1, pages 171–174 vol.1, June 2003.
- [60] Zhen Fang, Zhan Zhao, Yu Wu, Bojun Zhang, and YiZhong Wang. Integrated temperature and humidity sensor based MEMS. In *International Conference on Information Acquisition, 2004. Proceedings.*, pages 84–87, June 2004.
- [61] A. Baldi, W. Choi, and B. Ziaie. A self-resonant frequency-modulated micromachined passive pressure transensor. *IEEE Sensors Journal*, 3(6):728–733, December 2003.
- [62] Matthew Spletzer, Arvind Raman, Hartono Sumali, and John P. Sullivan. Highly sensitive mass detection and identification using vibration localization in coupled microcantilever arrays. *Applied Physics Letters*, 92(11):114102, March 2008.

- [63] P. Thiruvengatathan, J. Yan, and A. A. Seshia. Differential amplification of structural perturbations in weakly coupled MEMS resonators. *IEEE Transactions on Ultrasonics, Ferroelectrics, and Frequency Control*, 57(3):690–697, March 2010.
- [64] C. Zhao, G. S. Wood, J. Xie, H. Chang, S. H. Pu, and M. Kraft. Comparative study of different output metrics for a three weakly coupled resonator sensor. In *2015 Transducers - 2015 18th International Conference on Solid-State Sensors, Actuators and Microsystems (TRANSDUCERS)*, pages 2196–2199, June 2015.
- [65] C. Zhao, G. S. Wood, J. Xie, H. Chang, S. H. Pu, and M. Kraft. A Three Degree-of-Freedom Weakly Coupled Resonator Sensor With Enhanced Stiffness Sensitivity. *Journal of Microelectromechanical Systems*, 25(1):38–51, February 2016.
- [66] Chun Zhao, Graham S. Wood, Jianbing Xie, Honglong Chang, Suan Hui Pu, and Michael Kraft. A force sensor based on three weakly coupled resonators with ultrahigh sensitivity. *Sensors and Actuators A: Physical*, 232:151–162, August 2015.
- [67] C. Zhao, G. S. Wood, J. Xie, H. Chang, S. H. Pu, H. M. H. Chong, and M. Kraft. A sensor for stiffness change sensing based on three weakly coupled resonators with enhanced sensitivity. In *2015 28th IEEE International Conference on Micro Electro Mechanical Systems (MEMS)*, pages 881–884, January 2015.
- [68] Chun Zhao, Graham S. Wood, Suan H. Pu, and Michael Kraft. A Feasibility Study for a Self-oscillating Loop for a Three Degree-of-Freedom Coupled MEMS Resonator Force Sensor. *Procedia Engineering*, 120:887–891, January 2015.
- [69] Chun Zhao, Milind Pandit, Boqian Sun, Guillermo Sobreviela, Xudong Zou, and Ashwin Seshia. A closed-loop readout configuration for mode-localized resonant mems sensors. *Journal of Microelectromechanical Systems*, 26(3):501–503, 2017.
- [70] J. Yang, J. Huang, J. Zhong, H. Zhang, and H. Chang. Self-oscillation for mode localized sensors. In *2017 19th International Conference on Solid-State Sensors, Actuators and Microsystems (TRANSDUCERS)*, pages 810–813, June 2017.
- [71] H. Kang, J. Yang, J. Zhong, H. Zhang, and H. Chang. A mode-localized accelerometer based on three degree-of-freedom weakly coupled resonator. In *2017 IEEE SENSORS*, pages 1–3, October 2017.
- [72] H. Kang, J. Yang, and H. Chang. A mode-localized accelerometer based on four degree-of-freedom weakly coupled resonators. In *2018 IEEE Micro Electro Mechanical Systems (MEMS)*, pages 960–963, January 2018.
- [73] J. Juillard, P. Prache, P. Maris Ferreira, and N. Barniol. Ultimate Limits of Differential Resonant MEMS Sensors Based on Two Coupled Linear Resonators. *IEEE Transactions on Ultrasonics, Ferroelectrics, and Frequency Control*, 65(12):2440–2448, December 2018.
- [74] P. Thiruvengatathan, J. Woodhouse, J. Yan, and A. A. Seshia. Limits to mode-localized sensing using micro- and nanomechanical resonator arrays. *Journal of Applied Physics*, 109(10):104903, May 2011.

- [75] Siavash Pourkamali and Farrokh Ayazi. Electrically coupled MEMS bandpass filters: Part II. Without coupling element. *Sensors and Actuators A: Physical*, 122(2):317–325, August 2005.
- [76] Siavash Pourkamali and Farrokh Ayazi. Electrically coupled MEMS bandpass filters: Part I: With coupling element. *Sensors and Actuators A: Physical*, 122(2):307–316, August 2005.
- [77] S. Pourkamali, R. Abdolvand, and F. Ayazi. A 600 kHz electrically-coupled MEMS bandpass filter. In *IEEE The Sixteenth Annual International Conference on Micro Electro Mechanical Systems, 2003. MEMS-03 Kyoto*, pages 702–705, January 2003.
- [78] M. Müller, V. Maiwald, M. Käch, C. Hierold, and C. Roman. A passive micromechanical broadband amplifier for acoustic emission sensing. In *2015 Transducers - 2015 18th International Conference on Solid-State Sensors, Actuators and Microsystems (TRANSDUCERS)*, pages 1129–1132, June 2015.
- [79] J. E. Y. Lee and A. A. Seshia. Parasitic feedthrough cancellation techniques for enhanced electrical characterization of electrostatic microresonators. *Sensors and Actuators A: Physical*, 156(1):36–42, November 2009.
- [80] X. Xu, H. Y. Hu, and H. L. Wang. Stability, bifurcation and chaos of a delayed oscillator with negative damping and delayed feedback control. *Nonlinear Dynamics*, 49(1):117–129, Jul 2007.
- [81] Fan He, Raymond Ribas, Cyril Lahuec, and Michel Jézéquel. Discussion on the general oscillation startup condition and the barkhausen criterion. *Analog Integrated Circuits and Signal Processing*, 59(2):215–221, May 2009.
- [82] T. O. Rocheleau, T. L. Naing, and C. T. Nguyen. Long-term stability of a hermetically packaged MEMS disk oscillator. In *2013 Joint European Frequency and Time Forum International Frequency Control Symposium (EFTF/IFC)*, pages 209–212, July 2013.
- [83] M. Li, C. Chen, C. Li, C. Chin, C. Chen, and S. Li. Foundry-CMOS integrated oscillator circuits based on ultra-low power ovenized CMOS-MEMS resonators. In *2013 IEEE International Electron Devices Meeting*, pages 18.4.1–18.4.4, December 2013.
- [84] C. Liu, R. Tabrizian, and F. Ayazi. A ± 0.3 ppm Oven-Controlled MEMS Oscillator Using Structural Resistance-Based Temperature Sensing. *IEEE Transactions on Ultrasonics, Ferroelectrics, and Frequency Control*, 65(8):1492–1499, August 2018.
- [85] C. M. Jha, M. A. Hopcroft, S. A. Chandorkar, J. C. Salvia, M. Agarwal, R. N. Candler, R. Melamud, B. Kim, and T. W. Kenny. Thermal Isolation of Encapsulated MEMS Resonators. *Journal of Microelectromechanical Systems*, 17(1):175–184, February 2008.
- [86] R. Tabrizian, M. Pardo, and F. Ayazi. A 27 MHz temperature compensated MEMS oscillator with sub-ppm instability. In *2012 IEEE 25th International Conference on Micro Electro Mechanical Systems (MEMS)*, pages 23–26, January 2012.

- [87] E. J. Ng, C. H. Ahn, Y. Yang, V. A. Hong, C. Chiang, E. Ahadi, M. W. Ward, and T. W. Kenny. Localized, degenerately doped epitaxial silicon for temperature compensation of resonant MEMS systems. In *2013 Transducers Eurosensors XXVII: The 17th International Conference on Solid-State Sensors, Actuators and Microsystems (TRANSDUCERS EUROSENSORS XXVII)*, pages 2419–2422, June 2013.
- [88] S. Z. Asl, S. Mukherjee, W. Chen, K. Joo, R. Palwai, N. Arumugam, P. Galle, M. Phadke, C. Grosjean, J. Salvia, H. Lee, S. Pamarti, T. Fiez, K. Makinwa, A. Partridge, and V. Menon. 12.9 A 1.55×0.85mm² 23ppm 1.0uA 32.768khz MEMS-based oscillator. In *2014 IEEE International Solid-State Circuits Conference Digest of Technical Papers (ISSCC)*, pages 226–227, February 2014.
- [89] N. Arumugam, G. Hill, G. Clark, C. Arft, C. Grosjean, R. Palwai, J. Pedicord, P. Hagelin, A. Partridge, V. Menon, and P. Gupta. 2-die wafer-level chip scale packaging enables the smallest TCXO for mobile and wearable applications. In *2015 IEEE 65th Electronic Components and Technology Conference (ECTC)*, pages 1338–1342, May 2015.
- [90] T. A. Roessig, R. T. Howe, A. P. Pisano, and J. H. Smith. Surface-micromachined resonant accelerometer. In *Proceedings of International Solid State Sensors and Actuators Conference (Transducers '97)*, volume 2, pages 859–862 vol.2, June 1997.
- [91] M. Pandit, C. Zhao, G. Sobreviela, A. Mustafazade, X. Zou, and A. A. Seshia. A mode-localized MEMS accelerometer with 7ug bias stability. In *2018 IEEE Micro Electro Mechanical Systems (MEMS)*, pages 968–971, January 2018.
- [92] Chun Zhao, Graham S Wood, Jianbing Xie, Honglong Chang, Suan Hui Pu, and Michael Kraft. A three degree-of-freedom weakly coupled resonator sensor with enhanced stiffness sensitivity. *Journal of Microelectromechanical Systems*, 25(1):38–51, 2016.
- [93] J. Zhong, J. Yang, and H. Chang. The temperature drift suppression of mode-localized resonant sensors. In *2018 IEEE Micro Electro Mechanical Systems (MEMS)*, pages 467–470, January 2018.
- [94] A. A. Seshia. *Integrated micromechanical resonant sensors for inertial measurement systems*. PhD thesis, UNIVERSITY OF CALIFORNIA, BERKELEY, 2002.
- [95] M. A. Hopcroft, W. D. Nix, and T. W. Kenny. What is the young's modulus of silicon? *Journal of Microelectromechanical Systems*, 19(2):229–238, April 2010.
- [96] Hiromichi Watanabe, Naofumi Yamada, and Masahiro Okaji. Linear Thermal Expansion Coefficient of Silicon from 293 to 1000 K. *International Journal of Thermophysics*, 25(1):221–236, January 2004.
- [97] C. D. Do, A. Erbes, J. Yan, K. Soga, and A. A. Seshia. Vacuum packaged low-power resonant mems strain sensor. *Journal of Microelectromechanical Systems*, 25(5):851–858, Oct 2016.

- [98] Wan-Thai Hsu and C. T. Nguyen. Stiffness-compensated temperature-insensitive micromechanical resonators. In *Technical Digest. MEMS 2002 IEEE International Conference. Fifteenth IEEE International Conference on Micro Electro Mechanical Systems (Cat. No.02CH37266)*, pages 731–734, January 2002.
- [99] B. Kim, M. A. Hopcroft, R. N. Candler, C. M. Jha, M. Agarwal, R. Melamud, S. A. Chandorkar, G. Yama, and T. W. Kenny. Temperature Dependence of Quality Factor in MEMS Resonators. *Journal of Microelectromechanical Systems*, 17(3):755–766, June 2008.
- [100] Enrico Rubiola. *Phase Noise and Frequency Stability in Oscillators*. The Cambridge RF and Microwave Engineering Series. Cambridge University Press, 2008.
- [101] Enrico Rubiola. The Measurement of AM noise of Oscillators. *arXiv:physics/0512082*, December 2005. arXiv: physics/0512082.
- [102] J. R. Vig and Yoonkee Kim. Noise in microelectromechanical system resonators. *IEEE Transactions on Ultrasonics, Ferroelectrics, and Frequency Control*, 46(6):1558–1565, November 1999.
- [103] R. A. Kant and D. J. Nagel. Characteristics and performance of MEMS accelerometers. *AIP Conference Proceedings*, 368(1):166–176, April 1996.
- [104] A. N. Cleland and M. L. Roukes. Noise processes in nanomechanical resonators. *Journal of Applied Physics*, 92(5):2758–2769, August 2002.
- [105] T. B. Gabrielson. Mechanical-thermal noise in micromachined acoustic and vibration sensors. *IEEE Transactions on Electron Devices*, 40(5):903–909, May 1993.
- [106] F.W Sears and G. L Salinger. *Thermodynamics, Kinetic Theory, and Statistical Thermodynamics*. Addison-Wesle, Reading, MA, 1975.
- [107] C Kittel. *Elementary Statistical Physics*. Wiley, New York, 1958.
- [108] J. B. Johnson. Thermal Agitation of Electricity in Conductors. *Phys. Rev.*, 32(1):97–109, July 1928.
- [109] H. Nyquist. Thermal Agitation of Electric Charge in Conductors. *Phys. Rev.*, 32(1):110–113, July 1928.
- [110] M. V. Salapaka, H. S. Bergh, J. Lai, A. Majumdar, and E. McFarland. Multi-mode noise analysis of cantilevers for scanning probe microscopy. *Journal of Applied Physics*, 81(6):2480–2487, March 1997.
- [111] Giorgio Ferrari, Fabio Gozzini, Alessandro Molari, and Marco Sampietro. Transimpedance amplifier for high sensitivity current measurements on nanodevices. *IEEE Journal of Solid-State Circuits*, 44(5):1609–1616, 2009.
- [112] Giorgio Ferrari and Marco Sampietro. Wide bandwidth transimpedance amplifier for extremely high sensitivity continuous measurements. *Review of scientific instruments*, 78(9):094703, 2007.

- [113] Chun Zhao, Milind Pandit, Guillermo Sobreviela, Arif Mustafazade, Sijun Du, Xudong Zou, and Ashwin Seshia. On the noise optimization of resonant MEMS sensors utilizing vibration mode localization. *Appl. Phys. Lett.*, 112(19):194103, May 2018.
- [114] D. Yang, J. Woo, S. Lee, J. Mitchell, A. D. Challoner, and K. Najafi. A Micro Oven-Control System for Inertial Sensors. *Journal of Microelectromechanical Systems*, 26(3):507–518, June 2017.
- [115] Guillermo Sobreviela, G Vidal-Alvarez, M Riverol, A Uranga, F Torres, and N. Barniol. Suppression of the a-f mediated noise at the top bifurcation point in a mems resonator with both hardening and softening hysteretic cycles. *Sens. Actuators Phys.*, 256(2):59–65, 2017.
- [116] M. Agarwal, K. Park, R. Candler, M. Hopcroft, C. Jha, R. Melamud, B. Kim, B. Murrmann, and T. W. Kenny. Non-linearity cancellation in MEMS resonators for improved power-handling. In *IEEE International Electron Devices Meeting, 2005. IEDM Technical Digest.*, pages 286–289, December 2005.
- [117] H. K. Lee, P. A. Ward, A. E. Duwel, J. C. Salvia, Y. Q. Qu, R. Melamud, S. A. Chandorkar, M. A. Hopcroft, B. Kim, and T. W. Kenny. Verification of the phase-noise model for mems oscillators operating in the nonlinear regime. In *2011 16th International Solid-State Sensors, Actuators and Microsystems Conference*, pages 510–513, June 2011.
- [118] Hyung Kyu Lee, Renata Melamud, Saurabh Chandorkar, James Salvia, Shingo Yoneoka, and Thomas W Kenny. Stable operation of mems oscillators far above the critical vibration amplitude in the nonlinear regime. *Journal of microelectromechanical systems*, 20(6):1228–1230, 2011.
- [119] Eyal Kenig, MC Cross, LG Villanueva, RB Karabalin, MH Matheny, Ron Lifshitz, and ML Roukes. Optimal operating points of oscillators using nonlinear resonators. *Physical Review E*, 86(5):056207, 2012.
- [120] LG Villanueva, E Kenig, RB Karabalin, MH Matheny, Ron Lifshitz, MC Cross, and ML Roukes. Surpassing fundamental limits of oscillators using nonlinear resonators. *Physical review letters*, 110(17):177208, 2013.
- [121] Paul Ward and Amy Duwel. Oscillator phase noise: Systematic construction of an analytical model encompassing nonlinearity. *IEEE transactions on ultrasonics, ferroelectrics, and frequency control*, 58(1), 2011.
- [122] HK Lee, PA Ward, AE Duwel, JC Salvia, YQ Qu, R Melamud, SA Chandorkar, MA Hopcroft, B Kim, and TW Kenny. Verification of the phase-noise model for mems oscillators operating in the nonlinear regime. In *Solid-State Sensors, Actuators and Microsystems Conference (TRANSDUCERS), 2011 16th International*, pages 510–513. IEEE, 2011.
- [123] Guillermo Sobreviela, Chun Zhao, Milind Pandit, Cuong Do, Sijun Du, Xudong Zou, and Ashwin Seshia. Parametric noise reduction in a high-order nonlinear mems resonator utilizing its bifurcation points. *Journal of Microelectromechanical Systems*, 26(6):1189–1195, 2017.

- [124] Chun Zhao, Guillermo Sobreviela, Milind Pandit, Sijun Du, Xudong Zou, and Ashwin Seshia. Experimental observation of noise reduction in weakly coupled nonlinear mems resonators. *Journal of Microelectromechanical Systems*, 2017.
- [125] Milind Pandit, Chun Zhao, Guillermo Sobreviela, Aref Mustafazade, and Ashwin A Seshia. Reduction of amplitude ratio dependence on drive level in mode localized resonant mems sensors. In *SENSORS, 2017 IEEE*, pages 1–3. IEEE, 2017.
- [126] Alexander F Vakakis, Leonid I Manevitch, Yuri V Mikhlin, Valery N Pilipchuk, and Alexandr A Zevin. *Normal modes and localization in nonlinear systems*. Springer, 2001.
- [127] Alexander F Vakakis. Non-linear normal modes (nnms) and their applications in vibration theory: an overview. *Mechanical systems and signal processing*, 11(1):3–22, 1997.
- [128] M. Pandit, C. Zhao, A. Mustafazade, G. Sobreviela, and A. A. Seshia. Nonlinear cancellation in weakly coupled MEMS resonators. In *2017 Joint Conference of the European Frequency and Time Forum and IEEE International Frequency Control Symposium (EFTF/IFCS)*, pages 16–19, July 2017.
- [129] J. Juillard, A. Mostafa, and P. M. Ferreira. Nonlinear enhancement of locking range of mutually injection-locked oscillators for resonant sensing applications. In *2018 European Frequency and Time Forum (EFTF)*, pages 109–113, April 2018.
- [130] J. Juillard, A. Mostafa, and P.M Ferreira. Analysis of resonant sensors based on mutually injection-locked oscillators beyond the critical duffing amplitude. In *2018 European Frequency and Time Forum (EFTF)*, pages 114–118. IEEE, 2018.
- [131] LG Villanueva, E Kenig, RB Karabalin, MH Matheny, Ron Lifshitz, MC Cross, and ML Roukes. Surpassing fundamental limits of oscillators using nonlinear resonators. *Physical review letters*, 110(17):177208, 2013.
- [132] O. Lelièvre, V. Crozatier, G. Baili, P. Nouchi, D. Dolfi, L. Morvan, F. Goldfarb, F. Bretenaker, and O. Llopis. Low phase noise 10 ghz coupled optoelectronic oscillator. In *2017 Joint Conference of the European Frequency and Time Forum and IEEE International Frequency Control Symposium (EFTF/IFCS)*, pages 493–494, July 2017.
- [133] Regina C Elandt-Johnson and Norman L Johnson. *Survival models and data analysis*, volume 74. John Wiley & Sons, 1999. doi: 10.1002/9781119011040.
- [134] S. Finkbeiner. MEMS for automotive and consumer electronics. In *2013 Proceedings of the European Solid-State Device Research Conference (ESSDERC)*, pages 9–14, September 2013.
- [135] D. Hollocher, X. Zhang, A. Sparks, S. Bart, W. Sawyer, P. Narayanasamy, C. Pipitone, J. Memishian, H. Samuels, S. Ng, R. Mhatre, D. Whitley, F. Sammoura, M. Bhagavat, C. Tsau, K. Nunan, M. Judy, M. Farrington, and K. Yang. A very low cost, 3-axis, MEMS accelerometer for consumer applications. In *2009 IEEE SENSORS*, pages 953–957, October 2009.

- [136] D. Effa, P. Nieva, Z. Andrew, and S. Lancaster. Design and modeling of a MEMS accelerometer for a novel Virtual Button user interface. In *2009 IEEE Toronto International Conference Science and Technology for Humanity (TIC-STH)*, pages 597–602, September 2009.
- [137] A. P. Pisano. MEMS and Nano Technology for the Handheld, Portable Electronic and the Automotive Markets. In *TRANSDUCERS 2007 - 2007 International Solid-State Sensors, Actuators and Microsystems Conference*, pages 1–4, June 2007.
- [138] A. Ishizaki, S. Ikegami, T. Yamabe, S. Kitagami, and R. Kiyohara. Accelerometer-based HUD input for car navigation. In *2014 IEEE International Conference on Consumer Electronics (ICCE)*, pages 278–279, January 2014.
- [139] V. C. Jayanetti, W. A. D. M. Jayathilaka, K. I. Talawatta, and Y. W. R. Amarasinghe. Design and simulation of a MEMS based dual axis capacitive accelerometer. In *2015 Moratuwa Engineering Research Conference (MERCon)*, pages 194–198, April 2015.
- [140] R. T. Roushan, G. Saha, A. Boni, and S. Kal. FPGA implementation of an automobile pollution control system using a MEMS accelerometer. In *2006 IEEE International Conference on Industrial Technology*, pages 1607–1612, December 2006.
- [141] J. Wang and X. Li. Monolithic-integrated silicon bulk-micromachined accelerometer and pressure-sensor for tire-pressure-monitoring-system (TPMS) application. In *2011 16th International Solid-State Sensors, Actuators and Microsystems Conference*, pages 703–706, June 2011.
- [142] B. Y. Amirgaliyev, K. K. Kuatov, and Z. Y. Baibatyr. Road condition analysis using 3-axis accelerometer and GPS sensors. In *2016 IEEE 10th International Conference on Application of Information and Communication Technologies (AICT)*, pages 1–5, October 2016.
- [143] W. T. Pike, A. K. Delahunty, A. Mukherjee, G. Dou, H. Liu, S. Calcutt, and I. M. Standley. A self-levelling nano-g silicon seismometer. In *IEEE SENSORS 2014 Proceedings*, pages 1599–1602, November 2014.
- [144] P. Zwahlen, A. Nguyen, Y. Dong, F. Rudolf, M. Pastre, and H. Schmid. Navigation grade MEMS accelerometer. In *2010 IEEE 23rd International Conference on Micro Electro Mechanical Systems (MEMS)*, pages 631–634, January 2010.
- [145] R. S. Payne, S. Sherman, S. Lewis, and R. T. Howe. Surface micromachining: from vision to reality to vision [accelerometer]. In *Proceedings ISSCC '95 - International Solid-State Circuits Conference*, pages 164–165, February 1995.
- [146] K. H. Chau, S. R. Lewis, Y. Zhao, R. T. Howe, S. F. Bart, and R. G. Marcheselli. An Integrated Force-balanced Capacitive Accelerometer For Low-G Applications. In *Proceedings of the International Solid-State Sensors and Actuators Conference - TRANSDUCERS '95*, volume 1, pages 593–596, June 1995.
- [147] A. Selvakumar and K. Najafi. A high-sensitivity z-axis capacitive silicon microaccelerometer with a torsional suspension. *Journal of Microelectromechanical Systems*, 7(2):192–200, June 1998.

- [148] W. T. Pike, I. M. Standley, S. B. Calcutt, and A. G. Mukherjee. A broad-band silicon microseismometer with 0.25 NG/rHz performance. In *2018 IEEE Micro Electro Mechanical Systems (MEMS)*, pages 113–116, January 2018.
- [149] Cheng-Hsien Liu and T.W. Kenny. A high-precision, wide-bandwidth micromachined tunneling accelerometer. *Journal of Microelectromechanical Systems*, 10(3):425–433, September 2001.
- [150] S. Patra and T. K. Bhattacharyya. Design and fabrication of micromachined tunneling accelerometers with micro-g resolution and their comparison. In *2009 2nd International Workshop on Electron Devices and Semiconductor Technology*, pages 1–4, June 2009.
- [151] U. Krishnamoorthy, R. H. Olsson III, G. R. Bogart, M. S. Baker, D. W. Carr, T. P. Swiler, and P. J. Clews. In-plane MEMS-based nano-g accelerometer with sub-wavelength optical resonant sensor. *Sensors and Actuators A: Physical*, 145–146:283–290, July 2008.
- [152] R. P. Middlemiss, A. Samarelli, D. J. Paul, J. Hough, S. Rowan, and G. D. Hammond. Measurement of the Earth tides with a MEMS gravimeter. *Nature*, 531(7596):614–617, March 2016.
- [153] R. P. Middlemiss, A. Samarelli, D. J. Paul, J. Hough, S. Rowan, and G. D. Hammond. Measurement of the Earth tides with a MEMS gravimeter. *Nature*, 531(7596):614–617, March 2016.
- [154] L. M. Roylance and J. B. Angell. A batch-fabricated silicon accelerometer. *IEEE Transactions on Electron Devices*, 26(12):1911–1917, December 1979.
- [155] J. Grace Jency A. Ravi Sankar. Design, fabrication and testing of a high performance silicon piezoresistive Z-axis accelerometer with proof mass-edge-aligned-flexures. *Microsystem Technologies*, 18(1), 2012.
- [156] P. W. Barth, F. Pourahmadi, R. Mayer, J. Poydock, and K. Petersen. A monolithic silicon accelerometer with integral air damping and overrange protection. In *IEEE Technical Digest on Solid-State Sensor and Actuator Workshop*, pages 35–38, June 1988.
- [157] Li-Peng Wang, R. A. Wolf, Yu Wang, K. K. Deng, L. Zou, R. J. Davis, and S. Trolier-McKinstry. Design, fabrication, and measurement of high-sensitivity piezoelectric microelectromechanical systems accelerometers. *Journal of Microelectromechanical Systems*, 12(4):433–439, August 2003.
- [158] S. Kon and R. Horowitz. A High-Resolution MEMS Piezoelectric Strain Sensor for Structural Vibration Detection. *IEEE Sensors Journal*, 8(12):2027–2035, December 2008.
- [159] Analog Devices. Adxl213 low cost ± 1.2 g dual axis accelerometer, 2010.
- [160] iXblue. ixal a5 quartz vibration beam accelerometer, 2019.

- [161] A. Utz, C. Walk, A. Stanitzki, M. Mokhtari, M. Kraft, and R. Kokozinski. A high precision MEMS based capacitive accelerometer for seismic measurements. In *2017 IEEE SENSORS*, pages 1–3, October 2017.
- [162] D. J. Milligan, B. D. Homeijer, and R. G. Walmsley. An ultra-low noise MEMS accelerometer for seismic imaging. In *2011 IEEE SENSORS*, pages 1281–1284, October 2011.
- [163] B. Homeijer, D. Lazaroff, D. Milligan, R. Alley, J. Wu, M. Szepesi, B. Bicknell, Z. Zhang, R. G. Walmsley, and P. G. Hartwell. Hewlett packard’s seismic grade MEMS accelerometer. In *2011 IEEE 24th International Conference on Micro Electro Mechanical Systems*, pages 585–588, January 2011.
- [164] C. Comi, A. Corigliano, G. Langfelder, A. Longoni, A. Tocchio, and B. Simoni. A high sensitivity uniaxial resonant accelerometer. In *2010 IEEE 23rd International Conference on Micro Electro Mechanical Systems (MEMS)*, pages 260–263, January 2010.
- [165] C. Comi, A. Corigliano, G. Langfelder, A. Longoni, A. Tocchio, and B. Simoni. A new biaxial silicon resonant micro accelerometer. In *2011 IEEE 24th International Conference on Micro Electro Mechanical Systems*, pages 529–532, January 2011.
- [166] H. Zou, F. Chen, J. Wang, H. Bao, and X. Li. MEMS monolithic tri-axis high-shock accelerometers with MHz-level ultra-high resonant frequency. In *2017 IEEE 30th International Conference on Micro Electro Mechanical Systems (MEMS)*, pages 327–330, January 2017.
- [167] Xudong Zou, Pradyumna Thiruvenkatanathan, and Ashwin A Seshia. A seismic-grade resonant mems accelerometer. *Journal of Microelectromechanical Systems*, 23(4):768–770, 2014.
- [168] Seonho Seok, Hak Kim, and Kukjin Chun. An inertial-grade laterally-driven MEMS differential resonant accelerometer. In *2004 IEEE SENSORS*, pages 654–657 vol.2, October 2004.
- [169] D. D. Shin, C. H. Ahn, Y. Chen, D. L. Christensen, I. B. Flader, and T. W. Kenny. Environmentally robust differential resonant accelerometer in a wafer-scale encapsulation process. In *2017 IEEE 30th International Conference on Micro Electro Mechanical Systems (MEMS)*, pages 17–20, January 2017.
- [170] D. Yang, J. Woo, K. Najafi, S. Lee, J. Mitchell, and D. Challoner. ±2ppm frequency drift and 300x reduction of bias drift of commercial 6-axis inertial measurement units using a low-power oven-control micro platform. In *2015 IEEE SENSORS*, pages 1–4, November 2015.
- [171] F. Maspero, V. F. López-Rey, L. Joet, S. Hentz, and G. Langfelder. Combined electronics and algorithm development for offset drift characterization in MEMS accelerometers. In *2018 IEEE International Symposium on Inertial Sensors and Systems (INERTIAL)*, pages 1–4, March 2018.
- [172] J. Yang, J. Zhong, and H. Chang. A Closed-Loop Mode-Localized Accelerometer. *Journal of Microelectromechanical Systems*, 27(2):210–217, April 2018.

- [173] H. Kang, J. Yang, and H. Chang. A Closed-Loop Accelerometer Based on Three Degree-of-Freedom Weakly Coupled Resonator With Self-Elimination of Feedthrough Signal. *IEEE Sensors Journal*, 18(10):3960–3967, May 2018.
- [174] Michel Loéve. *Probability Theory*, volume 45 of *Graduate Texts in Mathematics*. Springer-Verlag, 4 edition, 1977.
- [175] F. Maspero, S. Delachanal, A. Berthelot, L. Joet, G. Langfelder, and S. Hentz. Small footprint, high-performance silicon capacitive accelerometer with a 3-d process. In *2018 IEEE Micro Electro Mechanical Systems (MEMS)*, pages 109–112, Jan 2018.
- [176] Hajime Okamoto, Adrien Gourgout, Chia-Yuan Chang, Koji Onomitsu, Imran Mahboob, Edward Yi Chang, and Hiroshi Yamaguchi. Coherent phonon manipulation in coupled mechanical resonators. *Nature Physics*, 9(8):480–484, August 2013.
- [177] Chun Zhao, Xin Zhou, Milind Pandit, Guillermo Sobreviela, Sijun Du, Xudong Zou, and Ashwin Seshia. Towards high-resolution inertial sensors employing parametric modulation in coupled micro-mechanical resonators. *Physical Review Applied*, under review.
- [178] M. Pandit, A. Mustafazade, C. Zhao, G. Sobreviela, X. Zou, Philipp Steinmann, and A. A. Seshia. An ultra-high resolution resonant mems accelerometer. In *2019 IEEE Micro Electro Mechanical Systems (MEMS)*, January 2019.
- [179] T. A. Roessig. *Integrated MEMS tuning fork oscillators for sensor applications*. PhD thesis, UNIVERSITY OF CALIFORNIA, BERKELEY, 1998.
- [180] Stephen Timoshenko, William Weaver, and Donovan Young. *Vibration problems in engineering*. John Wiley and Sons, 5th edition, 1990.
- [181] Allan Stuart and Keith Ord. *Kendall's Advanced Theory of Statistics*. Arnold, 6th edition, 1998.
- [182] Regina C. Elandt-Johnson and Norman L. Johnson. *Survival Models and Data Analysis*. John Wiley and Sons, 1980.
- [183] Kun Il Park. *Fundamentals of Probability and Stochastic Processes with Applications to Communications*. Springer, Switzerland, 1 edition, 2017.
- [184] Junseok Chae, H. Kulah, and K. Najafi. A hybrid Silicon-On-Glass (SOG) lateral micro-accelerometer with CMOS readout circuitry. In *Technical Digest. MEMS 2002 IEEE International Conference. Fifteenth IEEE International Conference on Micro Electro Mechanical Systems (Cat. No.02CH37266)*, pages 623–626, January 2002.
- [185] J. Li, S. Fan, C. Li, G. Zhanshe, G. S. Qiao, and L. H. Peng. Design and analysis of micromechanical resonant accelerometer. In *2012 8th IEEE International Symposium on Instrumentation and Control Technology (ISICT) Proceedings*, pages 16–19, 2012.
- [186] Xudong Zou. *High Resolution Resonant Accelerometer Based on MEMS Technology*. PhD thesis, University of Cambridge, Cambridge, Cambridgeshire, UK, November 2013.

- [187] Xiao-Ping Susan Su. *Compliant Leverage Mechanism Design for MEMS Applications*. PhD thesis, UNIVERSITY OF CALIFORNIA, BERKELEY, 2001.
- [188] Xiao-Ping Susan Su and Henry S Yang. Analytical modeling and FEM Simulations of single-stage microleverage mechanism. *International Journal of Mechanical Sciences*, 44:2217–2238, 2002.
- [189] Jing Zhang, Yan Su, Qin Shi, and An-Ping Qiu. Microelectromechanical Resonant Accelerometer Designed with a High Sensitivity. *Sensors (Basel)*, 15(12):30293–30310, December 2015.

Appendix A

Device Fabrication

The device used for most of the experimental characterisation was manufactured by MEMSCAP Inc. using the SOIMUMPS® process. The process is performed on a 150 mm n-type double-sided polished silicon on insulator (SOI) wafers. The process flow is shown in Fig. A.1 and can be divided into seven steps outlined below:

- **Silicon doping:** The first step is dope the top surface by depositing phosphosilicate glass (PSG) and annealing it at 1050 °C for 1 hour in Argon (Fig. A.1a). The PSG layer is then removed via wet chemical etching.
- **Pad metal liftoff:** A metal stack of 20 nm of chrome and 500 nm of gold is patterned through a liftoff process Fig. A.1b.
- **Silicon patterning:** The device layer is then patterned using DRIE using inductively coupled plasma (ICP) technology Fig. A.1c.
- **Substrate patterning:** Next, a protection material is applied on the top surface of the silicon device and the wafers are reversed in order to pattern the trench using a deep reactive ion etching (DRIE) process Fig. A.1d.
- **Oxide later removal:** The buried oxide layer is then removed with the help of a wet oxide etch process. The front side protection is then stripped off using a dry etch process in order to release the mechanical structures on the device layer Fig. A.1e. The remaining exposed oxide layers are removed using a vapor HF process to minimize stiction. This is done in order to allow for electrical contacts to the substrate and prevent metal shorts with the help of an undercut.

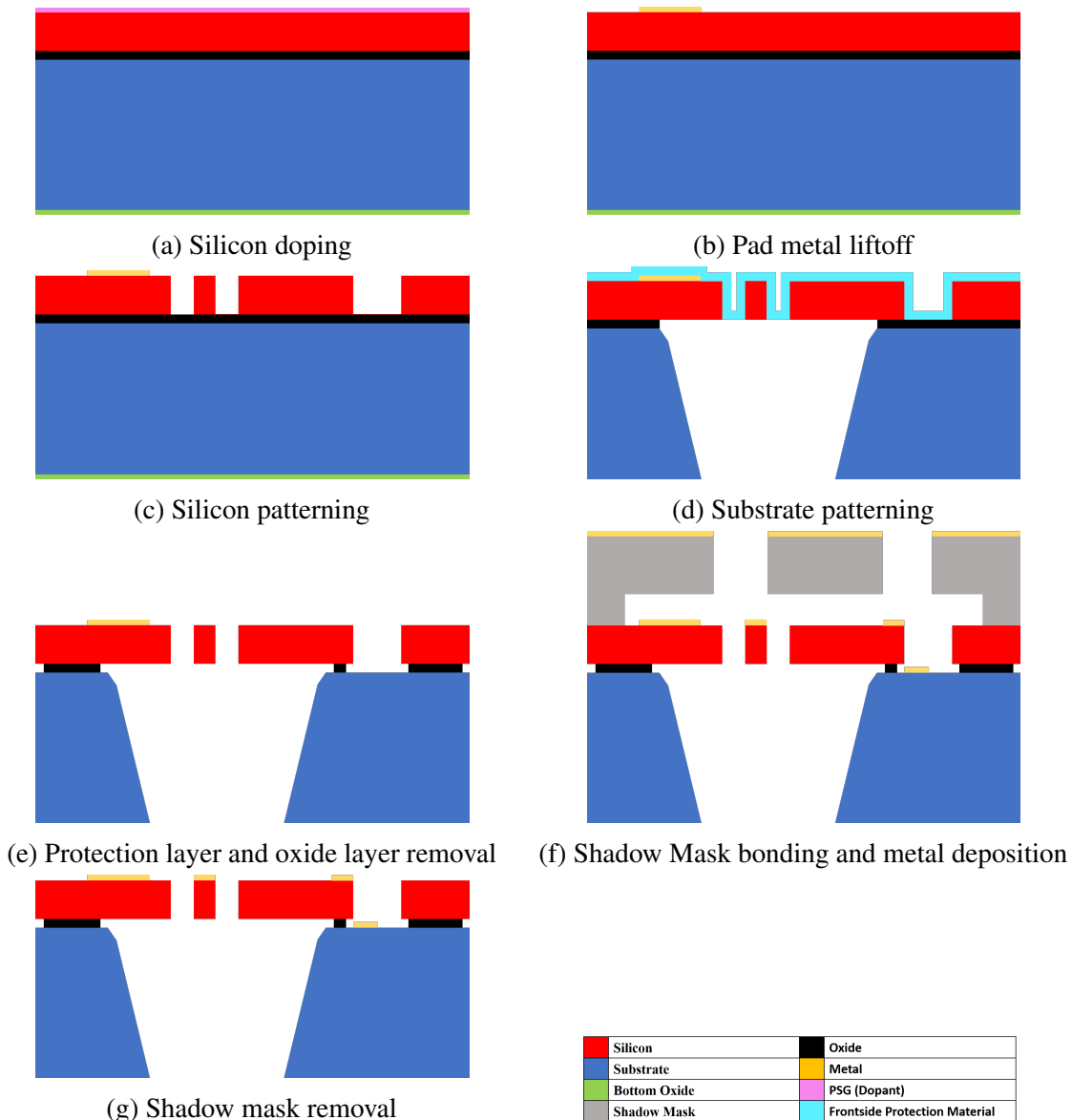


Fig. A.1 Device fabrication process flow

- **Shadow mask bonding and metal deposition:** The shadow mask is prepared by using a separate silicon wafer. "Standoffs" are used on the side of the shadow mask in order to ensure no contact with the device layer Fig. A.1f. Metal in the form of 50 nm Cr and 600 nm Gold is then deposited using e-beam evaporator. After evaporation, the shadow mask is removed, leaving a patterned metal layer on the SOI wafer Fig. A.1g.

Appendix B

Resonator Model

The basic structure of a DETF element involves two clamped-clamped (C-C) beams that are coupled strongly at the two ends. Two free-free beams acting as electrodes are then connected to the coupled beams at the anti-node in order to realise transduction and coupling. Mass can either be added or removed from this connection between the beam and the electrodes in order to tune the resonator frequency. Classical modelling of the element assumes the two tines to be separate 1-DoF C-C systems and has been well established [179, 94] and the analysis is summarized in this section. The mechanical model simplifies many dimensions but incorporates many of the different physical effects that occur within the DETF element. Fig. B.1 has the structure that this model takes into account and will be referred to in the equations following this modelling.

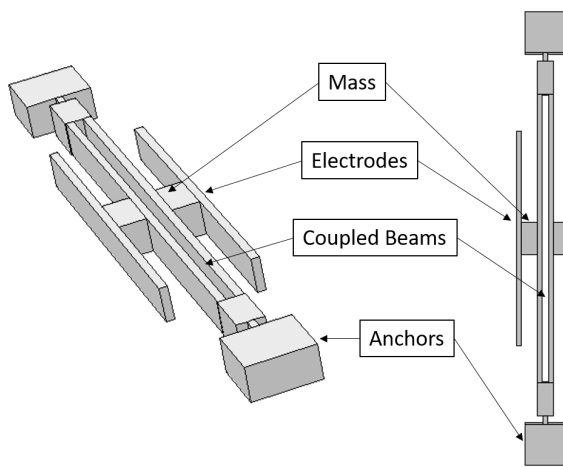


Fig. B.1 3-d view (left) and top view (right) of the DETF resonator.

The dynamic response of the undamped C-C resonator under axial loading is governed by the equation [180]:

$$\frac{\partial^2}{\partial x^2}(EI \frac{\partial^2 w(x,t)}{\partial x^2}) + \frac{\partial}{\partial x}(\frac{F}{2} \frac{\partial w(x,t)}{\partial x}) + \rho A \frac{\partial^2 w(x,t)}{\partial t^2} = P_e(x,t) \quad (\text{B.1})$$

In Eq. B.1, EI is the flexural bending stiffness in the x-y plane (as illustrate in Fig. B.2); F is the force applied axially to change the stiffness of the resonator (is the total force applied on both the tines); $w(x,t)$ is the deflection of the tines in both spacial and time domain; ρ is the density of material; A is the cross-sectional area of the tine, and P_e is the transverse actuation force applied on the electrodes that is assumed to be a point force concentrated at the middle of the tine (because of the actuation plates). In the case that there is no transverse force, P equals zero for every position except where the actuation masses are placed. Thus,

$$P = \sum_j m_j \ddot{w}(x_j) \dot{y} \quad (\text{B.2})$$

where, m_j is the j^{th} mass and the z_j is the position of the mass.

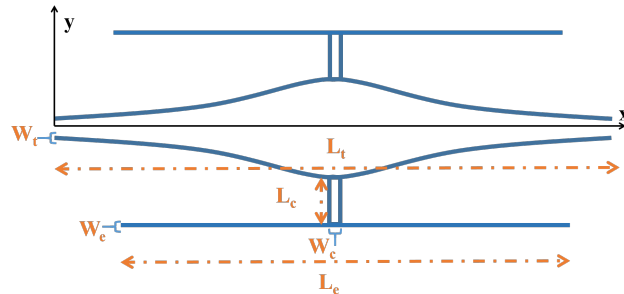


Fig. B.2 DETF element with geometrical variables and mode shapes assumed.

The boundary condition for this system is that the ends of the beam have zero deflection and zero slope:

$$\begin{aligned} w(0,t) &= w(L_t,0) = 0 \\ \left. \frac{\partial w}{\partial x} \right|_{x=0} &= \left. \frac{\partial w}{\partial x} \right|_{x=L_t} = 0 \end{aligned} \quad (\text{B.3})$$

Using separation of variables $w(x,t) = \phi(x)y(t)$ into spatial and time domain, we can simplify Eq. B.1 to just spatial coordinates:

$$\sum_i \left(EI \frac{\partial^4 \phi_i}{\partial x^4} + \frac{F}{2} \frac{\partial^2 \phi_i}{\partial x^2} y_i + \rho A \phi_i \ddot{y}_i + \sum_j m_j \ddot{w}(x_j) \ddot{y}_i \right) = 0 \quad (\text{B.4})$$

The response to individual modes i can be analysed by multiplying the above equation by the necessary mode shape and integrating over the length of the mode shape. Due to orthogonality, the cross-terms will cancel and the following relation remains:

$$\left(\int_0^L (\rho A \phi^2 dx + \sum_j m_j \phi_i^2(x_j)) \right) \ddot{y}_i + \left(\int_0^L (EI(\frac{\partial^2 \phi_i}{\partial x^2})^2 dx + \frac{F}{2}(\frac{\partial^2 \phi_i}{\partial x^2})^2) \right) y_i = 0 \quad (\text{B.5})$$

This can be simplified to the simple equation of an undamped mass-spring system:

$$m_{eff} \ddot{y} + k_{eff} y = 0$$

This makes the effective mass and stiffness of the DETF element to be

$$m_{eff} = \int_0^L \rho A \phi^2 dx + \sum_j m_j \phi_i^2(x_j) \quad (\text{B.6a})$$

$$k_{eff} = \int_0^L \left(EI(\frac{\partial^2 \phi_i}{\partial x^2})^2 dx + F(\frac{\partial^2 \phi_i}{\partial x^2})^2 dx \right) \quad (\text{B.6b})$$

These equations can be used to estimate the lumped stiffness and mass values for eigen and transfer function analysis shown in Chapter 2. They are also useful in Chapter 3 when designing the DETF resonator system for test structures. Eq. B.6a relates the dimensions of the resonator to the effective mass of the resonator when it is vibrating. It is to be noted that the total mass of the resonator also includes the mass of the electrodes and the connector beam when vibrating at its natural frequency. The first term in Eq B.6b corresponds to the elastic stiffness of the resonator while the second corresponds to stiffness added due to axial loading. The term due to axial loading is important when analysing the resonators are coupled to a proof mass in resonant accelerometer designs [8, 58].

Appendix C

COMSOL® Simulations

The two devices manufactured using the SOIMUMPS process used in the thesis have been analysed with the help of COMSOL® simulations in order to predict the amplitude ratio change and the eigenfrequency of the system. It is important to note that although the eigenfrequency analysis on COMSOL® is quite accurate in determining the resonant frequency of the system, it is not accurate in determining the absolute amplitude of vibration. Thus, only the amplitude ratio as an output metric is being analysed.

C.1 Mechanically coupled device

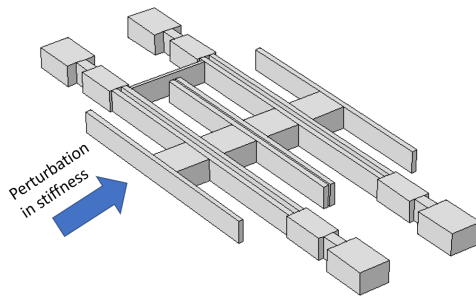


Fig. C.1 Mechanically coupled DETF device

The mechanically coupled device described in Tab. 4.1 is simulated using solid mechanics module in COMSOL®. The two DETF resonators are coupled using a mechanical beam at the nodal point. Stiffness perturbations are applied in the form of a "spring foundation"

that allows the user to add the desired amount of stiffness to one of the resonator bodies (as illustrated in Fig. C.1).

An eigenfrequency analysis is done to identify the two modes of interest – in-phase and anti-phase modes of the anti-phase DETF mode and are plotted in Fig. C.2. As expected of a mode-localised device, the energy is localised to a particular resonator depending on the amount of perturbations added to the system. The mode shapes to the left show the case where negative perturbations are added and the ones to the right show the case where positive perturbations are added.

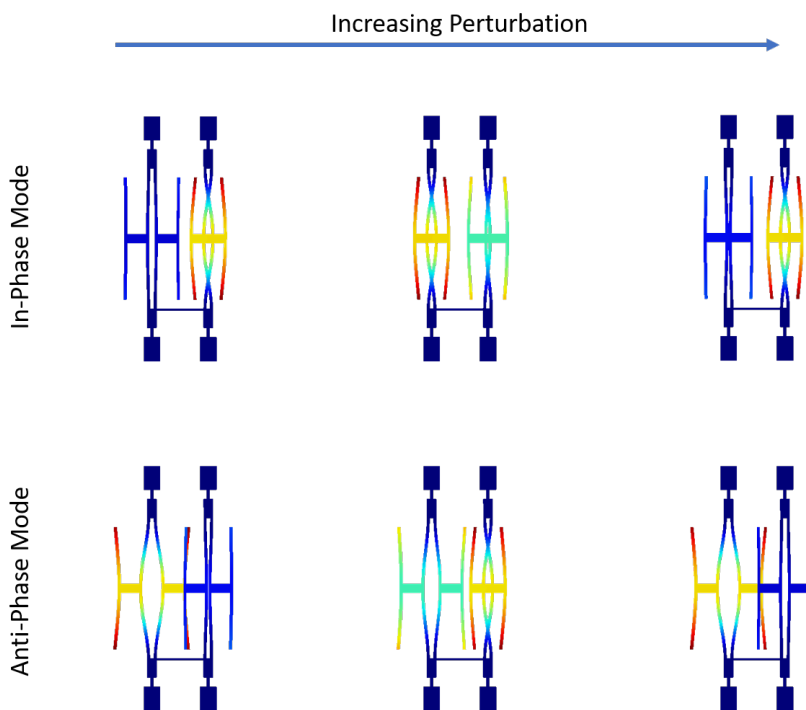
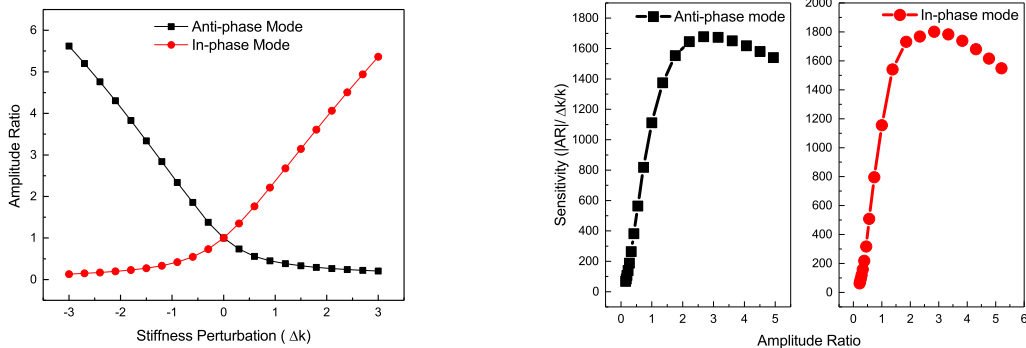


Fig. C.2 Mode shapes of the mechanically coupled device across different perturbations showing the localisation of energy

The maximum displacement amplitudes of each of the resonators across different perturbations are recorded and their ratio is plotted in Fig. C.3a. It is to be noted that this simulation by default assumes that both resonators are driven. Therefore, the drive configuration can be characterised as the DED configuration. The sensitivity at each amplitude ratio is calculated by taking the local slope around that operating amplitude ratio and is plotted in Fig. C.3b. Like its experimental counterpart explained in Chapter 4, the sensitivity is seen to increase as the amplitude ratio increases and then tends to decrease beyond that. This is limited to the design of this particular device and not a reflection on the sensitivity of mode-localised sensors as a whole.



(a) Amplitude ratio variation with across different perturbations
(b) Local sensitivity of the mechanically coupled device at various amplitude ratios.

Fig. C.3 Amplitude ratio variation and sensitivity to input perturbations of mechanically coupled device.

C.2 Electrically coupled device

The electrically coupled device described in thesis is simulated using electromechanics module in COMSOL®. The device has the same dimensions as outlined in Tab. 2.1. The resonators are coupled electrically where the coupling is realised by applying a voltage difference (in this case 10 V) between the two resonators. Perturbations are applied with the help of "spring foundation" that allows the user to add the desired amount of stiffness to one of the resonator bodies (as seen in Fig. C.4).

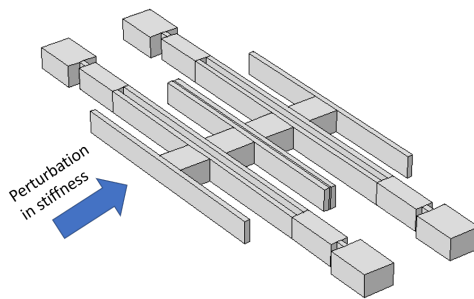


Fig. C.4 Electrically coupled DETF device

An eigenfrequency analysis is done by concentrating the study in the frequency range of interest. The mode shapes of the two modes (in-phase and anti-phase) across various perturbations states are shown in Fig. C.5. Again, the energy is localised to particular

resonators depending on the extent of perturbations added to the system. The mode shapes to the left show the case where negative perturbations are added and the ones to the right show the case where positive perturbations are added.

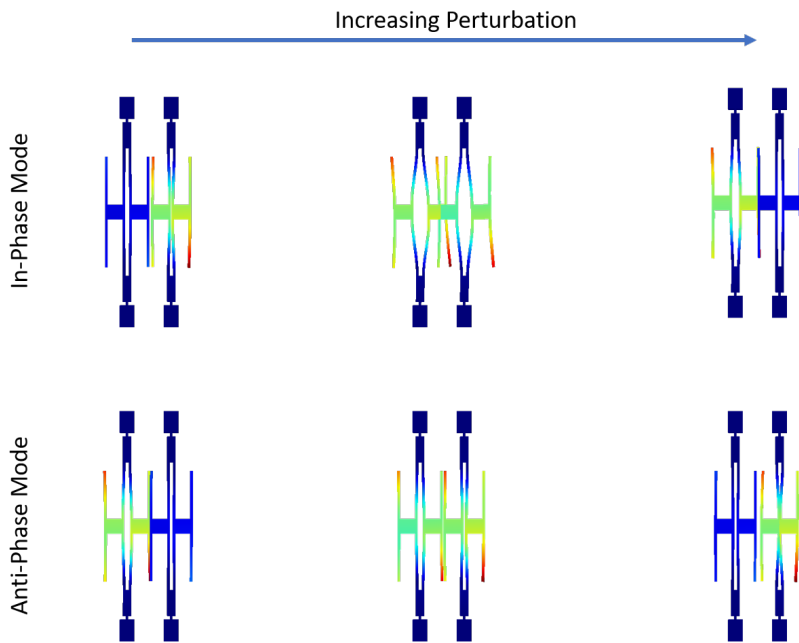
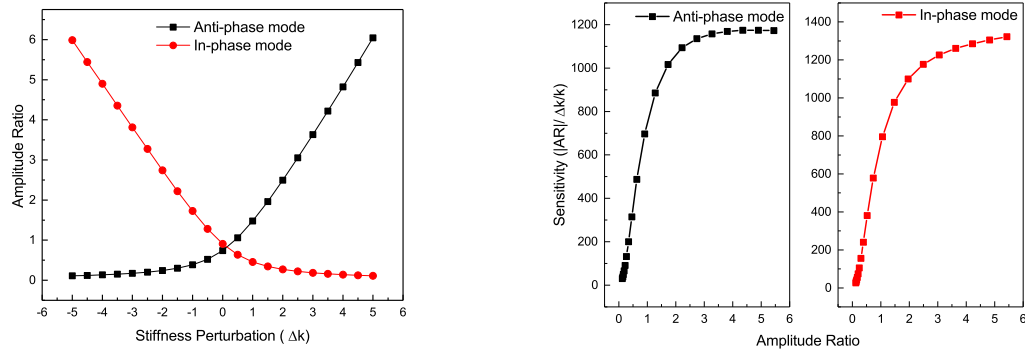


Fig. C.5 Mode shapes of the electrically coupled device across different perturbations showing the localisation of energy

The maximum displacement amplitudes of each of the resonators across different perturbations are recorded and their ratio is plotted in Fig. C.6a. The amplitude ratios of the two modes are symmetrical and change in opposite directions with the change in perturbations as expected. The sensitivity at each amplitude ratio is calculated by taking the local slope around that operating amplitude ratio and is plotted in Fig. C.6b. Unlike the mechanically coupled device with the same device parameters, the sensitivity of the electrically coupled device adheres more closely to that of an ideal mode-localised sensor. The sensitivity is seen to be low at lower amplitude ratios and increases as the amplitude ratios increase until it plateaus at high amplitude ratios. Since the only difference between the two mechanically and electrically coupled devices is the type and position of the coupler, it is prudent to assume that the mechanical coupler poses the problem of a reduced sensitivity at higher amplitude ratios as displayed in Fig. C.3b.

The finite element modelling of these two devices allows us to understand some of the more nuanced dynamics of the resonator systems. The issue with the mechanical coupled device can be solved by reducing the stress build up around the point of contact of the coupler



(a) Amplitude ratio variation with across different perturbations in an electrically coupled device.
(b) Local sensitivity of the electrically coupled device at various amplitude ratios.

Fig. C.6 Amplitude ratio variation and sensitivity to input perturbations of mechanically coupled device.

and the resonators by increasing the distance between the two tines of the DETF. Although not implemented in this particular design, it is a key in designing better MEMS devices.

Appendix D

Amplitude Ratio Noise

It is imperative that the noise calculation for the amplitude ratio needs to be derived from the noise in each channel. To do so, the noise is compared to a statistical variance ($\bar{\sigma^2} = \sqrt{\sigma^2(\cdot)}$) around a mean of a particular output metric. Thus, the variance of the amplitude ratio can be calculated by estimating the variance in each of the channels to the mean of each of the channel's amplitude.

The variance of any bivariate function $\text{Var}(f(X, Y))$ can be defined as [181, 182]:

$$\text{Var}(f(X, Y)) = E[f(X, Y) - E(f(X, Y))]^2 \quad (\text{D.1})$$

where $E(\cdot)$ is the expectation or the mean value of a variable and $f(X, Y)$ is the function of the two variables X and Y . Thus, in order to determine the variance an expression for $E(f(X, Y))$ needs to be derived. This can be done through the use of Taylor expansion of $f(X, Y)$ around a defined mean $\gamma = (\mu_x, \mu_y)$:

$$f(X, Y) = f(\gamma) + f'_x(\gamma)(X - \mu_X) + f'_y(\gamma)(Y - \mu_Y) + R \quad (\text{D.2})$$

where R is the remaining terms of higher orders which will be ignored for this calculation. Thus, $E(f(X, Y))$ can be approximated to be:

$$\begin{aligned} E(f(X, Y)) &= E[f(\gamma) + f'_x(\gamma)(X - \mu_X) + f'_y(\gamma)(Y - \mu_Y)] \\ &= E[f(\gamma)] + E[f'_x(\gamma)(X - \mu_X)] + E[f'_y(\gamma)(Y - \mu_Y)] \\ &= E[f(\gamma)] + f'_x(\gamma)E[(X - \mu_X)] + f'_y(\gamma)E[(Y - \mu_Y)] \\ &= E[f(\gamma)] \end{aligned} \quad (\text{D.3})$$

The last step in Eq. D.3 is achieved by using the fact that $E(X - \mu_X)$ and $E(Y - \mu_Y)$ are both equal to 0. Thus, having got approximations for both terms in Eq. D.1 the approximations of the variance can be derived as:

$$\begin{aligned}\text{Var}(f(X, Y)) &= E[f(X, Y) - f(\gamma)]^2 \\ &\approx E[f(\gamma) + f'_x(\gamma)(X - \gamma_x) + f'_y(\gamma)(Y - \gamma_y) - f(\gamma)]^2 \\ &= E[f'_x(\gamma)(X - \gamma_x) + f'_y(\gamma)(Y - \gamma_y)]^2 \\ &= E f'^2_x(\gamma)(X - \gamma_x)^2 + f'^2_y(\gamma)(Y - \gamma_y)^2 + 2f'_x(\gamma)(X - \gamma_x)f'_y(\gamma)(Y - \gamma_y)\end{aligned}\tag{D.4}$$

Defining $\text{Var}(X) = E|(X - \mu_X)^2|$ and $\text{Cov}(X, Y) = E|(X - \mu_X)(Y - \mu_Y)|$, Equation D.4 can be reduced to:

$$\text{Var}(f(X, Y)) = f'^2_x(\gamma)\text{Var}(X) + f'^2_y(\gamma)\text{Var}(Y) + 2f'_x(\gamma)f'_y(\gamma)\text{Cov}(X, Y)\tag{D.5}$$

For this particular situation, $f(X, Y) = X/Y$ where the X and Y represent the two amplitude of vibrations. Expanding the equation around γ when knowing $f'_X = 1/Y$ and $f'_Y = -X/Y^2$ the following relation can be derived, $f'^2_x(\gamma) = 1/\mu_Y^2$, $f'^2_y(\gamma) = \mu_X^2/\mu_Y^4$ and $f'_X(\gamma)f'_Y(\gamma) = -\mu_X/\mu_Y^3$.

Thus, accordingly the variance of the ratio can be deduced as

$$\sigma_{X/Y}^2 = \frac{\mu_X^2}{\mu_Y^2} \left[\frac{\sigma_X^2}{\mu_X^2} + \frac{\sigma_Y^2}{\mu_Y^2} - 2 \frac{\text{Cov}(X, Y)}{\mu_X \mu_Y} \right]\tag{D.6}$$

This relation can then be adapted to the coupled resonator system by equating the variables X and Y to the motional current i_1 and i_2 . Thus, Eq. D.6 can be remodelled to be:

$$\overline{AR^2} = \sqrt{\frac{\mu_{i1}^2}{\mu_{i2}^2} \left[\frac{\overline{i_1^2}}{\mu_{i1}^2} + \frac{\overline{i_2^2}}{\mu_{i2}^2} - 2 \frac{\text{Cov}(i_1, i_2)}{\mu_{i1} \mu_{i2}} \right]}\tag{D.7}$$

Furthermore, the $\text{Cov}(i_1, i_2)$ can be shown to be negligible when considering the noise sources pertaining to this study. This can be derived by representing the motional current (i) as a mixture of the mean of the signal (μ_i) and the noise associated with each channel ($\overline{i^2}$):

$$i_1 = (\mu_{i1}^2 + \overline{i_1^2})^{\frac{1}{2}} = \mu_{i1}^2 \left(1 + \frac{\overline{i_1^2}}{\mu_{i1}^2}\right)^{\frac{1}{2}}\tag{D.8a}$$

$$i_2 = (\mu_{i2}^2 + \bar{i}_2^2)^{\frac{1}{2}} = \mu_{i2}^2 \left(1 + \frac{\bar{i}_2^2}{\mu_{i2}^2}\right)^{\frac{1}{2}} \quad (\text{D.8b})$$

Using the Binomial expansion of the above expression and only keeping the linear term, they can be simplified as:

$$i_1 = \mu_{i1} \left(1 + \frac{1}{2} \frac{\bar{i}_1^2}{\mu_{i1}^2}\right) = \mu_{i1} + \frac{1}{2} \frac{\bar{i}_1^2}{\mu_{i1}} \quad (\text{D.9a})$$

$$i_2 = \mu_{i2} \left(1 + \frac{1}{2} \frac{\bar{i}_2^2}{\mu_{i2}^2}\right) = \mu_{i2} + \frac{1}{2} \frac{\bar{i}_2^2}{\mu_{i2}} \quad (\text{D.9b})$$

Since, covariance between two variances is defined as $\text{Cov}(X, Y) = E|(X - \mu_X)(Y - \mu_Y)|$, by expanding this expression and using i_1 and i_2 instead of X and Y , the following expression can be achieved[183]:

$$\text{Cov}(i_1, i_2) = E(i_1 i_2) - E(i_1)E(i_2) \quad (\text{D.10})$$

Substituting Eq D.9a and D.9b into Eq. D.10:

$$\begin{aligned} \text{Cov}(i_1, i_2) &= E \left(\left(\mu_{i1} + \frac{1}{2} \frac{\bar{i}_1^2}{\mu_{i1}} \right) \left(\mu_{i2} + \frac{1}{2} \frac{\bar{i}_2^2}{\mu_{i2}} \right) \right) - \\ &\quad E \left(\left(\mu_{i1} + \frac{1}{2} \frac{\bar{i}_1^2}{\mu_{i1}} \right) \right) E \left(\left(\mu_{i2} + \frac{1}{2} \frac{\bar{i}_2^2}{\mu_{i2}} \right) \right) \end{aligned} \quad (\text{D.11})$$

Expanding the equation and subtracting the components that are similar, the following expression for the covariance between the two motional currents can be achieved:

$$\begin{aligned} \text{Cov}(i_1, i_2) &= \frac{1}{4\mu_{i1}\mu_{i2}} E(\bar{i}_1^2 \bar{i}_2^2) - E(\bar{i}_1^2)E(\bar{i}_2^2) \\ &= \frac{1}{4\mu_{i1}\mu_{i2}} \text{Cov}(\bar{i}_1^2, \bar{i}_2^2) \\ &= \frac{1}{4\mu_{i1}\mu_{i2}} \text{Cov}(\text{Var}(i_1), \text{Var}(i_2)) \end{aligned} \quad (\text{D.12})$$

This is an interesting result since it points to the fact that the covariance between the two motional currents is actually equal to the covariance between the individual noises

associated with the two motional currents or as defined in this case, their variances. The variance of a variable X has been defined before as $E(X - E(X))^2$ which can be simplified to $E(X^2) - E(X)^2$. Expected values are considered to be constants and thus expanding the final relation in Eq. D.12 leads to the result $\text{Cov}(\text{Var}(i_1), \text{Var}(i_2)) = 0$.

Thus, it can be shown that Eq. D.7 can be simplified to the following relation that can estimate the amplitude ratio noise (AR^2) by including the relations between the individual motional currents i_1 and i_2 and their respective total noise values \bar{i}_1^2 and \bar{i}_2^2 as estimated in Eq. 5.17:

$$\overline{AR^2} = \frac{\mu_{i1}^2}{\mu_{i2}^2} \left[\frac{\bar{i}_1^2}{\mu_{i1}^2} + \frac{\bar{i}_2^2}{\mu_{i2}^2} \right] \quad (\text{D.13})$$

Using this noise model, the amplitude ratio noise can be predicted and studied very closely in order to optimise of the noise with respect to the various operating conditions such as the stiffness mismatch, the coupling stiffness and the quality factor.

Appendix E

Accelerometer Design

The design process behind each aspect of the resonant mode-localised accelerometer is discussed in detail here. The main components of the accelerometer are the resonator system, the proof mass and suspension design and the force amplification lever system.

E.1 Resonator system

Since a resonant technique is being used for sensing, optimising resonators play a key part in the sensor design. A simple C-C beam configuration ($700 \mu\text{m} \times 7 \mu\text{m}$) is chosen for the resonator over other designs such as double ended tuning fork (DETF) topologies that offer lower anchor losses. The simple design offers more control over the final fabricated device as manufacturing tolerances have minimum effect on the resonator. This means that the dimensions of the final sensor is closest to those of the simulated device. Furthermore, the axial force that is applied to the resonators is maximized in this configuration as compared to the stiffer DETF configuration. Thus, a C-C beam topology increases the relative stiffness applied on the resonator. Additionally, the simple design structure allows for the option to use the first and the second flexural modes for sensing as seen from the electrode configuration in Fig. E.1.

The stiffness and mass of the resonators can be estimated as follows in order to calculate the theoretical resonant frequency of the sensor:

$$k_{eff} = \frac{16Etw^3}{l^3} = \frac{16 \times 169e9 \times 40e-6 \times (7e-6)^3}{(700e-6)^3} = 108.4 \text{ N/m} \quad (\text{E.1a})$$

$$m_{eff} = 0.384 \times \rho w l t = 0.384 \times 2330 \times 7e-6 \times 700e-6 \times 40e-6 = 1.752e-10 \text{ Kg} \quad (\text{E.1b})$$

$$f_0 = \frac{1}{2\pi} \times \sqrt{\frac{k_{eff}}{m_{eff}}} = 125.2 \text{ kHz} \quad (\text{E.1c})$$

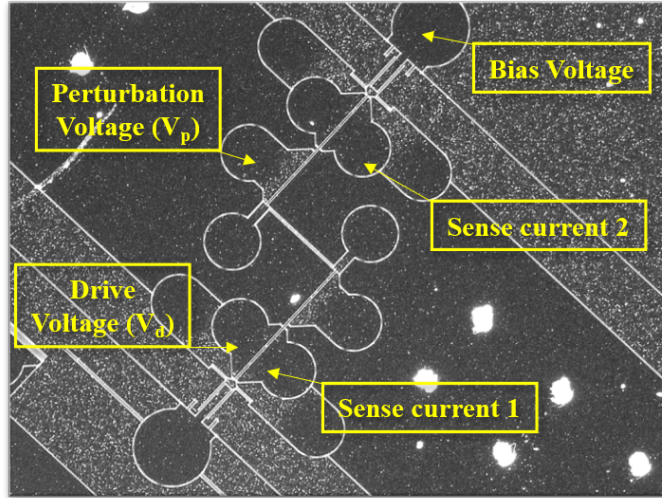


Fig. E.1 Optical micrograph of the coupled resonator system.

A mechanical coupler has been chosen in this particular design although an electrostatic coupling has been shown to provide greater flexibility with choosing coupling stiffness [34]. This is mainly to make the accelerometer more robust since an electrostatic coupler increases the chances of resonators pulling in or collapsing on each other due to external shocks. Additionally, it is more practical to use a mechanical coupler for a sensor as it minimizes the number of voltage sources needed for its operation as well. As it has been previously established that the sensitivity increases with a decrease in the coupling stiffness [23, 66], the coupler is designed to be $400 \mu\text{m} \times 4 \mu\text{m}$ (considering the limit of the aspect ratio achievable through this fabrication process is 100:1).

Due to the simplicity of the process, an experimental method is chosen to determine the coupling spring stiffness. The resonator systems are both tuned to the *veering* region where the frequency difference between the in-phase and anti-phase is the smallest. The relation between the angular frequencies ($\Delta\omega \ll \omega_l$) of the unperturbed system was derived in Eq. 2.5 and this can be used to estimate the coupling constant as follows:

$$\begin{aligned}
\omega_2^2 - \omega_1^2 &= \frac{k}{m} - \frac{k + 2k_c}{m} \\
\implies (\omega_2 + \omega_1)(\omega_2 - \omega_1) &= \frac{2k_c}{k} \omega_1^2 \\
\implies 2\omega_1(\omega_2 - \omega_1) &= \frac{2k_c}{k} \omega_1^2 \\
\implies \frac{\Delta f_{modes}}{f_0} &= \frac{k_c}{k}
\end{aligned} \tag{E.2}$$

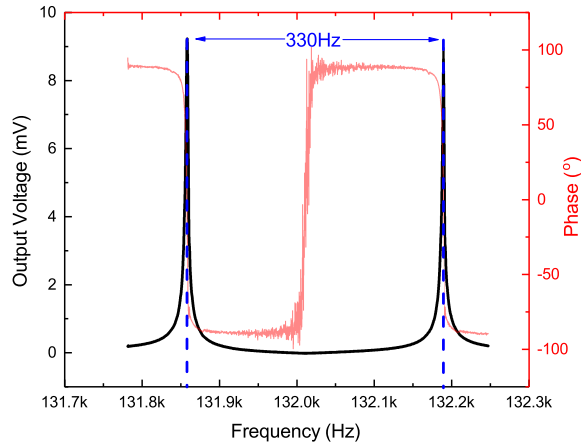


Fig. E.2 Open-loop sweep of one of the coupled resonator systems.

Hence, the experimental open-loop frequency sweep should be enough to accurately determine the coupling spring constant. The open-loop sweep results at *veering* of one system is shown in Fig E.2. A similar test is done for the second system and the frequency difference was found to be 332 Hz coupling spring constant of both systems are calculated as:

$$k_{c1} = k \frac{\Delta f_{modes}}{f_0} = 108.4 * \frac{330}{132000} = 0.2713 \text{ N/m} \tag{E.3a}$$

$$k_{c2} = k \frac{\Delta f_{modes}}{f_0} = 108.4 * \frac{332}{132000} = 0.2726 \text{ N/m} \tag{E.3b}$$

These analytical values are used later in the chapter to derive the theory of a differential amplitude ratio output metric.

E.2 Electrical ports

The transduction scheme has been designed so that either the first or the second flexural mode can be excited for the sensing purposes. The first mode offers higher sensitivity to input acceleration due to the axial force being transferred to the resonators being greater than in the second mode. Furthermore, as seen in Fig. 3.3b, the noise of the transimpedance amplifier (TIA) used for the amplitude readout has a corner frequency around 120 kHz and increases beyond that frequency. As the first mode is designed to be at 130 kHz, it offers lower amplifier noise than if the second mode (350 kHz) is in operation. However, since the first mode has lower stiffness, it is more susceptible to nonlinear effects that could be coupled into the results.

The bias voltage is added on the body of the resonator rather than using a Bias-T at the electrodes. This is done to avoid any charging effects that result in drifts in the output voltage and the frequency. However, it requires the substrate and the body of the proof mass to be at the same potential to avoid the proof mass from deforming in the z-direction. This method can be used since the fabrication process allows for substrate biasing. A voltage regulator is used to control the voltage applied on the body. Since any changes in this voltage directly result in a change in the output voltage, the regulator reduces the amplitude noise at the output. As low-noise regulators are limited to lower voltages, a 10 V voltage regulator (REF102U) is chosen to regulate the bias voltage for this sensor.

The transduction force can be modelled after the force applied by parallel plate capacitor of length(L), thickness (t) and gap (d) with an ac drive voltage (V_{ac}) and bias voltage (V_{DC}) as:

$$F_{drive} = -\frac{V_{ac}V_{DC}}{2} \frac{\partial C}{\partial x}$$

where, $C = \frac{\epsilon_0 l t}{d - x}$ (E.4)

Assuming the resonators are operating in linear region at small oscillation amplitudes, the drive force can be simplified to:

$$F_{drive} = -\frac{V_{ac}V_{DC}}{2} \frac{\epsilon_0 lt}{d^2} \quad (\text{E.5})$$

An electrical port has been used for perturbation voltage in addition to the stiffness perturbations added axially from acceleration. This is mainly to tune the operating amplitude ratios since fabrication tolerances lead to asymmetrical stiffness in the resonators. Furthermore, this port gives the user the chance to tune individual systems separately where as the axial perturbations would lead to both systems experiencing a differential change.

A negative stiffness perturbation is added by varying the voltage applied (V_p) on the perturbation port which can be calculated for the parallel plate capacitor as:

$$k_p = -\frac{V_{DC}^2}{2} \frac{\partial^2 C}{\partial x^2}$$

where, $C = \frac{\epsilon_0 lt}{d - x}$ (E.6)

Assuming small oscillation amplitudes, the stiffness perturbations added can be calculated as:

$$k_p = -\frac{V_{DC}^2}{2} \frac{\epsilon_0 lt}{d^3} \quad (\text{E.7})$$

There are several comb drive electrodes around the proof mass that allow for an electrical actuation of the proof mass that is useful in the bandwidth measurements. There are 4 sets of 440 inter-digitated comb fingers that are 20 μm and separated by 2 μm that can be used to actuate the proof mass to test the device without any physical external acceleration producing devices such as shakers. The force exerted by each individual comb finger ports with N comb fingers, l length, t thickness and d gap can be estimated to be:

$$F_{comb} = -\frac{V_{ac}V_{DC}}{2} \frac{\partial C}{\partial l}$$

where, $C_{\text{comb fingers}} = \frac{N\epsilon_0 lt}{d}$ (E.8)

The force is linear with respect to the various dimensions in the direction of the actuation and is calculated as:

$$F_{comb} = -\frac{V_{ac}V_{DC}}{2} \frac{N\epsilon_0 t}{d} \quad (\text{E.9})$$

E.3 Proof mass and force amplification levers

The design of the proof mass mainly revolves around the choice of the suspensions architecture. The suspensions need to be stiff to counter the effect of gravity in the cross-axis (z-axis and x-axis) but compliant in the sense axis (y-axis) to not hinder with the sensitivity. Furthermore, the suspensions alongside with the proof mass will determine the mechanical bandwidth of the sensor. The inertial force applied by the proof mass scales with its size. Thus, larger proof masses apply larger force; therefore, increasing the sensitivity of the sensor. However, a large proof mass would also reduce the mechanical bandwidth of the sensor as $\omega_{mass} = \sqrt{k_{sus}/m}$. Since the sensor's bandwidth is defined by the resonance of the proof mass, the bandwidth is inherently dependent on the resonance of the proof mass.

A folded beam configuration is used for the suspensions design of the proof mass. A micrograph of the four anchors for the proof mass each having 4 folded beams ($500 \mu\text{m} \times 6 \mu\text{m}$) (inset) that are connected in parallel is shown in Fig. E.3.

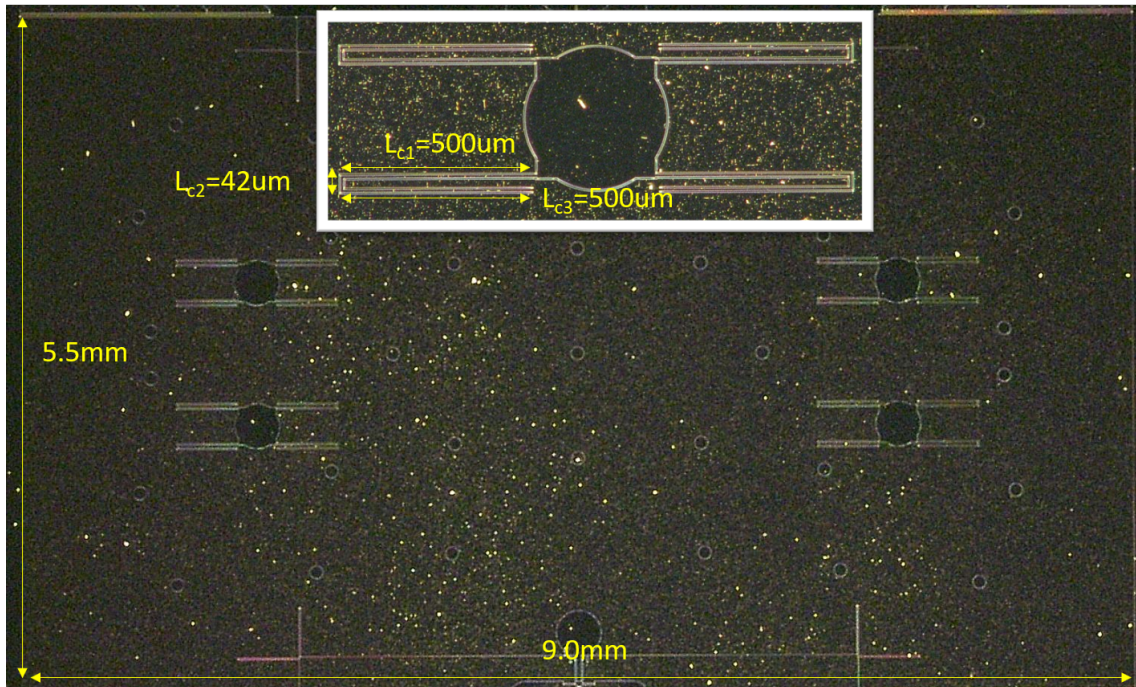


Fig. E.3 Optical micrograph of the suspensions of the proof mass.

The stiffness of all 16 folded beams in parallel in the sensitive axis can be estimated to be[180, 184]:

$$k_{sus} = 16 \times \frac{2Et w_{sus}^3}{l_{sus}^3} = 16 \times \frac{2 \times 169e9 \times 40e - 6 \times (6e - 6)^3}{(500e - 6)^3} \approx 374 \text{ N/m} \quad (\text{E.10})$$

The proof mass can be estimated roughly by excluding the etch holes and the area taken up by the suspensions and assuming it to be a solid of dimensions $9000 \mu\text{m} \times 5500 \mu\text{m} \times 40 \mu\text{m}$. Therefore, a rough estimation of the proof mass is:

$$m_{proof} = \rho l_m w_m h_m = 2330 \times 9000e - 6 \times 5500e - 6 \times 40e - 6 \approx 4.6 \times 10^{-6} \text{ kg} \quad (\text{E.11})$$

Thus, the mechanical bandwidth of the proof mass can be estimated by estimating the resonant frequency of the proof mass and the suspensions. As it behaves as a low pass filter, any frequencies before the resonant frequency can be sensed accurately by the accelerometer and is regarded as the bandwidth of the sensor:

$$f_{proof} = \frac{1}{2\pi} \sqrt{\frac{k_{sus}}{m_{proof}}} = \frac{1}{2\pi} \sqrt{\frac{374}{4.6e - 6}} = 1443 \text{ Hz} \quad (\text{E.12})$$

The force applied by the proof mass needs to be transduced to the resonators to afflict a change in the sensed amplitude ratio. There are traditionally two ways in which this can be implemented – (a) transversely, through the use of movable capacitive plates, and (b) axially, through the use of micro-levers. Force applied transversely consists of a proof mass attached to a movable electrode that applies negative stiffness perturbations when it moves. The stiffness perturbations are inversely proportional to the cubic factor of the gap distance (as derived seen in Eq. E.7). Although it may seem that this configuration applies a higher stiffness perturbation, the disadvantages are twofold- (1) the applied perturbations are highly nonlinear in nature and hence, reduce the dynamic range of the sensor, and (2) the sensor is highly probable to encounter pull-in effects with large input gravity changes which can structurally damage the sensor.

An axial force application system involves attaching one end of the C-C beam to the proof mass through the use of micro-levers. The force gets transduced through these micro-levers as a stiffness change. The advantage of this system is that (a) it provides a linear stiffness perturbation, and (2) it can apply a greater force without damaging the structure,

thus, allowing for a greater dynamic range. However, the applied stiffness perturbation is small. Therefore, there needs to be a micro-lever system to amplify the force being applied on the resonator. A simple lever system is shown below:

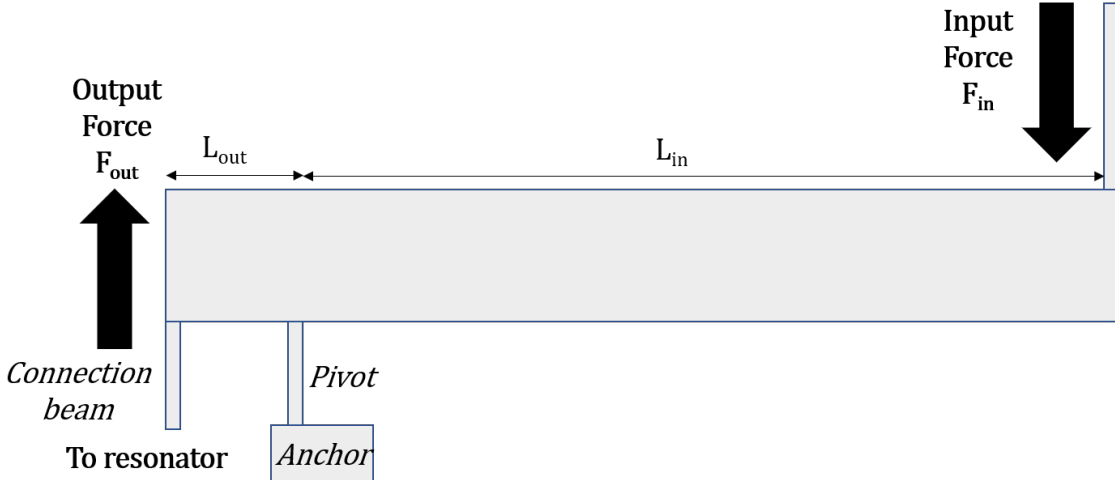


Fig. E.4 A schematic of the lever for force amplification.

The lever would have an amplification factor defined to be F_{out}/F_{in} . In an ideal lever, this would translate to L_{in}/L_{out} but unlike in the regime of macro-lengths, there is no way to implement a hinge in MEMS size [185]. Therefore, a lever needs to be constructed with the help of flexural beams. However, due to the non-zero rotational stiffness and the finite vertical stiffness of the beams used, energy loss occurs in translating the force from the proof mass to the resonator[186]. Hence, the lever amplification factor is always smaller than the ideal amplification factor. This is especially true when looking at large lever ratios (> 20) and finite element analysis should be used to simulate the actual amplification factor[187, 188].

However, it is not just the lever ratio that has an impact on the amplification factor but the stiffness of the suspensions and the vertical stiffness of the resonator also play a big role in determining the effective amplification factor. The effective amplification factor (EA_{lever}) can be defined as the translation of the inertial force experienced by the proof mass to the resonators. Hence,

$$EA_{lever} = \frac{F_{out}}{F_{inertial}} = \frac{F_{out}}{m_{proof}a_{in}} \quad (\text{E.13})$$

Since the suspensions supporting the proof mass have a non-zero stiffness in the sensing directions, they absorb some of the inertial force by deforming upon acceleration. Therefore, the inertial force can be split into:

$$F_{inertial} = F_{sus} + F_{in} \quad (\text{E.14})$$

Assuming that the displacement experienced by the input-end of the lever, the suspensions in the sensing axis and the proof mass is the same, Eq. E.14 can be simplified to:

$$m_{proof}a_{in} = k_{sus}x + k_{in}x \quad (\text{E.15})$$

Thus, the effective amplification factor can be reduced to:

$$EA_{lever} = \frac{k_{in}A_{lever}}{k_{sus} + k_{in}} \quad (\text{E.16})$$

Assuming that the beam deformations are negligible, k_{in} can be estimated in terms of the axial stiffness of the resonator (k_{ra}) under vertical load as:

$$k_{in} = \frac{k_{ra}}{A_{lever}^2} \quad (\text{E.17})$$

Substituting Eq. E.17 into E.16, the following relation can be achieved to include the suspension stiffness, axial stiffness of the resonator and the lever amplification factor:

$$EA_{lever} = \frac{k_{ra}A_{lever}}{k_{sus}A_{lever}^2 + k_{ra}} \quad (\text{E.18})$$

Hence, through Eq. E.18, the maximum effective amplification factor of the lever can be deduced to be $A_{lever}/2$ when $A_{lever} = \sqrt{k_{ra}/k_{sus}}$.

The axial stiffness of the resonator can be calculated as [180, 189]:

$$k_{ra} = \frac{2Etw_r}{L_r} = \frac{2 \times 169e9 \times 40e-6 \times 7e-6}{700e-6} = 135.2 \times 10^3 \text{ N/m} \quad (\text{E.19})$$

Using the values of stiffness from Eqs. E.10 and E.19, the amplification factor and the effective amplification factor can be deduced as:

$$A_{lever} = \sqrt{\frac{k_{ra}}{k_{sus}}} = \sqrt{\frac{135.2e3}{374}} \approx 19 \quad (\text{E.20a})$$

$$EA_{lever} = \frac{A_{lever}}{2} = 9.5 \quad (\text{E.20b})$$

The design values calculated in this section are further used in simulating the dynamics of the differential amplitude ratio output metric and its scale factor improvement as compared to a single amplitude ratio output metric and the traditional frequency shift output metric.